Sources and biogeochemistry of bio-active trace metals in the Southern Ocean and coastal Antarctica

Perspectives from their isotopes

Hung-An Tian

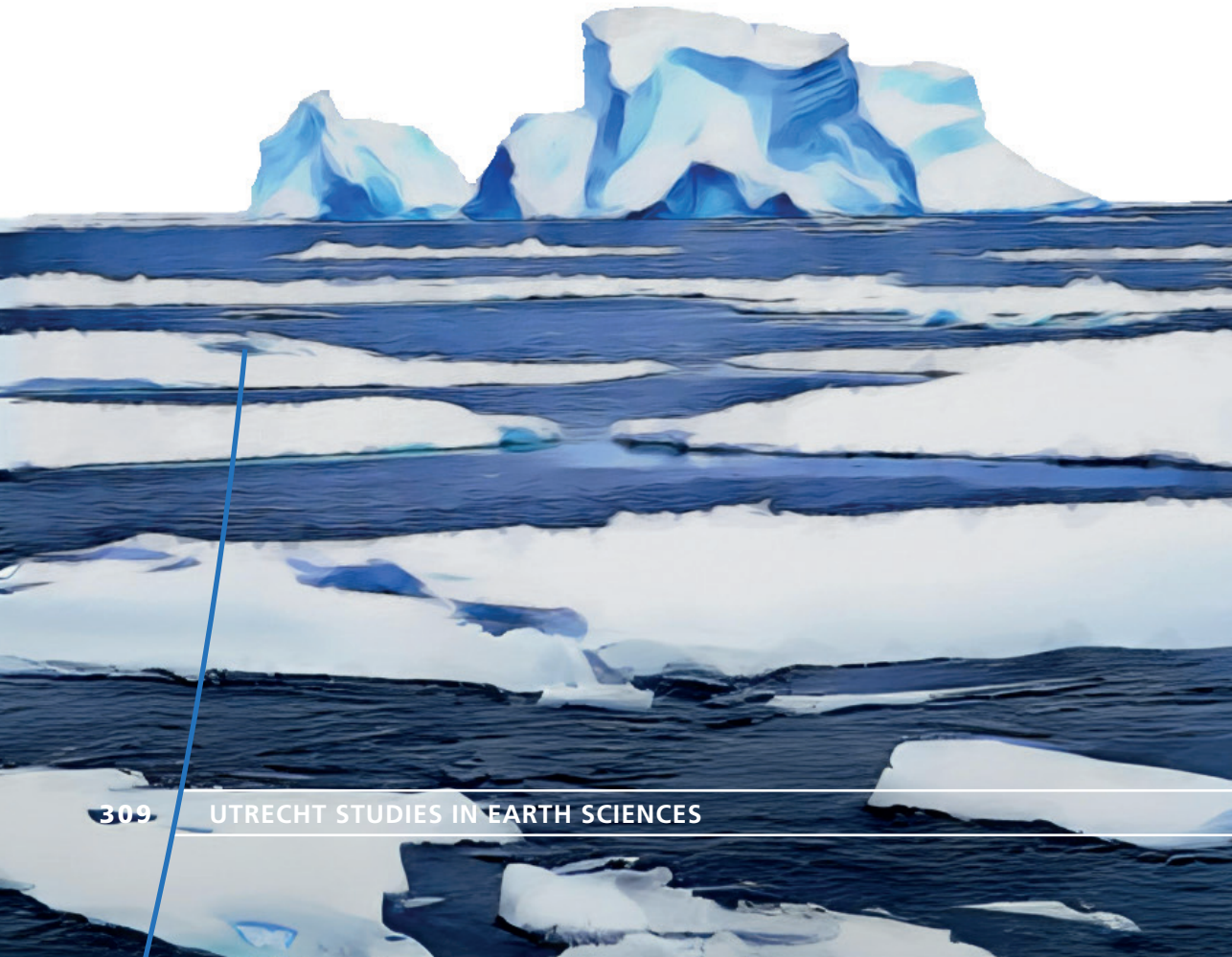

309 UTRECHT STUDIES IN EARTH SCIENCES

Layout & Design: Hung-An Tian
Cover design: Hung-An Tian & Margot Stoete
Print: Ipskamp Printing
ISBN: 978-90-6266-682-9
USES: 309

SOURCES AND BIOGEOCHEMISTRY OF BIO-ACTIVE TRACE METLAS IN THE SOUTHERN OCEAN AND COASTAL ANTARCTICA:

PERPECTIVES FROM THEIR ISOTOPES

BY HUNG-AN TIAN

Promotoren:

Prof. dr. R. Middag
Prof. dr. G.J. Reichart

Copromotor:

Dr. T.M. Conway

Beoordelingscommissie:

Dr. W. Abouchami
Prof. dr. H. Brinkhuis
Prof. dr. J.B.M. Middelburg
Prof. dr. K. Pahnke
Prof. dr. ir. C.P. Slomp

Sources and biogeochemistry of bio-active trace metals in the Southern Ocean and coastal Antarctica: perspectives from their isotopes

Bronnen en bio-geochemie van biologisch actieve sporenelementen in de Zuidelijke Oceaan en kustgebieden van Antarctica: inzichten vanuit de isotopen

(met een samenvatting in het Nederlands)

以海洋微量金屬之穩定同位素研究其於南大洋與南極洲沿岸地區之來源與生物地球化學

(附中文摘要)

Proefschrift

ter verkrijging van de graad van doctor aan de
Universiteit Utrecht
op gezag van de
rector magnificus, prof. dr. H.R.B.M. Kummeling,
ingevolge het besluit van het college voor promoties
in het openbaar te verdedigen op

vrijdag 15 maart 2024 des middags te 4.15 uur

door

Hung-An Tian

geboren op 18 oktober 1990
te Taitung, Taiwan

TABLE OF CONTENTS

SUMMARY IN ENGLISH

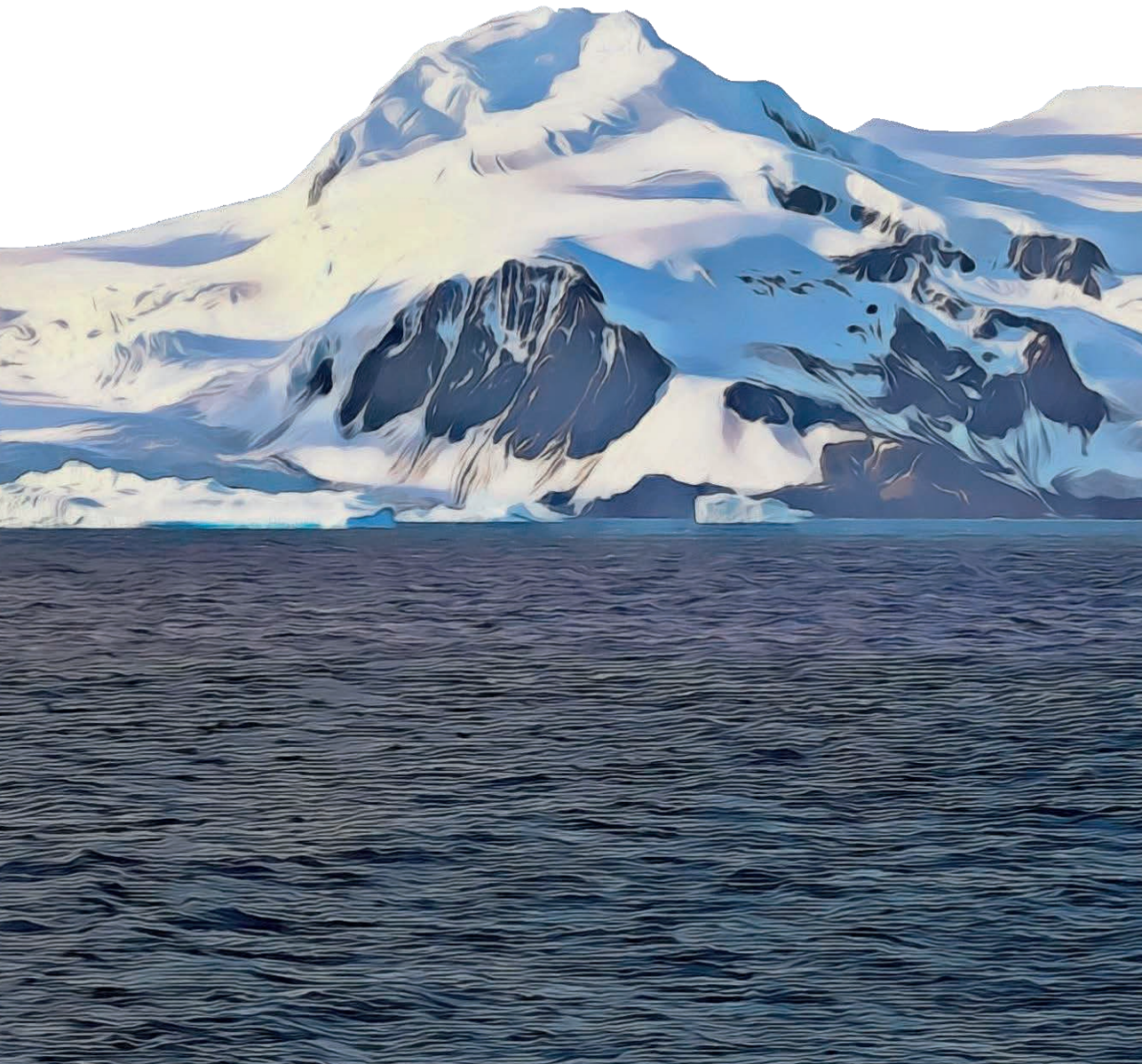

Bio-essential trace elements, such as iron (Fe) and zinc (Zn), also known as micronutrients, are critical for all life because of their biochemical roles in various metabolic processes. They are also pivotal for marine phytoplankton growth, the base of the marine food web. For instance, Fe participates in vital functions such as photosynthesis, respiration, and nutrient uptake, while Zn is present in nearly 300 enzymes and is utilized in common enzymes such as carbonic anhydrase (CA) and alkaline phosphatase (AP) for CO_2 hydration and organic phosphorus uptake, respectively. Moreover, other trace elements are not strictly bio-essential, for example, cadmium (Cd), has been shown to replace Zn in CA in marine diatoms when Zn becomes unavailable. As a result, the availability of these trace elements in oceans significantly impacts marine ecosystems and, hence, global climate. The availability of trace elements in oceans is influenced by external sources, chemical speciation, and biogeochemical processes such as biological uptake, remineralization, and scavenging, which regulate primary productivity in the surface ocean. However, dissolved concentrations of these elements are often low in the surface ocean where they are needed for primary productivity, making sampling and accurate analysis a challenge.

In the oceans, High-Nutrient Low-Chlorophyll (HNLC) surface regions are characterized by sufficient macronutrient (e.g., phosphate, nitrite/nitrate, sillicate) supply but limited primary productivity due to the lack of Fe and light. As the largest HNLC region, the Southern Ocean is suggested to have a great potential to absorb a large amount of atmospheric CO_2 if the phytoplankton requirements for Fe and light are fulfilled. For example, in coastal Antarctica, long-lasting phytoplankton blooms over spring and summer have been observed and attributed to increasing external Fe input, such as upwelling of deep water, continental sediments, and sea ice- or glacier-associated Fe. In addition to the exchange of atmospheric CO_2, the Southern Ocean plays a vital role in the redistribution of heat and freshwater in the global climate system. For instance, dense water formation driven by extensive sea ice production and brine rejection during winter in coastal Antarctic regions contributes to the formation of Antarctic Bottom Water (AABW) that circulates northward into multiple ocean

basins and facilitates advection of water masses between high and low latitude oceans. Overall, given the importance of the Southern Ocean to the global climate and ocean circulation, it is crucial to understand its marine biogeochemistry, notably the cycling of trace elements in coastal Antarctic regions, and their influence on globally relevant processes.

In the past two decades, the international GEOTRACES program has explored the biogeochemical cycles and oceanic distributions of trace elements and their isotopes in oceans. The combination of concurrent concentration and isotopic composition analyses of trace elements has greatly helped us to disentangle complex biogeochemical processes and identify different external sources. However, compared to the Pacific, Atlantic, Indian, and Arctic Oceans, dissolved trace element data in the Southern Ocean, especially around coastal Antarctica, are relatively scarce owing to limited sampling campaigns due to harsh weather conditions and poor accessibility related to extensive sea ice coverage in coastal Antarctica, as well as the requirement of relatively large water volumes needed to determine the extremely low concentrations (e.g., Fe) in the surface Southern Ocean. The scarcity of data has not only hindered our understanding of global nutrient cycling and how changes in coastal Antarctica (e.g., ice melting) impact nutrient supply, but also limited our computational ability (e.g., biogeochemical models) to accurately predict the changes in biogeochemistry and cycling of trace elements in the future at a global and long-term scale.

In this thesis, two bio-essential trace elements, Fe and Zn, together with Cd, and their isotopic compositions, are studied in two distinct coastal Antarctic regions – the Amundsen Sea (AS) and the Weddell Sea (WS). The AS is characterized by the extensive intrusion of warm modified Circumpolar Deep Water (mCDW) onto the continental shelf through glacial troughs that lead to rapid ice sheet melting as it flows under ice shelves (i.e., Dotson Ice Shelf, DIS). The upwelling of mCDW also accelerates sea ice melting, creating polynyas (i.e., open areas surrounded by sea ice) that harbour productive and long-lasting phytoplankton blooms in spring-summer – the Amundsen Sea Polynya

(ASP) shows the highest annual net primary production rate per unit area among Antarctica polynyas. The WS is part of the wind-driven Weddell Gyre, which is a crucial component of the global oceanic circulation as a primary formation region of deep-water masses. In the southern and western parts of the WS, dense, saline, cold shelf water forms through sea ice formation and brine rejection in winter, which subsequently descends along the continental slope, eventually exiting the WS through the Scotia Sea, contributing to AABW and the global ocean conveyor belt. Both the AS and the WS hold the potential to influence or be influenced by the global biogeochemical cycles of trace metals.

Given the lack of dissolved and particulate data of Zn and Cd in the AS, the impacts of mCDW intrusion and ice shelf melting on the cycling of these two elements and their biogeochemistry in the ASP are understudied. In **Chapter 2**, I report the first combined dataset of dissolved and particulate Zn and Cd in the AS and evaluate potential external sources. The study reveals that upwelled mCDW is the primary source of dissolved Zn (dZn) and Cd (dCd), with continental shelf sediments being a modest source. Ice shelf melting from the DIS and sea ice melting are not significant contributors for dZn and dCd. Additionally, I compare the relative contributions of particulate Zn and Cd using two common approaches for evaluating particle composition: the operationally-defined labile and refractory fraction, and the elemental composition-based biogenic and lithogenic fraction. Findings indicate that in productive bloom regions like the ASP, the labile fraction does not always equate to the biogenic fraction. This discrepancy is attributed to inaccuracies in representing true phytoplankton uptake ratios through the slope of dissolved metal-phosphate relationships, and varying phytoplankton communities. Lastly, this study suggests that local variations in Fe availability can influence the uptake ratios of Cd and Zn across short spatial scales in the ASP, with different phytoplankton groups (such as haptophytes and diatoms) having distinct Zn, Cd, and P quotas. These insights into marine cycling and phytoplankton uptake ratios of Zn and Cd in the AS contribute to a deeper understanding of their biogeochemistry in Antarctic phytoplankton blooms.

Although a handful of studies of dissolved Fe concentration ([dFe]) in the open Southern Ocean have contributed to our understanding of the biogeochemistry and marine cycling of Fe, the identification of external sources of Fe, notably sedimentary input, and the biogeochemical processes that affect Fe cycling in Antarctic waters remain relatively unclear. In **Chapter 3**, I employ a combination of [dFe] and Fe isotopic composition (δ^{56}Fe) to identify Fe sources and understand the biogeochemical processes in the region, especially around the DIS and within the ASP phytoplankton blooms. Firstly, I characterize two distinct sedimentary mechanisms – reductive dissolution (RD) and non-reductive dissolution (NRD). Along with upwelled mCDW, these two sedimentary sources are the primary Fe input in the AS, potentially fuelling phytoplankton blooms in the ASP. Secondly, I explore how rapid melting of the DIS impacts Fe cycling, hypothesising enhanced preservation of lithogenic colloidal Fe(III) from shelf melting and sedimentary NRD, and the differential loss of Fe^{2+} in combination with Fe-binding ligands. These factors predominantly influence [dFe] and δ^{56}Fe beneath the ice shelf system. Lastly, I observe distinct Fe isotopic fractionation within two phytoplankton blooms, dominated by haptophytes and diatoms. This indicates differences in uptake mechanisms and pathways between species and suggests that biogeochemical processes like ligand complexation, scavenging, and remineralization play crucial roles in the highly productive ASP. Overall, Chapter 3 offers a further understanding of external Fe sources and biogeochemical processes in the AS. It provides a baseline for how changing conditions in Antarctica might affect Fe cycling in the Southern Ocean and beyond.

Building on the insights from Chapter 2, in **Chapter 4** I delve deeper into the sources of dZn and dCd in the AS by examining the isotopic composition of Zn (δ^{66}Zn) and Cd (δ^{114}Cd). This analysis aligns with the findings from Chapter 2, which utilized dissolved concentrations of Zn ([dZn]) and Cd ([dCd]). These findings reconfirm that the primary source of dZn and dCd in the AS is upwelled mCDW, with minimal contributions from continental sediments and ice shelf meltwater. In the WS, I also explore the changes in [dZn], [dCd], δ^{66}Zn, and δ^{114}Cd during the formation of dense water, particularly focusing on the

precursor of Weddell Sea Bottom Water (pre-WSBW), Warm Deep Water (WDW), and Weddell Sea Deep Water (WSDW). The findings indicate that physical mixing of these water masses is the key factor influencing the evolution of [dZn] and [dCd] in the process of WSBW formation. Interestingly, this mixing process results in almost no change in δ^{66}Zn and δ^{114}Cd, as these water masses share similar isotopic compositions. Lastly, the chapter sheds light on the variability in isotopic signatures in the surface waters of the AS and WS. This variability underscores the differences in surface processes affecting the cycling of Zn and Cd in Antarctic waters, such as adsorption and ligand complexation for Zn, and biological uptake for Cd.

Besides Zn and Cd, I also focus on Fe in the WS, notably its potential sources and the processes influencing [dFe] and δ^{56}Fe during the formation of WSBW in **Chapter 5**. I find that meltwater from the Antarctic Peninsula and continental shelf sediments contribute substantially isotopically light Fe to the shelf water, predominantly through RD, accounting for up to 90% of the input. This primary isotopically light signature in shelf water is initially preserved across varying [dFe]. However, as the dense shelf water moves down the continental shelf slope, this signature gradually shifts towards heavier signatures. I suggest that this transition in δ^{56}Fe during the transformation of shelf water into pre-WSBW is mainly driven by physical mixing with WDW and WSDW. This implies that the sediment- and glacier-derived light Fe signature is likely diluted in the northward-flowing WSBW and AABW, underscoring the role of physical mixing in Fe cycling in these bottom waters. Additionally, I observe a consistent δ^{56}Fe minimum at intermediate depths in the WS, indicative of long-range transport of an isotopically light Fe signal. Previous hypotheses attributed this to either subsurface remineralization or sedimentary light input, where this research supports the latter. My work suggests that sedimentary derived light Fe from the Antarctic Peninsula shelves can be preserved and transported over long distances, offering a distinct endmember for tracing sediment-derived δ^{56}Fe beyond the shelf region. This insight enhances the potential of using δ^{56}Fe as a tracer for sediment supply in the open ocean.

Overall, this thesis presents the first set of observational data for $\delta^{56}Fe$ in both the AS and the WS, as well as the first data for $\delta^{66}Zn$ and $\delta^{114}Cd$ in the AS and greatly improved coverage of the WS. These insights are pivotal in understanding the external sources influencing the distributions of these elements in the Southern Ocean. Furthermore, this thesis delves into the isotopic systematics of these elements in the ocean. It illuminates the fractionation effects caused by various biogeochemical processes, such as biological uptake, adsorption, and ligand complexation. This investigation not only enhances our understanding of these processes but also provides valuable perspectives on using isotopic compositions as tools to investigate biogeochemical processes. Finally, given the limited availability of observational trace element data in the Southern Ocean and coastal Antarctica, the findings and discussions presented in this thesis can be applied to broader biogeochemical studies and enhancing the use and projection capability of environmental modelling.


DMC SWL 10T X 3-12M
ARACN


DMC SWL 10T X 3-12M

SAMENVATTING IN HET NEDERLANDS

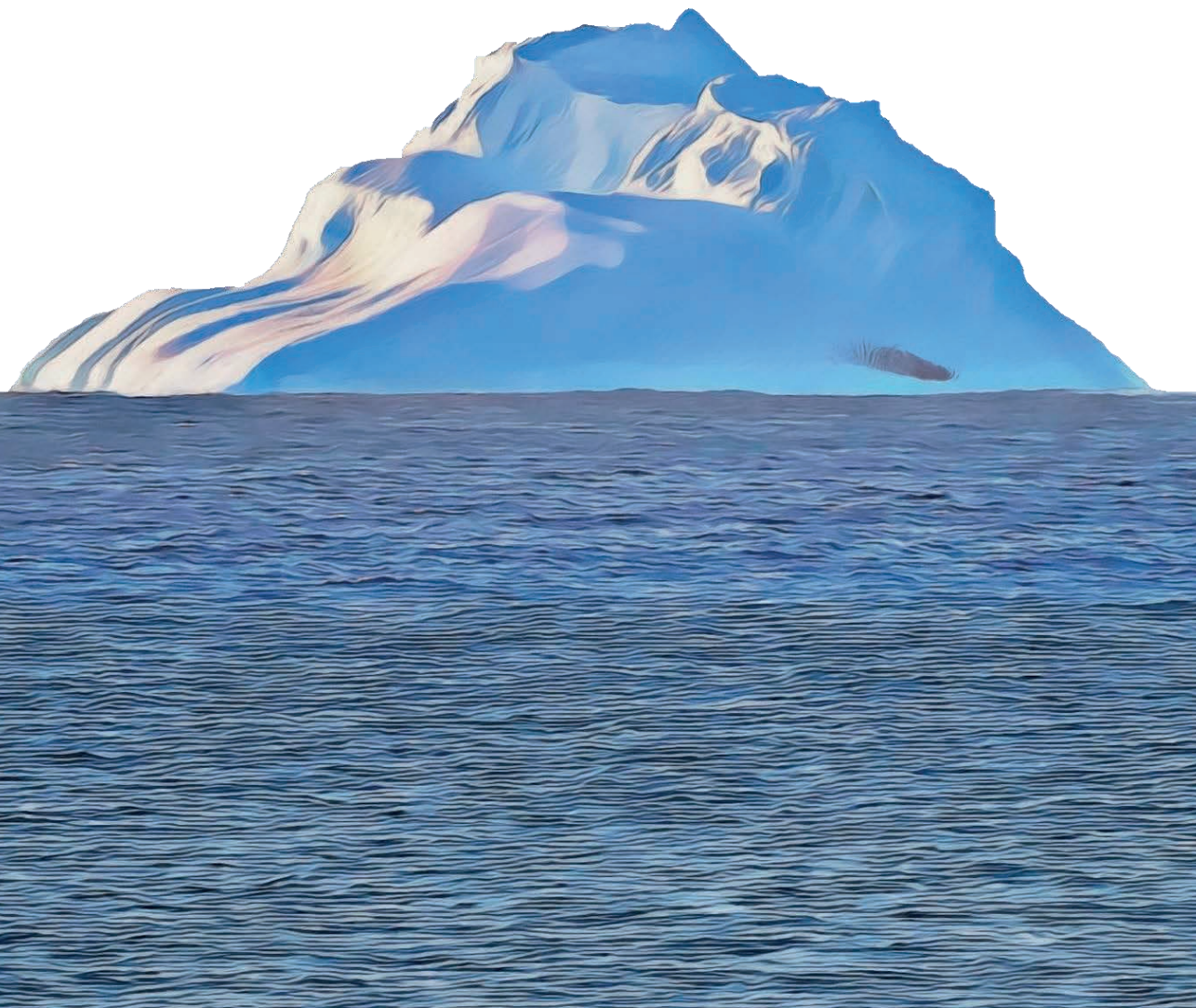

De sporenelementen ijzer (Fe) en zink (Zn) zijn micronutriënten, en cruciaal voor het leven vanwege de rollen die ze spelen in het geheel van biochemische processen dat plaatsvindt in cellen van organismen. Ze zijn dus ook essentieel voor de groei van marien fytoplankton, de basis van het mariene voedselweb. IJzer, bijvoorbeeld is onontbeerlijk in de fotosynthese, ademhaling en de opname van voedingsstoffen, terwijl Zn noodzakelijk is in bijna 300 enzymen waaronder koolzuuranhydrase (CA) en alkalische fosfatase (AP) voor respectievelijk CO_2-hydratatie en organische fosfor-opname. Daarnaast zijn sommige andere sporenelementen niet bio-essentieel; bijvoorbeeld voor cadmium (Cd), is aangetoond dat het Zn in CA in mariene diatomeeën functioneel vervangt wanneer er niet genoeg Zn beschikbaar is. Als gevolg hiervan heeft de beschikbaarheid van de bio-essentiële sporenelementen, maar ook elementen zoals Cd, in oceanen een aanzienlijke impact op mariene ecosystemen en dus op het wereldklimaat. De beschikbaarheid van sporenelementen in oceanen wordt beïnvloed door externe bronnen, de verdeling over de opgeloste en vaste (deeltjesvorm) fase, chemische speciatie en biogeochemische processen zoals biologische opname, remineralisatie en adsorptie aan neerdwarrelende deeltjes. Samen reguleren deze factoren de primaire productiviteit die plaats vindt in het oppervlaktewater van de oceanen. Echter, de opgeloste concentraties van deze elementen zijn vaak laag in het oppervlaktewater, wat bemonstering en nauwkeurige analyse een uitdaging maakt.

In de oceanen bestaan regio's waar ondanks voldoende toevoer van macronutriënten (bijv. fosfaat, nitriet/nitraat, silicaat) een beperkte primaire productiviteit is vanwege het gebrek aan Fe en licht, de zogenaamde High-Nutrient Low-Chlorophyll (HNLC) regio's. De grootste HNLC-regio is de Zuidelijke Oceaan die daardoor een groot potentieel heeft om een grote hoeveelheid extra atmosferische CO_2 op te nemen als de fytoplankton vereisten voor Fe en licht worden vervuld. In tegenstelling tot de open oceaan, is er in veel kustzeeën

van Antarctica wel een langdurige fytoplanktonbloei gedurende de lente en zomer. Deze bloei wordt toegeschreven aan een lokale externe aanvoer van Fe, via bijvoorbeeld opwelling van diep water, van zeebodem sedimenten en Fe aanvoer van smeltend zee-ijs of gletsjers, waar de aanvoer van het cruciale Fe aan het veranderden is door klimaatverandering. Naast de uitwisseling met atmosferische CO_2 speelt de Zuidelijke Oceaan een vitale rol in de herverdeling van warmte en van zoet water in het wereldwijde klimaatsysteem. Bijvoorbeeld, de vorming van water met relatief hoge dichtheid, aangedreven door uitgebreide zee-ijsproductie tijdens de winter in Antarctische kustzeeën draagt bij aan de vorming van Antarctic Bottom Water (AABW) dat noordwaarts stroomt in meerdere oceaanbekkens en de uitwisseling van watermassa's tussen hoge en lage breedtegraden vergemakkelijkt. Gezien het belang van de Zuidelijke Oceaan voor het wereldklimaat en de oceaancirculatie, is het cruciaal om de mariene biogeochemie te begrijpen. Hierin speelt de kringloop van sporenelementen in Antarctische kustzeeën een grote rol door hun invloed op processen die wereldwijd relevant zijn.

In de afgelopen twee decennia heeft het internationale GEOTRACES-programma de biogeochemische cycli en verspreiding van sporenelementen en hun isotopen in oceanen onderzocht. De combinatie van gelijktijdige analyses van de concentratie en de isotopische samenstelling van sporenelementen heeft ons enorm geholpen om complexe biogeochemische processen te ontwarren en externe bronnen te identificeren. Echter, vanwege beperkte bemonsteringscampagnes zijn gegevens over opgeloste sporenelementen in de Zuidelijke Oceaan, met name rondom Antarctica, relatief schaars vergeleken met de Stille, Atlantische, Indische en Arctische Oceanen. De barre weersomstandigheden en slechte toegankelijkheid door de uitgebreide zee-ijsbedekking rondom Antarctica, evenals de relatief grote waterhoeveelheden die nodig zijn om de extreem lage concentraties (bijv. Fe) in de oppervlakte Zuidelijke Oceaan te bepalen, liggen hieraan ten

grondslag. Dit gebrek aan gegevens heeft niet alleen ons begrip belemmerd over de wereldwijde cyclus van voedingsstoffen, maar ook hoe klimaatsveranderingen rondom Antarctica de toevoer van voedingsstoffen beïnvloeden. Dit beperkt ook ons vermogen om de veranderingen in de biogeochemie en kringloop van sporenelementen in de toekomst op een wereldwijde en lange termijn schaal nauwkeurig te voorspellen.

In dit proefschrift worden de concentraties en isotopische samenstellingen van twee bio-essentiële sporenelementen, Fe en Zn, samen met Cd, bestudeerd in twee Antarctische kust zeeën - de Amundsenzee (AS) en de Weddellzee (WS). De AS wordt gekenmerkt door een forse intrusie van warm gemodificeerd Circumpolair Diep Water (mCDW) via gletsjertroggen in het continentale plat. Wanneer dit relatief warme water onder een ijskap of gletsjer komt, zoals de Dotson Ice Shelf (DIS), kan dit leiden tot afsmelten van de ijskap. De intrusie van mCDW leidt ook tot het smelten van zee-ijs, waardoor polynya's ontstaan (ijsvrije zee omringd door zee-ijs) die een productieve en langdurige fytoplanktonbloei in lente-zomer herbergen. De Amundsenzee Polynya (ASP) heeft de hoogste jaarlijkse netto primaire productie per oppervlakte-eenheid van alle Antarctische polynya's. De WS, een primaire regio voor de vorming van diepwatermassa’s, maakt deel uit van de door wind aangedreven Weddell Gyre, en de WS is hiermee een cruciaal onderdeel van de wereldwijde oceaancirculatie. Met name in de zuidelijke en westelijke delen van de WS vormt zich zout, koud water met hoge dichtheid door zee-ijsvorming in de winter, dat vervolgens langs de continentale helling afdaalt en uiteindelijk de WS verlaat via de Scotiazee, waarna het onderdeel wordt van AABW en de wereldomvattende oceaancirculatie. Zowel de AS als de WS zijn van invloed op, en staan onder invloed van de wereldwijde biogeochemische cycli van sporenelementen.

Door het gebrek aan gegevens over opgeloste en deeltjesvormige Zn en Cd in de AS, zijn de effecten van de mCDW-intrusie en het smelten van ijskappen op de kringloop van deze twee elementen en hun biogeochemie in de ASP onderbelicht. In **hoofdstuk 2** rapporteer ik de eerste gecombineerde dataset van opgeloste en deeltjesvormige Zn en Cd in de AS en evalueer ik potentiële externe bronnen. Uit het onderzoek blijkt dat mCDW de primaire bron is van opgelost Zn (dZn) en Cd (dCd), met sedimenten van het continentale plat als een bescheiden bron. Het smelten van ijskappen, specifiek van de DIS, en het smelten van zee-ijs leveren geen significante bijdragen voor dZn en dCd. Daarnaast karakteriseer ik de deeltjes samenstelling van Zn en Cd met behulp van twee methoden: de operationeel gedefinieerde labiele en refractaire fractie, en de op elementaire samenstelling gebaseerde biogene en lithogene fractie. De bevindingen geven aan dat in productieve regio's zoals de ASP, de labiele fractie niet altijd overeenkomt met de biogene fractie in tegenstelling van wat vaak wordt aangenomen. Deze discrepantie wordt toegeschreven aan onnauwkeurigheden in het schatten van opnameratio's, en variërende fytoplanktongemeenschappen. Tot slot suggereert deze studie dat lokale variaties in Fe-beschikbaarheid de opnameratio's van Cd en Zn kunnen beïnvloeden op beperkte ruimtelijke schalen in de ASP, waarbij verschillende fytoplanktongroepen (zoals haptophyten en diatomeeën) verschillende Zn-, Cd- en P-quota hebben. Deze inzichten in de mariene kringloop en opname door fytoplankton in de AS dragen bij aan een beter begrip van de biogeochemie van Zn en Cd tijdens een Antarctische fytoplankton bloei.

Hoewel een handjevol studies van de opgeloste Fe-concentratie ([dFe]) in de open Zuidelijke Oceaan heeft bijgedragen aan ons begrip van de biogeochemie en mariene kringloop van Fe, blijft de identificatie van externe bronnen van Fe, met name sedimentaire, en de biogeochemische processen die de Fe-kringloop in Antarctische kustzeeën beïnvloeden relatief onduidelijk. In **hoofdstuk 3** gebruik ik een combinatie van [dFe] en isotopische samenstelling van Fe (δ^{56}Fe)

om Fe-bronnen te identificeren en de biogeochemische processen in de regio beter te begrijpen, vooral rond de DIS en binnen de ASP fytoplanktonbloei. Ten eerste karakteriseer ik twee verschillende sedimentaire processen - reductieve oplossing (RD) en niet-reductieve oplossing (NRD). Samen met mCDW vormen RD en NRD de primaire Fe bronnen in de AS, en dus een belangrijke drijvende factor voor de fytoplanktonbloei in de ASP. Ten tweede onderzoek ik hoe het smelten van de DIS de Fe-kringloop beïnvloedt. Dit leidt tot de hypothese dat lithogeen colloïdaal Fe(III) uit smeltende ijskappen en uit het sediment in de waterfase in suspensie blijft, terwijl Fe^{2+} in het zuurstofrijke water neerslaat waarbij de resulterende deeltjes in het onderliggende sediment terechtkomen. Samen met mogelijke isotopische fractionering door binding van ijzer aan liganden, beïnvloeden deze factoren [dFe] en $\delta^{56}Fe$ onder de ijskappen. Ten slotte observeer ik een verschil in isotopische fractionering binnen twee fytoplanktonbloei gemeenschappen, de ene gedomineerd door haptophyten en de andere door diatomeeën. Dit wijst op verschillen in opname mechanismen tussen verschillende soorten en suggereert dat biogeochemische processen zoals complexatie aan organische liganden, absorptie en remineralisatie cruciale rollen spelen in de zeer productieve ASP. Over het algemeen biedt hoofdstuk 3 een verdere verdieping van ons begrip van externe Fe-bronnen en biogeochemische processen in de AS. Het biedt inzicht in hoe veranderende omstandigheden in Antarctica de Fe-kringloop in de Zuidelijke Oceaan en daarbuiten kunnen beïnvloeden.

Voortbouwend op de inzichten uit hoofdstuk 2, verdiep ik me in **hoofdstuk 4** verder in de bronnen van dZn en dCd in de AS door ook de isotopische samenstelling van Zn ($\delta^{66}Zn$) en Cd ($\delta^{114}Cd$) te onderzoeken. Deze analyse sluit aan bij de bevindingen uit hoofdstuk 2, waarbij gebruik werd gemaakt van opgeloste concentraties van Zn ([dZn]) en Cd ([dCd]). Deze bevindingen bevestigen opnieuw dat de primaire bron van dZn en dCd in de AS mCDW is, met minimale bijdragen van sedimenten en het smeltwater van ijskappen. In de WS

onderzoek ik ook de veranderingen in [dZn], [dCd], δ^{66}Zn en δ^{114}Cd tijdens de vorming van diep bodemwater, met bijzondere aandacht voor de voorloper van Weddellzee Bodemwater (pre-WSBW), Warm Diep Water (WDW) en Weddellzee Diep Water (WSDW). De bevindingen geven aan dat fysieke menging van deze watermassa's de veranderende concentraties verklaart in het proces van WSBW-vorming. Interessant is dat dit mengproces ondanks de grote veranderingen in concentraties, bijna geen verandering in δ^{66}Zn en δ^{114}Cd tot gevolg heeft, aangezien deze watermassa's vergelijkbare isotopische samenstellingen delen. Tot slot werpt het hoofdstuk licht op de variabiliteit in isotopische samenstellingen in de oppervlaktewateren van de AS en WS. Deze variabiliteit benadrukt de verschillen in oppervlakteprocessen die de kringloop van Zn en Cd in Antarctische wateren beïnvloeden, zoals adsorptie en complexatie aan organische liganden voor Zn, en biologische opname voor Cd.

Naast Zn en Cd richt ik me in **hoofdstuk 5** ook op Fe in de WS, met name op de potentiële bronnen en de processen die [dFe] en δ^{56}Fe beïnvloeden tijdens de vorming van WSBW. Ik ontdek dat smeltwater van het Antarctisch Schiereiland en ijskappen voornamelijk lichte Fe isotopen bijdraagt aan het kustwater, voornamelijk door RD, wat tot 90% van de aanvoer kan uitmaken. Dit leidt tot een isotopisch lichte signatuur in het kustwater en deze blijft aanvankelijk constant bij variërende [dFe]. Echter, als het kustwater met hoge dichtheid de continentale helling afstroomt, verschuift deze signatuur geleidelijk naar zwaardere waardes wat dus aangeeft dat er een bron is van zware Fe isotopen. Ik stel voor dat deze overgang in δ^{56}Fe tijdens de transformatie van kustwater naar pre-WSBW voornamelijk wordt aangedreven door fysieke menging met WDW en WSDW. Dit impliceert dat de lichte Fe-signatuur van sedimenten en gletsjers waarschijnlijk verdund wordt in het noordwaarts stromende WSBW en AABW, waarmee de rol van fysieke menging in de Fe-kringloop in deze bodemwateren wordt benadrukt. Daarnaast observeer ik een consistent δ^{56}Fe-minimum op intermediaire dieptes in de WS, wat

wijst op langeafstandstransport van een isotopisch licht Fe-signaal. Eerdere hypotheses schreven dit toe aan ofwel remineralisatie danwel een sedimentair signaal, waarbij dit onderzoek het laatste ondersteunt. Mijn werk suggereert dat sedimentair Fe met een lichte signatuur vanuit de kustwateren van het Antarctisch Schiereiland over lange afstanden getransporteerd kan worden, wat de mogelijkheid biedt voor het traceren van de aanvoer van sedimentair Fe. Dit inzicht vergroot het potentieel van het gebruik van δ^{56}Fe als *tracer* voor sedimentaanvoer naar de open oceaan.

Samengevat presenteert dit proefschrift de eerste reeks observatiegegevens voor δ^{56}Fe in zowel de AS als de WS, evenals de eerste gegevens voor δ^{66}Zn en δ^{114}Cd in de AS, plus een aanzienlijk verbeterde dekking in de WS. Deze inzichten zijn cruciaal voor het begrijpen van de externe bronnen die de verdeling van deze elementen in de Zuidelijke Oceaan bepalen. Bovendien gaat dit proefschrift dieper in op de isotopische systematiek van Fe, Zn en Cd in de oceaan. Het belicht de fractioneringseffecten veroorzaakt door biologische opname, adsorptie en ligandcomplexatie. Dit onderzoek verbetert niet alleen ons begrip van deze processen, maar biedt ook waardevolle perspectieven op het gebruik van isotopische samenstellingen als hulpmiddelen om biogeochemische processen te onderzoeken en beter te begrijpen. Ten slotte, gezien de beperkte beschikbaarheid van observationele sporenelementengegevens in de Zuidelijke Oceaan en de kustzeeën van Antarctica, kunnen de resultaten, conclusies en discussies die in dit proefschrift worden gepresenteerd, worden toegepast op bredere biogeochemische studies en kunnen ze bijdragen aan het verbeteren van modellen en hun voorspellingen voor de toekomst van Antarctica en onze planeet.

中文摘要

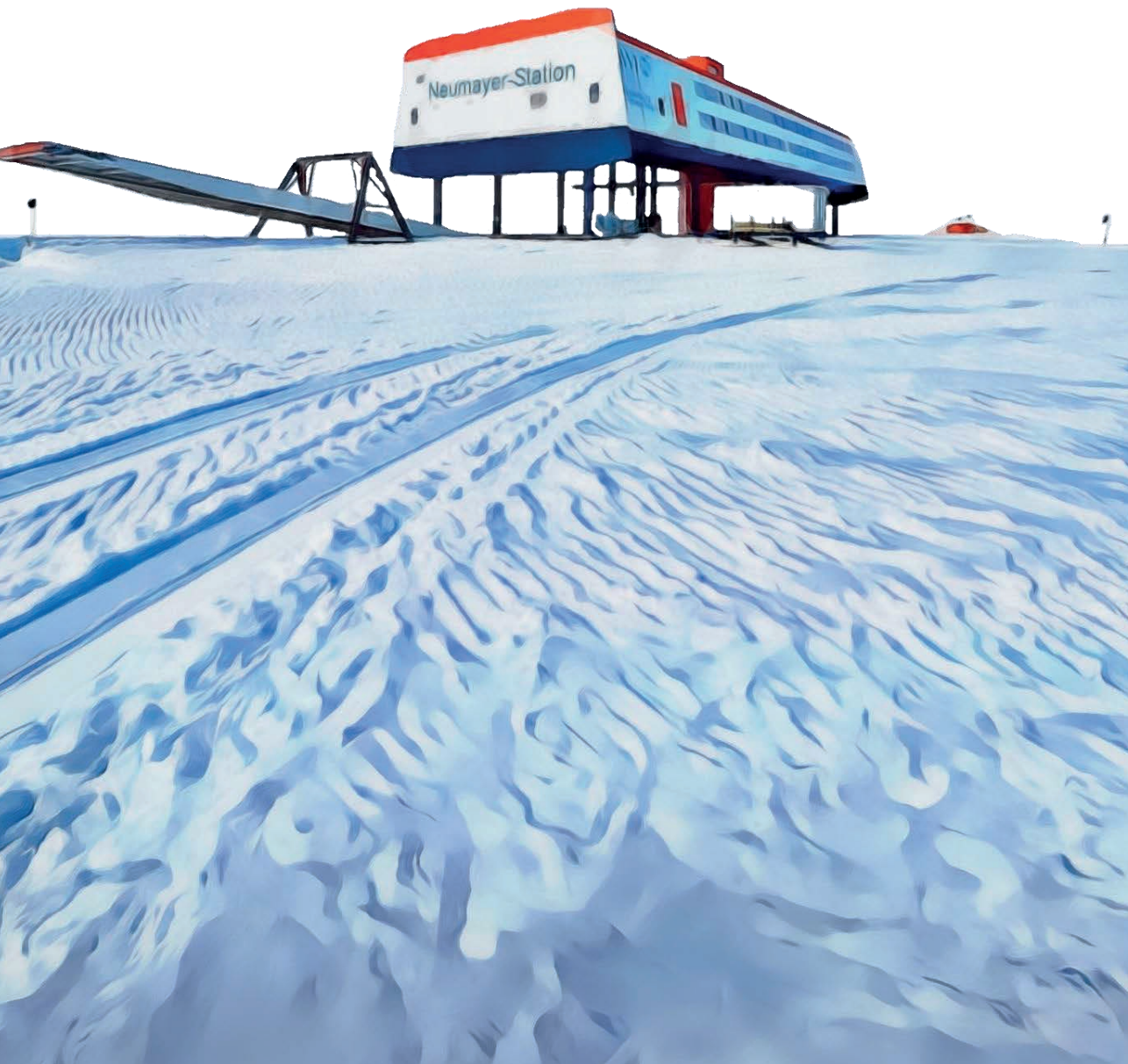

生物生長所必需的微量元素，例如鐵（Fe）和鋅（Zn），亦稱為微量營養素，因為它們參與各種重要的生物生長代謝作用中，因此對所有生命而言是不可或缺的。它們對海洋浮游植物 - 海洋食物鏈的基底 - 的成長也扮演關鍵的角色。例如，Fe 參與如光合作用、呼吸作用和營養鹽的攝取；Zn 存在於近三百種酶中，包含用於二氧化碳水合作用的碳酸酐酶和參與有機磷攝取的鹼性磷酸酶。此外，另一海洋微量元素，鎘（Cd），雖然並非生物生長所需之營養鹽，但是當海水中 Zn 的濃度降低時，Cd 在部分海洋矽藻中能夠取代 Zn 在碳酸酐酶的角色。因此，這些微量元素在海洋中的可用性和海洋生態系統及地球氣候習習相關。海洋中微量元素的可用性受到來源、化學物種型態以及生物地球化學（簡稱生地化）作用如生物攝取、再礦化和清除作用的影響，進而調節海洋表面的初級生產力。然而，在大部分浮游藻類生長的海洋表層中，這些元素的溶解態濃度通常極低，使潔淨採樣和準確分析成為極大的挑戰。

在海洋中，存在一種極具特色的區域 - 高營養低葉綠素（HNLC）區域 - 此區域具有充足的海洋營養素（例如，磷酸鹽、亞硝酸/硝酸鹽、矽酸鹽），但由於缺乏 Fe 和光線，海水表層的初級生產力受到抑制。假若 HNLC 內浮游植物對 Fe 和光線的需求能夠受到補充，作為最大的 HNLC 區域，南大洋被認為具有吸收大量大氣中的二氧化碳的潛力例如，在南極沿岸，大規模且持續性的浮游植物藻華現象經常發生在春夏季節，進而增加海水對二氧化碳的吸收。目前這個現象被歸因於 Fe 的輸入，來自於深層水的湧升、大陸沉積物以及與海冰和冰川融冰。除了調控與大氣的二氧化碳交換外，南大洋同時也對重新分配地球氣候系統中的熱量

和淡水發揮著至關重要的作用。例如，在南極沿海地區，冬季大量海冰生成及鹽水排斥產生高鹽度高密度的下沉海水，進而形成南極底層水（AABW），該水體向北流動進入多個低緯度海洋盆地，促進高緯度和低緯度海洋之間水團的交換。總體而言，鑑於南大洋對地球氣候和大洋環流的重要性，有必要對於其海洋生地化，尤其是在南極沿岸地區的微量元素循環以及它們對全球相關作用的影響，進行深入探討。

在過去二十年間，國際 GEOTRACES 計劃致力於探索海洋中微量元素及其同位素的生地化循環和分布。透過結合微量元素濃度和同位素組成，能幫助我們研究複雜的生地化過程以及鑒定不同的微量金屬來源。然而，相較於太平洋、大西洋、印度洋和北冰洋，目前於南大洋及南極沿岸所採集的微量元素數據相對稀少，這歸因於採樣航次受限於南大洋惡劣的天氣條件和與南極沿岸大面積海冰覆蓋，以及測定南大洋表層極低的微量元素濃度（例如 Fe）所需相對較大海水體積的要求。數據的稀缺不僅阻礙了我們對海洋營養鹽循環的理解以及南極沿岸變化（例如，冰融化）如何影響營養物供應的探討，同時也限制了我們在預測未來全球和長期尺度上微量元素的生地化和循環的變化的計算模擬能力（例如，生地化模型）及準確性。

在這篇論文中，研究了在兩個不同的南極沿岸地區 - 阿蒙森海和威德爾海 - 其中兩種生物必需的微量元素（Fe 和 Zn）以及一非分生必需微量元素（Cd），及其同位素組成。阿蒙森海受到水溫相對高的變化環極深層水（mCDW）通過海底峽谷大量侵入大陸棚，當其流動在冰架下（例如，道森冰架）時導致大量的冰架融冰。mCDW 的湧升也加速了海冰融化，促進了冰間湖的形

成（即被海冰包圍的開放區域），其在春夏季節孕育了生產力高且持久的浮游植物（藻華現象）。過去研究發現， 阿蒙森冰間湖（Amundsen Sea Polynya，簡稱 ASP）擁有在南極所有冰間湖中每單位面積最高的年淨初級生產率。另一方面，威德爾海是由風驅動的威德爾環流的一部分。位於威德爾海的南部和西部，高鹽度高密度的海水藉由冬季海冰形成和鹽水排斥形成，隨後沿著大陸棚坡下沉，最終通過斯科舍海離開威德爾海，形成南極底層水（AABW）。作為此下沉深水團的主要形成區域，威德爾海被視為全球海洋環流一個關鍵區域。綜合以上，阿蒙森海和威德爾海都具有影響全球微量金屬生地化學循環的潛力。

由於我們在阿蒙森海缺乏溶解態和顆粒態 Zn 和 Cd 的觀測數據，目前對於 mCDW 的侵入和冰架融化對這兩種微量元素在 ASP 的生地化循環尚未得到充分研究。在**第二章**中，我發表了首批結合溶解態和顆粒態 Zn 和 Cd 在阿蒙森海中的數據，並評估潛在的來源。結果顯示，湧升的 mCDW 是溶解態鋅（dZn）和鎘（dCd）的主要來源；大陸棚沉積物僅貢獻微量的 dZn 和 dCd。而來自道森冰架的融冰水和海冰融化對 dZn 和 dCd 的貢獻並不顯著。此外，我比較文獻上用於評估顆粒組成的兩種常見方法，並以此估算顆粒態鋅（pZn）和鎘（pCd）的相對貢獻。兩種方法分別為以化學分析定義顆粒的 labile 相和 refractory 相，以及基於元素組成的生物源（biogenic）相和岩石源（lithogenic）相。研究發現，即便在 ASP 如此高生產力的區域，labile 相並不總是等同於 biogenic 相。這種差異來自於用以估算 biogenic 相的溶解金屬-磷酸鹽關係並不能代表真正的浮游植物攝取比例，且無法反映浮游植物群落的變化。最後，這項研究表明，阿蒙森

海中 Fe 的區域可用性變化會影響 ASP 內浮游植物對於 Zn 和 Cd 的攝取比率，以及不同的浮游植物組成（如纖毛藻和矽藻）具有不同的 Zn、Cd 和磷配額。這些對阿蒙森海中 Zn 和 Cd 的海洋循環和浮游植物攝取比率的發現有助於深入了解其在南大洋藻華中的生地化反應與影響。

自 1980 年代以來，海洋學家在南大洋中對溶解 Fe 濃度（[dFe]）的測量已經促進我們對於 Fe 的海洋生地化循環已有一定程度的了解，然而，我們目前對於 Fe 外部來源，特別是海洋與大陸棚沉積物，以及影響南極水域 Fe 生地化循環及過程的了解仍相對有限。在**第三章**中，我使用[dFe]和 Fe 同位素組成（δ^{56}Fe）的組合來研究在道森冰架周圍水域和 ASP 的 Fe 來源並深入探討該地區藻華中的生地化反應。首先，我描述了兩種不同的沉積 Fe 輸出機制 - 還原性溶解（Reductive dissolution，簡稱 RD）和非還原性溶解（Non-reductive dissolution，簡稱 NRD）。這兩種沉積 Fe 來源，加上湧升的 mCDW，是阿蒙森海中 Fe 的主要輸入源，並為 ASP 中的浮游植物提供生長所需的 Fe。其次，我調查道森冰架的快速融化如何影響鐵循環 - 提出調控[dFe]和 δ^{56}Fe 於冰架系統底下的生地化作用，包含冰架融化和沉積物 NRD 中增強的岩石膠體三價鐵輸入、二價鐵的差異性移除與 Fe 結合的有機配位作用。最後，我在由纖毛藻和矽藻主導的兩個藻華中觀察到明顯的 δ^{56}Fe 分餾，這表明不同物種之間的攝取機制和途徑的差異，並顯示有機配位作用、移除反應和再礦化作用這樣的生地化過程在高生產力的 ASP 中扮演著關鍵角色。總體而言，第三章為我們進一步了解阿蒙森海中外部 Fe 源和生地化過

程提供了基礎，並為南極的環境變化可能如何影響南大洋及高緯度地區的 Fe 循環提供了一個基線。

在第二章的洞察基礎上，在**第四章**中，我利用分析 Zn 和 Cd 的同位素組成（δ^{66}Zn 和 δ^{114}Cd）深入探討了阿蒙森海中 dZn 和 dCd 的來源。這項分析與第二章使用溶解態 Zn 和 Cd 濃度（[dZn]和[dCd]）的發現一致。它再次證實阿蒙森海中 dZn 和 dCd 的主要來源為湧升的 mCDW，大陸棚沉積物和冰架融冰的貢獻極小。除此之外，在威德爾海，我還探討了高鹽度高密度的下沉水團形成過程中[dZn]、[dCd]、δ^{66}Zn 和 δ^{114}Cd 的變化，其中包含了威德爾底層水的前身（pre-WSBW）、溫暖深層水（WDW）和威德爾深層水（WSDW）。結果表明，這些水團的物理混合是影響[dZn]和[dCd]在威德爾底層水（WSBW）形成過程中的關鍵因素。有趣的是，因為這些水團具有相似的同位素組成，這種混合過程幾乎不會改變 δ^{66}Zn 和 δ^{114}Cd。最後，該章節揭示了阿蒙森海和在威德爾海表層水中同位素特徵的變化，這種變化強調了影響南極水域中 Zn 和 Cd 循環的作用的差異，如 Zn 的吸附和配位體複合作用，以及 Cd 的生物吸收作用。

除了 Zn 和 Cd 之外，在**第五章**中，我專注於研究威德爾海中的 Fe 的潛在來源和在 WSBW 形成過程中影響[dFe]和 δ^{56}Fe 的作用。我發現來自南極半島的融冰水和大陸棚沉積物通過 RD 貢獻了低 δ^{56}Fe 特徵的 Fe 到大陸棚上的水層中，佔整體 Fe 輸入的 90%。即便[dFe] 在此水層中從南極半島至大陸棚坡呈現降低趨勢，δ^{56}Fe 並無顯著改變，顯示這種輕同位素特徵在離開大陸棚沉積物後能夠受到保存。然而，隨著高密度高鹽度的下沉海水沿大陸棚坡向下移動，輕同位素逐漸轉變為較重的特徵。為此，我

發現這樣的 $\delta^{56}Fe$ 變化主要受於下沉海水與 WDW 及 WSDW 的物理混合驅動。這意味著沉積物和冰川輸出的輕同位素 Fe 可能在向北輸出的 WSBW 和 AABW 中被稀釋，強調了物理混合對於這些底層水中的 Fe 循環所扮演的角色。此外，我在威德爾海次表層觀察到一致的低 $\delta^{56}Fe$ 訊號 - 過去文獻將此現象歸因於次表層的再礦化作用或沉積物輕輸入，而這項研究支持後者。它表明，來自南極半島大陸棚沉積物輸入的輕同位素 Fe 可以被保存並透過長距離傳輸，增強了使用 $\delta^{56}Fe$ 作為開放海洋中沉積物供應追踪器的潛力。

總體而言，這篇論文發表了的首批於阿蒙森海 $\delta^{56}Fe$、$\delta^{66}Zn$ 和 $\delta^{114}Cd$ 觀測數據、首批於威德爾海的 $\delta^{56}Fe$ 觀測數據、以及對於威德爾海的 $\delta^{66}Zn$ 和 $\delta^{114}Cd$ 數據的深化。這些研究結果對於理解微量元素在南極海分布的來源至關重要。此外，本論文深入探討了這些微量元素在海洋中的同位素系統，闡明了由各種生地化作用 (如生物攝取、吸附和配位體複合作用) 引起的分餾效應。這項調查不僅增強了我們對這些作用的理解，還提供了使用同位素組成作為研究生地化學過程的知識。最後，鑑於目前於南大洋和南極沿岸有限的微量元素觀測數據，本論文中呈現的結果和討論可應用於更廣泛的生地化相關研究，如增強生地化模型的使用和預測。






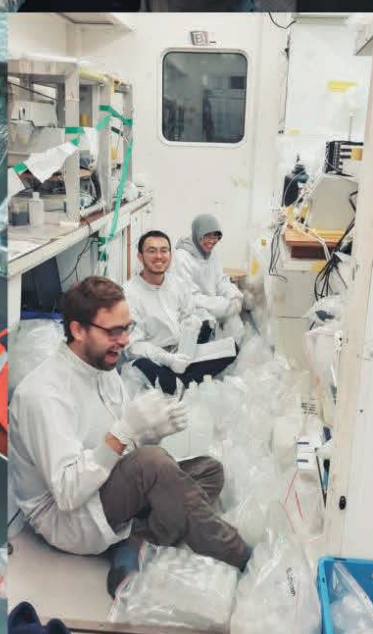

CHAPTER 1

INTRODUCTION

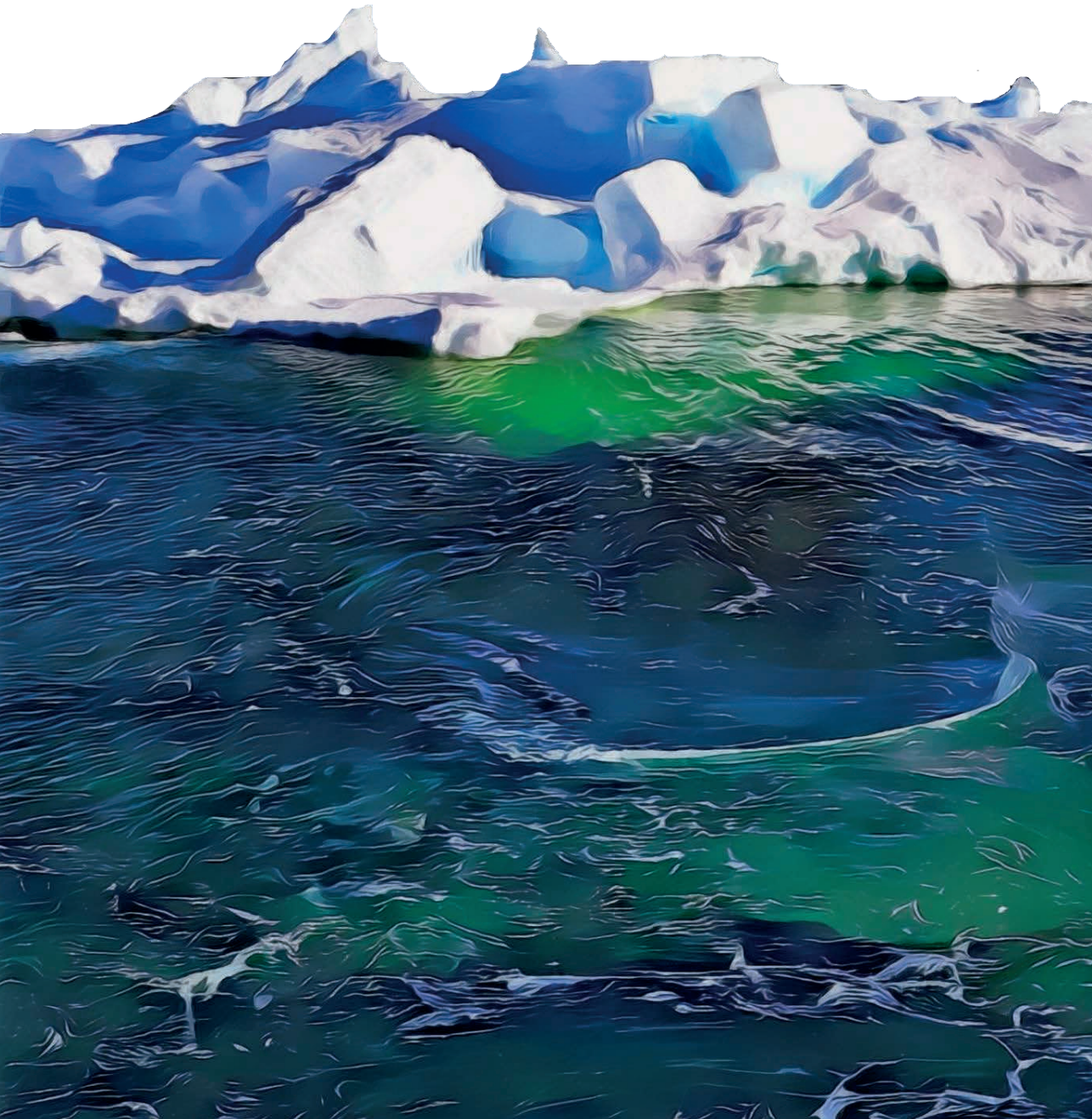

1.1 Bioactive trace metals in the ocean: iron, zinc, and cadmium

Biological importance

The ocean plays a vital role in regulating the global carbon cycle and global climate (Falkowski et al., 1998). The global ocean has been estimated to have absorbed around one-quarter of anthropogenic carbon dioxide (CO_2) emissions (Raven and Falkowski, 1999), in part due to the growth of marine phytoplankton. As the basis of the marine food web, marine phytoplankton control the energy cycle within marine ecosystems by performing photosynthesis to convert CO_2 and water into organic compounds and oxygen in the euphotic zone , and are responsible for about half the photosynthetic fixation of CO_2 on Earth (Field et al., 1998). Besides carbon, marine phytoplankton growth also requires macronutrients such as nitrate (NO_3^-), phosphate (PO_4^{3-}), and silicate ($Si(OH)_4$) (Redfield, 1934) with typical concentrations in the nmol L^{-1} to µmol L^{-1} range in the ocean, as well as micronutrients (e.g., trace metals) such as iron (Fe), zinc (Zn), copper (Cu), manganese (Mn), nickel (Ni), and cobalt (Co) that occur at much lower concentrations (fmol L^{-1} to nmol L^{-1}) in the ocean (Bruland et al., 2014; Morel et al., 2020).

Despite the general scarcity of such trace metals in seawater, they are in fact as crucial as macronutrients to phytoplankton growth due to the various functions in different metabolic processes (Twining and Baines, 2013). For example, as the most abundant trace metal in phytoplankton, Fe, is central to electron transport in multiple critical physiological processes such as photosynthesis (de Baar and La Roche, 2003; Tortell et al., 1996), respiration (Maranger et al., 1998), nutrient uptake via, for example, nitrogen fixation (Moore et al., 2001; Morel and Price, 2003) and nitrate reduction (Falkowski, 1997; Maldonado and Price, 1996). Another bio-essential trace metal, Zn, functions in nearly 300 enzymes (Vallee and Auld, 1990). The most important enzymes that require Zn are carbonic anhydrase (CA) (Lane and Morel, 2000; Morel et al., 2002) and alkaline phosphatase (AP) (Coleman, 1992; Plocke et al., 1962), which are responsible for hydration and

dehydration of CO_2 and uptake of organic phosphorus, respectively (Morel et al., 1994). Zn is also found in RNA polymerase that itself facilitates the interactions of subunits of enzymes and is involved in DNA duplication (Coleman, 1998). Compared to Fe and Zn, Cd is not a bio-essential trace metal. Nevertheless, Cd has been found to be able to substitute for Zn when Zn becomes less available in seawater (Sunda and Huntsman, 1995; Yee and Morel, 1996). This CA-Cd functionality has been ubiquitously observed in marine algae species (Kellogg et al., 2020; Morel and Price, 2003; Morel et al., 2020; Park et al., 2007; Saito et al., 2008; Sunda and Huntsman, 1995, 1998a, 2000, 2005; Xu and Morel, 2013), highting the potential biological role of Cd.

Overall, given the biological importance of these three trace metals to marine organisms coupled to their low abundances in seawater, their marine cycling and biogeochemistry have significant impacts on global climate and marine ecosystems (Moore et al., 2013; Moore et al., 2001). The effect of trace metals on carbon cycling and climate may be observed especially in regions where Fe availability is limited, such as the High-Nutrient Low-Chlorophyll (HNLC) Southern Ocean (Boyd et al., 2007; de Baar et al., 1990; de Baar et al., 1995; Martin et al., 1990) and the equatorial Pacific Ocean (Behrenfeld et al., 1996; Coale et al., 1996; Tagliabue et al., 2020), as well as where Zn availability is limited, such as the oligotrophic Tasman Sea (Hassler et al., 2012) and Sargasso Sea (Jakuba et al., 2008).

Oceanic distributions

For the past two decades, the international GEOTRACES program has been dedicated to exploring the biogeochemical cycles and oceanic distributions of trace metals and their isotopes throughout the oceans (e.g., Conway and John, 2014a, b, 2015; Conway et al., 2016; Fitzsimmons et al., 2013; John and Adkins, 2010; John and Conway, 2014; John et al., 2018; Radic et al., 2011; Schlitzer et al., 2018; Sieber et al., 2020, 2021; Sieber et al., 2023b; Wyatt et al., 2014). Distributions of trace metals are controlled by a combination of changes in their chemical speciation (e.g., redox reactions and complexation with organic compounds), biogeochemical processes

that transfer metals between the dissolved and particulate phases (e.g., biological uptake, remineralization, and scavenging/adsorption onto particles), input from external sources and/or removal into oceanic 'sinks' such as marine sediments (review by Bruland et al., 2014).

For Zn and Cd, although external sources (aerosol, rivers, marginal sediments) can be seen to affect their regional distributions, the global distributions of both elements follow nutrient-type distributions. Surface concentrations are depleted and as low as ~10 pmol L^{-1} and ~10 fmol L^{-1}, respectively, owing to biological uptake in surface waters, whereas in the underlying water column concentrations increase with depth to a maximum of ~10 nmol L^{-1} and ~1 nmol L^{-1}, respectively, due to remineralization of sinking biological particles (Bruland et al., 2014), and advection of water masses with different pre-formed nutrient concentrations (Middag et al., 2019; Middag et al., 2018; Vance et al., 2017). In general, the distributions of dissolved Zn ([dZn]) and Cd ([dCd]) are strongly correlated with $Si(OH)_4$ and PO_4^{3-}, respectively, with deeper remineralization for dissolved Zn and $Si(OH)_4$ than dissolved Cd and PO_4^{3-} (Boyle et al., 1976; Bruland, 1980; Bruland et al., 2014; Conway and John, 2014b; Middag et al., 2019; Middag et al., 2018; Sieber et al., 2020; Sieber et al., 2019b; Vance et al., 2019; Wyatt et al., 2014).

Initially, the coupling between Zn and Si was believed to result from the simultaneous uptake and regeneration of Zn and Si in the siliceous frustule of diatoms, or an association of Zn with a refractory organic phase, leading to the simultaneous release of Si and Zn at greater depth relative to other macronutrients and Cd, which behaves like phosphate (e.g., Lohan et al., 2002). However, studies have shown that the majority of assimilated Zn is associated with organic tissues, implying that the distribution of Zn should be coupled with NO_3^- and PO_4^{3-} rather than $Si(OH)_4$ (Ellwood and Hunter, 2000; Twining and Baines, 2013; Twining et al., 2004; Twining et al., 2003). Vance et al. (2017) showed the global Zn-Si coupling is mainly controlled by the deep convection and export of Zn-rich diatom cells to the deep Southern Ocean in the Antarctic, coupled with northward advection

of low Zn and $Si(OH)_4$ water to the low-latitude ocean, following the systematics previously described for silicate by Sarmiento et al. (2004). On top of this, it has been suggested that reversible scavenging of Zn is necessary to reproduce the whole ocean Zn distribution and Zn:Si ratios, notably in the Pacific (John and Conway, 2014; Sieber et al., 2023b; Weber et al., 2018).

For Cd, although the cellular utility and reason for uptake remains unresolved, the general coupled distribution of Cd with PO_4^{3-} results from uptake into by phytoplankton in surface waters and subsequent remineralization at depth (Boyle et al., 1976; Bruland, 1980). Despite the generally strong correlations of Zn-$Si(OH)_4$ and Cd-PO_4 in the global ocean, changes in the steepness of the slopes (so-called 'kinks') are observed among different water masses (e.g., Boyle, 1988; Cullen, 2006; de Baar et al., 1994; Middag et al., 2019; Middag et al., 2018). Such kinks are primarily driven by the advection and mixing of different water masses with various 'preformed' Zn-$Si(OH)_4$ and Cd-PO_4 ratios generated by variable uptake of Cd to P in high-latitude (often Fe limited regions), and then transport of these water masses through the global ocean to the low-latitude intermediate depths (e.g., Abouchami et al., 2014; Baars et al., 2014; de Souza et al., 2018; Middag et al., 2019; Middag et al., 2018; Sieber et al., 2019a; Vance et al., 2017; Xie et al., 2015). As such, it is both the one-dimensional cycle of uptake and regeneration and the three-dimensional movement of water masses that come together to create the global distributions of the nutrient-type trace metals.

For Fe, a hybrid-type distribution is shaped by a combination of internal cycling, speciation, complexation with organic ligands, removal, and external sources (Tagliabue et al., 2017). In the surface ocean, although complexation with prevalent organic ligands assists in preserving Fe in the dissolved pool (e.g., Liu and Millero, 2002), the dissolved Fe concentration ([dFe]) is generally low (as low as 10 pmol L^{-1}) due to biological assimilation, oxidation of Fe^{2+} to Fe^{3+} and subsequent precipitation as Fe(oxy)hydroxides, and adsorption onto particles (de Baar and de Jong, 2001; Gledhill and van den Berg, 1994; Johnson et al., 2007; Millero et al., 1995). Biogenic particles exported

from the euphotic zone remineralize, which leads to increasing [dFe] with depths (up to ~1 nmol L^{-1}). As such, this aspect for Fe's distribution is similar to a nutrient-type distribution (Bruland et al., 2014) and often observed in remote open oceans where dust deposition and terrestrial input are limited (e.g., the Southern Ocean) (Ellwood et al., 2020; Klunder et al., 2011; Sohrin et al., 2000; Tagliabue et al., 2012). However, concentrations generally do not increase above 1 nmol L^{-1} in the open ocean due to solubility constraints, in contrast to nutrient type elements for which concentrations increase in deep water masses as they flow through the ocean. Additionally, Fe can also exhibit a scavenged-type distribution with decreasing [dFe] from the surface towards the deep due to adsorption in areas where high dust input into surface waters is present (Bruland et al., 2014; Tagliabue et al., 2017), such as the central North Pacific (Bruland et al., 1994) and the Northeast Atlantic Ocean (Sarthou et al., 2007). On top of these processes, the GEOTRACES program has convincingly shown that deep external sources such as continental shelves, deep-sea sediments, and hydrothermal venting can dominate the deep distribution of Fe (Bruland et al., 2014; Conway and John, 2014a; Fitzsimmons et al., 2017; Homoky et al., 2012; Tagliabue et al., 2010), resulting in large location-dependent variability of [dFe] in the deep ocean (Schlitzer et al., 2018). It is worth noting that the vertical distributions mentioned above only consider two-dimensional changes (e.g., external input and removal), however, the ocean is essentially a three-dimensional body. Over the years, data collected for the GEOTRACES program has increasingly emphasised the importance of ocean circulation and water masses with different metal concentration on the global distributions of these metals (Schlitzer et al., 2018).

1.2 The marine stable isotopic system of iron, zinc, and cadmium

Delta notation

In the past 15 years, dissolved stable isotopic ratios of trace metals in the ocean have been increasingly investigated, although studies are still less numerous than investigations of dissolved concentrations (Schlitzer et al., 2018). The utilization of stable isotope ratios is based on isotopic fractionation effects – the partitioning of isotopes due to mass differences – induced by various chemical and physical processes (Conway et al., 2021; Dauphas et al., 2017; Horner et al., 2021). As such, variation in isotopic ratios between reactants and products and/or between phases (e.g., dissolved and particulate pools) provides additional information on trace metal sources and cycling. Of the isotopic systems studied in this thesis, Fe, Zn, and Cd, Fe has four stable isotopes (% abundance), ^{54}Fe (5.8%), ^{56}Fe (91.8%), ^{57}Fe (2.1%), and ^{58}Fe (0.3%); Zn five stable isotopes, ^{64}Zn (49.2%), ^{66}Zn (27.8%), ^{67}Zn (4.0%), ^{68}Zn (18.4%), and ^{70}Zn (0.6%); Cd has eight stable isotopes, ^{106}Cd (1.25%), ^{108}Cd (0.89%), ^{110}Cd (12.5%), ^{111}Cd (12.8%), ^{112}Cd (24.1%), ^{113}Cd (12.2%), ^{114}Cd (28.7%), and ^{116}Cd (7.49%). Stable isotope ratios of these metals are typically expressed in delta notation as of the measured ratios of samples relative to that of a reference material, or certified standard, in per mil (‰):

$$\delta\mathrm{M}\ (‰) = \left[\frac{R_{sample}}{R_{standard}} - 1\right] \times 1000$$

Here, δM denotes the isotopic composition for Fe (δ^{56}Fe), Zn (δ^{66}Zn), and Cd (δ^{114}Cd), whereas R denotes the isotopic ratio (^{56}Fe/^{54}Fe, ^{66}Zn/^{64}Zn, ^{114}Cd/^{110}Cd. The commonly used certified standards for δ^{56}Fe, δ^{66}Zn, and δ^{114}Cd are IRMM-014, JMC-Lyon, and NIST-3108, respectively. It is worth noting that different studies have chosen

different notation and isotope pairs but these three are the ones used most commonly, and by GEOTRACES data products.

Applications of trace metal isotopic ratios

Differences in isotopic ratio can arise due to a range of kinetic and equilibrium isotope effects (e.g., Dauphas et al., 2017). This makes stable isotopic ratios a promising tool to not only investigate biogeochemical processes that control the marine cycling and distribution of trace metals, but also to identify and constrain external sources (e.g., Bermin et al., 2006; Conway and John, 2014b; Conway et al., 2021; Ellwood et al., 2015; Fitzsimmons and Conway, 2023; Horner et al., 2021; John and Conway, 2014; Lacan et al., 2006; Radic et al., 2011; Ripperger et al., 2007; Sieber et al., 2021; Sieber et al., 2019b; Vance et al., 2017).

Applications of δ^{56}Fe in oceans

For Fe, one of the main applications of δ^{56}Fe is to identify external marine sources since different sources may exhibit distinct isotopic signatures that could serve as “fingerprints” (recently reviewed in detail by Fitzsimmons and Conway (2023)). Atmospheric dust is characterized by a δ^{56}Fe value of +0.1‰ (Beard et al., 2003; Conway et al., 2019), whereas anthropogenic combustion and biomass-burning aerosols range from –4 to +0.3‰ (Conway et al., 2019; Kurisu et al., 2016a; Kurisu et al., 2021; Kurisu et al., 2016b). Within sediments, reductive dissolution (RD) facilitated by bacterial respiration and other microbially mediated redox reactions results in an isotopically light signature in porewater (as low as –1‰), with subsequent oxidation and release leading to sedimentary Fe fluxes characterized by δ^{56}Fe ranging from –3.5 to –1‰ (Homoky et al., 2013; Homoky et al., 2009; Homoky et al., 2021; Johnson et al., 2020; Severmann et al., 2006; Severmann et al., 2010). In contrast, non-reductive pathways (NRD, e.g., desorption), notably via sediment resuspension, are found to have δ^{56}Fe (+0.1‰) almost identical to lithogenic δ^{56}Fe (i.e., upper crust) (e.g., Conway and John, 2014a;

Homoky et al., 2013; Homoky et al., 2021; Radic et al., 2011). Hydrothermal venting, a critical Fe source in the deep ocean, exhibits a wide range of δ^{56}Fe. For example, vent fluids are relatively well constrained (–0.7 to –0.1‰, Beard et al., 2003; Bennett et al., 2009; Nasemann et al., 2018; Rouxel et al., 2003; Rouxel et al., 2016; Severmann et al., 2004), whereas the dispersal plumes and distal signals away from the vent source range from –4 to +0.5‰ due to chemical reactions upon mixing with ocean waters (Ellwood et al., 2015; Fitzsimmons et al., 2017; Lough et al., 2017; Wang et al., 2021). Analogously, rivers exhibit large variability in δ^{56}Fe highly dependent on chemical conditions such as colloidal concentration, pH, and mineral compositions between river characteristics and locations (–1.3 to +1.8‰, Bergquist and Boyle, 2006; Dauphas et al., 2017; Escoube et al., 2009; Escoube et al., 2015; Mulholland et al., 2015). Compared to these sources, the cryosphere (e.g., sea ice/iceberg/glacial melting) is perhaps the least constrained source (–2.1 to +0.9‰, Fitzsimmons and Conway, 2023), which largely depends on glacial bed weathering and reductive processes within sediments, as well as interactions with underlying waters (Henkel et al., 2018; Mikucki et al., 2004; Sieber et al., 2021; Stevenson et al., 2017; Tian et al., 2023a; Zhang et al., 2021).

Possible retention of source signatures with transport of Fe across large distances has led to δ^{56}Fe being used to study Fe sources in GEOTRACES studies in the Atlantic, Pacific, Southern and Arctic oceans (e.g., Abadie et al., 2017; Conway and John, 2015; Radic et al., 2011; Sieber et al., 2021; Zhang et al., 2021). Taking advantage of the constraints of external sources, Conway and John (2014a) also quantified the relative contributions from each source to an oceanic sample using two-component isotope mixing models in the North Atlantic Ocean.

In addition to identification and quantification of external sources, δ^{56}Fe has also been applied to investigate a suit of biogeochemical processes, including biological uptake (e.g., Ellwood et al., 2020; Ellwood et al., 2015), organic ligand complexation (e.g., Dideriksen et al., 2008; Ilina et al., 2013; Morgan et al., 2010), adsorption (e.g.,

Johnson et al., 2008; Mulholland et al., 2015), scavenging (e.g., Radic et al., 2011), remineralization (e.g., Abadie et al., 2017; Klar et al., 2018), and redox reactions of Fe species (e.g., Beard and Johnson, 2004; Ellwood et al., 2015). Such processes are not easily disentangled based solely on dissolved Fe concentrations, and although it is also complicated to use δ^{56}Fe in this way, it may provide more insights. For example, Ellwood et al. (2015) revealed how biogeochemical processes shift from photochemical (and biological) reduction at the onset of a phytoplankton bloom to biological uptake at the peak of the bloom, based on δ^{56}Fe in the dissolved and particulate pool during the development of a subtropical phytoplankton bloom. Abadie et al. (2017) suggested the importance of non-reductive release of Fe from lithogenic particles, along with remineralization in the deep ocean. More recently, Sieber et al. (2021) used dissolved δ^{56}Fe to unravel the processes (e.g., biological uptake, recycling, and ligand binding) that dominated Fe cycling in surface waters across all major zones of the Southern Ocean.

Overall, the ongoing investigations on the constrains of isotopic signatures for different external sources and isotopic fractionation effects induced by different biogeochemical processes have improved our understanding of marine Fe cycling (Fitzsimmons and Conway, 2023). Recently global ocean biogeochemical computational models also highlighted the importance of both constrains of external sources and fractionation effects by distinct processes (e.g., remineralization and abiotic removal) on understanding the global Fe cycling and δ^{56}Fe systematics (König et al., 2021).

Application of δ^{66}Zn in oceans

For Zn, although knowledge of δ^{66}Zn signatures of external sources is perhaps not yet as extensive as for δ^{56}Fe, we have gained primary constraints on sources including rivers (+0.21 to +0.58‰, Little et al., 2014), aeolian dust (+0.08 to +0.54‰, Dong et al., 2013; Little et al., 2014; Maréchal et al., 2000), anthropogenic aerosol (+0.01 to +0.30‰, Liao et al., 2020; Rosca et al., 2019), hydrothermal fluids (–0.50 to +1.04‰, Conway and John, 2015; John et al., 2018; John et al.,

2008; Lemaitre et al., 2020), lithogenic (crustal) materials (+0.20 to +0.34‰, Dong et al., 2013; Little et al., 2014; Maréchal et al., 2000) and marginal sediments (–0.8 to +0.35‰, Conway and John, 2014b; Liao et al., 2020; Little et al., 2016). These external sources are characterized by relatively light isotopic signatures (mostly lower than +0.58‰) compared to known sinks of Zn (e.g., Fe-Mn sediments, biogenic carbonate, and opal, ranged from +0.53 to +1.47‰, Andersen et al., 2011; Little et al., 2014; Maréchal et al., 2000; Pichat et al., 2003). Such imbalance for δ^{66}Zn between sources and sinks implies an unknown light Zn sink, given that the global deep water exhibits homogeneous δ^{66}Zn values (+0.44±0.08‰, Bermin et al., 2006; Conway and John, 2014b; Lemaitre et al., 2020; Sieber et al., 2020; Sieber et al., 2023a; Takano et al., 2017). This unknown sink was later found to result from the cellular uptake of light Zn in surface waters and subsequent export to the deep ocean with preservation of this light signal due to authigenic mineral precipitation (e.g., Zn sulfides) within sediments (Little et al., 2016). This finding filled a gap in our understanding of the global marine Zn mass balance.

Another application of δ^{66}Zn is to investigate biogeochemical processes in the surface ocean. From culturing experiments, biological uptake is thought to preferentially take isotopically light Zn (John and Conway, 2014; John et al., 2007; Köbberich and Vance, 2017; Samanta et al., 2018). However, δ^{66}Zn in the surface water of the global ocean displays a large range in δ^{66}Zn values (~–0.20 to ~+0.70‰), within which the surface Southern Ocean exhibits similar δ^{66}Zn to deep water values (Sieber et al., 2020; Wang et al., 2019; Zhao et al., 2014), while low-latitude waters show much more variability (Conway and John, 2014b, 2015; John et al., 2018; Lemaitre et al., 2020; Liao et al., 2020; Vance et al., 2019). On the face of it, such patterns in surface δ^{66}Zn appear inconsistent with culturing experiment results. Several hypotheses have been put forward to explain this wide range in δ^{66}Zn in surface waters. For example, the culturing result (e.g., uptake of isotopically light Zn in culturing media) may be obscured by complexation with the used organic chelators (e.g., EDTA) in such experiments (Köbberich and Vance, 2019). This finding emphasizes the role of ligand complexation in Zn cycling and isotopic signatures in

the surface ocean and suggests that biological uptake may have a relatively small fractionation. Additionally, adsorption of isotopically heavy Zn is also found to play an essential role in setting surface δ^{66}Zn systematics (John and Conway, 2014; Sieber et al., 2023b; Weber et al., 2018). Furthermore, shallow remineralization and/or scavenging has been invoked to explain shallow surface and subsurface excursions to low δ^{66}Zn (Bermin et al., 2006; Ellwood et al., 2020; Sieber et al., 2020; Vance et al., 2019; Wang et al., 2019; Zhao et al., 2014). Taken together, the various processes that can drive the cycling of Zn as well as their importance have now been revealed via a combination of observations of [dZn] and δ^{66}Zn (Horner et al., 2021; Sieber et al., 2023b), making the use of combined concentrations and isotopic ratios a powerful tool.

Applications of δ^{114}Cd in oceans

For Cd, constraints on δ^{114}Cd in primary external sources have been investigated for lithogenic (crustal) materials (~–0.01‰, Rehkämper et al., 2012; Schmitt et al., 2009), hydrothermal vents (+0.05‰, Schmitt et al., 2009), rivers (–0.35 to +0.02‰, Gao et al., 2013; Lambelet et al., 2013;), and anthropogenic aerosols such as ash from metal (Pb-Zn) smelting (–0.70 to –0.10‰, Cloquet et al., 2006; Shiel et al., 2010) and ore minerals (Martinková et al., 2016; Wombacher et al., 2003). Constraints on δ^{114}Cd in anthropogenic aerosols might be especially useful for tracing anthropogenic influences in the ocean, where such influence is significant (Rehkämper et al., 2012). For example, anthropogenic input has been observed and invoked to explain the surface δ^{114}Cd systematic in some regions, such as the South China Sea (Yang et al., 2015) and the North Pacific Ocean (Sieber et al., 2023b).

Akin to δ^{56}Fe and δ^{66}Zn, δ^{114}Cd has also been utilized to investigate marine biogeochemical processes such as biological uptake. Although the actual reasons behind Cd uptake are not well understood, a strong influence of biological activity on δ^{114}Cd distributions underscores the biological uptake of Cd like a nutrient. Generally, in the surface ocean, δ^{114}Cd is primarily influenced by a biological preference for light Cd,

as observed both in culturing experiments and field observations, leading to isotopic signatures as high as ~+0.6 to +5‰ in seawater (e.g., Abouchami et al., 2011; Conway and John, 2015; John and Conway, 2014; John et al., 2018; Lacan et al., 2006; Ripperger et al., 2007). To explain the reasons behind Cd uptake, Horner et al. (2013) proposed a "non-specific uptake" of accidental Cd into cell membranes while turning on transporters for the uptake of Fe and Zn, regardless of the species and their ability to use Cd, based on subcellular Cd isotope analysis in heterotrophic bacteria *Escherichia coli.* Further, Abouchami et al. (2011) suggested that the phytoplankton community structure may affect the magnitude of fractionation, implying that different species have diverse Cd uptake mechanisms. On the other hand, some regions have been observed to exhibit "muted" surface δ^{114}Cd systematics where no apparent isotopically heavy Cd is observed in surface waters (Gault-Ringold et al., 2012; George et al., 2019; Janssen et al., 2017; Sieber et al., 2019a; Sieber et al., 2023b; Xie et al., 2017), explained by other processes such as ligand complexation, remineralization, and external inputs to the surface ocean. (Guinoiseau et al., 2018; Ratié et al., 2021; Sieber et al., 2019b; Xie et al., 2017; Xue et al., 2013). Combined with such insights into surface sources and processes derived from δ^{114}Cd measurements, the physical mixing and transport of Cd in different water masses can be further investigated using δ^{114}Cd. For example, upwelled Cd-rich deep water in the surface Southern Ocean leads to biological uptake of Cd with a preference for isotopically light Cd, leaving behind surface water masses characterized by 'preformed' isotopically heavy signatures. Such preformed heavy signatures are then subsequently imprinted into northward moving water masses Antarctic Intermediate Water (+0.45‰) and Subantarctic Mode Water (+0.65‰, Abouchami et al., 2014; Sieber et al., 2019a; Xue et al., 2013) that carry preformed Southern Ocean Cd:P and δ^{114}Cd into the Atlantic and Pacific Oceans (e.g., Abouchami et al., 2014; Conway and John, 2015; Sieber et al., 2019b; Xue et al., 2013). These observations provide additional evidence that Southern Ocean processes (e.g., surface biological uptake and mixing of different water masses) have significant impacts on the global distribution of

Cd and its isotopes (Middag et al., 2018; Sieber et al., 2019a; Vance et al., 2017). By contrast, the Southern Ocean appears to have little corresponding influence on global δ^{66}Zn distributions, showing that Zn is both more complex with multiple fractionation inducing processes, rather than fractionation mainly by biological activity (Sieber et al., 2020).

1.3 The Southern Ocean and coastal Antarctic regions: the Weddell and Amundsen Seas

The Southern Ocean is the fourth largest ocean on earth, constituting about 20% of the global ocean's surface area, situated between the Antarctic continent and the Polar Front (PF). It plays a vital role in the redistribution of heat and freshwater in the global climate system (Lumpkin and Speer, 2007; Marshall and Speer, 2012; Watson et al., 2014) and also in the exchange of CO_2 between the atmosphere and ocean (Boutin et al., 2008; Ito et al., 2010; Le Quéré et al., 2009; Sabine et al., 2004; Sallée et al., 2012).

One of the most critical circulation features of the Southern Ocean is the Antarctic Circumpolar Current (ACC), the largest wind-driven ocean current in the world, that circulates south of the Subantarctic Front (SAF) around Antarctica without encountering barriers (e.g., Belkin and Gordon, 1996; Deacon, 1959; Pollard et al., 2002). Since the ACC connects all the major oceans, including the Atlantic, Indian, and Pacific Oceans, the Southern Ocean acts as a global hub for the exchange of water masses from different basins, and, as such, influences global oceanic elemental distributions. Specifically, upwelling of the upper part of Circumpolar Deep Water (CDW) to the surface oceans occurs and this upwelled water advects both north and southwards. The northward advecting water crosses the Antarctic Polar Front (APF) and subsequently subducts to intermediate depths south of the SAF to form Antarctic Intermediate Water (AAIW, ~500 to 1000 m) and Subantarctic Mode Water (SAMW, overlying AAIW) north of the SAF, facilitating the transport of Southern Ocean surface

water northward to low latitude regions (review by Pollard et al., 2002).

In addition to northward transport in the surface and subsurface, the southward advecting portion of the upwelled CDW contributes to the formation of Antarctic Bottom Water (AABW) around coastal Antarctica flowing northward along the seafloor (> 4000 m), further transporting polar-derived waters into the low latitudes of the major basins. As one of the major sites of AABW formation, the Weddell Sea (WS) is estimated to supply ~50% of global AABW (Beckmann et al., 1999). Here, extensive sea ice production and brine rejection during winter form highly saline and dense water in the southern and western WS (e.g., Filchner-Ronne Ice Shelf); this dense water then mixes with Warm Deep Water (WDW) and Weddell Sea Deep Water (WSDW) as it descends along the continental shelf slope, eventually forming Weddell Sea Bottom Water (WSBW) (Nicholls et al., 2009; Orsi et al., 2002). Ultimately, part of WSBW and WSDW continue flowing northward and overflow into the Scotia Sea (e.g., Wilchinsky and Feltham, 2009), entering the Atlantic sector of the Southern Ocean as part of AABW. Another key feature in the WS is the wind-driven cyclonic Weddell Gyre (WG) around 50°S, between ~60°W and ~20ºE (Deacon, 1979; Park et al., 2001; Vernet et al., 2019). Following the eastward ACC, CDW enters the WG east of 20-30ºE and subsequently travels along the southern limb of the WG to the western boundary of the WG (50°W) bordered by the Antarctic Peninsula (Deacon, 1979; Gouretski and Danilov, 1993). The gyre turns northward along the Antarctic Peninsula and is completed by eastward movement along the northern boundary (55-60°S), bordered by the frontal structure of the southern ACC. Taken together, the deep-water formation and the WG circulation facilitate the exchange of WS water masses with the open Southern Ocean, connecting the influence of coastal Antarctica with the low latitude oceans (Vernet et al., 2019).

Another prominent feature of the Southern Ocean is that it is the largest HNLC region of the world oceans, with replete macronutrients (e.g., NO_3^- and PO_4^{3-}) in the surface water due to upwelling of nutrient-

rich deep water (Pollard et al., 2006) that are not fully utilised, in contrast to many other ocean regions. In the Southern Ocean, phytoplankton growth is primarily limited by the low availability of the micronutrient Fe due to few proximal local sources, low atmospheric dust input and low solubility of Fe in seawater (Boyd and Ellwood, 2010; Boyd et al., 2007; de Baar et al., 1990; de Baar et al., 1995; Martin et al., 1990). Phytoplankton may also be limited by low irradiance due to long dark winter and intense storm mixing as well as grazing pressure (Boyd et al., 2001; Mitchell et al., 1991; Strzepek et al., 2012) and or co-limitation or limitation by other metals such as manganese (Browning et al., 2021; Hawco et al., 2022) and cobalt (cobalamin, vitamin B_{12}, Bertrand et al., 2015). However, despite generally low primary productivity over most of the open Southern Ocean, long-lasting phytoplankton blooms are observed along the downstream of Antarctic islands and peninsula (Klunder et al., 2014; Sieber et al., 2021) and coastal polynyas (open areas surrounded by sea ice) that are driven by seasonal warming and upwelling of warm CDW, as well as the offshore movement of sea ice by katabatic wind or currents (Arrigo and van Dijken, 2003; Pease, 1987), during Austral spring and summer (Alderkamp et al., 2015; Arrigo and van Dijken, 2003; Arrigo et al., 2012; Gerringa et al., 2012, 2020b). Of the 37 known coastal polynyas around Antarctica, the Amundsen Sea (AS) possesses the most productive polynya with highest rate of annual NPP (per unit area) in the Amundsen Sea Polynya (ASP) (Arrigo and van Dijken, 2003; Arrigo et al., 2012). As such, the AS plays a disproportionate role in carbon uptake (Alderkamp et al., 2012; Lee et al., 2012; Mu et al., 2014). In such coastal polynyas, increasing irradiance and additional local Fe sources are thought to trigger and sustain phytoplankton blooms (Alderkamp et al., 2012; Arrigo et al., 2012; Gerringa et al., 2012, 2020b; Park et al., 2017). These additional Fe inputs are essentially associated with deeper water (CDW), benthic sediments, and/or glacial melting. The AS is one of the sites where warm and saline CDW intrudes onto the continental shelf via glacial troughs and flows underneath ice shelves (Jacobs et al., 1996; Kim et al., 2021; Kim et al., 2017; Miles et al., 2016; Thoma et al., 2008; Wåhlin et al., 2013), causing extensive melting of the Dotson Ice shelf

(DIS) (Gourmelen et al., 2017), Pine Island Glacier (PIG) (Dutrieux et al., 2014; Jacobs et al., 1996; Jenkins et al., 2010), and Getz Ice Shelf (GIS) (Jacobs et al., 2012). Upwelling of Fe-rich CDW, supplemented by subsequent melting of ice shelves and sea ice, and bottom resuspension of particles and porewater dFe induced by CDW, may supply additional Fe to the surface AS (Gerringa et al., 2012, 2020b; Sherrell et al., 2015; Tian et al., 2023a; van Manen et al., 2022). Given its high productivity, and resultant outsized impact on carbon cycling, the ASP is an ideal region to investigate the response of marine ecosystems to rapid environmental changes (e.g., intensive CDW intrusion and increasing ice shelf-derived materials input).

1.3 Objectives of this thesis

Considering the biogeochemical importance of the AS and WS to both coastal Antarctica and the Southern Ocean, it is crucial to comprehend the marine biogeochemistry and the cycling of bioactive Fe, Zn, and Cd within these regions, and their influence on globally relevant processes such as carbon cycling or nutrient export. Studies of dissolved concentrations of these elements and their isotope ratios can be useful in this regard (Fitzsimmons and Conway, 2023; Horner et al., 2021). To date, an array of studies have focused on examining dissolved Fe concentrations within the AS, including studies by Gerringa et al. (2012), Alderkamp et al. (2012), Sherrell et al. (2015), Alderkamp et al. (2015), Kim et al. (2016), van Manen et al. (2022), and Herbert et al. (2023). In contrast, research focusing on dissolved Zn and Cd concentrations in the AS is notably scarce (Sherrell et al., 2015). Further, despite the demonstrated utility of the isotopic compositions of these metals in probing biogeochemical processes, there have been no studies investigating the dissolved isotopic compositions of any of these three metals in the AS.

In the WS, investigations of dissolved Fe, Zn, Cd concentrations are more abundant compared to the AS (Baars and Croot, 2011; Baars et al., 2014; Buma et al., 1991; Croot et al., 2011; de Baar et al., 1990; Klunder et al., 2014; Lannuzel et al., 2008; Lin et al., 2011; Nolting et al., 1991; Sañudo-Wilhelmy et al., 2002; Westerlund and öhman,

1991). However, even though limited studies have examined dissolved δ^{56}Fe in the north-eastern WG (Abadie et al., 2017; Sieber et al., 2021), there are no δ^{56}Fe data from within the main WS, particularly the southern and western areas where dense waters form, nor from shelves that have been previously shown to be Fe sources (Hatta et al., 2013; Klunder et al., 2014; Sieber et al., 2021). The same is true for δ^{66}Zn and δ^{114}Cd, with only a single study available for the former (Zhao et al., 2014), and merely three for later (Abouchami et al., 2011; Abouchami et al., 2014; Xue et al., 2013). Furthermore, in the case of Cd, most of these investigations were based on a few stations and primarily focused on the eastern region of the WS along the Greenwich Meridian.

In light of the limited research conducted on the biogeochemistry and oceanic cycling of Fe, Zn, and Cd, and their isotopic systems within the Southern Ocean and coastal Antarctica, this thesis endeavours to expand our understanding of these crucial bioactive elements in the dynamic Southern Ocean. **Chapters 2, 3**, and **4** delve into the biogeochemical aspects of these elements in the AS, while **Chapters 4** and **5** focus on the WS. These regions hold particular significance due to their potential regional biogeochemical dynamics, which may have global repercussions. I utilized stable isotopic compositions as a tool to unravel the complex dynamics of these elements in these rapid changing environments.

In **Chapter 2**, the biogeochemistry of Zn and Cd in the AS in austral summer (December 2017 to February 2018) was studied. Firstly, I presented the distributions of dissolved and particulate Zn and Cd in the AS, following the inflow and outflow to and from both the Dotson and Getz Ice Shelf. Secondly, the compositions of suspended particles were investigated to estimate the relative contributions of biogenic and lithogenic sources. Lastly, I assessed the uptake ratios (Zn/P and Cd/P) by phytoplankton in two distinct bloom compositions (haptophytes versus diatoms) in the ASP, providing insights into the uptake mechanisms and nutrient requirements of both common Southern Ocean species in the costal phytoplankton blooms.

In **Chapter 3**, I studied [dFe] and δ^{56}Fe in the ASP during austral summer with the aim to gain insights for external Fe sources and to characterize Fe isotope systematics in coastal Antarctica. My primary objectives were to unravel external sources of Fe and to characterize the Fe isotope systematics within the coastal Antarctic region. By utilizing both [dFe] and δ^{56}Fe, I characterized two distinct sedimentary mechanisms – RD and NRD – which were responsible for supplying Fe from continental shelf sediments into the overlying waters. My efforts also entailed estimating the relative contributions of major Fe sources, including CDW, RD, and NRD, within the AS. Moreover, I probed into the influence of rapid melting of the DIS on the cycling of Fe. Lastly, I observed distinct Fe isotopic fractionation effects within two blooms characterized by different phytoplankton communities, shedding light on the various mechanisms involved in biological Fe uptake, as well as the interplay of other biogeochemical processes such as ligand complexation, scavenging, and remineralization, in addition to external sources.

In **Chapter 4**, I extended our research to encompass dissolved Zn and Cd within two distinct coastal Antarctic systems – the AS and WS – where the AS is influenced by the intrusion of CDW and the WS serves as a primary site of the formation AABW. Both regions hold the potential to influence or be influenced by the global oceanic circulation of trace metals. My investigation of δ^{66}Zn and δ^{114}Cd aligned with previously identified external sources of Zn and Cd from Chapter 2 that was primarily based on dissolved concentration data. Additionally, for the WS, I discussed the role of glacial meltwater input in the cycling of Zn and Cd, as well as the isotopic compositions (δ^{66}Zn and δ^{114}Cd) within different water masses contributing to the formation of AABW, including the precursor of WSBW, WDW, WSDW, and WSBW. Lastly, I highlighted the variability in isotopic signatures observed in surface waters of the AS and WS, indicating differences in surface processes governing the cycling of Zn and Cd within Antarctic surface waters.

In **Chapter 5**, the fate of sedimentary Fe and evidence for its long-term transport were investigated in the WG. Initially, I probed potential

sources of Fe, including meltwater and shelf sediments. Subsequently, I scrutinized the processes influencing [dFe] and δ^{56}Fe during the formation of WSBW, hence offering insights into the cycling of Fe as dense shelf water descends along the continental shelf slope and how δ^{56}Fe is set in deep waters before WSBW exits the WS. Finally, I presented indications of the transport of sedimentary Fe, particularly isotopically light Fe from sources such as RD, at intermediate depths within the WS, following the circulation of the WG. In conjunction with previous investigations of δ^{56}Fe in the open Southern Ocean, my findings underscored the critical role of external Fe sources in the Southern Ocean, with potential significant impacts on Fe cycling and supply to the WS.

CHAPTER 2

THE BIOGEOCHEMISTRY OF ZINC AND CADMIUM IN THE AMUNDSEN SEA, COASTAL ANTARCTICA

Hung-An Tian, Mathijs van Manen, Flora Wille, Jinyoung Jung, Sang Hoon Lee, Tae-Wan Kim, Shigeru Aoki, Charlotte Eich, Corina P.D. Brussaard, Gert-Jan Reichart, Tim M. Conway, Rob Middag

Published in *Marine Chemistry* in 2023

Abstract

The trace metals zinc (Zn) and cadmium (Cd) are involved in metabolic processes of marine phytoplankton, and both metals play important roles in ocean biogeochemical cycles. In Antarctica, the Amundsen Sea (AS) experiences rapid ice shelf melting and the Amundsen Sea polynya (ASP) hosts seasonal phytoplankton blooms in Austral summer, with important implications for atmospheric carbon drawdown. The impact of ice melt and phytoplankton blooms on Zn and Cd biogeochemistry in the ASP is not well-understood. This study presents the first dataset of dissolved and particulate Zn and Cd in the AS, including areas around the Dotson and Getz Ice Shelves. It evaluated the sources of these metals in the region and analysed particle composition in the ASP. We found the most prominent source for both dissolved Zn (dZn) and Cd (dCd) is Circumpolar Deep Water (CDW) with modest sedimentary input from the shelf sediments. Aerosol deposition, ice shelf melt, and sea ice melt are not deemed significant sources. Labile particulate Zn and Cd dominate the total particulate pool in the surface layer, indicating that biological uptake is a predominant process for the cycling of both metals, whereas sediment resuspension and ice shelf melt do not supply a significant amount of either particulate Zn or Cd. Additionally, we used two commonly used approaches to estimate biogenic and lithogenic particulate concentrations and relative contributions. The results show high surface biogenic particulate concentrations decrease over depth while lithogenic particulate concentrations remain low throughout the water column, indicating regeneration plays an important role in the cycling of particulate metals. We also found the estimated uptake ratios of Zn and Cd relative to phosphorus in the surface layer are lower than in the open Southern Ocean, likely related to spatial and temporal variability of Fe in the AS. Overall, these new observations provide insights into the biogeochemistry of Zn and Cd in the AS which may have implications for the larger scale cycling of trace metals in the Southern Ocean.

2.1 Introduction

Marine primary productivity is known to be regulated by the availability of sunlight, macronutrients (nitrate, phosphate, silicate), and micronutrients such as vitamin B_{12} and trace metals (e.g., iron (Fe), zinc (Zn), manganese (Mn), cobalt (Co), copper (Cu), and nickel (Ni), Morel et al., 2020; Twining and Baines, 2013; Croft et al., 2005). Among these bio-essential trace metals, Zn is involved in nearly 300 enzymes that are used in a range of processes in marine organisms (Vallee and Auld, 1990). For example, Zn is an essential component of both carbonic anhydrase (CA) and alkaline phosphatase (AP), enzymes which are responsible for the hydration/dehydration of carbon dioxide (CO_2) and the hydrolysis of phosphate esters, respectively (Morel et al., 1994). Similar to Zn, Cd may be involved in plankton metabolism, although Cd is not generally considered a bioessential metal. For instance, Cd, together with Co, has been shown to be able to replace Zn in CA function in marine algae *Thalassiosira weissflogii* (Morel and Price, 2003; Sunda and Huntsman, 1995, 1998b), *Phaeodactylum tricornutum* and *Pseudonitzschia delicatissima* (Kellogg et al., 2020), as well as *Emiliania huxleyi* (Saito et al., 2008; Sunda and Huntsman, 2000, 2005; Xu and Morel, 2013), when ambient bioavailable Zn becomes depleted.

The distributions of both Zn and Cd in the ocean typically correlate well with macronutrients; the global distribution of Zn is more closely correlated to Si than PO_4 or NO_3, with a concentration maximum at greater depth (e.g., Wyatt et al., 2014; Vance et al., 2017; Weber et al., 2018; Middag et al., 2019), whereas Cd is more closely correlated to PO_4 (e.g., Boyle et al., 1981; Bruland, 1980; Middag et al., 2018). Nevertheless, the relationship between either Zn and Si, or Cd and PO_4, is not linear globally – changes in the steepness of the slopes in both global Zn:Si and Cd:PO_4 relationships (so-called 'kinks') are observed (e.g., Boyle, 1988; Cullen, 2006; de Baar et al., 1994; Middag et al., 2019; Middag et al., 2018). Such kinks are primarily driven by the advection and mixing of different water masses with various preformed Zn:Si and Cd:PO_4 ratios that are transported from high latitude regions (e.g., the Southern Ocean) to low latitude oceans

(e.g., Baars et al., 2014; Vance et al., 2017; Sieber et al., 2019a; Abouchami et al., 2014; Xie et al., 2015; de Souza et al., 2018; Middag et al., 2019; Middag et al., 2018), underlining that the distribution of macro/micronutrients and their elemental ratios in the global ocean are influenced by the waters from – and thus processes occurring in – the polar regions (e.g., Abouchami et al., 2014; Xie et al., 2015; Sieber et al., 2019a; Sieber et al., 2020). Overall, the Southern Ocean is a hub of ocean circulation and a region of deep-water formation, playing a major role in redistributing elements through the global ocean. However, trace metal observations remain scarce in remote polar regions such as coastal Antarctica and the wider Southern Ocean.

Located adjacent to the Southern Ocean and West Antarctica, the Amundsen Sea (AS) is affected by the Southern Ocean circulation via Circumpolar Deep Water (CDW) (Fig. 2.1) (Jacobs et al., 1996; Kim et al., 2021; Kim et al., 2017; Miles et al., 2016; Thoma et al., 2008; Wåhlin et al., 2013), a relatively warm and saline water mass that blends with different deep-water masses, including North Atlantic Deep Water (NADW), Pacific Intermediate Water (PIW), Antarctic Bottom Water (AABW), and Antarctic Intermediate Water (AAIW). As CDW intrudes onto the continental shelves, it mixes with shelf waters and then becomes modified CDW (mCDW) (Arneborg et al., 2012). This mCDW flows underneath the ice shelves along the eastern flanks of deep troughs (inflow) (Assmann et al., 2013; Wåhlin et al., 2013), and subsequently leaves the ice shelves along the western flanks of these troughs (outflow) (Ha et al., 2014; Miles et al., 2016), which drives rapid melting of the Dotson Ice shelf (DIS) (Gourmelen et al., 2017), Pine Island Glacier (PIG) (Dutrieux et al., 2014; Jacobs et al., 1996; Jenkins et al., 2010), and Getz Ice Shelf (GIS) (Jacobs et al., 2012). Glaciers and ice shelves near the AS are observed to experience extremely fast thinning and collapsing (Rignot et al., 2008) and the AS is the primary area for accelerated melting of the West Antarctic Ice Sheet (WAIS). The melt of WAIS is currently contributing to global sea level rise with an increasing rate of currently 0.3 mm per year (Shepherd et al., 2012). Such massive melt water input has been attributed to an increasing extent of warm CDW intrusion onto Antarctic continental shelves (Jacobs et al., 2011; Jenkins et al., 2010;

Shepherd et al., 2004) and potentially affects the cycling and distribution of ice shelf-derived materials, notably bio-essential elements, and thus could alter the biogeochemistry in the AS (Gerringa et al., 2012; Henley et al., 2020; Miles et al., 2016; Planquette et al., 2013; Sherrell et al., 2015).

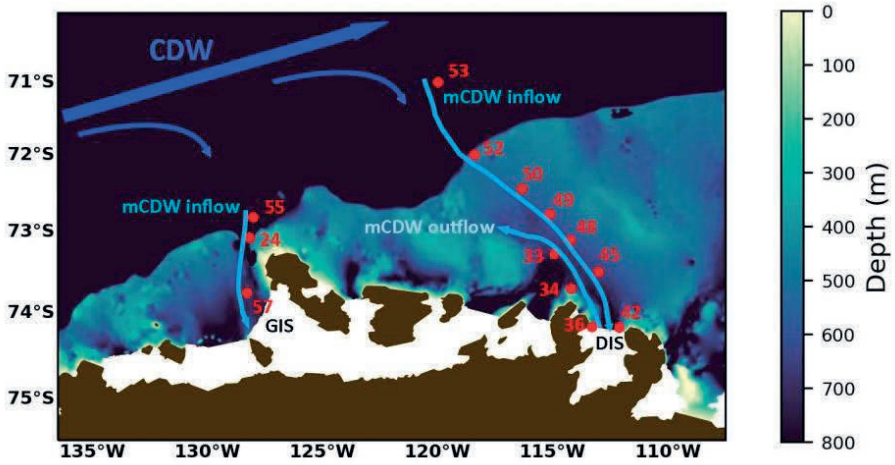

Figure 2.1 GPpr12 Sampling stations in the Amundsen Sea. Two transects – Dotson transect (DIS) that includes 10 stations (Stns 53, 52, 50, 49, 48, 45, 42, 36, 34, and 33) and Getz transect (GIS) that includes 3 stations (Stns 55, 24, and 57). Approximate location of water mass flows are shown.

Melting of sea ice by seasonal warming and upwelling of warm CDW, as well as the offshore movement of sea ice by katabatic wind or currents, results in the formation of seasonal or year-round Antarctic coastal polynyas (Anderson, 1993; Arrigo and van Dijken, 2003; Pease, 1987) – open areas surrounded by sea ice. In such polynyas, sunlight directly reaches surface waters, stimulating primary production (i.e., leading to phytoplankton blooms), but also allowing dramatic heat and air-sea exchange (Arrigo et al., 2012; Smith Jr and Gordon, 1997; Smith Jr and Comiso, 2008). Remarkably, the highest net primary production (NPP) recorded in the global ocean has been found in such coastal polynyas (Arrigo and van Dijken, 2003; Gerringa et al., 2012; Mu et al., 2014). The phytoplankton blooms in Antarctic coastal polynyas thus promote considerable atmospheric CO_2 uptake, even

though the largest CO_2 net sink occurs in the sub-Antarctic zone where productivity per unit area is lower, but the area is much larger (Lenton et al., 2013; Sallée et al., 2012). Specifically for the ASP bloom, the highest rate of annual NPP (per unit area) (Arrigo et al., 2012) among Antarctic polynyas has been observed, proposed to be fuelled by external Fe input which includes the upwelling of relatively Fe-rich CDW (Gerringa et al., 2012; Gerringa et al., 2020b), melting of the DIS (Sherrell et al., 2015), melting of sea ice (Lannuzel et al., 2007; Sherrell et al., 2015), sedimentary diffusion and sediment resuspension (Ardelan et al., 2010; Gerringa et al., 2012; Sherrell et al., 2015).

To date, studies in the AS have suggested changes in both biogeochemistry and elemental cycling, with variability in both also influencing local biological activity, under scenarios of continued rapid climate change. However, although Zn and Cd can regulate rates of primary production and influence phytoplankton community composition (Bruland et al., 1991; Sunda and Huntsman, 2000; Twining and Baines, 2013), less attention has been given to Zn and Cd in the AS compared to Fe. There has been only one dataset of dissolved Zn in the AS (Sherrell et al., 2015), and to date there are no published data for dissolved Cd. Sherrell et al. (2015) speculated that sedimentary Zn input from the trough walls at the shelf break, together with Zn brought in by CDW, were important sources of Zn to the AS. Furthermore, they concluded that strong biological removal in the surface layer and regeneration at depth was likely to be a dominant driver of the dissolved Zn distribution (Sherrell et al., 2015). Nevertheless, due to the limited amount of dissolved Zn data, a lack of particulate Zn data, and rapid changes in the region, we still have a limited understanding of the distributions and cycling of Zn and Cd, including the interaction between biological activity and these two metals, in coastal Antarctic regions.

In this study, to unravel the sources of both metals, we analysed both dissolved and particulate Zn and Cd in samples collected using trace-metal-clean procedures during Austral summer (December 2017 to February 2018) along transects that followed the main flow of mCDW (both inflow and outflow) in the AS (Fig. 2.1). Moreover, to investigate

the particle composition and the metal uptake ratios, two particulate fractions – labile and refractory – were operationally separated for further discussion. These results provide the first investigation and a better understanding of the biogeochemistry of these bioactive dissolved and particulate metals (Zn and Cd) in the AS.

2.2 Material and Methods

2.2.1 Sampling region and dissolved/particulate metal sampling

During Austral Summer 2017/2018 (December 2017 to February 2018), seawater samples and suspended particles were collected cleanly along two water column transects in the AS (Fig. 2.1) from the Korean icebreaker R/V Araon during a GEOTRACES process study (GPpr12; expedition ANA08B). The first transect followed CDW that intruded from the open Southern Ocean onto the Antarctic continental shelf via a subglacial trough, with CDW then becoming mCDW that flows south-eastward towards and underneath the DIS and subsequently leaves the DIS flowing north-westward (Fig. 2.1). The mCDW inflow and outflow were verified by shipboard measurement of current velocity and regular CTD data onboard R/V Araon (Kim et al., 2021). This transect is henceforth referred to as the Dotson transect and it included an open ocean station (Stn 53), a shelf break station (Stn 52), mCDW inflow stations (Stns 50, 49, 48, 45, 42), and mCDW outflow stations (Stns 36, 34, 33). The second transect followed CDW that flowed south-westward towards the GIS from the open ocean (Fig. 2.1). The second transect is henceforth referred to as the Getz transect, including an off-shelf station (Stn 55), a shelf break station (Stn 24), and a shelf station (Stn 57). Each station comprised 10-14 sampling depths from the near surface (~10 m) to 1000 m, or 10-20 m above the seafloor for the stations shallower than 1000 m. However, it is noted that samples below 200 m at Stn 36 (part of the mCDW outflow) were not successfully collected due to a malfunctioning of the sampling system and therefore no metal data

(and corresponding CTD and oxygen isotope data) is shown for this part of the water column.

Both dissolved and particulate samples from a total of 13 stations were collected using the Royal Netherlands Institute for Sea Research (NIOZ) "Titan" ultra clean sampling system for trace metals (de Baar et al., 2008) that is made of titanium and equipped with high purity, light-proof polypropylene (PP) samplers (modified from Rijkenberg et al., 2015). The sampling system was deployed on a 11 mm Dyneema cable without internal conducting wires and an SBE 17 plus V2 Searam in a titanium housing provided power, saved the CTD data, and closed the sampling bottles (23 L) at pre-programmed depths. After recovery, the "Titan" sampling system was immediately transported into a clean, positive pressure sampling container (temperature close to the ambient water temperature) where subsampling was conducted.

Dissolved seawater samples were filtered (0.2 µm filter cartridge, Sartorius, Sartobran-300, precleaned with sample seawater) into 125 mL Nalgene LDPE bottles (precleaned following GEOTRACES protocols, as described in Middag et al., 2019) under 0.5 bar of prefiltered nitrogen gas. The filtered samples were then acidified to 0.024 M HCl using 12 M ultrapure concentrated HCl (Baseline, Seastar Chemicals Inc), resulting in a final pH of ~1.8. Acidified samples were stored at room temperature for over 5 months before measurement of the concentrations back on shore at NIOZ. For particulate samples, unfiltered seawater (6-8 L) was subsampled as soon as the Titan system entered the sampling container, and the seawater was stored in acid-cleaned LDPE carboys that were covered by dark plastic bags until the moment of filtration (less than 3 hours) close to the in-situ water temperature (Rauschenberg and Twining, 2015; Planquette and Sherrell, 2012). Before filtration, polyethersulfone (PES) disc filters (25 mm, 0.45 µm Pall Supor) placed on polypropylene filter holders (Advantec) with polypropylene luer-locks (Cole-Palmer) attached to the carboy caps. Filters and filter holders were acid-cleaned beforehand with 3 times sub-boiled distilled 1.2 M HCl (VWR Chemicals – AnalaR NORMAPUR) at 60°C for 24 hours, then rinsed with ultrapure water (MQ, <18.2 MΩ cm^{-1}) water 5 times and

eventually stored in ultrapure water before use following Ohnemus et al. (2014). Subsequently, carboys were mounted upside down, hanging from the Titan frame and connected to filtered nitrogen gas (0.3 bar overpressure). The volumes of filtration ranged from 0.25 L (surface samples) to 8 L (deep ocean samples), with a maximum duration of filtration of 2 hours (GEOTRACES cookbook 2017). Eventually, the PES filters were folded in half and stored in acid-cleaned vials (Eppendorf) at –20˚C before analysis at NIOZ.

2.2.2 Sample processing and analysis

2.2.2.1 Basic parameters (salinity, temperature, depth, fluorescence, and nutrients)

For basic parameters, a calibrated CTD (Seabird SBE 911+) with auxiliary sensors was mounted on the Titan sampling system to measure salinity (conductivity), temperature, depth (pressure), and fluorescence. Unfiltered seawater samples (~50 mL) were collected for inorganic nutrients analysis, including phosphorus (PO_4) and silicic acid ($Si(OH)_4$). Inorganic nutrients were measured during the cruise using a four-channel Auto-Analyzer (QuAATRo, Seal Analytical, Germany), according to the Joint Global Ocean Flux Study (JGOFS) protocols described by Gordon et al. (2001). The precisions for the PO_4 and $Si(OH)_4$ measurements were ±0.02 and ±0.28 µmol kg^{-1}, respectively (Jeon et al., 2021).

2.2.2.2 Phytoplankton pigment composition analysis

On selected stations (Stns 33, 34, 36, 42, 45, 49, 55, 24 and 57), samples were taken for pigment-based phytoplankton taxonomic composition analysis at one depth in the upper few tens of meters. Seawater samples were filtered at 1°C through a GF/F glass fiber filter (45 mm diameter; Whatman, Cytiva, Marlborough, USA), using a vacuum pump (Pall, Port Washington, NY, USA) set at 200 mbar. The average sample volume that was needed to display green colour on the filter was 1.7 L (range from 0.75 to 2.7 L). Filters were double-

wrapped in aluminium foil, snap-frozen in liquid nitrogen and stored at –80°C until analysis. For analysis, the filters were freeze dried and pigments were dissolved in acetone (van Leeuwe et al., 2006). A Zorbax Eclipse XDB-C8 column (3.5 µm particle size) was used for High-Performance Liquid Chromatography (HPLC) pigment separation (Van Heukelem and Thomas, 2001). Detection based on retention time and diode array spectroscopy (Waters 996) at 436 nm was used. Most pigments were quantified manually using standards (DHI LAB products). The taxonomic composition of the phytoplankton (expressed as % of total chlorophyll a concentration) was determined using CHEMTAX (version 1.95, Mackey et al., 1996) as described by Selz et al. (2018). The starting ratios used for analysis have previously been used for Antarctic shelf regions (Selz et al., 2018). The endmember pigment compositions are re-defined and reported by Eich et al. (2022).

2.2.2.3 $\delta^{18}O$ analysis

The stable oxygen isotope ratio of a water sample is expressed as $\delta^{18}O$ with respect to Vienna Standard Mean Ocean Water (VSMOW). Water samples for $\delta^{18}O$ were drawn from the Niskin bottles mounted on the regular CTD rosette of the R/V Araon rather than the Titan system, that was deployed at the same stations. Water from matching depths was collected by gravity filtration through inline pre-combusted filters held in acid-cleaned polycarbonate filter holders. A 30 mL glass vial with polypropylene cap and polypropylene-coated insert was used to collect the water sample. The glass vial was sealed with a Parafilm and stored in refrigerators at 4°C until analysis.

The $\delta^{18}O$ samples were processed using Finnigan DELTA plus and Elementar Isoprime precision mass spectrometers at ILTS laboratory, Hokkaido University, Japan. The DELTA plus was coupled with an equilibration system, automatically shaking for about 8 hours in an 18°C water bath to equilibrate with CO_2, while the Isoprime Precision was coupled with an equilibration system consisting of a metal insulator set up for about 16 hours at 30°C. The accuracy of the

analysis was estimated to be 0.02‰ based on duplicated measurements (Nakamura et al., 2014).

2.2.2.4 Dissolved metal sample processing

Back on shore, in the NIOZ clean laboratory (ISO class 7, ISO class 5 in working hoods), various trace metals including dissolved Zn (dZn) and dissolved Cd (dCd) were extracted and preconcentrated from acidified filtered seawater samples using a commercially available seawater preconcentration system (seaFAST-pico, ESI). The SeaFAST-pico preconcentration procedure used followed Gerringa et al. (2020a).

2.2.2.5 Particulate metal sample processing

As described by van Manen et al. (2022), particulate samples were operationally divided into two fractions – a labile particulate metal (LpMe) including Zn (LpZn) and Cd (LpCd), defined based on Berger et al. (2008), as modified by Rauschenberg and Twining (2015), and a refractory particulate metal (RpMe) phase including Zn (RpZn) and Cd (RpCd), defined based on Planquette and Sherrell (2012). For LpMe, briefly, 1.8 mL of a solution of 4.35 M acetic acid (double distilled from VWR NORMAPUR by PFA Savillex Stills) and 0.02 M hydroxylamine hydrochloride (Sigma-Aldrich, 99.999% trace metal basis) was added to each Eppendorf vial (containing PES filters). The vials were then heated at 95˚C in a water bath for 10 minutes and subsequently cooled down to room temperature. Once the total contact time of samples and leach solution reached 2 hours, the filters were removed and placed into 30 mL perfluoroalkoxy beakers (PFA, Savillex) to facilitate further RpMe digestion. The remaining leachates were centrifuged at 16000 Relative Centrifugal Force (RCF) for 10 minutes. Subsequently, without disturbing the remaining particles, 1.8 mL of the solution was transferred to another PFA Teflon beaker and 100 µL of concentrated HNO_3 (AnalaR NORMAPUR, 2 times Savillex distillation) was added. This mixture was subsequently dried down at 110˚C. Once dried, the samples were re-dissolved in 2 mL 1.5 M HNO_3 with 10 ng mL^{-1} Rh as internal standard and refluxed again at 110˚C

for 30 minutes. This final fraction was ready for ICP-MS analysis and was considered to contain LpMe.

For RpMe, the solution and particles that remained after centrifugation in the LpMe leaching procedure, were then placed in the same PFA beakers in which the filters removed from the Eppendorf vials were placed, with addition of a solution of 8 M HNO_3 and 2.9 M HF (Supelco, Ultrapur 48%). Given that the remaining solution (0.2 mL) is assumed to contain a small portion of LpMe, hence a correction was applied to RpMe. The samples were refluxed capped at 110˚C for 4 hours. Afterwards, the solutions were transferred into a second set of PFA beakers, and the filter remained in the original vial. Ultrapure water was used to rinse the remaining filters in the original beakers and the rinsing solution was transferred into the second PFA beakers with the samples. These samples were then dried down at 110˚C. Subsequently, samples were re-dissolved and refluxed with 1 mL of solution of 8 M HNO_3 and 15% H_2O_2 at 110˚C for 1 hour and dried down again at 110˚C afterwards. Finally, a solution of 2 mL 1.5 M HNO_3 with 10 ng mL^{-1} Rh was added to samples and refluxed at 110˚C for 30 minutes to re-dissolve. This final fraction was ready for analysis and was considered RpMe. The sum of LpMe and RpMe is defined as total particulate metal (TpMe, labile+refractory).

2.2.3 Trace metal concentration measurements

All samples were analysed for trace metal concentrations using Inductively Coupled Plasma Mass Spectrometry (ICP-MS) on a Thermo Scientific Sector Field High Resolution Element 2 at NIOZ. A microFAST introduction system (ESI, USA) equipped with a PFA nebulizer with a sample introduction rate of 55 µL min^{-1} was used. The analytical procedure for ICP-MS measurements for dissolved and particulate metals are similar, and based on Gerringa et al. (2020a). For the dissolved samples, an average of concentration of triplicate measurements (performed in three different analytical runs) was calculated and calibrated by a suite of calibrations prepared by adding a mixed stock solution of multiple standards to both low-metal seawater and 1.5 M HNO_3 – the former was preconcentrated in the

same way as samples through seaFast and used to quantify the concentration of dissolved samples; the latter was used to monitor the recovery of the seaFast on a daily basis after Biller and Bruland (2012). For particulate metals, a calibration was prepared based on standard additions to the same 1.5 M HNO_3 as used to dissolved samples.

2.2.3.1 Blank, precision, and accuracy of ICP-MS measurement

(1) Dissolved metals

The procedural blank for dissolved Zn and Cd (n=9) were established at NIOZ by analysing acidified MQ (~1.8 pH) processed using the same procedure as for real samples (Table 2.1); blank values are the equivalent of less than 2% of real samples (Table 2.1). The precision and accuracy of measurements was evaluated by analysis of GEOTRACES reference seawater (n=3, SAFe D1, Johnson et al., 2007) and GSC (n=3, GEOTRACES coastal surface seawater, 2009), which was treated identically to dissolved samples. Measurements of both reference seawaters in this study were mostly within the community consensus range (Table 2.1).

(2) Particulate metals

For particulate metals, the procedural blank (n=9) was evaluated using a blank filter that had not been in contact with seawater, processed through the leach and digestion procedure as done for real samples. The procedural blank of selected element – aluminium (Al), phosphorus (P), and Cd only accounted for less than 2% of average concentrations of real samples (total fraction), whereas for Zn the procedural blank accounted ~20% of real samples. These blank values of this study were in the same order of magnitude as the blank values found by previous studies (Table 2.2) (Ohnemus et al., 2014; Rauschenberg and Twining, 2015). To assess the accuracy of the analysis of particulate metals, two certified reference materials

(CRMs) – BCR-414 (freshwater phytoplankton, European Commission's Joint Research Centre) and PACS-2 (marine sediments, National Research Council of Canada), were processed and measured identically to the particulate filter samples (filters included). The recovery of target elements (Zn, Cd, Al, and P) from both CRMs was 93-113% (Table 2.2). It should be noted that [RpCd] is significantly lower than [LpCd] (20-50 times lower). Given that [RpCd] is corrected for carry-over from the labile leach (0.2 mL solution from the labile leach ends up in the refractory fraction), this leads to additional uncertainty of the refractory fraction. Assuming 5% uncertainty in the labile leach measurement, this adds an additional uncertainty of ~9% if there is a factor 20 difference between liable and refractory, and an additional ~28% if the difference is a factor 50.

Table 2.1. Blank, precision, and accuracy of selected reference seawater (SAFe D1 and GSC) of dissolved metal measurement. SaFe D1 seawaters were collected at the North Pacific Ocean at 1000 m during Sampling and Analysis of Fe program (2004) and the consensus values were reported by May 2013; GSC seawaters were GEOTRACES standards collected at 2 m at the North Pacific Ocean (coastal Santa Barbara Channel, 2009). All consensus values can be found on GEOTRACES website (https://www.geotraces.org/). Both selected reference seawater were measured in one analytical session. All units are in nmol L^{-1}, converted from nmol kg^{-1} to nmol L^{-1} by using average seawater density (1.025 g/cm^{-3}).

Dissolved metal (mean±1SD)		Blank	SAFe D1 (n=3)	GSC (n=3)
Zn	this study	0.02±0.01	7.81±0.04	1.34±0.01
	consensus value	n/a	7.59±0.35	1.43±0.10
Cd	this study	0.002±0.001	1.01±0.01	0.35±0.01
	consensus value	n/a	1.02±0.03	0.36±0.02

Table 2.2 Blank, precision, and accuracy of selected certified reference materials (BCR-414 and PACS-2) of particulate metal measurement. BCR-414 is reference standard (plankton) certified by BCR (Community Bureau of Reference, the former reference materials programme of the European Commission), details can be found on the website of European Commission's Joint Research Centre (JRC, https://ec.europa.eu/info/departments/joint-research-centre_en). PACS-2 is reference standard (marine sediment) collected and certified by the National Research Council of Canada's (NRC, https://nrc.canada.ca/en). Units are a: nmol filter^{-1}; b: pmol filter^{-1}; c: µg g^{-1}; d: ng g^{-1}; e: mg g^{-1}.

Particulate metal (mean±1SD)		Blank (n=9)			BCR-414 (n=6)	PACS-2 (n=3)
		labile	refractory	total		
Zn	This study	0.22[a]±0.08	0.04[a]±0.02	0.26[a]±0.09	107[c]±3	400[c]±56
	Certified value	n/a	n/a	n/a	112[c]±3	364[c]±3
	Recovery (%)	n/a	n/a	n/a	95±2	110±15
Cd	This study	0.13[b]±0.04	0.05[b]±0.05	0.19[b]±0.08	355[d]±10	2248[d]±184
	Certified value	n/a	n/a	n/a	383[d]±14	2110[d]±150
	Recovery (%)	n/a	n/a	n/a	93±3	107±9
Al	This study	0.36[a]±0.15	0.37[a]±0.21	0.73[a]±0.33	n/a	74[e]±7
	Certified value	n/a	n/a	n/a	n/a	66[e]±3.2
	Recovery (%)	n/a	n/a	n/a	n/a	113±11
P	This study	0.09[a]±0.08	0.15[a]±0.21	0.24[a]±0.09	n/a	966[c]±99
	Certified value	n/a	n/a	n/a	n/a	960[c]±40
	Recovery (%)	n/a	n/a	n/a	n/a	101±10

2.3 Results

2.3.1 Hydrographic conditions

2.3.1.1 Water masses

The water column of the AS during our study comprises the three major water masses that are typically observed in the AS (Randall-Goodwin. et al., 2015; Yager et al., 2012): Antarctic Surface Water (AASW), Winter Water (WW), and the least modified CDW that becomes more modified CDW on the continental shelf due to the mixing with overlying water (Fig. 2.2a). Located at the surface, AASW is relatively warm and fresh (Fig. 2.2a, Θ: –0.6 - –0.7˚C, S<33.8), a result of enhanced solar irradiation in summer and associated sea ice melt. Along the Dotson transect, AASW is observed in the upper 40 m at mCDW inflow stations (Stns 50, 49, 48, and 45) and mCDW outflow stations (Stns 34 and 33) (Figs 2.3a and 2.3b). In contrast, AASW is not

clearly observed in the surface along the Getz transect (Figs 2.3d and 2.3c). Underlying AASW, remnant WW from the winter season is colder and more saline (Fig. 2.2a, Θ: –1.7 - –1.8˚C, S: 34.3-34.4) due to brine rejection during sea ice formation, as well as the cooling of surface water during the cold season. Underlying WW, the least modified CDW consists of warmer and more saline water (Fig. 2.2a, Θ>1˚C, S>34.7).

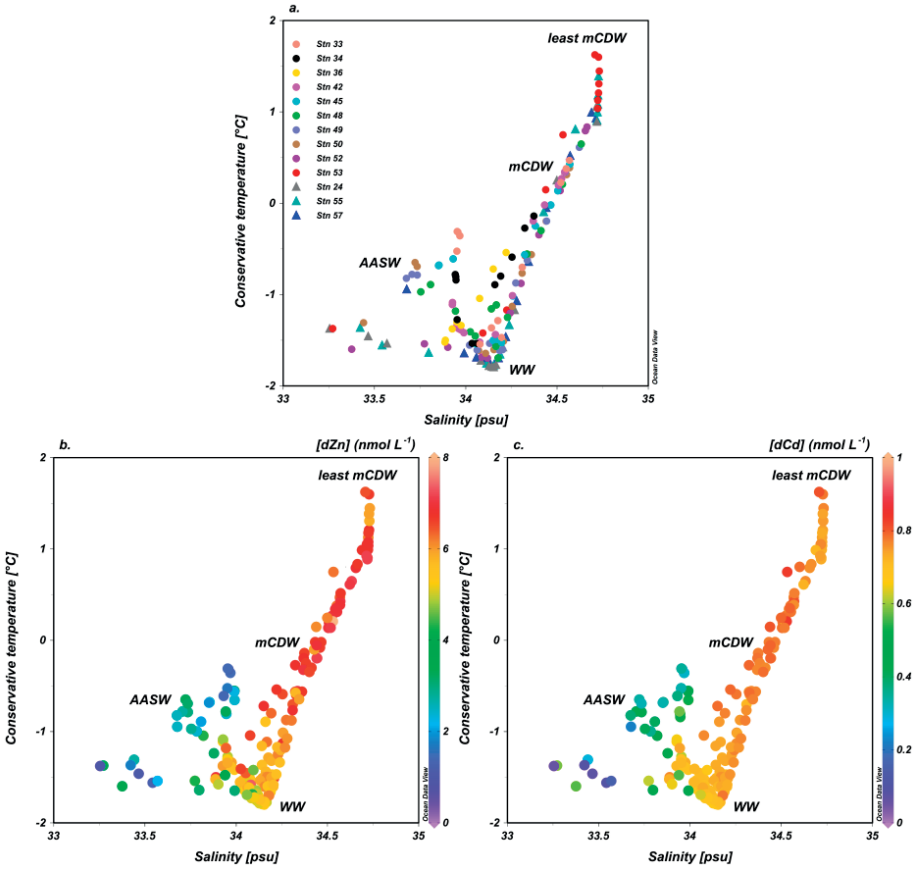

Figure 2.2 Potential temperature (˚C), salinity, [dZn] and [dCd] (nmol L^{-1}) plotted against salinity for all GPpr12 stations. a. Θ-S diagram, three water masses are identified: Antarctic Surface Water (AASW), Winter Water (WW), and Circumpolar Deep Water (CDW). b. [dZn] on Θ-S diagram. c. [dCd] on Θ-S diagram. Θ was derived using ODV version 5.3.0 (Schlitzer, 2020).

Due to the mixing with overlying WW and melt water from the ice shelf, the temperature and salinity of mCDW is diluted along the transects (Fig. 2.3). Relatively high temperatures are observed at 500 m at the mCDW inflow stations (Stns 45 and 42) and below 200 m at the mCDW outflow stations (Stns 36 and 34) (Figs 2.3a and 2.3b), identifying the core of mCDW inflow and mCDW outflow, respectively.

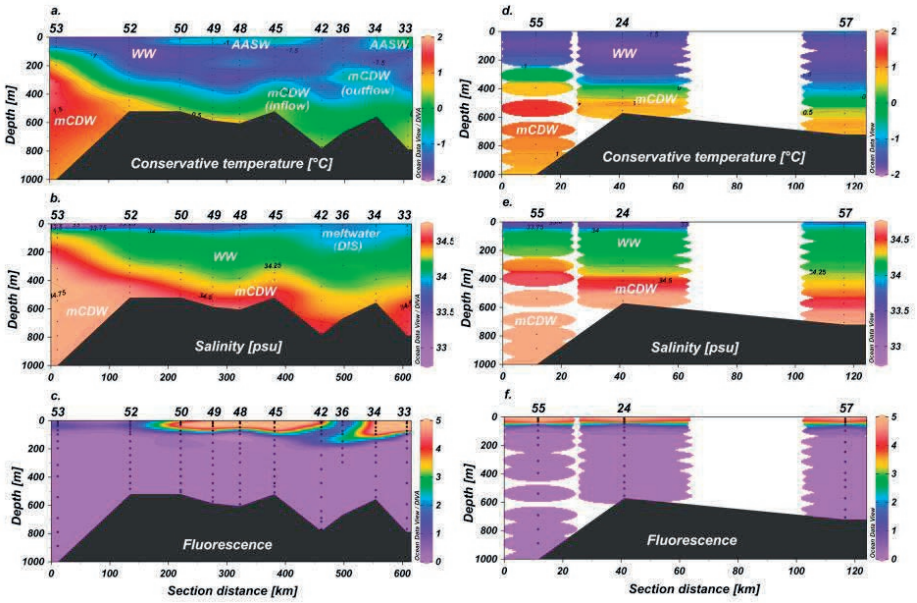

Figure 2.3 Section plots of ancillary hydrographic parameters along both transects of GPpr12. Dotson: a. potential temperature (˚C), b. salinity, and c. fluorescence; Getz: d. potential temperature (˚C), e. salinity, and f. fluorescence. It is noted that in Fig 2.3a there is an artefact at below 300 m at Stn 36 due to a malfunction of sampling bottles and therefore no data is shown for this depth interval.

2.3.1.2 Freshwater input ($\delta^{18}O$)

The size of the ASP changes during Antarctic summer due to seasonal melting and wind-driven transport of surrounding sea ice. To assess the change of sea ice coverage in the ASP during our sampling period, satellite data with 0.05˚×0.05˚ resolution from the Operational Sea Surface Temperature and Ice Analysis (OSTIA) system is used. In the

beginning of the sampling period (23-01-2018) (Fig. 2.4a), the ASP was enclosed. It gradually opened to the open ocean by the end of the sampling period (02-02-2018) (Fig. 2.4b). Along the Dotson transect, 6 stations (Stns 33, 34, 36, 42, 45, and 48) were in the ASP during the entire sampling period, whereas the other 4 stations (Stns 49, 50, 53, and 53) were either on the edge of the sea ice or covered by sea ice. Along the Getz transect, Stns 24 and 55 were covered by sea ice during the sampling period, whereas Stn 57 was on the edge of the sea ice in the beginning and became ice free during the sampling period.

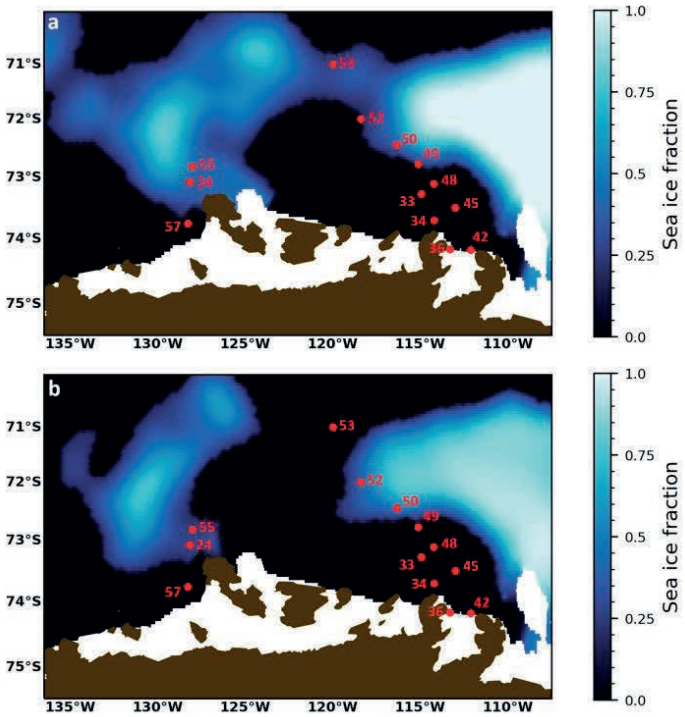

Figure 2.4 Sea ice coverage during GPpr12 sampling. Data are derived from the Operational Sea Surface Temperature and Ice Analysis (OSTIA) system (0.05 × 0.05 degree) from a. the beginning of the sampling period (23-01-2018), and b. the end of the sampling period (02-02-2018).

To further assess freshwater input into the ASP during the sampling period, measurements of oxygen isotopes ($\delta^{18}O$) of seawater and salinity are utilized to differentiate between sea ice melt, meteoric

input, and CDW, which are quantified in a three end-member mass balance approach after Östlund and Hut (1984) and Meredith et al. (2013). Following Randall-Goodwin. et al. (2015), we assign three different endmembers in the AS, based on salinity and $\delta^{18}O$. A mass balance is calculated utilizing three equations:

$$f_{sim} + f_{met} + f_{CDW} = 1 \text{..... (Eq. 1)}$$

$$f_{sim} \times S_{sim} + f_{met} \times S_{met} + f_{CDW} \times S_{CDW} = S_{obs} \text{..... (Eq. 2)}$$

$$f_{sim} \times \delta_{sim} + f_{met} \times \delta_{met} + f_{CDW} \times \delta_{CDW} = \delta_{obs} \text{..... (Eq. 3)}$$

Here, *sim*, *met*, *CDW*, and *obs*, denote sea ice melt, meteoric water, circumpolar deep water, and observed values, respectively, and *f*, *S*, and *δ*, represent fraction, salinity, and oxygen isotope value ($\delta^{18}O$), respectively. S_{sim}, S_{met}, S_{CDW}, δ_{sim}, δ_{met}, δ_{CDW}, are required to be constrained to obtain the contributions of each fraction (f_{sim}, f_{met}, f_{CDW}). Following Randall-Goodwin. et al. (2015), we assign 7, 0 and 34.62, as the salinity of S_{sim}, S_{met}, and S_{CDW}, respectively, and 2.1‰, –25‰, and –0.059‰ as the $\delta^{18}O$ endmember values for δ_{sim}, δ_{met}, and δ_{CDW}, respectively. The observed salinity in CDW at some stations appears higher than the endmember as used by Randall-Goodwin. et al. (2015) but as noted by them, all endmembers are likely to vary seasonally and yearly. For consistency and comparison to previous studies, we adopt the same endmembers as used before. The results of this calculation show the extent of melting of sea ice/ice shelves and the distribution of CDW (Fig. 2.5). It should be noted the CDW endmember represents inflowing seawater that gets modified by the processes of sea ice melt and formation and meteoric water input that contribute to formation of AASW and WW. Thus, AASW and WW are not further distinguished in this model.

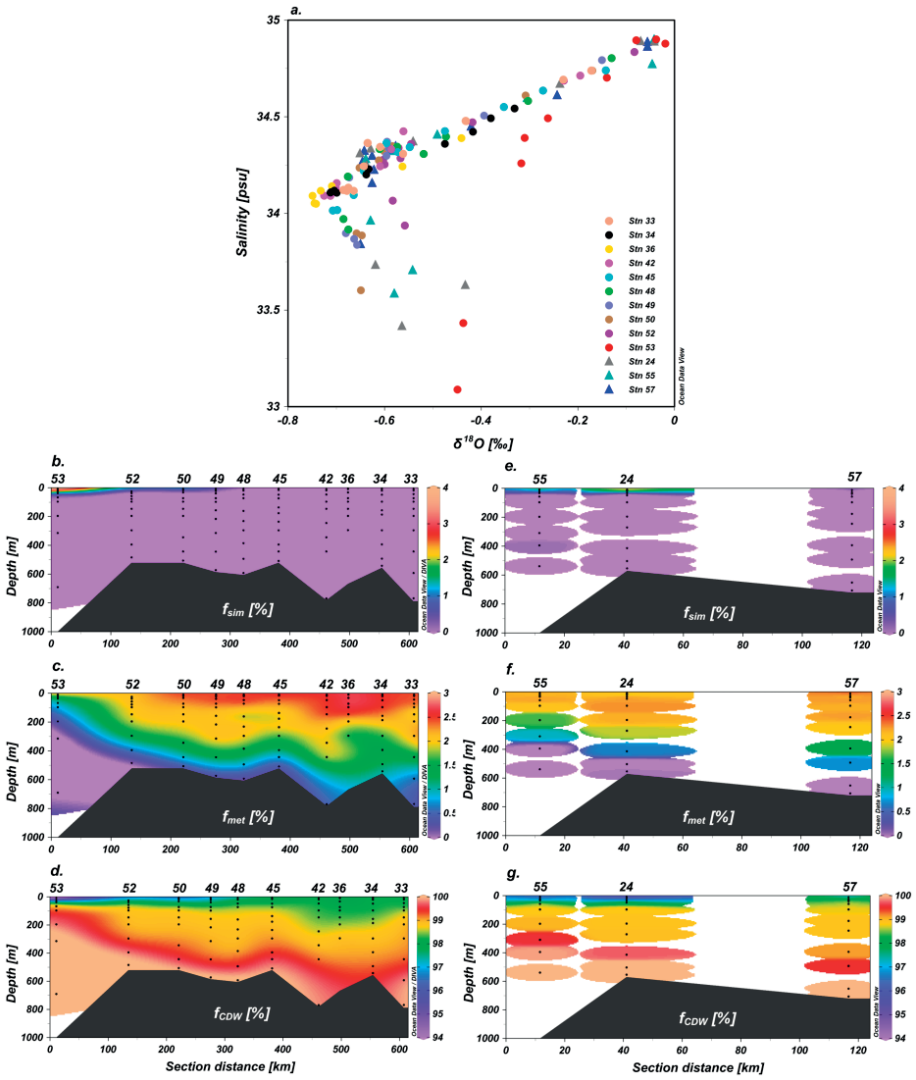

Figure 2.5 a. GPpr12 Oxygen isotope composition ($\delta^{18}O$) versus salinity, and b. – g. section plots of the fraction of freshwater and CDW along both transects. The fraction of sea ice melt (f_{sim}), meteoric water (f_{met}), and CDW (f_{CDW}) along the DIS transect – b. to d., and the GIS transect – e. to g. Endmembers of $\delta^{18}O$ of f_{sim}, f_{met}, and f_{CDW}, are 2.1, -25, -0.0059, respectively; whereas the endmembers of S are, 7, 0, 34.62, respectively. Note that the scales differ between Figs 2.5b to 2.5g.

Relatively elevated f_{sim} (1-3%) was observed in the upper 40 m along both transects, specifically at the open ocean station (Stn 53), the

shelf break station (Stn 52), and mCDW inflow stations (Stns 50 and 49) along the Dotson transect (Fig. 2.5b), and the off-shelf station (Stn 55), and the shelf break station (Stn 24) along the Getz transect (Fig. 2.5e). This result corresponds with the observations of the changing sea ice cover during the sampling period – the stations with elevated f_{sim} (Stns 53, 52, 50, 49, 55, and 24) were located either within the sea ice or on the edge of the sea ice (Fig. 2.4). Secondly, along the Dotson transect, elevated fmet (>2.5%) was observed in the upper 145 m at the mCDW inflow station (Stn 42) and mCDW outflow stations (Stns 36, 34, and 33) (Fig. 2.5c), indicating surface meltwater input form the ice shelf in the surface, consistent with the distribution of salinity (Fig. 2.3b). Along the Getz transect, comparatively smaller f_{met} (2-2.5%) than along the Dotson transect was observed in the upper 245 m of the shelf station (Stn 57) and the maximum depth extent of f_{met} gradually decreased offshore (Fig. 2.5f).

2.3.2 Phytoplankton abundance

Along the Dotson transect, chlorophyll a autofluorescence was relatively elevated in the upper 100 m of most stations (Fig. 2.3c, Stns 33, 34, 36, 42, 45, 48, 49, and 50). At the shelf break station (Stn 52) and the open ocean station (Stn 53), fluorescence had a maximum at a shallower depth compared to the other stations (Fig. 2.3c). Along the Getz transect (Stns 55, 24, and 57), elevated fluorescence occurred over a shallower depth range (upper 40 m) at all three stations (Fig. 2.3f) than the Dotson transect. From here on, the surface layer is referred to as the water column between the surface and the depth where maximum fluorescence was observed. Deeper than this surface maximum, the fluorescence signal rapidly declined. The stations with elevated fluorescence in the surface layer (relative to other stations) along the Dotson transect (Stns 33, 34, 36, 42, 45, 48, 49, and 50) and Getz transect (Stn 55, 24, and 57) are referred as phytoplankton bloom stations in the following sections as they have high standing stock and it is well established there is an annual phytoplankton bloom in the ASP (Alderkamp et al., 2015; Arrigo et al., 2012; Gerringa et al., 2012; Yager et al., 2012). The phytoplankton

community composition along the Dotson transect was dominated by haptophytes (59% to almost 100%) with highest values at Stn 45 and Stn 49 (99.98 and 99.36%, respectively) (Fig. 2.6), whereas the Getz stations were dominated by diatoms (54-91%), especially at Stn 55 (91.3%) and Stn 24 (87.9%) (Fig. 2.6).

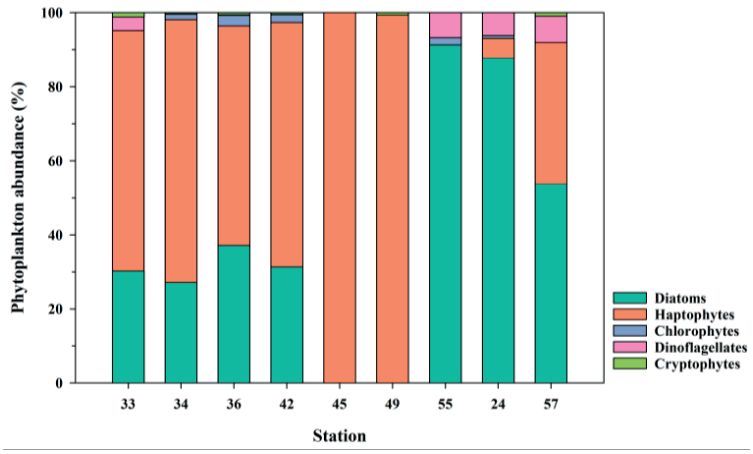

Figure 2.6 Abundance of different phytoplankton groups in the surface layer along both Dotson transect (Stns 33, 34, 36, 42, 45, 49) and Getz transect (Stns 55, 24, 57).

2.3.3 Dissolved metal concentration

Generally, dissolved Zn concentrations ([dZn]) and dissolved Cd concentrations ([dCd]) were elevated in mCDW compared to WW and AASW (Figs 2.2b and 2.2c). Along the Dotson transect, [dZn] ranged from 1.22 to 8.12 nmol L^{-1} (Fig. 2.7a), whereas [dCd] ranged from 0.29 to 0.83 nmol L^{-1} (Fig. 2.8a). The highest [dZn] and [dCd] were observed close to the sea floor (~540 m) of Stn 48 (Figs 2.7a and 2.8a), with the lowest [dZn] and [dCd] observed in the upper 50 m of most of the bloom stations (Stns 33, 34, 45, 48, 49, 50), where fluorescence was relatively high compared to the other stations (Figs 2.3c, 2.7a, and 2.8a). Generally, the distribution trends of dZn and dCd were similar, with elevated [dZn] (>5.2 nmol L^{-1}) and [dCd] (>0.73 nmol L^{-1}) following the distribution of mCDW (Fig. 2.3a and 2.3b). Along the Getz transect, [dZn] and [dCd] ranged from 0.91 to 7.14 nmol L^{-1} and 0.06 to 0.79

nmol L^{-1}, respectively – much lower dissolved concentrations of both metals were observed in the upper 40 m of the off-shelf station (Stn 55) and the shelf break station (Stn 24), where fluorescence was elevated (Figs 2.3f, 2.7d, and 2.8d), compared to the Dotson transect. Akin to the Dotson transect, the distribution of [dZn] followed the distribution of mCDW, with highest concentrations near the seafloor (Figs 2.3a, 2.3b and 2.7d). However, in contrast to [dZn], the highest [dCd] along the Getz transect were not observed near the sea floor; instead, elevated [dCd] (0.75 to 0.79 nmol L^{-1}) were observed in the water column at 300-400 m at the off-shelf station (Stn 55), 400-500 m at the shelf break station (Stn 24), and 310-570 m at the shelf station (Stn 57) (Fig. 2.8d).

2.3.4 Particulate metal concentration

2.3.4.1 Labile particulate metal concentrations

The distributions of LpZn and LpCd followed similar patterns; labile particulate Zn concentrations ([LpZn]) and labile particulate Cd concentrations ([LpCd]) were both generally low below 100 m along the Dotson transect and below 40 m along the Getz transect (all [LpZn]<0.2 nmol L^{-1}; all [LpCd]<0.01 nmol L^{-1}, Figs 2.7b, 2.7e, 2.8b and 2.8e). In the surface layer along the Dotson transect, relatively elevated [LpZn] (>1.5 nmol L^{-1}) and [LpCd] (>0.1 nmol L^{-1}) were found at the off-shelf station (Stn 53) and the shelf break station (Stn 52), most mCDW inflow stations (Stns 49, 48, and 45), and most mCDW outflow stations (Stns 33 and 34) (Figs 2.7b, and 2.8b), whereas low [LpZn] (<0.56 nmol L^{-1}) and [LpCd] (<0.01 nmol L^{-1}) were observed at the same depth at Stn 42 (inflow) and Stn 36 (outflow), coinciding with lower fluorescence (Fig. 2.3c). In the surface layer of the Getz transect, [LpZn] (>2 nmol L^{-1}) and [LpCd] (0.2 to 0.4 nmol L^{-1}) were higher than along the Dotson transect, particularly at the off-shelf station (Stn 55) and the shelf break station (Stn 24); whereas at the shelf station (Stn 57) [LpZn] (~1.3 nmol L^{-1}) and [LpCd] (0.1 to 0.2 nmol L^{-1}) were lower than Stn 55 and Stn 24. (Figs 2.7e and 2.8e).

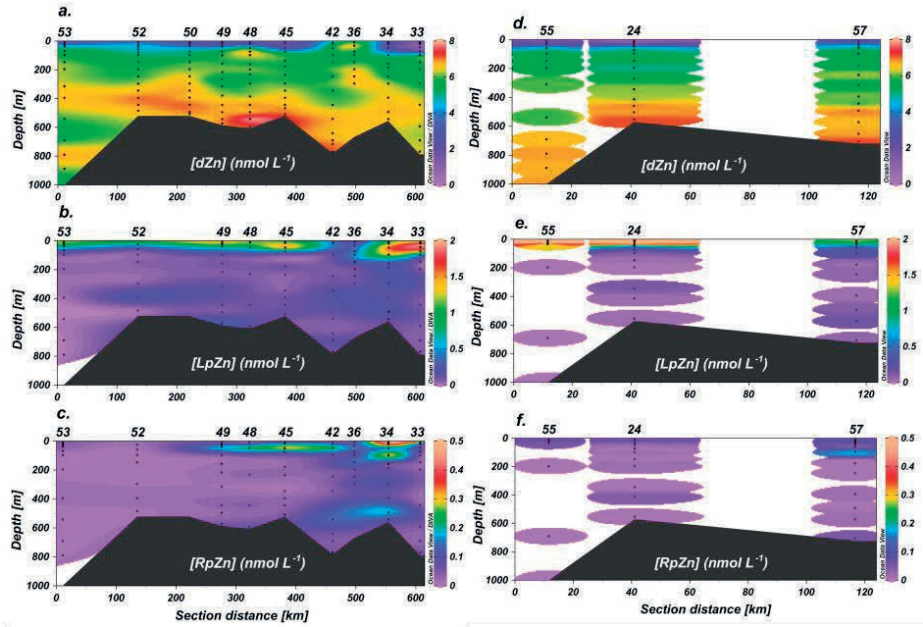

Figure 2.7 GPpr12 section plots of [dZn], [LpZn], and [RpZn] (nmol L^{-1}) along both transects. Dotson transect: a. dZn, b. LpZn, c. RpZn; Getz transect: d. dZn, e. LpZn, f. RpZn.

2.3.4.2 Refractory particulate metal concentrations

Generally, [RpMe] were much lower than [LpMe] in this study – refractory particulate Zn concentrations ([RpZn]) were 3 to 5 times lower than [LpZn], and refractory particulate Cd concentrations ([RpCd]) were 20 to 50 times lower than [LpCd]. Along the Dotson transect, compared to the deep, relatively elevated [RpZn] were observed at ~50 m at one of the mCDW inflow stations (Stn 45), and in the upper 20 m and around ~100 m of the mCDW outflow station (Stn 34) (Fig. 2.7c). Furthermore, a slight increase in [RpZn] was found at 500-550 m of Stn 42 (0.14 nmol L^{-1}) and Stn 34 (0.2 nmol L^{-1}) (Fig. 2.7c). Along the Getz transect, [RpZn] were generally low (<0.1 nmol L^{-1}), except for an elevation (0.17 nmol L^{-1}) at 100 m at the shelf station (Stn 57) (Fig. 2.7f).

In the case of RpCd, elevated [RpCd] were observed in the surface layer of most stations (with the exception of Stns 42 and 36), along

the Dotson transect; particularly, maxima in [RpCd] were found in the upper 50 m of the mCDW inflow station (Stn 45, 0.005 nmol L^{-1}) and the mCDW outflow station (Stn 33, 0.005 nmol L^{-1}) (Fig. 2.8c). Along the Getz transect, [RpCd] were relatively elevated (~0.01 nmol L^{-1}) in the upper 40 m of the shelf break station (Stn 24) and the shelf station (Stn 57), whereas concentrations were lower (<0.01 nmol L^{-1}) at the same depth for off-shelf station (Stn 55) (Fig. 2.8f). Below the surface later, [RpCd] were homogeneously low (<0.001 nmol L^{-1}) along both transects. Since [RpCd] were significantly lower than [LpCd], such discrepancy results in a large uncertainty for measured [RpCd], especially in the surface layer where [LpCd] were elevated (see details in section 2.4.2.2).

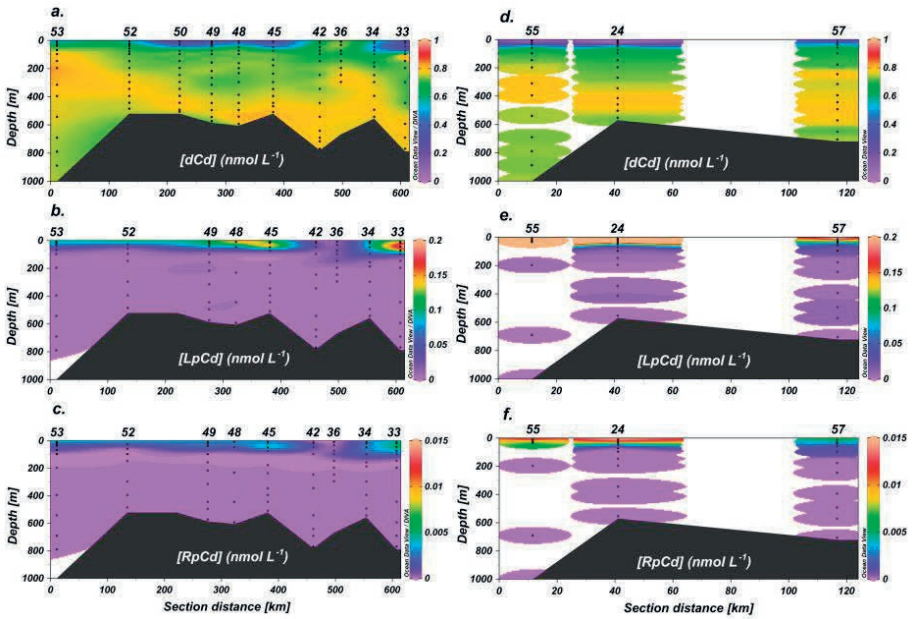

Figure 2.8 GPpr12 Section plots of [dCd], [LpCd], and [RpCd] (nmol L^{-1}) along both transects. Dotson transect: a. dCd, b. LpCd, c. RpCd; Getz transect: d. dCd, e. LpCd, f. RpCd.

2.4 Discussions

2.4.1 Sources of dZn, dCd, pZn, and pCd to the AS

In this study, the results demonstrate that the dissolved phase dominates the total particulate (labile+refractory) concentrations at depth – [dZn] and [dCd] were generally 9 to 13 times higher than total particulate Zn concentrations ([TpZn]) and total particulate Cd concentrations ([TpCd]), compared to nearly equivalent particulate and dissolved concentrations for both metals in the surface layer (Figs 2.7 and 2.8). This implies that scavenging by, and/or precipitation onto particles, are not dominant processes for the cycling for Zn and Cd, relative to external dissolved sources and regeneration of biogenic particles. However, external input of pZn and pCd followed by solubilization could also serve as a potential source of dZn and dCd. To understand the cycling of both metals in the coastal Antarctic area, one of the objectives of this study is to assess the diverse sources of both dissolved and particulate Zn and Cd in the ASP. Here we evaluate the potential sources of trace metals to our transects and the wider region, including (i) atmospheric deposition; (ii) mCDW; (iii) shelf sediment sources; (iv) Dotson Ice Shelf (meltwater induced by mCDW); (v) sea ice.

2.4.1.1 Atmospheric deposition

Atmospheric deposition is an important input route of trace metals to the ocean (Mahowald et al., 2018). Aerosols supply trace metals via dissolution of particles. It has also been suggested that atmospheric deposition (notably of anthropogenic particles) may be an important source for Zn and Cd in some oceanic regions (Liao et al., 2020; Ho et al., 2011). Although dust from continental landmasses and inter-hemispheric transport from the Northern Hemisphere has been observed in the surface waters of the open Southern Ocean (Li et al., 2008), it is believed that the transport of atmospheric terrigenous and anthropogenic aerosols from lower latitudes to the Antarctic region is limited because of its remoteness from non-ice covered continents (Planquette et al., 2013; Fan et al., 2021; Gerringa et al., 2012).

In this study, [LpZn] and [LpCd] in the surface were relatively elevated, whereas [dZn] and [dCd] were relatively low in the surface of both Dotson and Getz transects, except for the stations right in front of the DIS (Stns 42 and 36; Figs 2.7 and 2.8). The low dissolved concentrations in combination with elevated LpMe implies biological uptake. On the other hand, both [RpZn] and [RpCd] in the surface were much lower than [LpZn] and [LpCd] (Figs 2.7 and 2.8), implying little addition of lithogenic material. In fact, [RpZn] were only relatively elevated at Stn 34 which was close to the shore (Figs 2.1 and 2.7c), implying an input of lithogenic particles from the coast, rather than atmospheric deposition. For RpCd, relatively elevated concentrations (<0.004 nmol L^{-1}) in the surface layer compared to at depth (<0.0001 nmol L^{-1}) at most of bloom stations, coincided with both high fluorescence and elevated [LpCd] (Figs 2.3 and 2.8). Given that dust deposition is believed to be limited in this area and the lithogenic pCd only accounts for a minor fraction of the particle composition (further discussed in section 2.4.2), we believe that the elevation of RpCd in the surface likely result from incomplete leaching of biogenic Cd in the labile phase (perhaps relatively refractory biogenic pCd) and thus partly shows up in the refractory fraction, as the elevated RpCd was two orders of magnitude lower than LpCd (~0.2 nmol L^{-1}). Overall, we conclude that atmospheric deposition is not a significant source of either Zn or Cd to the ASP during our study, consistent with that concluded for Fe in the AS (Gerringa et al., 2012; Planquette et al., 2013) and for Zn on the west Antarctic Peninsula (Fan et al., 2021).

2.4.1.2 mCDW as a source of Zn and Cd to the AS region

It has been suggested that mCDW is a potential source of trace metals to shallower coastal Antarctic waters as it is a macro/micronutrient-rich water mass and it upwells along the continental slope or intrudes via glacial troughs (e.g., Gerringa et al., 2012; Planquette et al., 2013; Sherrell et al., 2015). Previous work in the AS by Sherrell et al. (2015) showed [dZn] of 5 to 7 nmol L^{-1} in mCDW. In this study we observed

similar [dZn] within the least modified CDW (6.47±0.39 nmol L^{-1}, mean±1 SD) (Fig. 2.2b), namely deeper than 145 m at the open ocean station (Stn 53) and deeper than 310 m at the off-shelf station (Stn 55) (Figs 2.7a, and 2.7d), consistent with the previous observation that nutrient-rich mCDW carried dZn into the AS (Sherrell et al., 2015).

In the case of Cd, however, although [dCd] was also elevated in the least modified CDW (0.75±0.02 nmol L^{-1}, mean±1 SD) (Fig. 2.2c) at the open ocean station (Stn 53) and the off-shelf station (Stn 55), the relative dCd maximum within mCDW was shallower than that of dZn (Figs 2.8a and 2.8d). This could be explained by the regeneration of dZn at greater depth (Lohan et al., 2002; Zhao et al., 2014) and/or higher [dCd] in upper mCDW relative to lower mCDW (Sieber et al., 2019a). Nevertheless, [dCd] (0.73-0.79 nmol L^{-1}, mean±1 SD) in mCDW were generally higher than in WW and AASW (Figs 2.2c), suggesting that mCDW is a source of dCd to the AS. To the best of our knowledge, there are no previous data reported on dCd in mCDW in the AS region. However, [dCd] in mCDW reported in this study are comparable to prior observations in the nearby Ross Sea region by Gerringa et al. (2020a), who reported an average [dCd] of 0.78±0.02 nmol L^{-1} in overall mCDW and suggested that mCDW is a source of dCd to Antarctic shelf regions.

Since our results confirm that mCDW is an important source of both dZn and dCd to the AS, we estimate the metal flux from mCDW to the AS. Arneborg et al. (2012) reported a estimation of CDW flux (~0.21 Sv) in the Amundsen Sea in 2010. Based on this estimation of CDW flux, we estimate that dZn and dCd fluxes from mCDW to the AS are 42.8 mol $year^{-1}$ and 5.0 mol $year^{-1}$, respectively. However, Ha et al. (2014) reported that CDW flux increased to ~0.34 Sv in 2011, which results in the metal fluxes to the AS from mCDW rising to 69.4 nmol $year^{-1}$ and 8.0 mol $year^{-1}$ for Zn and Cd, respectively. Such a large interannual variability of mCDW intrusion onto Antarctic continental shelf has been attributed to not only the variability of the wind field and atmospheric circulation (Connolley, 1997; Hosking et al., 2013) but also the local Ekman pumping induced by spatial stress imbalance due to sea ice dynamic in austral summer (Kim et al., 2021). Our result

shows that this interannual fluctuation of mCDW intrusion could influence the flux of dZn and dCd (and potentially other trace metals) to the AS, potentially affecting the biogeochemistry and inventories of these metals in the AS.

In contrast to dZn and dCd, both LpMe and RpMe displayed consistently and extremely low concentrations within CDW at Stn 53 and Stn 55 (Figs 2.7 and 2.8), likely since mCDW is a mixture of old and deep-water masses from which particles have settled or have been remineralized. Therefore, mCDW does not appear to be a source of pZn or pCd to the AS.

2.4.1.3 Sedimentary input of Zn and Cd to mCDW at depth

Based on the observation of high dZn and dCd in mCDW (Figs 2.3, 2.7, and 2.8), we are confident that the intrusion of nutrient rich mCDW brings metal-rich waters onto the continental shelf that are subsequently mixed with overlying, relatively trace metal-poor seawater, with relatively high [dZn] and [dCd] present even after mixing (Figs 2.7 and 2.8). Since mCDW travels along the seafloor of the continental shelf (Fig. 2.3), sedimentary input induced by particle (and porewater) resuspension or porewater diffusion might supply additional dZn and dCd to mCDW (Schmitt et al., 2009; Sherrell et al., 2015). However, such sedimentary input was suggested to be only a modest source for dZn in the AS, compared to the incoming mCDW (Sherrell et al., 2015). To assess whether sediment-derived dZn and dCd is added to mCDW along its transport path, as well as to quantify any such contribution, we evaluated the conservative mixing lines in waters up to 100 m above the seafloor at stations located on the continental shelf and the shelf break (Fig. 2.9).

Based on the Θ-S diagram and section profile of the inflow (Figs 2.2a and 2.3), WW and the least modified CDW were the two primary water masses involved in mixing over this depth range (100 m above the seafloor). Assuming that WW and the least modified CDW (referred to as CDW in this section) were the only two components of

mixing, changes in [dZn] and [dCd] in mCDW should follow the mixing line of WW-CDW if distributions of the metals were only controlled by conservative mixing. The endmembers for salinity (S), [dZn], and [dCd] used for this mixing line are the average values (mean±1 SD) of WW (S_{WW}: 34.18±0.03, $[dZn]_{WW}$: 5.81±0.44 nmol L^{-1}, $[dCd]_{WW}$: 0.73±0.02 nmol L^{-1}) and CDW (S_{CDW}: 34.72±0.03, $[dZn]_{CDW}$: 6.47±0.39 nmol L^{-1}, $[dCd]_{CDW}$: 0.75±0.02 nmol L^{-1}) respectively. Specifically, the endmember for CDW is selected from the observed salinity from this study (Stns 53 and 55, where the least modified CDW was located), rather than using the value reported by Randall-Goodwin. et al. (2015) as used for freshwater calculation in section 2.3.1.2. This is because there is no reported [dZn] endmember data for pure CDW in this region and this calculation assesses the effects of mixing between local, already partly modified water masses. This mixing line can then be used differentiate and quantify any local input (source; points above the mixing line) or output (sink; points below the mixing line) (Fig. 2.9).

In the case of dZn, all samples from both the Dotson and Getz transects plot above the mixing line (Fig. 2.9a), indicating a consistent external dZn source to mCDW. By calculating the average difference between the mixing line and individual samples, we estimate that this Zn source supplies ~0.42±0.22 nmol L^{-1} (mean±1 SD) of dZn to mCDW. This result agrees with previous suggestions that benthic input supplies modest dZn to the AS (Sherrell et al., 2015), compared to dZn originating within CDW. This additional Zn source could result from sediment resuspension followed by desorption and/or porewater diffusion (e.g., Conway and John, 2014b; Lemaitre et al., 2020). The same assessment for dCd, however, suggests only limited sedimentary dCd input at most stations along the Dotson transect (0.030±0.023 nmol L^{-1}, mean±1 SD), which is an order of magnitude smaller than dZn (Fig. 2.9b). In contrast, along the Getz transect, the near-bottom samples at Stn 24 and Stn 57 plot below the mixing line with an estimated dCd reduction of 0.025±0.016 nmol L^{-1} (mean±1 SD). Thus, compared to dZn, our results show that the sedimentary input of dCd is spatially variable and a relatively small influence, if at all, in the AS. Although sedimentary input contributes modest dZn and

dCd relative to CDW along the DIS transect, which accounts for 7% and 4% for dZn and dCd respectively in mCDW, it is still considered a source for this part of the AS (but not for the GIS transect). We estimated fluxes from the sediment for both Zn and Cd, assuming the volume of CDW intrusion onto the continental shelf remains constant; estimated sedimentary metal fluxes are about 4.5 mol year^{-1} and 0.3 mol year^{-1} of dZn and dCd to the overlying water, based on the calculated CDW flux in the AS in 2011 (Ha et al., 2014). However, it should be noted that these values are first-hand estimates which could vary since the spatial and temporal variability of sedimentary fluxes are unknown in the region.

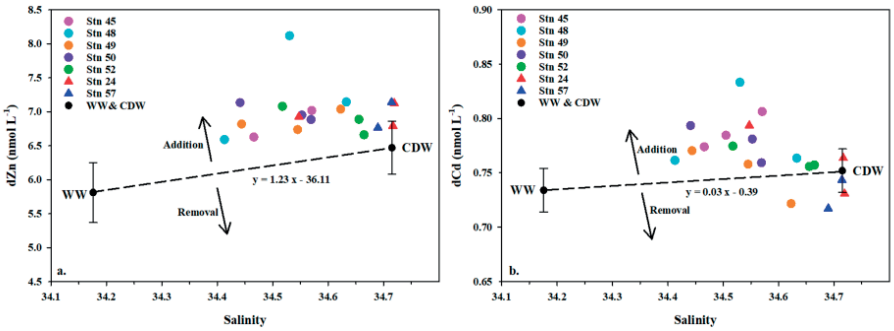

Figure 2.9 [dZn] and [dCd] versus salinity close to the AS seafloor (~ 100 m). a. [dZn] versus salinity. b. [dCd] versus salinity. Black circles represent the average dissolved metal, as well as average salinity for both WW and CDW. Average values were selected using Θ-S diagram (Fig. 2.2) and section profile (Figs 2.7a, 2.7d, 2.8a, and 2.8d). The endmembers (mean±1SD) for salinity (S), [dZn], and [dCd], in WW and CDW are – S_{WW}: 34.18±0.03, $[dZn]_{WW}$: 5.81±0.44 nmol L^{-1}, $[dCd]_{WW}$: 0.73±0.02 nmol L^{-1}; S_{CDW}: 34.72±0.03, $[dZn]_{CDW}$: 6.47±0.39 nmol L^{-1}, $[dCd]_{CDW}$: 0.75±0.02 nmol L^{-1}. Dashed lines represent the mixing line between WW and CDW.

In the case of the particulate metals, both [LpZn] and [LpCd] decreased with depth ([LpZn]<0.2 nmol L^{-1}; [LpCd]<0.01 nmol L^{-1}, Figs 2.7b, 2.7e, 2.8b and 2.8e) compared to the surface layer along both transects and near bottom. Similarly, [RpCd] were extremely low at depth (<0.01 nmol L^{-1}) along both transects (Figs 2.8c and 2.8f), implying that sedimentary input does not contribute a significant amount of LpZn, LpCd, or RpCd to the water column and/or

regeneration of labile particles at depth. On the other hand, [RpZn] is elevated between 400-600 m in the near-shore area (~0.09 nmol L^{-1}, Stns 42 and 34) (Fig. 2.7c), suggesting a source of RpZn limited to shelf sediments near the ice shelf which potentially consists of glacial particles (terrestrial input).

2.4.1.4 The influence of the DIS on Zn and Cd in the AS

Ice shelves are considered sources of both dissolved and particulate trace metals, with potential offshore transport of these metals. For example, it has been suggested that basal melt beneath the DIS adds dissolved Fe (e.g., mCDW) (Alderkamp et al., 2015; Sherrell et al., 2015; Yager et al., 2012) as well as particulate Fe (van Manen et al., 2022) to underlying waters. Additionally, mCDW may carry sediment-derived and ice shelf-derived particles into Antarctic coastal waters – Herraiz-Borreguero et al. (2016) found significant Fe input from the Amery Ice Shelf due to the melting of marine ice (i.e., an accreted ice layer formed by supercooling of accumulated frazil ice platelets underneath the ice shelf) potentially contain fine sediments and biogenic materials. However, whether the melting of ice shelves could be a source of dissolved and particulate Zn and Cd, to Antarctic coastal waters remains practically unknown. Previously, Sherrell et al. (2015) suggested that mCDW outflow from the DIS brings only modest amounts of dZn to the Amundsen Sea. For dCd, there is no evidence showing that the DIS melting adds Cd to mCDW outflow, however, Sieber et al. (2019a) suggested a Cd input associated with the meltwater of the Mertz Glacier to nearby surface waters in East Antarctica.

In our study, according to the distribution of salinity, temperature, and $\delta^{18}O$ (Figs 2.3 and 2.5) – the inflowing mCDW (with additional sediment derived trace metals) was characterized close to the floor of the continental shelf (~500 m), whereas the outflowing mCDW was observed between 200 and 400 m, which is in general agreement with previous observations (Randall-Goodwin. et al., 2015; Miles et al., 2016), although the depth can change depending on the geographical location. In addition to the mCDW inflow, mCDW outflow, and ice

shelf melt water, the water at the edge of the DIS (a mixture of WW and AASW, hereby referred to as shelf water) also plays an important role in the cycling of metals in the ice shelf system due to physical mixing process (van Manen et al., 2022). Here, we utilize the same three-endmember mass balance approach described in section 2.3.1.2, but with different (local) endmembers. Assuming physical mixing between three water masses – mCDW inflow, shelf water, and ice shelf meltwater – was the main mechanism that altered dissolved metal concentrations, the equations can be modified:

$$f'_{IS} + f'_{inflow} + f'_{sw} = 1 \text{..... (Eq. 4)}$$

$$f'_{IS} \times \delta'_{IS} + f'_{inflow} \times \delta'_{inflow} + f'_{sw} \times \delta'_{sw} = \delta'_{outflow} \text{...(Eq. 5)}$$

$$f'_{IS} \times S_{IS} + f'_{inflow} \times S_{inflow} + f'_{sw} \times S_{sw} = S_{outflow} \text{.....(Eq. 6)}$$

$$f'_{IS} \times M_{IS} + f'_{inflow} \times M_{inflow} + f'_{sw} \times M_{sw} = M_{outflow} \text{...(Eq. 7)}$$

Here, f' , δ , δ , and M denote the volume fraction, endmember $\delta^{18}O$ value, salinity, and endmember metal concentration (depth-weighted averages, i.e., data integrated over depth and divided by the depth of (part of) the water column to account for unequal spacing between sampled depths), respectively, whereas IS , $inflow$, sw and $outflow$, stand for ice shelf meltwater, mCDW inflow, shelf water, and mCDW outflow, respectively. To get four unknowns (f'_{IS}, f'_{inflow}, f'_{sw}, and M_{IS}), the other endmembers are defined based on observations or previously reported values (Table 2.3). For the mCDW inflow, the endmembers are defined based on Stn 45 and Stn 48 (between the sediments and 100 m above the seafloor). Please note that the endmembers of δ and δ of mCDW used here are different than the CDW endmember used in section 2.3.1.2 that is based on values reported by Randall-Goodwin. et al. (2015) for consistency with previous studies. The purpose of that calculation was to evaluate the freshwater input (sea ice melt water and ice shelf melt water). However, in this section, the aim is instead to assess the mixing of

inflowing mCDW, ice shelf melt water, outflowing mCDW, and shelf water at a much smaller scale and thus we choose the endmembers based on observations in this study. For shelf water, the endmembers are chosen based on temperature (Θ<–1.5˚C) at Stn 45 (72-235 m) (Table 2.3). However, depths from 72 m to 136 m are excluded in this definition due to high production of labile particles produced from intense biological activity. It is noted that Stn 42 is excluded in the selection for both mCDW inflow and shelf water as it is deemed to be strongly influenced by terrestrial input, based on elevated [dFe] (van Manen et al., 2022). However, it is possible the Zn endmember is likely an under"stimation as mCDW may pick up more sediment-derived dZn between Stn 45 and the ice shelf, resulting in an overestimation of ice shelf-derived Zn. For the mCDW outflow, the endmembers are chosen from the first outflow station (Stn 36, 294 m) (Fig. 2.3 and Table 2.3). Using this approach, the output ($f'_{IS} \times M_{IS}$) gives a first order estimate of the concentration contributed by ice shelf melt – a positive value would imply ice shelf melt contributes dissolved metals to mCDW outflow, whereas a negative value would imply net removal.

The results of this calculation show that the mCDW outflow Is composed of 0.6% ice shelf meltwater, 24.5% shelf water, and 74.9% mCDW inflow, with positive ($f'_{IS} \times M_{IS}$) values (Table 2.3), implying a contribution from ice shelf melt. In the case of Zn, estimated [dZn] in the ice shelf meltwater (5.3±5.9 nmol L^{-1}, mean±1 SD) are lower than other water masses involved in the mixing (Table 2.3) with an estimated input of 0.034±0.038 nmol L^{-1} (Table 2.3). This implies that the ice shelf meltwater is not a relatively important source of dZn, even though there is a large uncertainty on this estimate and the endmember. Furthermore, [dZn] in shelf water (5.76±0.16 nmol L^{-1}) was lower than in the incoming mCDW (7.01±0.19 nmol L^{-1}); whereas in the mCDW outflow (6.69 nmol L^{-1}) it appeared to be comparable to the mCDW inflow, although given the single observation available to estimate the outflow endmember, this cannot be stated with certainty. This observation also implies DIS meltwater does not add a significant amount of dZn and suggests an effective dilution by mixing with shelf water once the outflowing mCDW leaves DIS, similar to recent observations for Fe (van Manen et al., 2022). On the other

hand, estimated [dCd] in the ice shelf meltwater (4.5±0.1 nmol L^{-1}) are much higher than in other water masses (Table 2.3), meaning the DIS is a source of dCd to the outflowing mCDW. However, the overall [dCd] in the inflow and outflow are similar (Table 2.3), and it is estimated that DIS melt only adds 0.029±0.0004 nmol L^{-1} of dCd to the outflow, likely due to a small contribution of meltwater (0.6%). The same calculations were also done for both fractions of particulate metals. A negligible contribution (or minor removal) is estimated from ice shelf melt ([LpZn]: –0.03±0.01 nmol L^{-1}, [RpZn]: 0.047±0.0001 nmol L^{-1}, [LpCd]: 0.001±0.0001 nmol L^{-1}, and [RpCd]: 0.001±0.00001 nmol L^{-1}) (Table 2.3). In a previous study, Sieber et al. (2019a) suggested that glacial melt water may contribute dCd to surface waters from the Mertz Glacier (east Antarctica), possibly originated in particulate form. However, input of pCd from the DIS is not observed in the current study.

Our results thus suggest that DIS melt is only a negligible source of dZn and dCd, which agrees with the findings of Sherrell et al. (2015), and that DIS melt is not a discernible source of pZn and pCd. However, the caveat of this approach is that it is based solely on physical mixing with best estimates for the endmembers involved. From the measurements in this study, we are unable to quantify any biogeochemical process (e.g., adsorption onto particles and regeneration) or physical processes (e.g., particle settling) that might remove/add both metals underneath DIS. To further investigate this issue, a more direct proxy than dissolved metal concentrations is required, such as trace metal isotope ratios that could help to differentiate between coinciding metal sources and sinks during mCDW-induced ice sheet melt (e.g., Conway and John, 2014b; Sieber et al., 2019a; Sieber et al., 2020).

Table 2.3 Endmembers and the output of the three-endmember mass balance approach used in section 2.4.1.4. The symbols $f'_{\square}$, $\delta'_{\square}$, S, and $M_{\square}$ denote the fraction (%), weight-averaged $\delta^{18}O$ (‰), salinity, and weight-averaged metal concentration (nmol L^{-1}) (mean±1 SD), respectively, whereas $IS_{\square}$, $inflow_{\square}$, $sw_{\square}$ and $outflow_{\square}$, stand for the observed values in ice shelf meltwater, mCDW inflow, shelf water, mCDW outflow, respectively. a: $\delta^{18}O$ value in ice shelf is referred from Randall-Goodwin. et al., 2015. b: values are calculated based on the interpolation of $\delta^{18}O$ between 442 m and 507 m as $\delta^{18}O$ of 467 m was not analyzed.

Endmembers

	station	depth (m)	δ'	S	M_{dZn}	M_{dCd}	M_{LpZn}	M_{RpZn}	M_{LpCd}	M_{RpCd}
ice shelf (IS)			–25[a]	0						
inflow (mCDW)	45	442	–0.27	34.47	6.63	0.77	0.10	0.003	0.03	0.0001
	45[b]	467	–0.22	34.50	6.98	0.78	0.11	0.003	0.03	0.0001
	45	507	–0.14	34.57	7.02	0.81	0.14	0.003	0.04	0.0001
	bottom	520								
	48	592	–0.13	34.63	7.14	0.76	0.15	0.003	0.07	0.0001
	bottom	605								
	wt. avg		–0.18±0.07	34.57±0.09	7.01±0.19	0.77±0.01	0.13±0.03	0.003±0.0002	0.05±0.03	0.0001±0.0002
shelf water (sw)	45	176	–0.55	34.18	5.75	0.74	0.13	0.004	0.029	0.0001
	45	235	–0.60	34.20	5.97	0.74	0.04	0.004	0.031	0.0001
	bottom	238								
	wt. avg		–0.55±0.03	34.18±0.01	5.76±0.16	0.74±0.001	0.12±0.06	0.004±0.0001	0.029±0.001	0.0001±0.000001
outflow (mCDW)	36	294	–0.44	34.22	6.69	0.79	0.10	0.004	0.092	0.0001

Output

f'_{IS}	f'_{inflow}	f'_{sw}	dZn_{IS}	dCd_{IS}	$dZn_{IS} \times f'_{IS}$	$dCd_{IS} \times f'_{IS}$
0.6	74.9	24.5	5.3±5.9	4.5±0.1	0.034±0.038	0.029±0.0004
			$LpZn_{IS}$	$LpCd_{IS}$	$LpZn_{IS} \times f'_{IS}$	$LpCd_{IS} \times f'_{IS}$
			–4.95±2.26	0.09±0.01	–0.03±0.01	0.001±0.0001
			$RpZn_{IS}$	$RpCd_{IS}$	$RpZn_{IS} \times f'_{IS}$	$RpCd_{IS} \times f'_{IS}$
			7.33±0.04	0.015±0.0001	0.047±0.0001	0.001±0.0001

2.4.1.5 Sea ice as a negligible source of dissolved metals to the ASP

Sea ice is considered an important local source of trace metals in the polar regions, notably for Fe (Duprat et al., 2020; Lannuzel et al., 2008; Moreau et al., 2019; Arrigo et al., 1997; Lannuzel et al., 2010; Sedwick and DiTullio, 1997). Although observations for Zn and Cd in sea ice are relatively scarce, Lannuzel et al. (2011) reported that dZn and dCd are not particularly enriched in sea ice near East Antarctica, relative to seawater concentrations, suggesting that that sea ice is not a significant source of dZn and dCd to surface waters in that region. However, given the strong melt of sea ice in the AS during the period of sampling (Fig. 2.4), sea ice melt might be a source of trace metals, especially in the offshore area. In this study, several stations (Stns 53, 52, 50, 49, 55, and 24) were located within the sea ice or on the edge of the sea ice region (Fig. 2.4). Furthermore, a positive sea ice melt fraction was found in the upper 20 m of these stations, as well as at Stn 48 and Stn 57 (Fig. 2.5), suggesting these stations are subject to the influence of sea ice melt. To further evaluate the influence of sea ice melt on the metal concentrations in the surface (~20 m), the open ocean station (Stn 53), the shelf break station (Stn 52), and the bloom stations (Stns 50, 49, 48, 55, 24, and 57) are selected for comparison.

If sea ice melt were a strong source and the main driver of dissolved metal concentrations in the surface, both [dZn] and [dCd] should co-vary with salinity and f_{sim} (i.e., concentrations increase with decreasing salinity and increasing f_{sim}). However, [dZn] and [dCd] in the region with a positive f_{sim} displays an increasing trend with increasing salinity and decreasing f_{sim} (Fig. 2.10). Additionally, in the surface layer, higher metal concentrations are observed at the non-bloom stations, whereas at the bloom stations lower metal concentrations are found (Figs 2.3, 2.7, and 2.8). This implies that the dissolved metal concentrations in the upper 20 m in the region with a positive f_{sim} are not only influenced by sea ice melt, but predominantly controlled by other processes – biological uptake and/or sorption onto (biogenic) particles, which is supported by increasing LpMe observed at the bloom stations (Figs 2.3, 2.7, and

2.8). This complicates any assessment of sea ice melt as a metal source since biological uptake and scavenging processes could balance out any primary contribution from sea ice melt. Nevertheless, with the parameters obtained in this study, we speculate that sea ice melt is not a strong source of either dZn or dCd in the AS. Similar observations are reported for sea ice in East Antarctic waters (Lannuzel et al., 2011). This is contrast to observations in Arctic sea ice which is found to be enriched in Zn and Cd, compared to surface seawater and therefore suggested to be a significant source to seawater (Tovar-Sánchez et al., 2010). The discrepancy between Arctic and Antarctic sea ice might result from the influence of anthropogenic aerosol deposition in the Arctic – Marsay et al. (2018b) found Zn and Cd in aerosol particles collected in the Arctic region to be significantly higher than crustal values, implying the transport of anthropogenic aerosols from nearby landmasses. More direct measurements, such as metal concentrations in sea ice and meltwater, and other proxies such as metal stable isotopic composition, are needed to further unravel the dynamics of dissolved metals and assess the relative influence of chemical (e.g., biological assimilation and sorption) and physical (e.g., mixing with underlying waters) processes in Antarctic coastal regions.

Likewise, since biological activity is dominant in the surface layer, leading to a significant production of labile particles, it is impossible to distinguish whether sea ice melt released LpZn and LpCd to the surface or not, based on the available data. In contrast to labile particles, refractory particles are not expected to be produced or influenced by biological activity, and accordingly RpZn and RpCd at the stations located within the sea ice or on the edge of the sea ice region (Stn 53, 52, 50, 49, 55, and 24) are consistently low ([RpZn]: ~0.1 nmol L^{-1}, [RpCd]: <4 pmol L^{-1}) in the upper 20 m. Based on these low refractory concentrations, we thus conclude that sea ice melt is not a strong source of RpZn and RpCd. Nevertheless, [RpCd] in the surface layer were elevated compared to deeper water, suggesting there might be a small source of RpCd. However, the much higher labile concentrations lead to a large uncertainty in the determination of the refractory fraction; this effect, in addition to the possibility of incomplete leaching of LpCd as noted in section 2.4.2.2, means a

minor contribution from sea ice melt cannot be ruled out based on the current data.

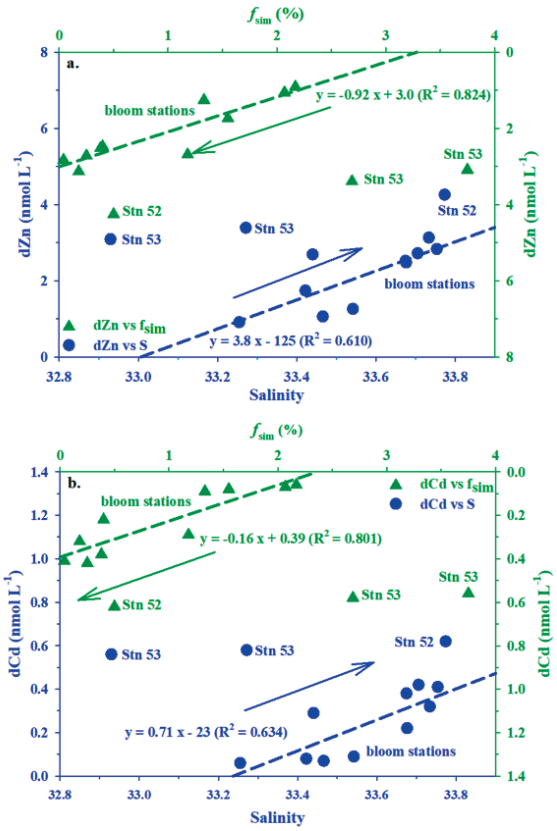

Figure 2.10 GPpr12 [dZn] and [dCd] versus salinity (in blue) and the fraction of sea ice melt (f_{sim}) (in green) at the surface (~ 20 m) of the open ocean station (Stn 53), the shelf break station (Stn 52) and the bloom stations (Stn 50, 49, 48, 55, 24, 57). a. [dZn] b. [dCd]. The regression lines show significant trends (all p values < 0.05) excluding Stn 52 and 53 and the arrows indicate the direction of the trends.

To sum up, mCDW, together with sedimentary input (7% for dZn and 4% for dCd in the DIS region), is the main source for both dZn and dCd to the AS, whereas sea ice melt does not seem to supply either dissolved metal to the water column, and the effect of ice shelf melt is convoluted by water mass mixing process. Our results imply that the increasing flux of warm mCDW intruding into the AS (Jacobs et al., 2011) could potentially increase the flux of both dZn and dCd, by

enhancing the ice shelf melt-driven circulation (meltwater pump, St-Laurent et al., 2017), affecting the biogeochemical cycling of the ASP. Such stronger circulation would increase the supply via both mCDW upwelling (with its sedimentary derived component) and any supply from the ice shelf. Although particulate metals are only a relatively minor component of the overall metal pools in this study, especially below the surface layer, biogenic particles could play an important role in the cycling of dZn and dCd in the upper ocean due to (varying) uptake by different phytoplankton communities, as discussed in the next sections.

2.4.2 Particle composition

The highest [LpZn] and [LpCd] were found in surface waters, notably at the bloom stations, coinciding with relatively low [dZn] and [dCd]. Observed concentrations of both particulate and dissolved phases were roughly equal (or particulate concentrations were 1-2 times less than dissolved concentrations at some stations) (Figs 2.7 and 2.8); this likely indicates strong biological uptake of dissolved metals and/or scavenging onto suspended particles. Consistent with this, the phytoplankton biomass (indicated by fluorescence) was also relatively high at these stations. Generally, there are multiple pathways for bioactive metals to partition between the dissolved phase and the particulate phase – biological assimilation, adsorption onto particles (e.g., biogenic/authigenic/abiotic particles), competition between metal binding ligands and particles, and regeneration (e.g., Bruland et al., 2013). The importance of each process varies per metal depending on the environmental conditions (e.g., biological activity and redox conditions), which could alter the compositions of particulate metals. Furthermore, particulate metal compositions can also be controlled by external sources and interactions near the sea floor, such as sediment resuspension and authigenic mineral formation (e.g., Planquette et al., 2013; Raiswell et al., 2016). To understand the interaction between dissolved and particulate phases, we discuss (i) origins of particles collected in the surface layer, and (ii) the

concentration and relative origin contributions to particulate metal concentrations (biogenic and lithogenic) of both metals.

2.4.2.1 Particle origins based on relationships with Al and P

To assess the particle origin, we assume all P in the particles is biogenic and all Al is from lithogenic materials (e.g., Planquette et al., 2013). The total particulate Zn (TpZn), total particulate Cd (TpCd), total particulate P (TpP), total particulate Al (TpAl), and the inter-relationships (intercept not forced to 0) between these quantities can be used to assess whether there is a consistent biogenic or lithogenic fraction of Zn and Cd. The regression between TpMe and TpP indicates that biogenic metals dominate the TpMe pools in the surface layer at both the bloom stations ($R^2_{TpZn\text{-}TpP}$=0.69, $R^2_{TpCd\text{-}TpP}$=0.88, n=37, both $p<0.05$) and the non-bloom stations ($R^2_{TpZn\text{-}TpP}$=0.66, $R^2_{TpCd\text{-}TpP}$=0.85, n=8, both $p<0.05$). Subsequently, the coefficient of determination (R^2) decreases below the surface layer (Table 2.4), suggesting a smaller contribution of particles of biogenic origin to the overall particulate pool, likely due to regeneration of biogenic particles. Interestingly, at the bloom stations, the R^2 value for Cd remains high below the surface layer, while that for Zn decreases more notably (Table 2.4). This suggests that either biogenic pZn remineralizes much faster than biogenic pCd in the water column, or there is a possible input of abiotic pZn (e.g., sedimentary or scavenging-derived pZn) increases with depth much more than for pCd (details discussed in section 2.4.2). On the other hand, the coefficients of determination of the regressions between TpMe and TpAl in the surface layer of the bloom stations are comparable ($R^2_{TpZn\text{-}TpAl}$=0.36, $R^2_{TpCd\text{-}TAl}$=0.41, n=37, both $p<0.05$), and slightly increases for TpZn-TpAl (but not TpCd-TpAl) below the surface layer, (Table 2.4). Together with the weakening regression between TpZn and TpP below the surface layer, this result implies lithogenic pZn becomes more prevalent at depth, whereas this effect is less profound for pCd.

Table 2.4 Regression of TpMe/TpP (and TpAl) in (and below) the surface layer.

		within the surface layer			below the surface layer		
		R^2	P value	n	R^2	P value	n
bloom stations	TpZn/TpP	0.69	1.9×10^{-10}	37	0.24	3.0×10^{-4}	51
	TpCd/TpP	0.88	5.9×10^{-18}	37	0.70	1.5×10^{-14}	51
	TpZn/TpAl	0.36	1.0×10^{-4}	37	0.42	2.4×10^{-7}	51
	TpCd/TpAl	0.41	2.5×10^{-5}	37	0.004	>0.05	51
non-bloom stations	TpZn/TpP	0.66	1.4×10^{-2}	8	0.14	>0.05	9
	TpCd/TpP	0.85	1.0×10^{-3}	8	0.06	>0.05	9
	TpZn/TpAl	0.13	>0.05	8	0.62	1.2×10^{-2}	9
	TpCd/TpAl	0.06	>0.05	8	0.02	>0.05	9

2.4.2.2 Estimated biogenic (and lithogenic) metal concentrations and relative contributions

The varying regression between TpMe and TpP (and TpMe-TpAl) only indicates relative changes in particle composition and inferred origin – quantifying the concentrations of particles of biogenic and lithogenic origin requires further investigation. To date, there are several common approaches taken to estimate biogenic and lithogenic components of bulk particles. The first approach is to separate bulk particles into labile and refractory fractions by using chemical leaching techniques (Berger et al., 2008; Fitzwater et al., 2003; Tang and Morel, 2006; Tovar-Sanchez et al., 2003), and assuming labile and refractory fractions represent biogenic and lithogenic fractions, respectively. A second approach is to use uptake ratios (metal/P) by phytoplankton to calculate the biogenic particulate metal concentrations, assuming that all P measured in bulk particles is biologically assimilated (i.e., lithogenic or authigenic P is negligible). The metal/P uptake ratios used in this approach come from uptake experiments using phytoplankton or from the slope of regression between dissolved metals and PO_4 in the upper ocean, assuming biological uptake is the main driver for variation in metal concentrations and nutrients (Liao et al., 2017; Planquette et al., 2013). In a similar fashion, this approach can also be used to estimate lithogenic metal concentrations, by multiplying crustal ratios (metal/Al or metal/Ti) with particulate Al or Ti concentrations in bulk particles (Liao et al., 2017; Little et al., 2016; Planquette et al., 2013) based on the assumption that all Al measured

in bulk particles has a lithogenic origin and the used ratio is representative for all lithogenic particles.

Here, we compare the estimated biogenic and lithogenic metal concentrations and their relative contributions to the bulk particle concentration in both the productive (the bloom stations) and less productive areas (Stns 53 and 52, here referred to as the non-bloom stations) using the two approaches described above – the first approach is referred to as "analytical leaching approach" the hereafter and the second approach is referred to as the "fixed ratio approach" hereafter. The concentrations and relative contributions are calculated by both approaches for each sample and summarized in depth intervals (depth-weighted averages for data in the bins, 0-50 m, 50-100 m, 100-200 m, 200-400 m, 400-600 m, 600-800 m, 800-1000 m, Fig. 2.11).

(1) Biogenic metal concentration and contribution

For the "analytical leaching approach", biogenic concentrations and contributions are derived from [LpMe] and [LpMe]/[TpMe], respectively, assuming LpMe is biogenic. Within 0-50 m at the bloom stations, elevated biogenic [pZn] and [pCd] are estimated (1.22±0.61 nmol L^{-1}; n=10, and 0.14±0.10 nmol L^{-1}; n=10, mean±1 SD, respectively), with concentrations decreasing with depth (Table 2.5, Figs 2.11b and 2.11f). Similarly, a decreasing trend in biogenic pZn contributions from the surface (86%, 0-50 m) to greater depths (60%, 600-800 m) is calculated (Fig. 2.11a). Together, as suggested by the relationship of TpP and TpZn, these results indicate a consistent and significant production of biogenic pZn in the surface of the ASP, as well as regeneration of biogenic pZn over depth. On the other hand, while elevated biogenic pCd within 0-50 m compared to deeper depths at the bloom stations (Table 2.5 and Fig. 2.11f), biogenic pCd contribution does not decrease significantly over depth (95-97%, Fig. 2.11e). This indicates that biogenic pCd still dominates the particulate pool at depth, despite regeneration. At the non-bloom stations, lower biogenic [pZn] (0.86±0.21 nmol L^{-1}) and biogenic [pCd] (0.08±0.01 nmol L^{-1}) are estimated in the upper water layer (0-50 m) compared

to the bloom stations, and both biogenic concentrations decrease over depth (Table 2.5). Lower biogenic metal concentrations at the non-bloom station suggests a relatively small biogenic particle production in the surface layer, coincident with lower fluorescence (Fig. 2.3c), likely due to the decreased availability of Fe compared to the bloom stations (van Manen et al., 2022). Interestingly, within 0-50 m, higher biogenic pZn contribution is estimated at the non-bloom stations (96%) than the bloom station (86%) within 0-50 m implies less abiotic pZn input to the non-bloom stations. On the other hand, akin to the bloom stations, biogenic pCd contribution is equally high (~97%) within 0-50 m (Figs 2.11e and 2.11g), suggesting abiotic pCd input is not significant compared to biogenic pCd at both non-bloom and bloom stations.

In comparison to the "analytical leaching approach", for the "fixed ratio approach", we use TpP combined with the slope of regression between dissolved metals and PO_4 in the surface layer (Table 2.5) as an estimation of the metal uptake ratios to estimate the biogenic concentration and relative contribution (Planquette et al., 2013; van Manen et al., 2022). The slope of regression is used as there is a lack of culture studies on metal and P uptake by haptophytes, and the discrepancy in phytoplankton community between blooms may affect in-situ metal uptake ratios. Lower biogenic concentrations and contributions (LpMe/TpMe) are derived (Fig. 2.11) – within all depth intervals, biogenic concentrations calculated by the "analytical leaching approach" are up to 5.1 times and up to 2.6 times higher than estimated by the "fixed ratio approach" for Zn and Cd, respectively (Fig. 2.11). However, the decreasing trends for both metals from the surface to the deep are similar between two approaches. One explanation for the discrepancy between these two commonly used approaches is that the ratios derived from the slope of the metal-PO_4 relationships do not accurately represent the true phytoplankton uptake ratios. Indeed, it is well established that care should be taken when assuming regression slopes are representative of uptake ratios, as such slopes may also be influenced by both water mass mixing and sources or sinks not associated with uptake and regeneration (e.g., Middag et al., 2019; Middag et al., 2018). Additionally, the uptake of

metal and PO_4 also differs between different phytoplankton species and under different environmental conditions (e.g., Ho et al., 2003), meaning that a universal slope of the dissolved metal-PO_4 may not represent true (variable) uptake ratios. On the other hand, our definition of the 'labile' fraction might not necessarily equate to the biogenic fraction. For example, it has been found that labile pMe can include not only metals of biogenic origin such as living organisms (soft tissue and hard skeletal materials such as calcite and aragonite) and biodetritus (e.g., dead phytoplankton cells, fecal pellets), but also metals associated with fresh authigenic particles (e.g., amorphous Fe-Mn oxyhydroxide), as well as metals weakly bound to lithogenic particles (e.g., alumino-silicate clay minerals or crystalline oxyhydroxide minerals) (Berger et al., 2008, Rauschenberg and Twining, 2015). Moreover, other sources of labile particles such as sediments that have different metal/P values, can result in variation in the observed ratios. Nevertheless, from this dataset, both approaches showed dominant biogenic contributions in the surface compared to the deep, indicating that the TpMe pool in the surface of the ASP is mainly controlled by biological activity.

Overall, by comparing two different approaches, we found that there is no perfect approach to accurately determine the biogenic fraction – the estimation strongly depends on the chosen fixed ratios and the leaching selectiveness – in regions with high productivity and without significant input of other labile particulate sources, the "analytical leaching approach" could give representative results and would be less labor intensive, although inherently there is a risk of including adsorbed/scavenged metals or authigenic particles. On the other hand, the "fixed ratio approach" would be an ideal fit if the phytoplankton community and its uptake ratio during the development of blooms could be simultaneously monitored, rather than relying on estimates based on dissolved concentrations. Overall, with the data available in this study, we deem a variation of the "analytical leaching approach" most suitable to assess the metal uptake ratios in the biogenic fraction.

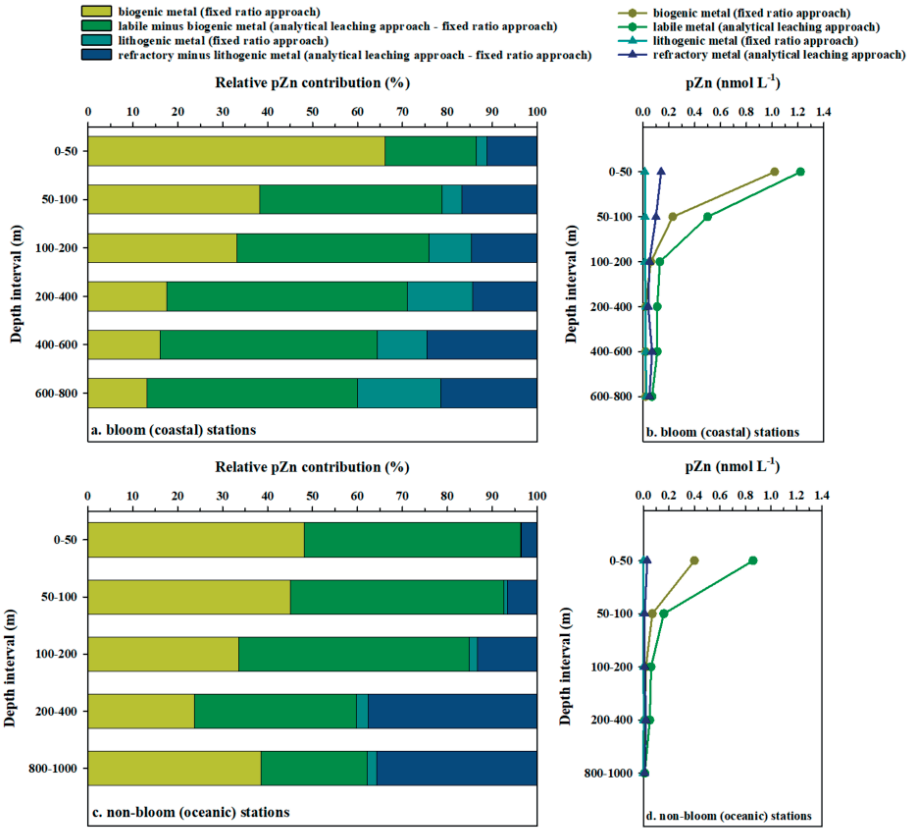

Figure 2.11. Relative contributions and concentrations of biogenic, labile, lithogenic, and refractory fractions at both bloom (coastal) stations and non-bloom (oceanic) stations during GPpr12. Biogenic and lithogenic contributions (and concentrations) were calculated using the "fixed ratio approach", whereas labile and refractory contributions (and concentrations) were calculated using the "analytical leaching" approach. a. and c. relative biogenic pZn contributions. b. and d. biogenic pZn concentrations. e. and g. relative biogenic pCd contributions. f. and h. biogenic pCd concentrations. Each contribution is calculated based on the corresponding ratios described in section 2.4.2.2.

(Continue for Figure 2.11)

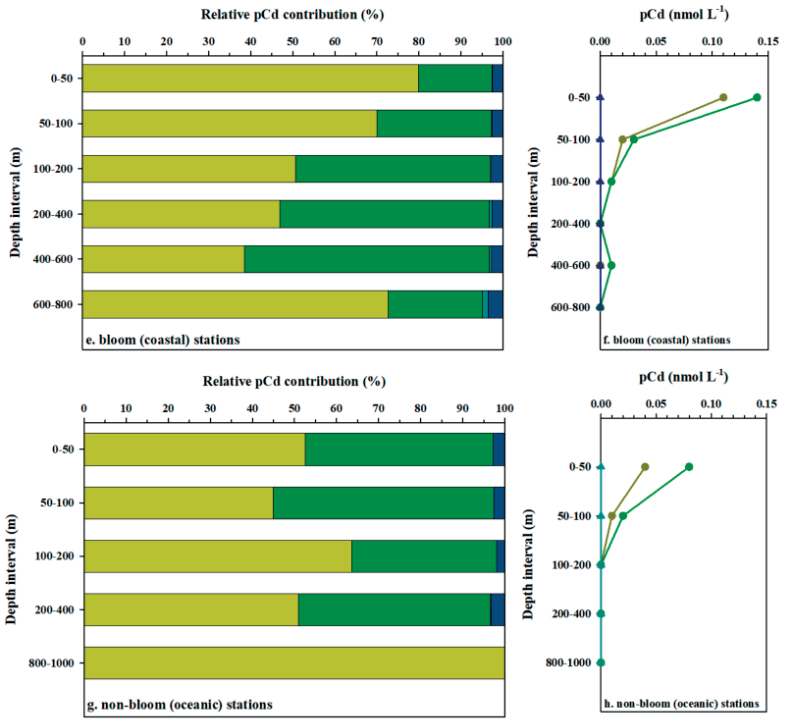

(2) Lithogenic metal concentration and contribution

To estimate the lithogenic concentration and contribution, the "analytical leaching approach" assumes RpMe is lithogenic and uses RpMe/TpMe for the estimation of contribution, whereas the "fixed ratio approach" uses upper crustal metal/Al ratios (Zn/Al: 0.34 mmol mol^{-1}; Cd/Al: 0.45 µmol mol^{-1}, Rudnick and Gao, 2003) to derive lithogenic concentrations (based on TpAl) and contributions (lithogenic metals/TpMe). Since the bloom stations are on the shelves (close to the coast), we refer to them as the coastal stations in this section, whereas the non-bloom stations are referred to as the oceanic stations.

Based on the "analytical leaching approach", elevated lithogenic [pZn] (but much lower than biogenic [pZn]) are estimated at the coastal stations (75±38 pmol L^{-1}, mean±1 SD) compared to the oceanic stations (17±10 pmol L^{-1}) (Table 2.5). A similar elevation of lithogenic [pZn] at the coastal stations (18±5 pmol L^{-1}) is estimated by the "fixed ratio approach", compared to the oceanic stations (1.2±0.7 pmol L^{-1}). Both approaches thus indicate some lithogenic pZn input from the Antarctic continental shelf. In contrast, lithogenic [pCd] derived by the "analytical leaching approach" are very low and variable for both station groups (bloom stations: 0.95±1.49 pmol L^{-1}; oceanic stations: 0.59±0.91 pmol L^{-1}). For the "fixed ratio approach", estimated lithogenic [pCd] are even lower at both station groups (<0.03 pmol L^{-1}; Table 2.5), suggesting that the input of lithogenic pCd is negligible. Interestingly, the "analytical leaching approach" estimates higher coastal lithogenic concentrations in the surface (within 0-50 m) than in the deep (600-800 m) for both metals at both station groups (Table 2.5). This decreasing trends over depth are reversed compared to estimation by the "fixed ratio approach" (Table 2.5). We speculate that the surface elevation of lithogenic concentrations (derived by the "analytical leaching approach") is likely affected by the high labile particle concentration in the surface layer where some LpMe is inevitably leached into refractory fraction, given that RpMe was very low and nearly 8 (for Zn) and 35 (for Cd) times lower than LpMe in the surface (Fig. 2.7). The lithogenic pZn contribution at the coastal stations increase from the surface to the deep, ranging from 2% (0-50 m) to 18% (600-800 m) estimated by the "fixed ratio approach", which is lower than the estimation by the "analytical leaching approach" that ranges from 13% (0-50 m) to 40% (600-800 m) (Fig. 2.11). A similar scenario is also observed at the oceanic stations. Together with decreasing biogenic [pZn] (and contribution) over depth (Fig. 2.11), this indicates degradation of biogenic particle at depth as well as increasing (but relatively small) lithogenic input from shelf sediment.

Table 2.5 Estimated biogenic and lithogenic metal concentrations by two approaches compared in section 4.2.2. Concentrations (mean±1 SD) are calculated from samples within corresponding depth intervals. All units are in nmol L^{-1} except the ones labeled with "a" (in pmol L^{-1}).

		fixed ratio approach				analytical leaching approach			
Station		biogenic [pZn]	lithogenic [pZn][a]	biogenic [pCd]	lithogenic [pCd][a]	labile [pZn] (biogenic)	refractory [pZn][a] (lithogenic)	labile [pCd] (biogenic)	refractory [pCd][a] (lithogenic)
Bloom (coastal) station	0-50 m (n=10)	1.02±0.76	13±12	0.11±0.08	0.02±0.02	1.22±0.61	139±77	0.14 ± 0.10	3.91±3.00
	50-100 m (n=8)	0.23±0.22	15±13	0.02±0.02	0.02±0.02	0.50±0.51	105±106	0.03 ± 0.04	1.02±1.13
	100-200 m (n=8)	0.06±0.06	14±11	0.01±0.01	0.02±0.01	0.13±0.08	46±45	0.01 ± 0.01	0.27±0.20
	200-400 m (n=7)	0.02±0.01	22±17	<0.01	0.03±0.02	0.11±0.05	44±28	0.01 ± 0.01	0.16±0.04
	400-600 m (n=8)	0.02±0.01	21±17	<0.01	0.03±0.02	0.11±0.06	69±62	0.01 ± 0.01	0.20±0.08
	600-800 m (n=3)	0.02±0.01	23±7	<0.01	0.03±0.01	0.07±0.01	50±13	< 0.01	0.12±0.01
	Average	0.23±0.40	18±5	0.02±0.04	0.02±0.01	0.36±0.45	75±38	0.03 ± 0.05	0.95±1.49
non-bloom (oceanic) stations	0-50 m (n=2)	0.40±0.13	0.89±0.27	0.04±0.01	<0.01	0.86±0.21	33±15	0.08 ± 0.01	2.19±0.09
	50-100 m (n=2)	0.07±0.03	1.08±0.22	0.01±0.01	<0.01	0.16±0.08	13±7	0.02 ± 0.01	0.51±0.36
	100-200 m (n=2)	0.02±0.01	1.38±0.94	<0.01	<0.01	0.06±0.01	11±1	< 0.01	0.09±0.04
	200-400 m (n=2)	0.01±0.01	2.18±2.58	<0.01	<0.01	0.05±0.05	19±5	< 0.01	0.09±0.06
	800-1000 m (n=1)	0.01	0.34	<0.01	<0.01	0.01	6	< 0.01	0.05
	Average	0.10±0.17	1.2±0.7	<0.01	<0.01	0.23±0.36	17±10	0.02 ± 0.03	0.59 ± 0.91

2.4.3 Different uptake ratios (Zn/P and Cd/P) in the two sampling regions

As discussed in section 2.4.2, high biogenic particulate metals in the surface of the ASP correspond with phytoplankton blooms. However, assessing the biogenic contribution to the particulate metal pool is complicated, with both the fixed ratio and the leaching approach having caveats. Given that the blooms were dominated by different phytoplankton species – haptophytes (typically *Phaeocystis* spp.) and diatoms were the main groups dominating in the Dotson and the Getz regions, respectively (Fig. 2.6), the uptake of Zn and Cd is expected to vary both in different blooms as well as during the development of the bloom through time. In this setting, we deem using the slopes of the regression between LpMe and labile pP (LpP) has fewer underlying assumptions and may thus be better than using reported fixed ratios (fixed ratio approach) in addition to averaging out variation in individual labile fractions (analytical leaching approach). Hence, we use the slopes of LpMe and LpP (intercept set to 0, referred as to LpMe/LpP slope ratios hereafter) in the surface layer at the bloom stations to evaluate differences in uptake ratios of both metals.

Uptake of Cd by phytoplankton is thought to be related to Zn^{2+} availability, which in turn can affect the uptake ratios of both metals. For example, Sunda and Huntsman (2000) reported increased Cd uptake relative to PO_4 by some oceanic diatoms (e.g., *Thalassiosira oceanica*) under Zn-depleted conditions (when $[Zn^{2+}]$ decreased to 0.01 nmol L^{-1}). When dZn is depleted, Cd may substitute for Zn in some carbonic anhydrases, with some species even containing a Cd-based enzyme (Morel et al., 2020, and references therein). However, even though we have no estimates of $[Zn^{2+}]$, [dZn] in the ASP is always relatively high (>1 nmol L^{-1}), even in the surface layer where strong biological uptake occurs, implying relatively high $[Zn^{2+}]$ as well (e.g., Baars and Croot, 2011). As such, it is unlikely that such effects (Cd substitution for Zn) play an important role in driving dCd uptake or Cd:P ratios in the ASP and indeed no relationships between uptake ratios and dissolved metals concentrations were apparent in the current data that suggested a dominant role for substitution.

Therefore, we do not focus on the interplay between Zn and Cd substitution in our discussion of the ASP.

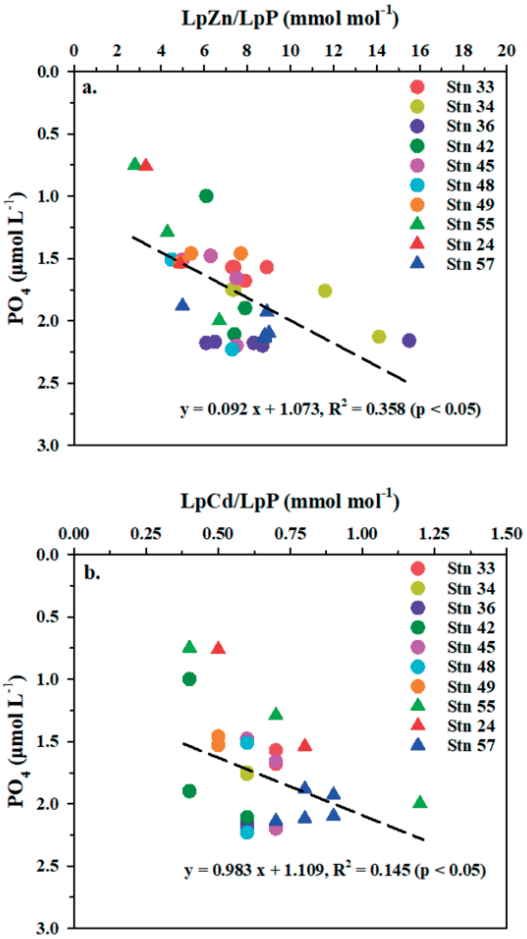

Figure 2.12 Labile particulate composition (LpMe/LpP) versus dissolved PO_4 in the surface layer at the GPpr12 bloom stations. a. LpZn/LpP vs PO_4 b. LpCd/LpP vs PO_4. The black dash line represents the regression line.

We compare LpMe/LpP slope ratios with reported metal stoichiometric values for *Phaeocystis antarctica* (*P. antarctica*) and Antarctic diatoms, from published field observations in the Southern Ocean and coastal Antarctica, as well as culture experiments (Table 2.6). In the diatom-dominated bloom, The LpZn/LpP (3.19±0.30 mmol

mol^{-1}) and LpCd/LpP (0.48±0.04 mmol mol^{-1}) ratios are lower than previously reported in the Southern Ocean (Table 2.6). This variation is likely related to the availability of Fe as it has been suggested Fe replete conditions can increase the uptake of P relative to Zn and Cd ("growth rate dilution", Cullen et al., 2003), and/or reduce Zn and Cd uptake through putative non-specific divalent metal transporters that are up-regulated under Fe-limitation condition (Kustka et al., 2007; Lane et al., 2008; Lane et al., 2009). Both mechanisms would result in higher uptake ratios of Zn and Cd in the Fe-depleted open Southern Ocean (de Baar et al., 1990; de Baar et al., 1999; Martin et al., 1990). The ASP is expected to be supplied by Fe from the melting of ice shelves and/or sea ice (Gerringa et al., 2012, 2020b; Sherrell et al., 2015; van Manen et al., 2022), as well as upwelling of Fe-rich deep water (Sherrell et al., 2015), which could lead to higher Fe supply. Indeed, for the non-bloom stations (Stns 53 and 52) where less phytoplankton biomass was observed (most likely due to less available Fe supply; van Manen et al., 2022), higher LpZn/LpP (11.6±1.87 mmol mol^{-1}) and LpCd/LpP (1.02±0.10 mmol mol^{-1}) ratios are observed compared to both bloom stations (Table 2.6). This gradient in LpMe/LpP slope ratios between the bloom stations and the non-bloom stations is consistent with the effect of Fe availability on Zn and Cd uptake in the ASP as suggested previously based on culture experiments (Twining et al., 2004) and shipboard incubations (Cullen et al., 2003; Table 2.6). Additionally, a significant regression is found between LpMe/LpP slope ratios and dissolved PO_4 (both $p<0.05$) in the surface layer for the bloom stations. This relationship suggests that LpMe/LpP slope ratios decrease when PO_4 decreases, indicating a growth rate dilution effect in the central ASP as lower PO_4 implies more growth (Fig. 2.12). In contrast, no co-variance is observed for the non-bloom stations (Fig. 2.12), most likely due to lower Fe supply and smaller PO_4 uptake. The observed gradients in LpMe/LpP slope ratios suggests uptake ratios could vary even over short distances or with depth in the ASP due to differences in Fe or light availability; such variation in uptake ratios has been suggested before (e.g., Alderkamp et al., 2015; Twining and Baines, 2013), but mainly as differences between geographical regions and between Fe-addition (culture)

experiments. Our data suggest that (known) local gradients in Fe availability can indeed affect uptake ratios of Cd and Zn over short spatial scales in the ASP, notably between coastal and open ocean regions.

The LpZn/LpP (7.16±0.40 mmol mol^{-1}) and LpCd/LpP (0.64±0.02 mmol mol^{-1}) ratios observed in the haptophyte-dominated bloom are comparable to those found at a *P. antarctica*-dominated station in the Ross Sea (7.7 mmol mol^{-1} and 0.65 mmol mol^{-1} for Zn and Cd , respectively, Gerringa et al., 2020a), implying the haptophyte-dominated bloom could be *P. antarctica*-dominated. These ratios in the *P. antarctica*-dominated bloom are higher than in the diatom-dominated bloom, which suggests *P. antarctica* might have higher metal/P ratios than diatoms in Antarctic coastal waters. This result is different from previous studies that suggested diatoms have higher cellular metal/P ratios than *Phaeocystis* in the Southern Ocean (e.g., Twining and Baines, 2013). A potential explanation is that *Phaeocystis* regulates cellular nutrient (metal) requirements in adaptation to dynamic environmental conditions (e.g., McCain et al., 2022) – Sedwick et al. (2007) suggested that *Phaeocystis* lowers its Fe requirement under increasing irradiation enabling a longer bloom period in the Ross Sea. Since the interplay between the availability of Fe and light controls the development of phytoplankton blooms in the ASP (Park et al., 2017), we speculate that *P. antarctica* might increase their Zn and Cd uptake (relative to P) towards the end of the *P. antarctica*-dominated bloom period when Fe is scarce and growth rates are reduced, resulting higher LpMe/LpP slope ratios than estimated for diatoms in this study.

Table 2.6 Compilation of Zn/P and Cd/P ratios from published values and this study. [dMe] stands for dissolved metal concentrations.

	Zn/P (mmol mol^{-1})	Cd/P (mmol mol^{-1})	Approach	Reference
Field observations				
The Amundsen Sea				
DIS bloom stations	3.94±0.66	0.42±0.06	slope of [dMe] and [PO_4] (the surface layer) (values for the "fixed ratio approach" in section 4.2.2.1)	this study
GIS bloom stations	2.74±0.51	0.45±0.08		
Non-bloom stations (Stns 52 & 53)	8.47±0.73	0.60±0.07		
DIS bloom stations (Haptophyte, 59-100%)	7.16±0.40	0.64±0.02	slope of [LpMe]/[LpP] (intercept: 0)	this study
GIS bloom stations (Diatoms, 54-91%%)	3.19±0.30	0.48 ± 0.04		
Non-bloom stations (Stns 52 & 53)	11.6±1.87	1.02±0.10		
P. Antarctica	3.37		slope of [dMe] and [PO_4]	Sherrell et al., 2015
The Ross Sea				
P. Antarctica (74%)	7.7	0.65	calculated by the deficits compared to High Salinity Shelf Water for each nutrient in the mixed layer	Gerringa et al., 2020b
Diatom (88%)	3.7-4.0	0.54-0.57		
The Weddell Gyre				
Diatom (~80%)	6.36±0.69	0.32	slope of [dMe] and [PO_4]	Viljoen et al., 2019
The Southern Ocean				
Diatom	11.1±0.67	1.29±0.07	bulk particles (Fe limited seawater)	Cullen et al., 2003
Average	6±2.6	0.65±0.3	slope of [dMe] and [PO_4]	Loscher 1999; Ellwood 2008; Lane et al. 2009; Saito et al. 2010; Croot et al. 2011
Culture experiments				
P. antarctica	n/a	0.20±0.01 (Fe-deplete)		Lane et al., 2009
	n/a	0.042±0.005 (Fe-replete)		
Diatom	8.1 (Fe-deplete)	n/a		Twining et al., 2004
	6.2 (Fe-replete)	n/a		

2.5 Conclusions

In this study we report the first combined dataset of dissolved and particulate Zn and Cd for the AS shelf region and the ASP. Our results reveal the most prominent sources of both metals to the ASP and highlight the importance of biological uptake and recycling for both the particle composition. We conclude that the inflowing mCDW is the main source of dZn and dCd to the AS, with mCDW picking up a relatively small amount of additional dZn and sometimes dCd from shelf sediments (Fig. 2.13). Ice shelf melt is not a significant source for either metals due to the small melt water contribution and mixing with low metal shelf waters, whereas an assessment of sea ice melt-derived metal remains obscured by strong biological uptake in the surface layer. For pZn and pCd, our data indicate that LpZn and LpCd are largely controlled by biogenic particle formation in the surface layer during the bloom period. We attribute RpZn to resuspension of lithogenic particles from the shelf sediments and terrestrial material near the ice shelf, whereas by contrast no significant lithogenic source of pCd was observed (Fig. 2.13). High concentrations and contributions of biogenic particulate metals in surface waters that decreased with depth along both transects were calculated using two commonly used approaches and gave the same pattern, despite absolute differences. Our estimated LpMe/LpP slope ratios in the diatom-dominated stations are much lower than published for the open Southern Ocean, which may be linked to the availability of Fe in coastal Antarctic regions and the Southern Ocean. Additionally, we observe different LpMe/LpP slope ratios between two different blooms in this study that were dominated by haptophytes and diatoms, implying these two phytoplankton groups might have different Zn, Cd, and P quota in the biogeochemically dynamic ASP.

Given that the volume of mCDW intruding onto the continental shelf is increasing as a result of global climate change (Jacobs et al., 2011, Mankoff et al., 2012), the supply of dZn and dCd to the AS would

potentially increase from both mCDW and the coastal sediments. Both these sources would be expected to increase nutrient (macronutrients as well as micro-nutrients including Fe and Zn etc) supply as well. Such spatial and temporal variability could potentially affect the productivity and biogeochemistry in the ASP (e.g., changes in uptake and uptake ratios of bioavailable metals). Albeit regional, the findings of this study may have implications for the larger scale cycling of trace metals in the Southern Ocean and this should be further explored in future studies.

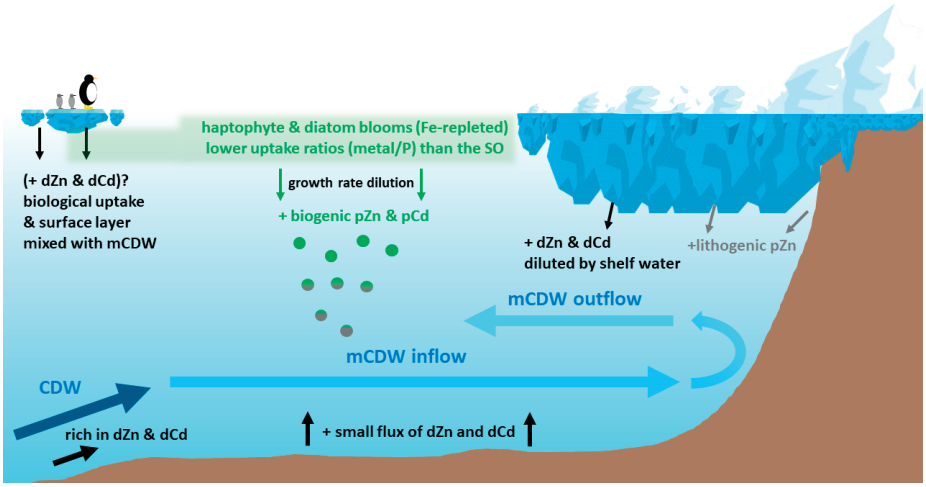

Figure 2.13 Schematic of the sources of dissolved and particulate metals (Zn and Cd), as well as biogeochemical processes in the ASP. Blue arrows (from dark blue to light blue) represent the route of mCDW from the open SO to the ASP, modified by mixing with other water masses. Black and gray arrows indicate the sources of dMe and lithogenic pZn, respectively. Green arrows represent the production of biogenic pMe.

CHAPTER 3

BIOGEOCHEMISTRY OF IRON IN COASTAL ANTARCTICA – ISOTOPIC INSIGHTS FOR EXTERNAL SOURCES AND BIOLOGICAL UPTAKE IN THE AMUNDSEN SEA POLYNYAS

Hung-An Tian, Mathijs van Manen, Zach B. Bunnell, Jinyoung Jung, Sang Hoon Lee, Tae-Wan Kim, Gert-Jan Reichart, Tim M. Conway, Rob Middag

Published in *Geochimica et Cosmochimica Acta* in 2023

Abstract

Seasonal phytoplankton blooms in the Amundsen Sea Polynyas are believed to be fuelled by iron (Fe). However, largely due to the limited amount of Fe data reported for the Amundsen Sea Polynyas, understanding of the sources and processes that affect the biogeochemistry of Fe in this region remains limited. Here, we present the first investigation of dissolved Fe isotopic compositions (δ^{56}Fe) in the Amundsen Sea. This dataset allows us to characterize and compare the dissolved δ^{56}Fe signatures of incoming modified Circumpolar Deep Water (mCDW) and of sedimentary sources from the continental shelf. The range in dissolved δ^{56}Fe (–1 to +0.1‰), coupled with elevated dissolved Fe concentrations ([dFe], up to 1.6 nM), observed close to the seafloor, suggests Fe is released from shelf sediments via a combination of reductive and non-reductive processes, with the latter being relatively more important (20-56%) than the former (4-12%) at this location. At the Dotson Ice Shelf, comparison of δ^{56}Fe in the mCDW inflow (–0.70‰) with the mCDW outflow (–0.23‰), together with a negligible change in [dFe], points to modification of Fe biogeochemistry underneath the ice shelf. We speculate that this shift in dissolved δ^{56}Fe is driven by a combination of enhanced preservation (and addition) of lithogenic colloidal Fe(III), together with the differential loss of Fe^{2+} and complexation with Fe-binding ligands. We also found distinct δ^{56}Fe in surface waters, with modest isotopic fractionation in a bloom dominated by haptophytes (~+0.68‰) and apparent preferential uptake of isotopically light Fe in another bloom dominated by diatoms (up to +1.06‰), compared to winter water. Despite prominent biological uptake, we suggest other factors such as adsorption, regeneration, bacterial regeneration, and complexation with organic ligands, together with the supply of lithogenic particles also play important roles in setting surface dissolved δ^{56}Fe in the Amundsen Sea Polynyas. Overall, this study provides a further understanding of the external Fe sources and the biogeochemical processes in the Amundsen Sea and thus a baseline on how changing conditions in Antarctica can affect Fe cycling in the Southern Ocean and beyond.

3.1 Introduction

Iron (Fe) is an essential micronutrient participating in many important metabolic processes (e.g., nitrogen fixation and photosynthesis) for marine phytoplankton (e.g., Morel and Price, 2003). In the Southern Ocean, the largest high-nutrient low-chlorophyll region, the availability of Fe and the intensity of irradiation are generally the limiting factors for the growth of marine organisms (Boyd et al., 2007; de Baar et al., 1995; Martin et al., 1990). Pervasive Fe limitation over large regions of the surface Southern Ocean results from a combination of a limited supply of dissolved Fe (dFe) from upwelling deep waters compared to macronutrients, and very limited external Fe sources to the region (e.g., Tagliabue et al., 2014b). However, in contrast to the open Southern Ocean, coastal polynyas – areas of reduced ice cover driven by offshore katabatic winds and/or the intrusion and subsequent upwelling of warm and saline Circumpolar Deep Water (CDW) (Jacobs et al., 2011; Jenkins et al., 2010; Vaughan, 2008; Wåhlin et al., 2010; Walker et al., 2007) – are observed to be seasonally highly productive, notably in austral spring and summer (Arrigo et al., 2008; 2012). The intrusion of CDW in the Amundsen Sea (AS) occurs on the continental shelf as CDW passes the continental shelf break and/or upwells via local Ekman pumping (e.g., Jacobs et al., 1996; Jenkins et al., 2010; Kim et al., 2021). Depending on the extent of mixing, CDW may be modified and is then described as modified CDW (mCDW) (Wåhlin et al., 2010). The inflowing mCDW subsequently flows underneath (and flows out from under) the Dotson Ice Shelf (DIS), causing significant basal melting of the ice shelf in the shelf cavity. Such upwelling of CDW accelerates the thinning, melting and subsequent collapse of Antarctic ice shelves that form drifting icebergs (Gourmelen et al., 2017; Jacobs et al., 2011; Rignot et al., 2008) and releases glacial/ice sheet-derived Fe to seawater (Klunder et al., 2011; Raiswell et al., 2006; Sedwick and DiTullio, 1997). Moreover, the reduction of ice cover in the polynya and consequent enhanced irradiation, in combination with an additional Fe supply, enables the formation of phytoplankton blooms in Antarctic coastal polynyas (Alderkamp et al., 2012; Arrigo et al., 2008), which are

potentially responsible for a large proportion of carbon uptake in the Southern Ocean (Arrigo and van Dijken, 2003; Sarmiento et al., 2004). Amongst all the Antarctic polynyas, the Amundsen Sea Polynya (ASP), in which the rates of ice-sheet thinning are the highest of all Antarctica (Paolo et al., 2015; Rignot et al., 2019), exhibits the highest rate of annual net primary production per unit area (160±37 g C $m^{-2}y^{-1}$, Arrigo and van Dijken, 2003; Arrigo et al., 2008).

As the ASP is one of the most productive polynyas, understanding rapid changes in the ice sheet dynamics and biogeochemistry (e.g., Fe supply to coastal waters) is key to understanding how climate change impacts both the Antarctic ecosystem and elemental cycling in the Southern Ocean. However, due to the remoteness of Antarctica and limited accessibility underneath ice shelves, there was an absence of data on whether mCDW-induced melting serves as an additional Fe supply for spring/summer phytoplankton blooms in the ASP until the first investigation of dissolved Fe (dFe) at the Pine Island Glacier (Alderkamp et al., 2012; Gerringa et al., 2012, 2020b) and subsequent studies focusing on dFe and particulate Fe (pFe) in the CDW inflow and outflow at the Dotson Ice Shelf (DIS) (Planquette et al., 2013; Sherrell et al., 2015). Based on dFe and pFe concentrations, these investigations suggested that the inflowing mCDW, characterized as 'Fe-rich' deep water, with an addition of sedimentary Fe input and ice-shelf derived Fe, provides a continuous dissolved Fe supply fuelling phytoplankton blooms in the surface of the ASP via buoyancy-driven mixing ('the meltwater pump') underneath the ice shelf (Sherrell et al., 2015; St-Laurent et al., 2019). However, a recent study in the ASP argued instead that ice-shelf dFe is most likely negligible compared to sediment input and mCDW, based on a conservative mixing model (van Manen et al., 2022); that study also speculated that a fast equilibrium between dFe and labile pFe underneath the DIS moderated the concentrations of dFe in the mCDW outflow, as well as the amount of Fe supplied to the surface polynya via the 'meltwater pump'.

In the last 10-15 years, dissolved Fe isotope ratios (δ^{56}Fe) has provided considerable insight into the differing regional importance of external

sources of Fe to the ocean, as well as enhancing understanding of the internal biogeochemical cycling processes that affect the distribution and cycling of Fe in the oceans (recently reviewed in detail by Fitzsimmons and Conway (2023)). The δ^{56}Fe endmember signatures of different external sources to the oceans are now reasonably well constrained, although uncertainties and caveats remain. For example, atmospheric desert dust is well characterized at +0.1‰ (Beard et al., 2003; Conway et al., 2019), while anthropogenic combustion and biomass burning aerosols may range from –4‰ to +0.3‰ (Conway et al., 2019; Kurisu et al., 2016a; Kurisu et al., 2021; Kurisu et al., 2016b). In sediments, different mechanisms lead to diverse sedimentary δ^{56}Fe signatures. For example, reductive dissolution (RD) leads to elevated concentrations of reduced Fe in porewater that can diffuse into bottom waters, where the size of the flux depends on the absence/presence (and thickness) of an overlying oxygenated surface sediment layer where Fe^{2+} can be oxidized prior to diffusion. However, likely due to differences in the intensity of reduction processes within sediments and oxidation of Fe in an oxygenated surface sediment layer or in near bottom seawater, reductive dissolution is characterized by a wide range of isotopically light signatures (–3.5 to –1‰, e.g., Homoky et al., 2021; Johnson et al., 2020; Severmann et al., 2006). Conversely, non-reductive dissolution (NRD) induced via particle and colloid weathering and ligand mediated dissolution, often facilitated by sediment resuspension, have been suggested to exhibit a relatively consistent isotopic signature (~+0.1‰, e.g., Homoky et al., 2013; Homoky et al., 2021; Radic et al., 2011) compared to RD. High temperature hydrothermal vent fluids are also fairly well constrained (–0.7 to –0.1‰), but chemical complications upon mixing with ocean waters lead to a wide range of vent-specific signatures (–4 to +0.5‰; e.g., Ellwood et al., 2015; Fitzsimmons et al., 2017; Lough et al., 2017; Wang et al., 2021). Rivers are perhaps the least well constrained (–1.3 to +1.8‰), with large variability in δ^{56}Fe between river types and locations highly dependent on chemical conditions such as colloidal concentration, pH, and mineral compositions (Dauphas et al., 2017; Fitzsimmons and Conway, 2023). Most relevant for this work, a limited number of studies suggests that dissolved δ^{56}Fe signatures of polar

sources are often driven by biogeochemical processes rather than being representative of source material. For example, while dissolved δ^{56}Fe measured in Greenland glacier streams was close to crustal due to physical weathering (Schroth et al., 2011; Stevenson et al., 2017; Zhang et al., 2015), in Arctic subglacial streams dissolved δ^{56}Fe reached values as light as –2.1‰, attributed to silicate weathering, pyrite oxidation and dissimilatory Fe reduction from glacial sediments (Henkel et al., 2018; Stevenson et al., 2017). Dissolved δ^{56}Fe measured in arctic sea ice, meltwater ponds and snow has also been found to be isotopically light, due to photoreduction or biological activity (Marsay et al., 2018a). In Antarctica, the saline Fe-rich 'Blood falls' from the Taylor Glacier had an δ^{56}Fe signature of –2.6±0.5‰ (Mikucki et al., 2004), indicative of reductive dissolution of sediments. At the broader scale, recent polar Fe and δ^{56}Fe studies have implicated Antarctic and Arctic marginal processes in supplying isotopically light Fe from non-reductive dissolution to Arctic shelf environments and to Antarctic coastal and offshore waters (Sieber et al., 2021; Zhang et al., 2021), with evidence of long distance transport of Antarctic margin derived-Fe into the Southern Ocean and the South Atlantic (e.g., de Jong et al., 2012; Hatta et al., 2013; Klunder et al., 2014; Measures et al., 2013; Sieber et al., 2021). However, despite the obvious importance of the Southern Ocean to the global ocean and global climate, and the role of sedimentary margins in fuelling productivity in coastal Antarctica and beyond, there is still a paucity of dissolved δ^{56}Fe data from the Southern Ocean and coastal Antarctica, with only three studies published (Abadie et al., 2017; Ellwood et al., 2015; Sieber et al., 2021).

In addition to constraining external Fe sources, various processes including biological uptake (e.g., Ellwood et al., 2020; Ellwood et al., 2015), organic ligand complexation (e.g., Dideriksen et al., 2008; Ilina et al., 2013; Morgan et al., 2010), adsorption (e.g., Johnson et al., 2008; Mulholland et al., 2015), scavenging (e.g., Radic et al., 2011), regeneration (e.g., Abadie et al., 2017; Klar et al., 2018), and redox reactions of Fe species (e.g., Beard and Johnson, 2004; Ellwood et al., 2015) may fractionate Fe isotope ratios. In turn, δ^{56}Fe provides additional opportunities to disentangle a suite of processes that are

not easily evaluated by [dFe] alone. For example, Ellwood et al. (2015) utilized δ^{56}Fe of dFe and pFe during the development of a subtropical phytoplankton bloom to reveal how the dominant processes that influenced Fe cycling developed from photochemical (and biological) reduction at the onset of the bloom to biological uptake at the peak of the bloom. More recently, Sieber et al. (2021) used dissolved δ^{56}Fe to fingerprint the processes (e.g., biological uptake, recycling, and ligand binding) that dominated Fe cycling in surface waters across all major zones of the Southern Ocean. In the ASP, the interplay of multiple biogeochemical processes and long-lasting phytoplankton blooms provide an ideal opportunity to investigate δ^{56}Fe systematics.

Here, following a previous study on dissolved and particulate Fe concentrations in the ASP (samples collected during the same expedition as this study, van Manen et al., 2022), we present the first dataset of δ^{56}Fe from the Amundsen Sea (AS), from a transect following the inflowing mCDW and its passage through the AS and its outflow from the DIS. We use this dataset to build on the previous study and further evaluate the sources of sedimentary Fe and ice-shelf melt derived Fe, as well as to investigate the processes occurring underneath the DIS that determine the speciation and magnitude of Fe being released by the meltwater pump. Additionally, we characterize dissolved Fe isotopic signatures in ASP surface waters during two austral summer phytoplankton blooms dominated by two different phytoplankton communities (haptophytes and diatoms), specifically allowing us to study a combination of biological fractionations and physical processes that result in variable Fe isotope signatures in the surface waters of the polynyas.

3.2 Material and Methods

3.2.1 Sampling region and sampling for dissolved Fe

GEOTRACES process study (ID: GPpr12; expedition: ANA08B) was conducted on the Korean icebreaker R/V Araon in the AS during Austral Summer 2017/2018 (December 2017 to February 2018). Seawater samples from two transects through the ASP presented in

this study were collected between 24th January and 2nd February 2018. The first transect (24th-29th January) followed CDW intrusion from the Antarctic continental shelf break onto the continental shelf via the Dotson-Getz trough (modified to mCDW since it mixes with overlying shelf waters), the subsequent flow south-eastward into the cavity underneath the Dotson Ice Shelf (DIS), and then the later emergence at shallower depths from underneath the DIS. The second transect (1st-2nd February) followed mCDW inflow along Siple trough towards Getz Ice Shelf (GIS) (Fig. 3.1). Each station comprised 10-14 sampling depths from the near-surface (~10 m) to 1000 m, or 10-20 m above the seafloor for stations shallower than 1000 m. The stations located in the mCDW inflow (Stns 50, 49, 48, 45, and 42) and the mCDW outflow (Stns 36, 34, and 33) in the DIS region are henceforth referred to as the $DIS_{(inflow)}$ stations and the $DIS_{(outflow)}$ stations, respectively. Additionally, seawater samples were also collected at three stations in GIS region (referred to as the $GIS_{(inflow)}$ stations: Stns 55, 24, and 57) along the mCDW inflow (Fig. 3.1).

The sampling procedure for dissolved metals was as previously reported by van Manen et al., 2022. Briefly, samples for dissolved Fe isotope analysis were collected using the Royal Netherlands Institute for Sea Research (NIOZ) “Titan” ultra-clean sampling system for trace metals (de Baar et al., 2008; Rijkenberg et al., 2015), equipped with multiple auxiliary sensors for basic parameters (e.g., salinity, temperature, and fluorescence). Subsequently, seawater samples were filtered through 0.2 µm filter cartridge (Sartobran-300, Sartorius, precleaned with MQ water, 18.2 MΩ cm^{-1}) into 4 L LDPE cubitainers (for surface samples) and 1 L LDPE bottles. All containers used in the sampling were precleaned following GEOTRACES cookbook (version 3.0, 2017) and Middag et al. (2019). The filtered samples were then acidified to 0.024 M HCl using 12 M ultrapure concentrated HCl (Baseline, Seastar Chemicals Inc.), resulting in a final pH of ~1.8. Acidified samples were stored at room temperature for over five months before processing for isotope ratios at NIOZ.

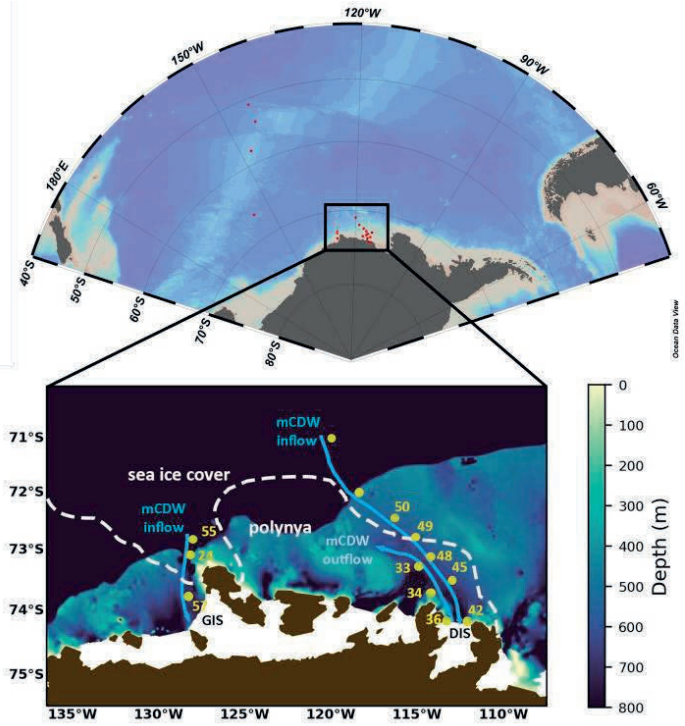

Figure 3.1 GPpr12 sampling stations at the Dotson Ice Shelf (DIS) and Getz Ice Shelf (GIS) regions in the Amundsen Sea. Stations are grouped based on the direction of mCDW intrusion – the $DIS_{(inflow)}$ stations (Stn 50, 49, 48, 45, and 42), the $DIS_{(outflow)}$ stations (Stn 36, 34, and 33), and the $GIS_{(inflow)}$ stations (Stn 55, 24, and 57). The white dashed line indicates the sea ice cover during the sampling period.

3.2.2 Analytical methods for Fe isotopes

Initial chemical processing of samples took place at NIOZ, with subsequent purification and analysis at the University of South Florida (USF). Dissolved Fe isotope ratios were measured by Thermo Neptune multi-collector ICPMS (MC-ICPMS) using a double spike analytical technique modified from Conway et al. (2013). Sample processing for Fe isotope analysis was carried out in the clean room at NIOZ (ISO class 7, ISO class 5 in working hoods), or in an ISO class 6 clean laboratory at USF. All containers and components used for chemical analysis were precleaned following GEOTRACES cookbook (version 3.0, 2017) and Middag et al. (2019), and all reagents were double distilled from

VWR NORMAPUR (NIOZ) or Fisher Scientific Trace Metal Grade (USF) by PFA Savillex Stills prior used for analysis. Acidified seawater samples were spiked with a ^{57}Fe-^{58}Fe double spike at least 48 hours prior to further treatment (extraction and purification) with a sample-to-spike ratio of 1:2 (nmol L^{-1}: nmol L^{-1}) (Sieber et al., 2021), guided by sample dFe concentrations measured independently by a SeaFAST system and Element 2 ICPMS as reported previously (van Manen et al., 2022).

3.2.2.1 Extraction and purification

An extraction and purification procedure for Fe from seawater was based on Conway et al. (2013) and was modified at NIOZ. The extraction procedure is shown in Table 3.1; for exaction, polypropylene tubes with polyethylene frits fitted to the bottom of the tubes were attached under separatory FEP funnels (Thermo Scientific™ Nalgene™, volume: 1 and 2 L). The tubes were filled with Nobias PA-1 chelating resin (~2 mL) and rinsed with MQ (15 mL, repeat three times) prior to loading samples. The pH values of samples were adjusted to 4.5±0.05 using ammonia acetate (pH=6.5) before eluted with 8 mL 3 M HCl (Table 3.1). After processing each sample, funnels and tubes (with resins loaded) were cleaned with 3 M HNO_3 and samples were then purified using LDPE microcolumns (with polyethylene frits) loaded with 30 µL Biorad™ AGMP-1 resin to separate Fe from interfering elements (the purification procedure is shown in Table 3.1). After processing each sample, AGMP-1 resin was discarded and the microcolumns (with frits) were cleaned in 1 M HCl at 60°C. The samples (0.5-1 mL) were shipped to USF for Fe isotope analyses in 8 mL LDPE bottles (Nalgene) that are routinely used for trace metal sampling. Samples were then re-purified using AGMP-1 microcolumns at USF (Sieber et al., 2021) prior to MC-ICPMS analysis. This second purification at USF was to ensure complete removal of Ca and Na from samples, as these elements can cause inaccuracy in Fe isotope analysis (Lacan et al. (2021) and our in-house experience).

Table 3.1 Extraction and purification procedure implemented in this study, modified from Conway et al. (2013).

Extraction	
1.	Preclean Nobias PA-1 resin with 4 mL 3M HNO_3
2.	Precondition resin with 4 mL diluted buffer (ammonia acetate, pH = 6.5) (MQ:buffer = 5:1)
3.	Adjust pH in samples to 4.5 ± 0.05 with concentrated buffer (ammonia acetate, pH = 6.5)
4.	Pass samples through resin by gravity with a duration less than 12 hours
5.	Rinse resin with 3 changes of 15 mL MQ
6.	Elute metals with 8 mL 3M HNO_3
7.	Evaporate samples at 180 °C. Reconstitute and reflux samples in 3 mL of concentrated HNO_3 and 10% H_2O_2 to dissolve organics fo
8.	Evaporate samples at 180 °C. Reconstitute and reflux samples in 200 µL of 7M HCl + 0.001% H_2O_2 for purification
Purification	
1.	Load 30 µL precleaned AG-MP 1 resin to microcolumns
2.	Clean microcolumns (with resin loaded) with 2 × 250 µL 7M HCl + 0.001% H_2O_2
3.	Rinse resin with 4 × 60 µL MQ
4.	Precondition columns with 200 µL 7M HCl + 0.001% H_2O_2
5.	Add samples
6.	Elute salts, Cu, Ni, Pb, and Co with 16 × 30 µL 7M HCl + 0.001% H_2O_2
7.	Elute Fe with 10 × 30 µL 1M HCl.
8.	Elute Zn with 10 × 30 µL 2M HNO_3 + 0.1 M HBr
9.	Elute Cd with 10 × 30 µL 2M HNO_3
10.	Evaporate samples at 180 °C. Reconstitute and reflux samples in 3 mL of concentrated HNO_3 and 10% H_2O_2 to dissolve organics fo
11.	Evaporate samples at 180 °C. Reconstitute in 0.1M HNO_3 for MC-ICPMS analysis

An estimation of the procedural blank for the method was determined by processing acidified ultrapure water through the full method described in Table 3.1. The extraction blank was 0.38±0.08 ng (n=11), the NIOZ purification blank was 0.15±0.09 ng (n=6), and the USF second purification blank was 0.13±0.15 ng (n=5). The total blank value (~0.66 ng per sample) is generally two orders of magnitude lower than natural Fe in our samples after the pretreatment, as well as being too small to measure the blank isotopic composition; as such we follow Sieber et al. (2021) and do not apply blank corrections to dFe or δ^{56}Fe.

3.2.2.2 Measurements of Multi-Collector ICPMS (MC-ICPMS)

Fe isotope analysis was carried out using a double-spike technique on a Thermo Neptune Plus MC-ICPMS in the Tampa Bay Plasma Facility at USF. The details of the instrumental settings, including introduction system, cones, cup configuration, mass bias correction, and double spike technique performance, are identical to those described by Sieber et al. (2021). Here, we express Fe isotope ratios in typical delta notations relative to the IRMM-014 standard:

$$\delta^{56}Fe\ (‰) = \left[\frac{(^{56}Fe/^{54}Fe)_{sample}}{(^{56}Fe/^{54}Fe)_{IRMM-014}} - 1\right] \times 1000$$

External precision at USF is approximated by the long-term instrumental precision on the secondary NIST SRM 3126a, with a value of +0.36±0.05‰ (mean±2SD, n=524) obtained over 37 sessions (Hunt et al., 2022), which agrees with literature values (Conway et al., 2013; +0.35±0.08‰; +0.39±0.13‰, Rouxel and Auro, 2010; +0.32±0.02‰, Sun et al., 2021). We thus consider 0.05‰ to be a conservative estimate of uncertainty and apply this to all samples, except for those where the 2 SE of an individual analysis is larger, in which case we use

this as a measure of uncertainty. The accuracy of the modified extraction and purification procedure was also tested by doping the same secondary Fe standard (NIST-3126) into acidified MQ that was processed as a sample and measured alongside natural samples. The average δ^{56}Fe of +0.35±0.02‰ (2 SD, n=3) of this test agrees with the expected value.

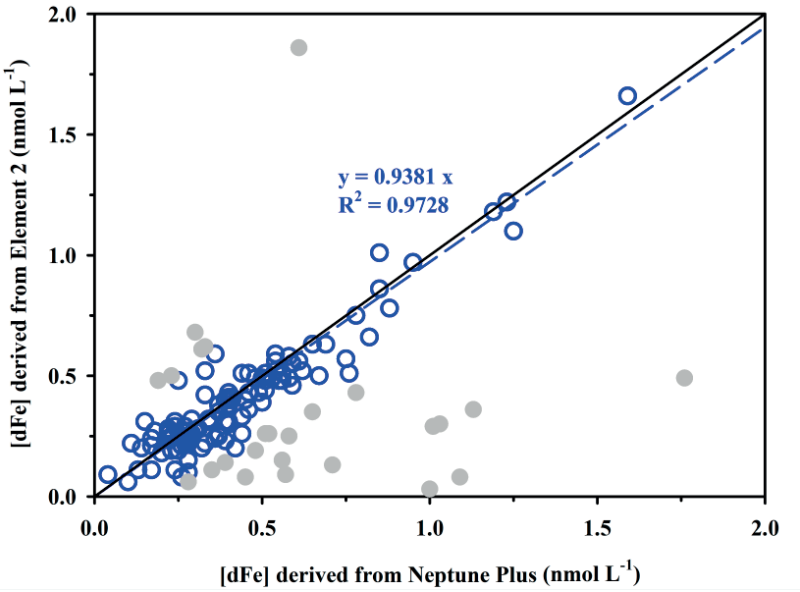

Figure 3.2 Linear regressions of dissolved Fe concentrations ([dFe]) derived from ICPMS (Element 2) versus concentrations derived from ICPMS (Neptune Plus) for ANA08B expedition. Measurements were conducted at NIOZ (Element 2) and the USF (Neptune Plus). The blue-dashed line and the black solid line represents the regression line and 1:1 line. Note that the intercept of regression is set to 0. [dFe] used in this study are means of two measurements. However, for samples that showed large absolute difference of concentrations between two measurements – namely, the absolute difference is larger than 0.1 nmol L^{-1} plus 10% of Element 2-derived [dFe] – [dFe] are selected based on oceanic consistency; these data is highlighted in grey. If only the Element 2-derived [dFe] was selected (i.e., the Neptune Plus-derived [dFe] was excluded), the δ^{56}Fe value was also not included in this study. In contrast, if only Neptune Plus-derived [dFe] was selected (i.e., Element 2-derived [dFe] was excluded), the δ^{56}Fe value was still included. The average of absolute standard deviation for both measurements is 0.08±0.07 nmol L^{-1} (mean±1 SD).

Uncertainty on Fe concentrations using this method is typically assumed to be 2% (Conway et al., 2013), and the accuracy of this method has been demonstrated previously (Conway et al., 2016; Conway et al., 2013). Further, dFe concentrations derived from the isotope dilution technique after measurement using the Neptune Plus MC-ICPMS agreed well with dFe concentration obtained from the SeaFAST based measurements on the Element 2 ICPMS (Fig 3.2; van Manen et al., 2022). In this study, since there is good agreement between the two methods for dFe in most samples, we use the mean dFe concentration calculated for each sample from the two methods.

3.3 Results

3.3.1 Oceanographic setting

In the AS, three water masses – Antarctic Surface Water (AASW), Winter Water (WW), and CDW (and mCDW) – are typically observed during austral summer (Randall-Goodwin. et al., 2015; Yager et al., 2012) and were observed during this expedition (Fig. 3.3). AASW is a result of enhanced solar irradiation and associated sea ice melt in summer, with conservative temperature (Θ) from –0.6 to –0.7˚C and absolute salinity (S_A) less than 33.8. AASW was observed in the upper 40 m at the $DIS_{(inflow)}$ stations and $DIS_{(outflow)}$ stations (Fig. 3.4a); whereas it was not clearly observed in the surface waters of the $GIS_{(inflow)}$ stations (Fig. 3.4d). WW, located below AASW, is a remnant from the winter season due to brine rejection and cooling of surface water, with an Θ minimum (~–1.8˚C) and S_A from 34.3 to 34.4 (Fig. 3.4). As CDW (i.e., off-shelf waters before intruding onto the continental shelf) mixes with overlying WW, it is modified from the off-shelf endmember to form mCDW, with Θ ranging from –0.5 to 1.5˚C and S_A higher than 34.7 (Figs 3.3 and 3.4).

3.3.2 Chlorophyll a Fluorescence

Chlorophyll a fluorescence was relatively elevated in the upper 100 m of most $DIS_{(inflow)}$ stations and $DIS_{(outflow)}$ stations and in the upper 40 m of all $GIS_{(inflow)}$ stations (Figs 3.4c and 3.4f), except one $DIS_{(outflow)}$

station (Stn 36) where fluorescence is relatively low compared to other stations. From here on, we define the surface layer as the water column between the surface and the depth where maximum fluorescence was observed; the fluorescence signal declined rapidly below this surface maximum (mostly within upper 200 m). The stations with elevated fluorescence are referred to as phytoplankton bloom stations (DIS bloom: Stns 33, 34, 42, 45, 48, 49, and 50; GIS bloom: Stns 24, 55, and 57) in this study as they have high chlorophyll a standing stock. These observations agree broadly with previous observations of annual phytoplankton blooms in the ASP (Alderkamp et al., 2015; Arrigo et al., 2012; Gerringa et al., 2012, 2020b; Yager et al., 2012).

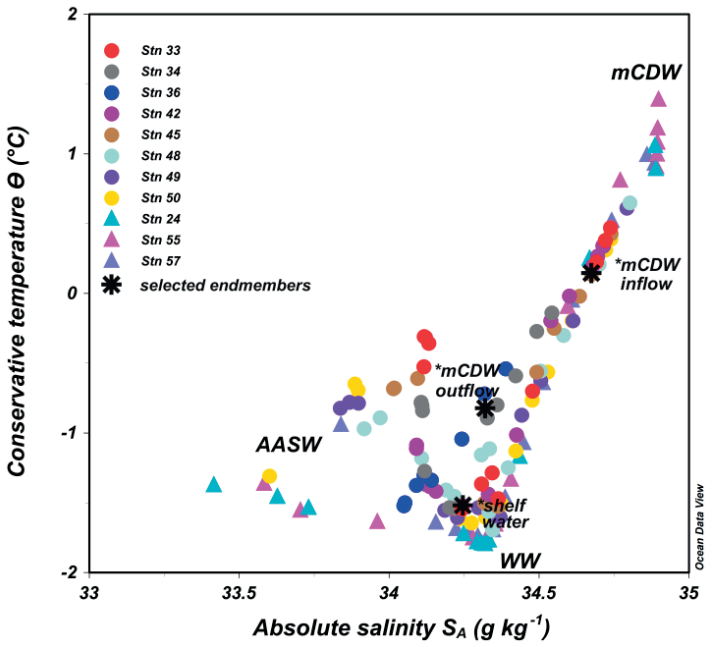

Figure 3.3 Conservative temperature (Θ)-absolute salinity (S_A) diagram. Three water masses are identified – Antarctic Surface Water (AASW), Winter Water (WW), and modified Circumpolar Deep Water (mCDW). The star signs represent the selected members used for conservative mixing discussed in section 3.4.2.1.

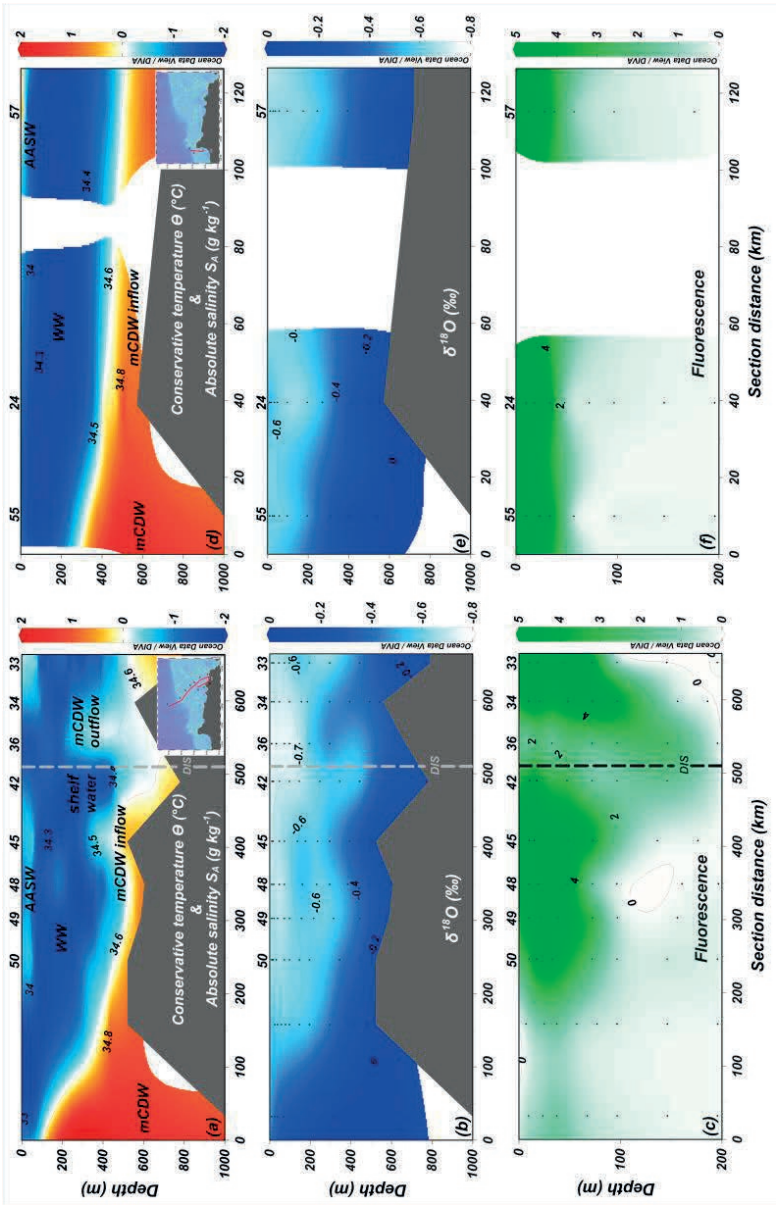

Figure 3.4 Sections of conservative temperature Θ, absolute salinity (S_A), and fluorescence of all GPpr12 stations included in this study. (a) to (c) the DIS$_{(inflow)}$ stations and the DIS$_{(outflow)}$ stations; (d) to (f) the GIS$_{(inflow)}$ stations. Note that (c) and (f) only show the upper 200 m of fluorescence.

3.3.3 Dissolved δ^{56}Fe and [dFe]

In the surface layer, dissolved Fe concentrations ([dFe]) were generally low at all stations – the $DIS_{(inflow)}$ stations (average: 0.25 nmol L^{-1}, ranging from 0.12 to 0.59 nmol L^{-1}); the $DIS_{(outflow)}$ stations (average: 0.14 nmol L^{-1}, ranging from 0.03 to 0.26 nmol L^{-1}); and the $GIS_{(inflow)}$ stations (average: 0.18 nmol L^{-1}, ranging from 0.08 to 0.26 nmol L^{-1}) (Fig. 3.5). On average, dissolved δ^{56}Fe exhibited elevated values in the $GIS_{(inflow)}$ stations (mean: +0.58‰, ranging from +0.22 to +1.06‰), and lower (near to crustal values) in both the $DIS_{(inflow)}$ stations (mean: +0.10‰, ranging from –0.23 to +0.68‰) and the $DIS_{(outflow)}$ stations (mean: –0.03‰, ranging from –0.23 to +0.21‰) (Fig. 3.5). Between 200 and 400 m in the $DIS_{(outflow)}$ stations, [dFe] was elevated compared to the surface layer, with an average of 0.46 nmol L^{-1} that ranged from 0.29 to 0.66 nmol L^{-1} (the highest at Stn 36) (Fig. 3.5), which was lower than [dFe] in the core of mCDW inflow (Stns 45 and 42, 400-750 m) (Fig. 3.5). In terms of δ^{56}Fe, it was generally lower than that of the surface layer, ranging from –0.36 to +0.01‰ with a mean of –0.19‰ (Fig. 3.5).

Within 200 m above the seafloor, [dFe] increased at all stations compared to the water column above. In particular, elevated [dFe] was observed at depth in the $DIS_{(inflow)}$ stations (average: 0.76 nmol L^{-1}, ranging from 0.41 to 1.63 nmol L^{-1}) and the $DIS_{(outflow)}$ stations (average: 1 nmol L^{-1}, ranging from 0.57 to 2.03 nmol L^{-1}) with only relatively modest near-bottom elevations at the $GIS_{(inflow)}$ stations (average: 0.48 nmol L^{-1}, ranging from 0.39 to 0.64 nmol L^{-1}) (Fig. 3.5). For δ^{56}Fe, light Fe signals were observed close to the seafloor, with an average of –0.33‰ (ranging from –0.97 to +0.1‰), –0.56‰ (ranging from –1.08 to –0.24‰), and –0.11‰ (ranging from –0.25 to +0.08‰), for the $DIS_{(inflow)}$ stations, the $DIS_{(outflow)}$ stations, and the $GIS_{(inflow)}$ stations, respectively (Fig. 3.5). Stns 36 and 55 are excluded from the discussion below on sedimentary input as the bottom is much deeper than the Titan sampling system could reach due to the limited length of the cable used (Stn 55) and a malfunction of the system (Stn 36) respectively.

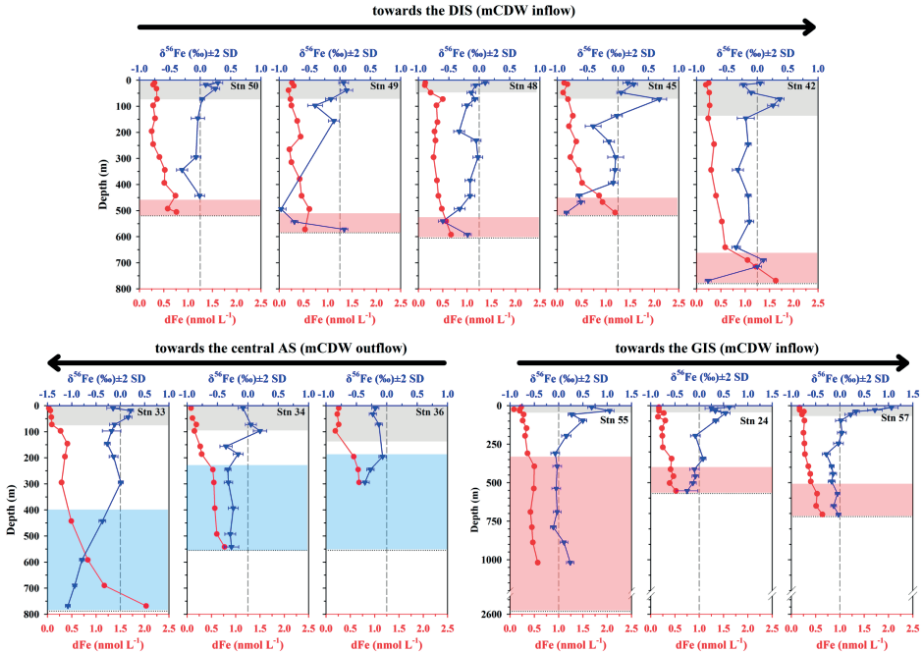

Figure 3.5 Vertical water column profiles of dissolved Fe concentration ([dFe]) and δ^{56}Fe from GPpr12 stations. dFe (red dots) corresponds to the bottom x-axis; whereas δ^{56}Fe (blue dots) corresponds to the top x-axis (error bar show two standard deviation (SD) for most samples, for samples that have 2 standard error lower than the long-term 2 SD of the internal standard – NIST SRM 3126a (+0.36±0.05‰, n=524), 0.05 is assigned as 2 SD). The grey dashed line indicates 0‰ of δ^{56}Fe, whereas the black dotted line indicates the bottom depth. The grey shading marks the surface layer (surface to fluorescence maximum depth); whereas the red and blue bars mark the depth of the mCDW inflow and outflow, respectively.

3.4 Discussion

In this study, we use the first dataset of dissolved δ^{56}Fe from the AS to investigate the varying importance of the external sources of dFe and the processes that control the biogeochemistry of dFe in the ASP. First, we discuss the importance of benthic sedimentary input, identifying the likely sedimentary release mechanisms (non-reductive vs reductive dissolution), and quantifying their relative contributions to the dFe pool. Second, we investigate the effect of potential

processes occurring in the cavity under the DIS on dFe and δ^{56}Fe in the outflow, and discuss the hypothesis that relatively low [dFe] in the outflow is due to conservative mixing of the inflow with low dFe waters that are adjacent to the ice shelf, and dissolved-particle interactions (van Manen et al., 2022). Finally, we explore the isotopic fractionation of dFe in two different phytoplankton blooms, dominated by haptophytes and diatoms, and thus provide insights into the dynamics of Fe isotope composition in productive Antarctic coastal polynyas.

3.4.1 Benthic shelf sediments and CDW as dFe sources to the AS

Before intruding onto the continental shelf and transforming into mCDW, CDW exhibits relatively elevated [dFe] compared to surface waters (0.2-0.4 nmol L^{-1}, Sedwick et al., 2008; Sieber et al., 2021; Tagliabue et al., 2012; van Manen et al., 2022). Previously, it was estimated that incoming mCDW and benthic sediments contributed roughly equal amounts to the observed [dFe] (0.38 nmol L^{-1} and 0.33 nmol L^{-1}, respectively) in the mCDW near the DIS (van Manen et al., 2022), based on the distribution of dFe. However, with merely [dFe] it is difficult to distinguish different sources and processes as both RD and NRD could lead to release of dFe to bottom waters. Hence, while benthic sediments have previously been confirmed as an important Fe source in the AS, the dominant release mechanisms for sedimentary dFe input into the AS remain unknown. Here, we use dissolved δ^{56}Fe measurements in mCDW along the flow path into the AS to identify the different sedimentary input sources of dFe (RD-dFe and NRD-dFe) and present a first attempt to quantify their relative contributions to mCDW in this region. As the core of mCDW inflow was located within 200 m above the seafloor (relatively well oxygenated with dissolved oxygen concentrations of 193-228 mol L^{-1}) in our dataset (van Manen et al., 2022), we only include samples in this depth range in our discussion.

3.4.1.1 Constraining RD and NRD contributions to mCDW using $\delta^{56}Fe$

Within 200 m above the seafloor at the $DIS_{(inflow)}$ stations, $\delta^{56}Fe$ ranged from +0.10 to –0.97‰ with values becoming lower from offshore towards the DIS, while [dFe] increased from 0.41 nmol L^{-1} to 1.63 nmol L^{-1} (Fig. 3.5). Both of these findings provide clear evidence for Fe addition from benthic sediments as mCDW travels towards the DIS. Likewise, at $GIS_{(inflow)}$ stations (Stns 24 and 57), low $\delta^{56}Fe$ (down to –0.25‰) with elevated [dFe] (up to 0.64 nmol L^{-1}) was observed close to the seafloor near the ice shelf (Fig. 3.5). In both cases, these isotopically light Fe signatures linked to elevated [dFe] are diagnostic of an input of dFe from RD (e.g., Homoky et al., 2009; John et al., 2012; Severmann et al., 2006; Severmann et al., 2010). Previously, elevated [Fe^{2+}] (e.g., RD derived) was observed in porewater samples collected in the AS, where a shallow oxygen penetration depth of only 1.8-3.6 cm (Kim et al., 2016) can enable diffusion of Fe^{2+} from porewaters into bottom water. Typically, RD-derived dFe initially ranges from −2 to −1.5‰; but the values can become even lower following precipitation of relatively heavy Fe(III) oxyhydroxides (typically ≥−3.5‰) (Crosby et al., 2007; Fitzsimmons and Conway, 2023; Homoky et al., 2009; Severmann et al., 2010). To date, a range of endmember $\delta^{56}Fe$ compositions have been previously reported or assumed for the signature of the benthic flux of Fe derived from RD into bottom waters (–3.5 to –0.93 ‰ as summarised by Johnson et al. (2020) and Fitzsimmons and Conway (2023)), with variability likely dependent on sediment and bottom water conditions (e.g., redox cycles in porewater particulates).

Previously, the proportion of dFe in mCDW to dFe in sediment was estimated to be 1.2:1 (0.38:0.31 nmol L^{-1}) based on concentration data and the assumption that there were no other sources involved at the same depth along the DIS inflow transect (van Manen et al., 2022). If RD was the main sedimentary process supplying dFe to the mCDW inflow, then the expected dissolved $\delta^{56}Fe$ in the outflow should range from –1.6 to –0.4‰, based on the roughly equal proportions of dFe in the mCDW to dFe in sediment (1.2:1) and assuming similar $\delta^{56}Fe$ as

previously reported elsewhere for RD fluxes to bottom waters (–3.5 to –0.93‰) and a mCDW signature of ~0‰ (Sieber et al., 2021) (see also section 3.4.1.2). However, while this range overlaps with our observations near the DIS, some of our samples are notably heavier (up to +0.1‰), suggesting an additional heavier dFe source (e.g., NRD) other than CDW and RD. Previously, a near-crustal δ^{56}Fe value for NRD (+0.2±0.2‰) was reported for porewater samples collected from the Cape margin (South Africa), a passive-tectonic and semi-arid ocean margin (Homoky et al., 2013; Homoky et al., 2009), as well as from seawater near the Papua New Guinea coast (Radic et al., 2011). Most recently, the signature of NRD was more tightly constrained at +0.07±0.07‰ based on lithogenic colloidal Fe in porewaters collected from across the Southwest Atlantic Ocean (Homoky et al., 2021). Such lithogenic colloidal Fe has been suggested to result from physical weathering of sediments, which is more likely decoupled from organic matter content and oxygen concentrations, in contrast to RD, and has potential to enable long term transport of Fe after it leaves the sediments (e.g., Conway and John, 2014a; Homoky et al., 2021; Jensen et al., 2020).

Therefore, although there are no direct porewater δ^{56}Fe measurements in the AS, we note that, with higher δ^{56}Fe compared to RD endmembers, NRD (~+0‰) likely contributes isotopically-heavier crustal dFe to the mCDW, explaining the higher δ^{56}Fe signal than expected based solely on a binary mixture of background CDW and RD. Using a simple mixing model based on both concentrations and isotopic composition, we are thus able to estimate the relative contributions of these three sources.

3.4.1.2 Relative contribution of dFe from CDW, RD and NRD

Using the combination of δ^{56}Fe and [dFe] within 200 m above the seafloor, we identified sedimentary dFe input from two different processes (section 3.4.1.1). Here, we use a simple two-component isotope mixing model to estimate the relative contribution of RD and

NRD for the samples collected within 200 m above the seafloor at the $DIS_{(inflow)}$ stations, assuming negligible isotope fractionation following addition to the water column. This assumption is consistent with a growing range of studies which suggest that the characteristically isotopically light Fe signatures from RD can persist in oxygenated ocean waters (e.g., Hunt et al., 2022; Severmann et al., 2010). The mixing model is described using the following equations:

$$dFe_{observed} = dFe_{CDW} + dFe_{sediment} \text{... (Eq. 1)}$$

$$f_{CDW} + f_{sediment} = 1 \text{... (Eq. 2)}$$

$$f_{sediment} = f_{RD} + f_{NRD} \text{... (Eq. 3)}$$

$$\delta^{56}Fe_{sediment} = \delta^{56}Fe_{observed} - \delta^{56}Fe_{CDW} = f_{RD} \times \delta^{56}Fe_{RD} + f_{NRD} \times \delta^{56}Fe_{NRD} \text{... (Eq. 4)}$$

where dFe, f, and $\delta^{56}Fe$ denote the dissolved Fe concentration, fraction, and Fe isotopic signature, respectively. To derive $dFe_{sediment}$, dFe_{CDW} was taken from van Manen et al. (2022) (0.38 nmol L^{-1}) where the least modified CDW was observed in the AS but located distant from the continental shelf (Stns 52 and 53, which were not measured for their Fe isotopic composition). To derive f_{RD} and f_{NRD}, an endmember estimate for $\delta^{56}Fe_{NRD}$ of +0.1‰ (Homoky et al., 2021) was used. For $\delta^{56}Fe_{RD}$, since a wide range has been reported (–3.5 to –0.93‰), we chose the minimum (–3.5‰), the maximum (–0.93‰), and the mean of the two extremes (–2.2‰), to account for uncertainty in the anticipated $\delta^{56}Fe_{RD}$ benthic flux endmember. For $\delta^{56}Fe_{CDW}$, the endmember (0‰) was taken from Sieber et al. (2021) observed in the upper CDW in the Southern Ocean, as no unmodified CDW was measured for δ^{56}Fe in this study. Consequently, the relative contribution of each of the three components – CDW-dFe (f_{CDW}), RD-dFe (f_{RD}), and NRD-dFe (f_{NRD}) – was estimated for two depth intervals of (1) within 200 m above the seafloor; and (2) within 100 m above the seafloor.

Table 3.2 Results of estimation of individual fraction of RD, NRD, and CDW within 200 m above the seafloor, as well as within 00 m above the seafloor.

		dFe			δ^{56}Fe		δ_{RD} = –3.5‰; δ_{NRD} = +0.1‰; δ_{CDW} = 0‰					δ_{RD} = –2.2 ‰; δ_{NRD} = +0.1‰; δ_{CDW} = 0‰					δ_{RD} = –0.93 ‰; δ_{NRD} = +0.1‰; δ_{CDW} = 0 ‰				
	station	observed	sediment	CDW	observed	sediment	dFe_{RD}	dFe_{NRD}	f_{CDW}	f'_{RD}	f'_{NRD}	dFe_{RD}	dFe_{NRD}	f_{CDW}	f'_{RD}	f'_{NRD}	dFe_{RD}	dFe_{NRD}	f_{CDW}	f'_{RD}	f'_{NRD}
within 200 m above seafloor	50	0.60	0.22	0.38	-0.16	-0.16	0.02	0.21	63%	3%	34%	0.02	0.20	63%	4%	33%	0.06	0.17	63%	9%	28%
	49	0.55	0.17	0.38	-0.75	-0.75	0.04	0.13	69%	7%	24%	0.06	0.11	69%	12%	20%	0.14	0.03	69%	26%	5%
	48	0.50	0.12	0.38	-0.35	-0.35	0.02	0.11	76%	3%	21%	0.02	0.10	76%	5%	20%	0.05	0.07	76%	11%	14%
	45	0.69	0.31	0.38	-0.33	-0.33	0.04	0.27	55%	5%	39%	0.06	0.25	55%	8%	36%	0.13	0.18	55%	19%	26%
	42	1.00	0.62	0.38	-0.13	-0.13	0.04	0.58	38%	4%	58%	0.06	0.56	38%	6%	56%	0.14	0.48	38%	14%	48%
within 100 m above seafloor	50	0.99	0.61	0.38	-0.01	-0.01	0.02	0.60	38%	2%	60%	0.03	0.59	38%	3%	59%	0.07	0.55	38%	7%	55%
	49	0.61	0.23	0.38	-0.75	-0.75	0.05	0.17	63%	9%	29%	0.08	0.14	63%	14%	24%	0.19	0.04	63%	31%	6%
	48	0.62	0.24	0.38	-0.40	-0.40	0.03	0.21	61%	5%	33%	0.05	0.19	61%	8%	30%	0.12	0.12	61%	19%	20%
	45	0.95	0.57	0.38	-0.66	-0.66	0.12	0.45	40%	13%	47%	0.19	0.38	40%	20%	40%	0.42	0.15	40%	44%	16%
	42	1.22	0.84	0.38	0.03	0.03	0.02	0.83	31%	1%	68%	0.02	0.82	31%	2%	67%	0.06	0.79	31%	5%	64%

The results of this calculation are shown in Fig. 3.6 and Table 3.2. Generally, f_{NRD} was higher than f_{RD}, with relatively small uncertainty (color shadings in Fig. 3.6) in f_{NRD} at most stations, except a large uncertainty in both f_{NRD} and f_{RD} at Stn 45 within 100 m above the seafloor when applying the minimum $\delta^{56}Fe_{RD}$ and maximum $\delta^{56}Fe_{RD}$ (Fig. 3.6b). This overall limited variability in f_{NRD} indicates that the choice of $\delta^{56}Fe_{RD}$ endmembers does not significantly affect our estimation of f_{NRD}. This finding is helpful because it means that any possible fractionation of the RD isotope endmember by removal processes within bottom waters would not change our conclusions. Therefore, we use the mean $\delta^{56}Fe_{RD}$ of the two extreme endmembers of the reported ranges (–2.2 ‰) as the general endmember for RD for the following discussion. Notably, this value is similar to that used previously by Conway and John (2014a), who chose –2.40‰ to best represent reductive sedimentary endmember, based on modelled RD Fe fluxes from the San Pedro basin (John et al., 2012).

At the $DIS_{(inflow)}$ stations, f_{CDW} within 200 m of the seafloor ranged from 38 to 76%, generally decreasing from the open ocean towards the DIS; meanwhile, f_{NRD} increased from 20 to 56% while f_{RD} remained relatively stable (4-12%) (Fig. 3.6a, Table 3.2). Since sediment resuspension is considered to be an important release pathway for NRD-dFe colloids (Homoky et al., 2021), our calculated higher f_{NRD} than f_{RD} at these stations suggests resuspension is important for supplying dFe to bottom waters, linked to the turbulent flow of mCDW. Such resuspension would bring both RD-dFe (e.g., porewater reduced Fe^{2+}, Kim et al., 2016) into the overlying water as well as NRD-dFe, contributing more dFe than simple diffusion of Fe by RD from the sediment pore waters. In fact, f_{NRD} was highest at Stn 42 (up to 56%, higher than both f_{CDW} and f_{RD}, Fig. 3.6a), suggesting accumulation of colloidal phase NRD-dFe in the inflow as it travelled towards the coast, and/or terrestrial input of lithogenic colloids from the Antarctic shore (van Manen et al., 2022). This finding, from an isotopic perspective, also corroborates the previous idea that particle resuspension from benthic sediment influences the magnitude and

distribution of [dFe] in the AS (Sherrell et al., 2015). Alternatively, spatial and temporal heterogeneity of sediment conditions can also result in the difference in f_{NRD} and f_{RD}, assuming dFe derived from CDW stays constant during the course of inflow transport: more reducing sediment or thinner oxygenated surface layers may lead to more RD-dFe in porewater (e.g., Henkel et al., 2018), whereas more oxygenated sediments may result in relatively higher colloidal NRD-dFe in porewaters (e.g., Homoky et al., 2021). Indeed, δ^{56}Fe exhibits heterogeneity in the bottom-most samples along the $DIS_{(inflow)}$ stations (Fig. 3.5), suggesting both the flux and mechanism of supply of dFe varies geographically within the AS. However, as sediment samples were not collected during the ANA08B expedition and the composition of sediments was not determined, we cannot determine whether spatial heterogeneity or simultaneous release of both RD and NRD is the main driver of the observed isotopic signatures.

When investigating closer to the seafloor in the AS, and comparing samples from within 100 m to within 200 m from the seafloor (see above), a similar increasing trend in each sediment-derived fraction and [dFe] towards the DIS is observed (Fig. 3.6b); however, f_{NRD}, f_{RD}, and total [dFe] (i.e., sum of CDW-dFe, NRD-dFe, and RD-dFe) are all greater within 100 m compared to within 200 m above the seafloor (Table 3.2), indicating that benthic sediment input has a greater effect on dFe closer to the sediments, linked to the core of mCDW being situated close to the bottom, while dFe may be lost due to removal (e.g., particle scavenging) or dilution (i.e., conservative mixing) further above the seafloor.

The relationship between [dFe] and absolute salinity (S_A) within 100 m (and 200-300 m) above the seafloor provides insights for assessing the role of conservative mixing – at stations distant from the DIS (Stns 50, 49, and 48) (Fig. 3.7a), the relationship follows a mixing line which indicates that physical mixing and dilution drive reduction of dFe away from the source, whereas close to the DIS (Stns 42 and 45), a sudden increase of dFe (up to 1.6 nM) at high salinity indicates a prominent addition of dFe, compared to Stns 50, 49, and 48 (Fig. 3.7a), accompanied by lower δ^{56}Fe values observed close to the seafloor at

Stns 42 and 45 (down to –0.85‰) than at Stns 50, 49, and 48 (Fig. 3.5). A strong correlation (R^2=0.822, p<0.05, excluding one sample at 689 m at Stn 42) between the fractions of RD-dFe and NRD-dFe indicates simultaneous addition of dFe from both sources (Fig. 3.7b), lending weight to the idea that sediment resuspension is important, as Fe derived from the two sources are thought to be present in different forms and sediment disturbance – not just simple diffusion from pore waters – is needed to release both at once (dFe^{2+} vs colloidal Fe(III), Homoky et al., 2013; Homoky et al., 2009; Homoky et al., 2021).

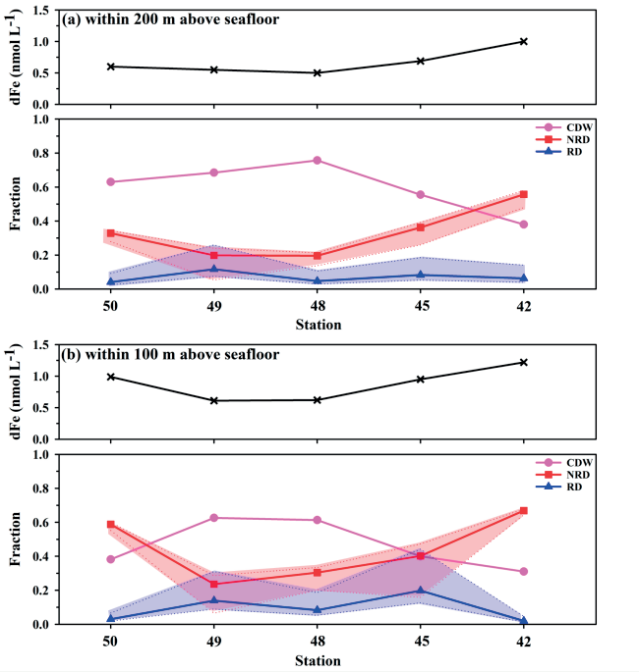

Figure 3.6 Fractions of reductive dissolution (RD) (f'_{RD}), non-reductive dissolution (NRD) (f'_{NRD}) and circumpolar deep water (CDW) (f_{CDW}) and [dFe] at the GPpr12 $DIS_{(inflow)}$ stations (in each depth interval the means were calculated). RD (blue triangle), NRD (red square), and CDW (pink dot) corresponds to left y-axis, whereas dFe (black solid line) corresponds to the right y-axis. For RD, three different endmembers are used to account for the uncertainties – solid line (–2.2 ‰) and upper and lower estimates (–0.93‰ and –3.5‰). The coloured shading indicates the range, simply based on interpolation of the upper and lower estimates. (a) samples located within 200 m above the seafloor; (b) samples located within 100 m above the seafloor.

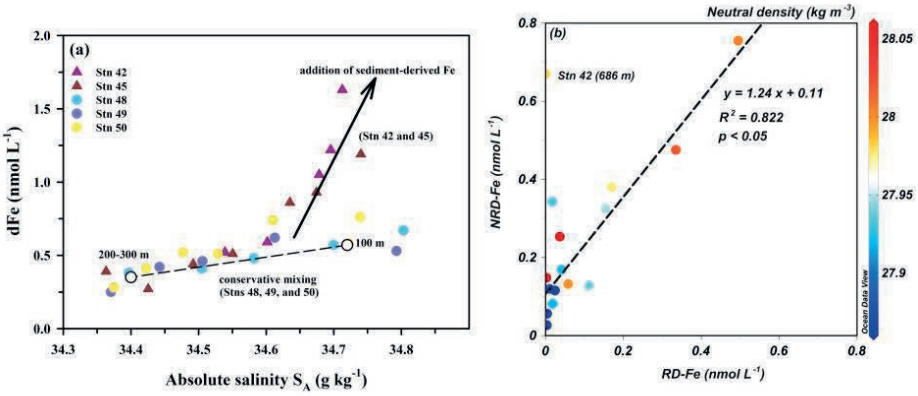

Figure 3.7 Relationship of [dFe] and absolute salinity (S_A), dFe derived from non-reductive dissolution (NRD-dFe) and from reductive dissolution (RD-dFe) (coloured for neutral density) within 300 m above the seafloor, of the GPpr12 DIS$_{(inflow)}$ stations. (a) [dFe] versus S_A. Solid coloured dots and triangles represent stations relatively far from the DIS (Stn 48, 49, and 50) and stations close to the DIS (Stn 42 and 45), respectively. Empty black dots represent the averages (within 100 m above the seafloor and 200-300 m above the seafloor) from Stn 48, 49, and 50; whereas the black arrow and the dashed line indicate the addition of sediment-derived Fe and the conservative mixing line, respectively. (b) NRD-dFe versus RD-dFe. The dashed line represent the regression line. Note that the correlation excludes Stn 42 (689 m).

3.4.2 Biogeochemical processes under the DIS

Due to global warming, ice shelves and glaciers located near the AS have been experiencing rapid collapsing and melting (Gourmelen et al., 2017; Jacobs et al., 1996; Jenkins et al., 2010; Rignot et al., 2008). It was previously proposed that rapid melting of glaciers and ice sheets could be an important source of Fe (Alderkamp et al., 2012; Gerringa et al., 2020a; Gerringa et al., 2012, 2020b). For example, Sherrell et al. (2015) observed elevated dFe (0.62-0.77 nmol L^{-1}, 80-600 m) in the mCDW outflow from the DIS compared to surface polynya waters (~0.15 nmol L^{-1}) , likely sourced from a combination of mCDW, shelf sediments, and DIS-sourced dFe. This [dFe] range is comparable to [dFe] observed in the mCDW outflow in this study (0.64±0.06 nmol L^{-1}, 195-294 m, Stn 36). However, from our previous

work, the addition of DIS-sourced dFe itself to the mCDW outflow was estimated to be negligible (van Manen et al., 2022). In fact, [dFe] effectively decreased slightly in the outflow compared to the inflow (average of 0.99±0.17 (n=3) vs 0.64±0.06 (n=3) nmol L^{-1}; Fig. 3.5), likely due to extensive mixing of the dFe-rich outflow with relatively low dFe water close to the ice shelf, based on a conservative mixing model (van Manen et al., 2022). However, the observations from van Manen et al., 2022 were solely based on [dFe] and as such, any change in [dFe] underneath the DIS due to biogeochemical processes or from different sources/sinks remained unconstrained. Therefore, although the $\delta^{56}Fe$ of cryospheric sources and processes involved remain relatively poorly constrained (Fitzsimmons and Conway, 2023), in the following section we attempt to use $\delta^{56}Fe$ to investigate the sources of dFe and potential biogeochemical processes in the ice shelf cavity.

3.4.2.1 Is conservative mixing and addition of heavy Fe driving dissolved δ56Fe underneath the DIS?

In our study, we observed a change in $\delta^{56}Fe$ of –0.70±0.13 to –0.23±0.15‰ between DIS inflow and outflow ($\Delta\delta^{56}Fe_{DIS}$ of +0.47‰), coupled with the decline in [dFe] of ~1 to 0.6 nmol kg^{-1} that was previously attributed to the effects of conservative mixing (van Manen et al., 2022). To evaluate whether conservative mixing can feasibly explain this observed change in the $\delta^{56}Fe$ distribution underneath/adjacent to the DIS (or whether other processes are required), we compared $\delta^{56}Fe$ values from four water masses (defined as endmembers from representative samples) that are most probably the main components involved in conservative mixing:

(1) mCDW inflow: we chose a Θ isotherm of 0°C which is ~100 m above the seafloor (usually around 500 m) for the $DIS_{(inflow)}$ stations to represent the mCDW inflow (Fig. 3.4a). This depth interval for the mCDW inflow has been previously described for this region (Miles et al., 2016; Sherrell et al., 2015; van Manen et al., 2022), and is characterized by $\delta^{18}O$ (>–0.2‰) and high S_A (>34.5) (Figs 3.4a and 3.4b). This depth interval is also comparable

to the depth of the grounding line of the DIS (~420 to 500 m, Jordan et al., 2020). To represent the properties of the mCDW inflow prior to entering the ice cavity, we selected samples at Stn 45 (442 to 507 m). The Fe isotopic composition of the defined mCDW inflow endmember ($\delta^{56}Fe_{inflow}$) is –0.70±0.13‰ (mean±1 SD) (Table 3.3). Here, it should be noted that we choose Stn 45 over Stn 42 (i.e., the closest station to the DIS in the mCDW inflow) to represent the mCDW inflow better because the samples in deep water at Stn 42 were found to be affected by lithogenic material from the DIS and perhaps also by mCDW outflow (based on elevated dissolved Fe and particulate Fe concentrations; van Manen et al., 2022); this assertion is also supported by a $\delta^{56}Fe$ anomaly (close to 0‰) observed between 690 and 715 m at Stn 42, different from the samples above and below (Fig. 3.5), indicating a lithogenic signal at this depth.

(2) ice shelf meltwater: the meltwater from the ice shelf where the melting is induced by inflow of relatively warm mCDW. Since we do not have direct measurements of meltwater, this water mass has an unknown Fe isotopic composition ($\delta^{56}Fe_{icemelt}$) that will be further evaluated in this section.

(3) shelf water: we defined a water mass geographically adjacent to the ice shelf, which mixes with the mCDW inflow and ice shelf meltwater as a third component for the conservative mixing model. The Fe isotopic composition of the shelf water endmember ($\delta^{56}Fe_{shelfwater}$) is –0.22±0.09‰ (mean±1 SD) (Table 3.3). Samples collected at similar depth as the mCDW outflow, but outside the region where outflow occurs, were chosen to represent the endmember for shelf water (Stn 42, 145 to 300 m, Figs 3.3 and 3.4a). The rationale of choosing Stn 42 is that it is the station closest to the DIS that thus may best exhibit the properties of this water immediately prior to mixing. This shelf water has similar Θ and S_A to WW (Fig. 3.3).

(4) mCDW outflow: the water mass that is the result of conservative mixing between the mCDW inflow, shelf water, and ice shelf meltwater. This outflowing water mass was identified below ~200 m at Stn 36, based on elevated Θ (>–1°C), $\delta^{18}O$ (~–0.4‰), and S_A

(>34.1), compared to the remainder of the water column (Figs 3.3, 3a and 3b). The Fe isotopic composition of the defined mCDW outflow endmember ($\delta^{56}Fe_{outflow}$) is –0.23±0.15‰ (mean±1 SD) (Table 3.3). Since samples below 400 m at Stn 36 were not available due to a technical issue with the sampling system, we chose samples collected between 200 and 400 m at this station to represent the mCDW outflow. This depth interval is comparable to previously reported depths for the core of mCDW outflow in the same region (Miles et al., 2016; Randall-Goodwin. et al., 2015).

Table 3.3 Endmembers selected for section 3.4.2.1. Between these three $\delta^{56}Fe$ endmembers based on averaged observations ($\delta^{56}Fe_{outflow}$, $\delta^{56}Fe_{inflow}$, and $\delta^{56}Fe_{shelfwater}$), there was a significant difference ($p<0.05$), determined using a test of analysis of variance (one-way ANOVA), where a follow-up Post-Hoc test (Bonferroni correction) showed that $\delta^{56}Fe_{inflow}$ differed significantly from (was lighter than) the other two endmembers ($\delta^{56}Fe_{outflow}$ and $\delta^{56}Fe_{shelfwater}$).

Endmember	Station	Depth (m)	δ^{56}Fe±2 SD (‰)	Θ (°C)	S_A (g kg^{-1})
$\delta^{56}Fe_{inflow}$	45	442	–0.64±0.05	–0.02	34.64
		467	–0.61±0.06	0.14	34.67
		507	–0.85±0.04	0.43	34.74
		Mean±1 SD	–0.70±0.13	0.18±0.23	34.68±0.05
$\delta^{56}Fe_{shelfwater}$	42	145	–0.19±0.14	–1.42	34.16
		245	–0.15±0.05	–1.52	34.24
		344	–0.32±0.09	–1.44	34.33
		Mean±1 SD	–0.22±0.09	–1.46±0.05	34.24±0.09
$\delta^{56}Fe_{outflow}$	36	195	–0.07±0.06	–1.04	34.24
		245	–0.27±0.06	–0.72	34.32
		294	–0.36±0.07	–0.54	34.389
		Mean±1 SD	–0.23±0.15	–0.77±0.25	34.32±0.07

Previously, the fractions of each water mass were estimated based on $\delta^{18}O$, where the mCDW inflow, ice shelf meltwater, and shelf water, accounted for 74.9%, 0.6%, and 24.5%, respectively (Tian et al., 2023b). Based on these estimated fractions and selected endmembers, $\delta^{56}Fe_{icemelt}$ can be estimated (assuming conservative mixing) based on the following mixing model:

$$0.749 \times \delta^{56}Fe_{inflow} + 0.245 \times \delta^{56}Fe_{shelfwater} + 0.006 \times \delta^{56}Fe_{icemelt} = \delta^{56}Fe_{outflow} \text{ ... (Eq. 5)}$$

Using this equation, we calculated a $\delta^{56}Fe_{icemelt}$ endmember of +5.78‰. Although there is a paucity of data for $\delta^{56}Fe$ values in Antarctic glacial systems (Henkel et al., 2018; Mikucki et al., 2004; Sieber et al., 2021), and the variability in dissolved $\delta^{56}Fe$ in meltwater is highly dependent on subglacial weathering (physical and chemical) in individual glacial systems (Krisch et al., 2021; Stevenson et al., 2017; Zhang et al., 2015), a value of +5.78‰ is clearly unfeasible for $\delta^{56}Fe_{icemelt}$, which is more likely close to crustal $\delta^{56}Fe$ (+0.09‰, Beard and Johnson, 2004) as most Fe in an ice shelf derives from lithogenic materials when the ice sheets move towards the shore and interact with the underlying bedrock (Raiswell et al., 2006), or perhaps slightly isotopically lighter due to reductive dissolution. Indeed, van Manen et al. (2022) found the mCDW outflow was enriched in refractory particulate Fe (most likely lithogenic Fe) compared to labile particulate Fe and dissolved Fe. Further, +5.78‰ is much heavier than any $\delta^{56}Fe$ values reported for any dFe source in the marine system (Fitzsimmons and Conway, 2023; Johnson et al., 2020). If we instead assign a crustal signature to $\delta^{56}Fe_{icemelt}$ (+0.09‰), the constrained contribution of 0.6% from ice shelf melt could not result in the $\delta^{56}Fe_{outflow}$ as observed – the estimated overall $\delta^{56}Fe$ signal in the outflow would be –0.61‰, which is much lighter than the observed $\delta^{56}Fe_{outflow}$ (–0.23±0.15‰). Obviously, choosing a lighter endmember for $\delta^{56}Fe_{icemelt}$ would only exacerbate this issue. Thus, although conservative physical mixing with shelf water provides a plausible explanation for the observed [dFe] changes between the inflow and outflow, it cannot explain the observed positive change in $\delta^{56}Fe$ (at best only a $\Delta\delta^{56}Fe$ of +0.09‰, from –0.70 to –0.61‰). Instead, other processes must be driving an apparent fractionation in dissolved $\delta^{56}Fe$ within the DIS system.

Indeed, it has been hypothesized, based on Arctic systems, that the residence time of inflowing water underneath ice shelf/glacier system

may enable significant chemical alternation (e.g., changes in nutrient availability and/or input of ice sheet-derived materials) between the inflow and the outflow, especially for non-conservative elements (e.g., Fe) (Krisch et al., 2021), especially if the residence time of water is long. For example, the residence time of inflowing water masses underneath the '79°N Glacier' is around 5.4 months (Schaffer et al., 2020). Krisch et al. (2021) suggested that thermodynamic equilibrium between dFe, labile particulate Fe, and ligands in the ice cavities could play an important role in subglacial nutrient supply as well as driving the δ^{56}Fe of the dFe pool to heavier values than known Fe sources. Although the residence time of the mCDW inflow underneath the DIS is much shorter than the '79°N Glacier' (estimated to only be approximate 2 months; Girton et al., 2019; Yang et al., 2022), our isotopic data imply that, in addition to ice shelf-derived Fe and mixing with shelf water, processes occurring underneath the DIS may be responsible for an additional δ^{56}Fe shift ($\Delta\delta^{56}$Fe of at least +0.38‰, from –0.61 to –0.23‰), which cannot be easily explained by simple addition of dFe without further fractionation.

3.4.2.2 Potential processes occurring underneath the DIS leading to heavier Fe in the outflow

While understanding the fractionation of Fe isotope ratios resulting from different processes in the oceans is the subject of ongoing investigations (Fitzsimmons and Conway, 2023), studies have identified various internal cycling processes that could result in isotopic fractionation of the dissolved pool. Here, we evaluate several processes that could potentially result in a shift towards isotopically heavy dFe ($\Delta\delta^{56}$Fe=+0.38‰) underneath the DIS; these include the enhanced preservation and addition of lithogenic colloidal Fe(III) together with the preferential loss of Fe^{2+}, and complexation with Fe-binding ligands.

Preferential preservation of one Fe species over another underneath the ice shelf could result in an overall change in the δ^{56}Fe of the whole dFe pool. For example, addition and preservation of 'lithogenic'

derived colloidal Fe(III) that is matched by an equivalent loss of Fe^{2+} or Fe(III) species could be responsible for an overall change in 'dissolved' $\delta^{56}Fe$. Previously, the speciation of NRD-dFe as lithogenic colloidal Fe(III) has been highlighted by Homoky et al. (2021) who observed near-crustal $\delta^{56}Fe$ in the colloidal fraction in core-top porewater and suggested such colloidal Fe is likely formed by weathering of lithogenic particles via a non-reductive process. In this study, benthic sediments supply both particles and NRD-derived dFe (see Section 3.4.1.1), and ice shelf melt (or glacial melt) supplies a significant amount of particulate Fe into the AS via the mCDW outflow (Gerringa et al., 2012, 2020b; Planquette et al., 2013; van Manen et al., 2022). Notably, particulate Fe concentrations ([pFe]) were two to three orders of magnitude higher than [dFe] in the AS, and elevated [pFe] was observed especially in the $DIS_{(outflow)}$ stations (van Manen et al., 2022), with refractory [pFe] (34.4±11.4 nmol L^{-1}, 2 SD) and labile [pFe] (12.6±2.2 nmol L^{-1}, 2 SD) relative to 0.6 nM [dFe]. Such high loading of pFe could facilitate exchange of Fe between the dissolved pool and labile particulate pool ('a reversible equilibrium'; Fitzsimmons et al., 2017; van Manen et al., 2022), acting to 'reset' or moderate dissolved $\delta^{56}Fe$ signatures whilst [dFe] stays relatively stable. This idea is consistent with previous suggestions that isotopic composition can be modified due to extensive exchange between particles and seawater whilst dissolved concentrations do not change significantly; this concept, termed 'boundary exchange', was observed for Neodymium isotope systematics (e.g., Lacan and Jeandel, 2005) and later inferred for other trace metals (e.g., Fe, Jeandel, 2016), as well as being observed in deep nepheloid layers of the North Atlantic, where dissolved $\delta^{56}Fe$ values approach crustal composition with no accompanying change in [dFe] (Conway and John, 2014a). It has also been observed that isotopically light Fe^{2+} (ranging from –0.89 to –0.12‰) released from basal meltwater and/or subglacial discharge was lost during extensive reworking of Fe phases (e.g., dissolved, ligand-bound, particulate and sedimentary phases) in the glacial cavity of the '79°N Glacier', leading to a near-crustal $\delta^{56}Fe$ signature (+0.07±0.09 ‰) in the glacial outflow (Krisch et al., 2021) where sediment resuspension in nepheloid layers of the ice cavity was

suggested a main driver of lithogenic Fe input (Chen et al., 2022). This observation implies that the loss of Fe^{2+} may be more significant than the addition of Fe(III) species underneath the ice sheet systems, especially in systems where particle loading is prominent (van Manen et al., 2022).

Organic ligand complexation could also contribute to the change in $\delta^{56}Fe$ under the ice shelf. Complexation of Fe by organic ligands tends to bind isotopically heavy Fe, leading to high $\delta^{56}Fe$ values for the dissolved Fe pool, especially due to ligands with a strong affinity for Fe (e.g., siderophores) (Dideriksen et al., 2008; Morgan et al., 2010). Additionally, although the jury remains out on the effect of particle scavenging on $\delta^{56}Fe$, with limited open ocean studies showing negligible to only small fractionation (0 to –0.3‰; Fitzsimmons and Conway, 2023; Radic et al., 2011), particle dissolution coupled to organic-ligand complexation as well as scavenging has been invoked to explain isotopically heavy dFe in North Atlantic surface waters (+0.8‰, Conway and John, 2014a; John and Adkins, 2012). In the AS, Thuróczy et al. (2012) found organic ligands (originating from mCDW and/or sediments) to be nearly saturated with Fe near the ice shelves of Pine Island Glacier, with only modest capacity for complexing additional dFe from glacial meltwater. Under such conditions, the ligands are already saturated before the mCDW enters the ice shelf cavity, leaving little capacity for either complexation or a role in adjusting the composition of dissolved $\delta^{56}Fe$. However, in the DIS outflow, van Manen et al. (2022) showed that ligand to dFe ratios were above two at Stns 36 and 42, indicating Fe-binding ligands were unsaturated, which implies a potential for ligands to bind additional dFe under the ice shelf. However, that study also showed that even though the outflow was rich in Fe-binding ligands, dFe did not seem to increase in contrast to particulate Fe, implying the ligands were not strong enough to compete with adsorption onto particles that were also supplied from ice shelf melt (van Manen et al., 2022), consistent with a possible preferential loss of reactive species such as Fe^{2+} or Fe(III) species, balanced by an increase in lithogenic colloids under the DIS. A similar scenario of weak complexation by organic ligands compared to particle scavenging was also observed near the terminus

of the '79°N Glacier' (Ardiningsih et al., 2020). However, even if ligands are not strong enough to effectively compete with particle scavenging in the ASP, and weak ligands would be expected to drive a smaller fractionation factor than strong ligands (Morgan et al., 2010), they could still play a role in setting the resulting overall isotopic signature of the dFe pool in the DIS outflow.

Overall, although we cannot tease out the effects of these competing processes, we propose that particles, together with colloids from NRD-dFe, contribute 'lithogenic' colloidal Fe(III) (with near-crustal δ^{56}Fe) to the dissolved pool in the DIS outflow, with particles also likely scavenging truly dissolved Fe species (e.g., Fe^{2+}) in competition with Fe binding ligands. The net effect of these processes on the isotopic composition would be to drive dissolved δ^{56}Fe towards crustal values under the DIS, as was observed at the '79°N Glacier' (Krisch et al., 2021).

3.4.3 Fractionation of Fe isotopes in ASP phytoplankton blooms

Phytoplankton blooms are an annual feature in the ASP during austral spring and summer (Alderkamp et al., 2015; Arrigo et al., 2012; Park et al., 2017) where the surface dFe distribution was found to be the opposite of the distribution of phytoplankton mass (Alderkamp et al., 2012). In our study in the surface layer of both the DIS and GIS regions, low [dFe] also coincided with elevated fluorescence, indicative of phytoplankton blooms (Figs 3.4 and 3.5). It is thus likely biological uptake is the main process driving the drawdown of dFe in the surface ASP (Alderkamp et al., 2012; Sherrell et al., 2015; van Manen et al., 2022). Biological uptake may also affect dissolved Fe isotopic composition. We observed elevated remnant dissolved δ^{56}Fe in the surface layer of the GIS bloom (up to +1.06‰), that was significantly higher than that following the DIS bloom (~+0.68‰) ($p<0.05$, Table 2). Generally, isotopically heavier remnant dFe following biological uptake is consistent with the limited previous studies that looked at

blooms or the effect of uptake (Ellwood et al., 2020; Ellwood et al., 2015; Sieber et al., 2021).

The difference in δ^{56}Fe between blooms could result from the extent of Fe uptake in the surface layer, namely, with more dFe assimilated, one might expect to observe heavier δ^{56}Fe in seawater – Yager et al. (2016) argued that a longer opening time of the polynya may lead to higher Fe uptake, hence potentially also a stronger biological-driven isotope fractionation effect. Here, we compared [dFe] in the pre-bloom stage (estimated starting concentrations) and the bloom stage (observed concentrations) to evaluate the Fe uptake in the DIS and GIS bloom respectively. The sampling period for the two blooms was from 24th January to 2nd February. For the pre-bloom stage, we assume [dFe] in WW (Θ<–1.5˚C) represented the starting concentrations as WW is a remnant of the cold winter mixed layer overlain by a relatively warm and fresh AASW that forms from WW by sea ice melting and warming due to incident irradiance during summer (e.g., Mosby, 1936). The comparison is detailed in Table 3.4. The results showed no statistically significant difference of starting [dFe], nor of observed [dFe], between the DIS and GIS bloom (Table 3.4), suggesting a comparable amount of Fe uptake between two blooms (assuming there were no differences in supply during the bloom period). Additionally, integrated particulate organic carbon (POC) and nitrogen (PON) concentrations are also not significantly different between two regions (Table 3.4), implying that primary production was likely at comparable levels in the two blooms. Therefore, a differential degree of Fe uptake with the same fractionation factor cannot explain the observed difference in δ^{56}Fe in the surface layers of the two regions.

Alternatively, different phytoplankton communities in the two blooms could potentially fractionate Fe isotope ratios via different fractionation factors during uptake (Ellwood et al., 2015). Pigment-based phytoplankton taxonomic composition analysis showed that the dominant phytoplankton species differed between the blooms; haptophytes dominated the DIS bloom (64-94% of total abundance),

whereas diatoms dominated the GIS bloom (40-91% of total abundance) (Fig. 2.6, Chapter 2). We thus hypothesize that the difference in remnant surface dissolved δ^{56}Fe between blooms could result from different dominant phytoplankton communities. Although there is little understanding about how different species fractionate Fe via biological uptake, the utilization of Fe and uptake mechanisms by phytoplankton are better constrained. For example, diatoms and haptophyte species have different strategies in terms of utilizing Fe and may allocate resources (e.g., Fe and other nutrients) distinctly (Alexander et al., 2015; Litchman et al., 2007; Margalef, 1978). For instance, diatoms tend to maximize growth rates under nutrient-replete environments (Endo et al., 2018), whereas haptophytes allocate nutrients not only to reproduction but also to other activities to maintain a constant population size (Endo et al., 2018; Parry, 1981).

Table 3.4 Comparison of δ^{56}Fe, [dFe], and POC and PON, in the surface layer of two ASP blooms. Starting [dFe] is estimated based on [dFe] in WW (Θ<–1.5˚C). Note that WW samples for determining the starting [dFe] were selected from the $GIS_{(inflow)}$ stations and the $DIS_{(inflow)}$ stations (except Stn 42 due to extensive particles exported from the DIS that could already alter [dFe] (e.g. scavenging and regeneration, van Manen et al., 2022). All values are presented as mean ± 1 SD.

The surface layer	DIS bloom	GIS bloom	t-Test (two-tail)
observed δ^{56}Fe (‰)	+0.08 ± 0.20 (n = 27)	+0.58 ± 0.33 (n = 9)	P < 0.05
starting [dFe] (nmol L^{-1})	0.30 ± 0.05 (n = 12)	0.26 ± 0.05 (n = 12)	P = 0.07
observed [dFe] (nmol L^{-1})	0.20 ± 0.09 (n = 28)	0.18 ± 0.05 (n = 10)	P = 0.60
POC (integrated) (g m^{-3})	3.87 ± 1.82 (n = 3)	1.80 ± 0.21 (n = 3)	P = 0.32
PON (integrated) (g m^{-3})	25.3 ± 12.1 (n = 3)	8.86 ± 1.03 (n = 3)	P = 0.29

Such diversity in the use of Fe between diatoms and haptophytes implies they assimilate Fe via different pathways, such as transporters for specific Fe compounds, direct Fe(II) transporters, or reduction of Fe(III) to Fe(II) on the cell surface (e.g., ligand-bound Fe) (Hutchins et al., 1999; Morel et al., 2008), which could result in different isotopic

fractionation factors. Moreover, Ellwood et al. (2015) pointed out that small phytoplankton (e.g., Synechococcus) and large phytoplankton (e.g., diatoms) may cause isotopic fractionation at different levels. Similarly, the size of haptophytes (generally <5 µm) and diatoms (2 to 200 µm) is markedly different (e.g., Cuvelier et al., 2010; Halse and Syvertsen, 1996; Masquelier et al., 2011), implying haptophytes and diatoms might induce different Fe isotopic effects during assimilation. However, further investigations such as culture experiments on biological fractionation by these two common Southern Ocean phytoplankton are required to support our speculation.

Although biological uptake is considered to be the main process controlling [dFe] in the surface of the ASP (Alderkamp et al., 2015; van Manen et al., 2022; this study), we do not exclude the idea that other processes may also influence surface dissolved δ^{56}Fe. If biological uptake was the dominant process fractionating dFe isotopes in the bloom under a closed system, the isotopic fractionation could be described with a Rayleigh fractionation factor. Previously, such a trend was observed and the fractionation factor (α) ($\alpha = R_{biomass}/R_{seawater}$) of biological uptake was predicted to range from 0.9977 to 0.9990 in Southern Ocean eddies (Ellwood et al., 2020) and in the Mertz Glacier Polynya (α=0.999, Sieber et al., 2021). In our δ^{56}Fe data, while the dFe systematics of the GIS diatom bloom can be described using a closed Rayleigh model with an α of between 0.9982 and 0.9990 (except Stn 24), the DIS haptophyte bloom cannot be described simply in this way (Fig. 3.8). This suggests that biological assimilation may be a dominant factor in the fractionation of dFe in the GIS bloom, but not in the DIS bloom. This disparity could imply that any biological fractionation in the DIS region is overprinted by other dFe sources (e.g., icebergs and ice shelves), rendering the assumption of a closed system less valid, or that uptake by haptophytes does not follow a simple Rayleigh trend. When comparing the two regions, both meteoric water input and higher refractory particulate Fe input were estimated to be higher in the DIS region (van Manen et al., 2022), potentially suppling more dFe with a lithogenic isotopic signature (~0‰) to the DIS bloom and buffering the isotopic composition of the remnant dFe pool (Fig. 3.5). Alternatively, other processes such as rapid recycling (e.g., adsorption

and regeneration), bacterial regeneration, and complexation with organic ligands may also play a role in fractionating Fe along with biological uptake (Ellwood et al., 2015; Sieber et al., 2021), resulting in a non-Rayleigh fractionation trend in the DIS bloom. Indeed, a combination of these factors was found to best explain surface data previously in Southern Ocean eddies by Ellwood et al. (2020). Overall, while our findings do provide support for uptake of light Fe and also for variable fractionation factors between species, our results suggest that the role of biogeochemical conditions (the interplay of biological uptake and other processes) in setting surface δ^{56}Fe are variable in the surface ASP and likely between Antarctic polynyas.

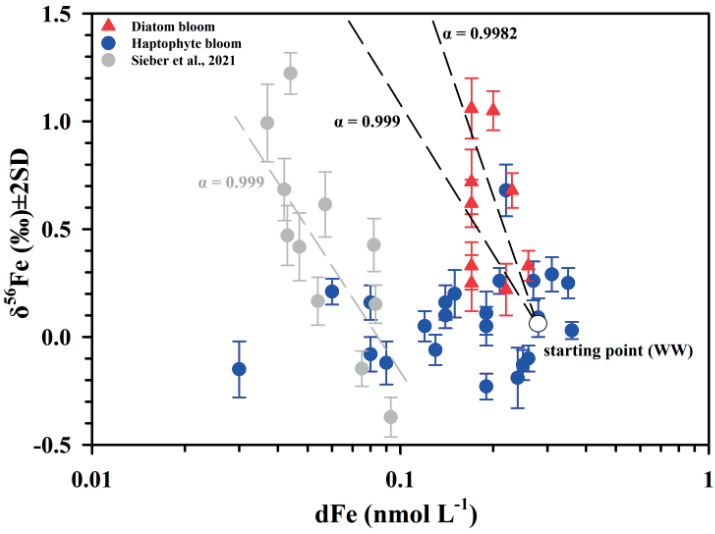

Figure 3.8 Fe isotope systematics in the surface layer of the GPpr12 'bloom' stations (red: GIS diatom bloom; blue: DIS haptophyte bloom), in comparison with data derived from Mertz glacier polynya (Sieber et al., 2021). The dashed lines represent predicted Rayleigh fractionation trends with different fractionation factors ($\alpha=R_{biomass}/R_{seawater}$) based on a defined starting point (empty white dot, observed [dFe] and δ^{56}Fe values in winter water).

3.5 Conclusions

In this study, we characterized Fe isotope systematics in one of the most productive Antarctic coastal polynyas (the ASP), focusing on external Fe sources, the change of [dFe] and δ^{56}Fe in the Dotson ice shelf system that experiences rapid melting due to the intrusion of mCDW, and Fe isotopic fractionation resulting from different phytoplankton blooms (summarized in Fig. 3.9). By utilizing the isotopic composition of Fe, we show that two sedimentary processes (RD and NRD) both supply dFe from benthic **sedimenzts** into overlying mCDW within the AS. Additionally, we show that while NRD is a more important process than RD for releasing dFe from benthic sediments into overlying waters in the AS (with 20-56% from NRD and 4-12% from RD), both are derived from sediment resuspension. While inflowing mCDW is enriched in dFe from sediments, the DIS itself does not appear to add any extra dFe, previously attributed to the mixing of the outflow with relatively Fe-poor shelf waters. From an Fe isotopic perspective, however, a concomitant observed change in δ^{56}Fe cannot be explained solely by conservative mixing with low [dFe] shelf water. Instead, we propose that [dFe] and δ^{56}Fe are affected by a combination of enhanced preservation and addition of lithogenic colloidal Fe(III) together with the differential loss of Fe^{2+} and complexation with Fe-binding ligands, driving δ^{56}Fe to heavier values in the outflow than the inflow. The phytoplankton bloom regions in the ASP displayed distinct Fe isotopic signatures in the surface layer where δ^{56}Fe is much heavier in the diatom (GIS) bloom compared to the haptophyte (DIS) bloom. Based on our field data, we speculate that haptophytes and diatoms may fractionate Fe differently or to different extent due to different uptake mechanisms for Fe, however, this requires further investigation, for example using culture experiments. Furthermore, we found that, even in productive surface waters, differences in dissolved δ^{56}Fe are not likely to be controlled by biological activity alone; external sources (e.g., particulate and dissolved Fe input from ice shelf melt) and various other biogeochemical processes such as adsorption and regeneration, and complexation with organic ligands also likely play a role.

Overall, our isotopic data provides insights about the external sources of Fe, the role of the DIS in regional Fe cycling, and potential biological fractionation effects within phytoplankton blooms. However, it is worth noting that the ASP is a complex and understudied system in terms of nutrient cycling, biological activity and mixing of different water masses. Therefore, any prediction about how ongoing rapid changes in Antarctic coastal regions (e.g., nutrient supply) will affect marine ecosystems (notably phytoplankton communities) remains challenging and speculative. For example, as ice shelf melting increases due to increased inflow of mCDW (Jacobs et al., 2011; Mankoff et al., 2012), more ice shelf-derived particles are expected in the water column, but in how far this affects the current dissolved-particulate balance is unknown. Hence, we do not have enough information to predict how Fe sources and sinks might change, nor what the net effect would be on dFe cycling in this region. Additionally, increasing CDW intrusion would also result in increasing supply of other bio-active metals, such as Zn, Cd, and Co since CDW is a major source of various metals to the ASP (Sherrell et al., 2015; Tian et al., 2023b; van Manen et al., 2022). As a result, the dominant species of phytoplankton blooms could experience several shifts in species composition over a longer bloom period as susceptibility to (co-)limitation (e.g., Fe and B_{12}, and the requirements for various metals differs between different species , Bertrand et al., 2007; Bertrand et al., 2015). However, we have little knowledge on how these shifts would affect the cycling of various bio-active metals or how the availability of bio-active metals influences community composition and the development of phytoplankton blooms in the ASP. Thus, while continued climate change will undoubtedly affect the biogeochemical cycling of trace metals in the ASP, sustained interdisciplinary investigations are required to better understand this system and predict the local and global consequences of changes in the ASP.

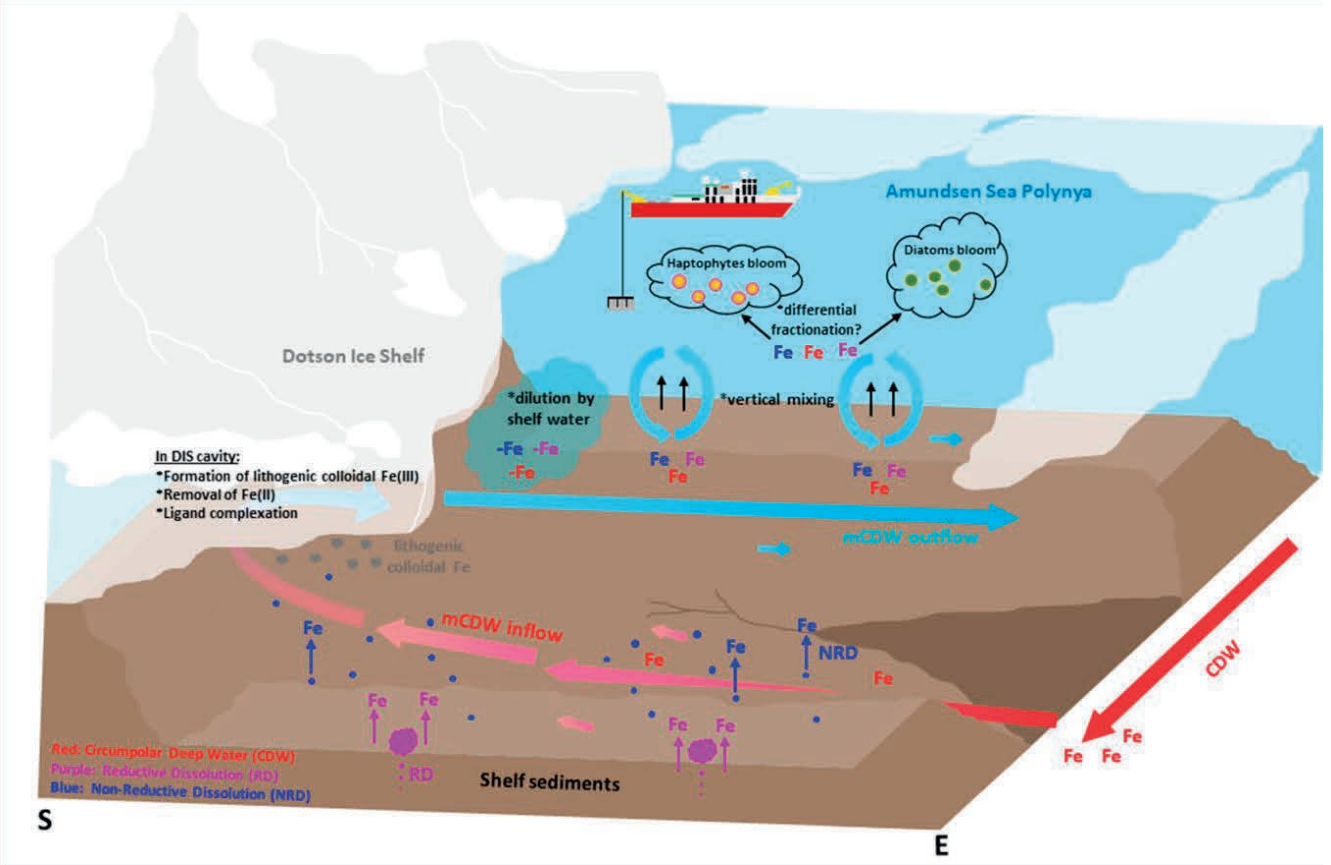

Figure 3.9 Conceptual summary of the sources and biogeochemical processes of dFe in the ASP.

CHAPTER 4

DISSOLVED ZINC AND CADMIUM ISOTOPIC SYSTEMATICS IN THE AMUNDSEN AND WEDDELL COASTAL ANTARCTIC MARGINAL SEAS

Hung-An Tian, Mathijs van Manen,
Gert-Jan Reichart, Tim M. Conway, Rob Middag

In preparation

Abstract

Coastal Antarctica is experiencing rapid environmental climate change with potential effects on regional marine trace metal biogeochemistry. This research investigates the biogeochemistry of two dissolved bioactive trace metals, zinc (dZn) and cadmium (dCd), and their isotopic ratios (δ^{66}Zn and δ^{114}Cd) in two coastal marginal seas with distinct oceanographic features – the Amundsen Sea (AS) the Weddell Sea (WS). In the AS, our isotopic data are consistent with previous studies indicating only a negligible addition of Zn and Cd from continental sediments and ice shelf meltwater. In the WS, δ^{66}Zn and δ^{114}Cd exhibited homogeneity in the waters across the Antarctic Peninsula shelf as well as through different deep-water masses. As a result, while Zn and Cd concentrations increase via physical mixing with deep water masses, isotope ratios remain unchanged. We observed apparent isotopic fractionation of Cd induced by biological uptake of Cd in the surface waters of both regions, with distinct Rayleigh uptake fractionation factors ($\alpha = R_{biomass}/R_{seawater}$) observed between haptophyte (0.99930 to 0.99960) and diatom (0.99970 to 0.99990) blooms. In contrast, surface δ^{66}Zn seem to be governed instead by a complex interplay of biological uptake and other factors such as ligand complexation and adsorption. Nevertheless, estimated α values for δ^{66}Zn in haptophyte (0.99995) and diatom (0.99980 to 0.99995) blooms are comparable to previously reported values in the Southern Ocean for biological uptake (0.99995±0.00001). At depths of 250-1500 m in the WS, significantly lower δ^{114}Cd was found in the inner gyre compared to the outer gyre, possibly related to regeneration of Cd and reduced water ventilation in the inner gyre. This pattern was not seen in δ^{66}Zn, and we postulate that the small difference falls within analytical uncertainty. This study not only highlights the role of Circumpolar Deep Water as a dominant source of Zn and Cd in the AS, and the importance of physical mixing to global dissolved Zn and Cd distribution during the formation of Antarctic Bottom Water in the WS, but also presented the first order observation of isotopic systematics of both bio-active metals in the surface water of two distinct coastal systems.

4.1. Introduction

Marine phytoplankton significantly impact global climate via photosynthesis and their role in the marine carbon cycle (Field et al., 1998; Martin et al., 1990). Besides essential macronutrients (phosphate, nitrate, and silicate), various 'micronutrients' are required in the metabolic processes of phytoplankton. For instance, zinc (Zn) is the second most abundant micronutrient in marine phytoplankton (Twining and Baines, 2013) and is necessary for metalloproteins like carbonic anhydrase and alkaline phosphatase, which are related to carbon fixation and phosphate acquisition, respectively (Morel et al., 1994; Shaked et al., 2006). Additionally, although Cd is generally considered toxic to organisms, multiple marine algae have evolved to utilize Cd as a substitute for Zn in carbonic anhydrase (e.g., Park et al., 2007; Price and Morel, 1990; Sunda and Huntsman, 1995). Consequently, Zn and Cd exhibit nutrient-type distributions similar to major macronutrients like silicate (Si) and phosphate (PO_4) throughout the oceans, with lower dissolved Zn and Cd concentrations ([dZn] and [dCd]) in the upper ocean due to biological uptake and increasing concentrations with increasing depth due to remineralization (Bruland, 1980) and advection of nutrient-rich deep water masses (Middag et al., 2019; Middag et al., 2018). Notably, the vertical profile of dZn is more closely correlated to Si, whereas dCd is more closely coupled to PO_4 (Bruland et al., 2014). These differences are thought to be driven by differences in the biogeochemical processes and physical controls on the coupling of these elements (Middag et al., 2019; Middag et al., 2018; Vance et al., 2017; Weber et al., 2018). Nevertheless, given their coupled characteristics, the cycling and distribution of Zn and Cd can provide insights into global macro nutrient cycling in the past and the future.

Over the past 15 years, measurements of oceanic dissolved Zn and Cd isotopic ratios ($\delta^{66}Zn$ and $\delta^{114}Cd$) have added to our understanding of the marine Zn and Cd biogeochemistry and their cycling (Conway et al., 2021; Horner et al., 2021; Schlitzer et al., 2018). The deep ocean is relatively homogenous for both isotope systems with values of +0.44±0.08‰ (mean±2 SD) for $\delta^{66}Zn$ (e.g., Bermin et al., 2006;

Conway and John, 2014b; Lemaitre et al., 2020; Sieber et al., 2020; Sieber et al., 2023a; Takano et al., 2017) and +0.25±0.06‰ for δ^{114}Cd (Abouchami et al., 2014; Conway and John, 2015; George et al., 2019; Xie et al., 2017). In the surface ocean, dissolved δ^{114}Cd is influenced by a biological preference for light Cd, as observed both in culturing experiments and field observations, leading to isotopic signatures as high as ~+1 to +5‰ in seawater (e.g., Abouchami et al., 2011; Conway and John, 2015; John and Conway, 2014; John et al., 2018; Lacan et al., 2006; Ripperger et al., 2007). Cadmium isotopic fractionation during biological uptake of Cd is especially influential in the Southern Ocean where nutrients are high in surface waters – the upwelling of upper Circumpolar Deep Water (UCDW) at the Antarctic Polar Front (APF) supplies nutrient-rich waters to the surface, facilitating phytoplankton growth and resulting in isotopically heavy dissolved Cd signatures in the surface (e.g., Antarctic Surface Water). Subsequently, subduction of this water forms northwards advecting Subantarctic Mode Water (SAMW) and Antarctic Intermediate Water (AAIW) by deep winter convection, carrying heavy Cd signatures further north into the subsurface of the Atlantic Ocean (Abouchami et al., 2014; Conway and John, 2015; Xie et al., 2017) and the Pacific Ocean (Sieber et al., 2019b; Sieber et al., 2023b). The imprint of these Antarctic processes on the δ^{114}Cd distribution of the lower latitudes oceans highlights the importance of the Southern Ocean as a driving force for the global Cd (and other nutrient-type element) distributions. While biological uptake and ocean circulation are a first order control on the distribution of δ^{114}Cd, other processes such as ligand complexation (Ratié et al., 2021) and shallow remineralization (Sieber et al., 2019b; Xue et al., 2013), as well as supply from external Cd sources (Cloquet et al., 2006; Lambelet et al., 2013; Schmitt et al., 2009; Sieber et al., 2023a; Yang et al., 2015) may also influence surface water dissolved δ^{114}Cd.

For Zn, the pattern is much less clear, with surface waters displaying a large range in δ^{66}Zn values (~–0.20 to ~+0.70‰), seemingly inconsistent with culturing experiments that suggested the preferential uptake of isotopically light Zn isotopes (John and Conway, 2014; John et al., 2007; Köbberich and Vance, 2017; Samanta et al.,

2018). This may also vary regionally, as surface Southern Ocean waters are generally similar to deep water values (Wang et al., 2019 Sieber et al., 2020; Wang et al., 2019; Zhao et al., 2014), while low-latitude waters show much more variability (Conway and John, 2014b, 2015; John et al., 2018; Lemaitre et al., 2020; Liao et al., 2020; Vance et al., 2019). As such, a range of processes have been invoked to explain the patterns of light or heavy Zn seen in surface waters. For example, Köbberich and Vance (2019) noted that the uptake of light Zn in culturing media might be obscured by complexation with organic chelators (e.g., EDTA), emphasizing the role of ligand complexation in Zn cycling and isotopic signatures in the surface ocean. Furthermore, a combination of field data and culturing experiments suggested that adsorption favours isotopically heavy Zn, highlighting reversible scavenging, as an essential factor to explain δ^{66}Zn systematics in lower latitudes surface oceans (John and Conway, 2014; Sieber et al., 2023b; Weber et al., 2018). Shallow remineralization may also play an important role in driving dissolved δ^{66}Zn isotopically light in the surface and subsurface (Bermin et al., 2006; Ellwood et al., 2020; Wang et al., 2019; Zhao et al., 2014). Thus, together with biological uptake, the interplay of all these processes leads to more complex surface δ^{66}Zn systematics (Horner et al., 2021; Sieber et al., 2023b).

The current study focusses on two different coastal Antarctic regions – the Amundsen Sea (AS) and the Weddell Sea (WS). In the AS, the intrusion of warm modified Circumpolar Deep Water (mCDW) onto the continental shelf through glacial troughs drives rapid ice sheet melting as it flows beneath ice shelves (Dutrieux et al., 2014; Gourmelen et al., 2017; Jacobs et al., 2012; Jacobs et al., 1996; Kim et al., 2021; Miles et al., 2016; Wåhlin et al., 2013). Outflowing mCDW emerging from under ice shelves can also accelerate sea ice melting, resulting in the formation of polynyas where highly productive and long-lasting austral spring-summer phytoplankton blooms are observed (Arrigo and van Dijken, 2003). Among all the Antarctic polynyas, the Amundsen Sea Polynya (ASP) exhibits the highest recorded rate of annual net primary production (per unit area) (Arrigo and van Dijken, 2003; Arrigo et al., 2012), likely due to additional dissolved Fe input from Fe-rich mCDW and particulate Fe input from

ice shelf melting (Gerringa et al., 2012, 2020b; Planquette et al., 2013; Sherrell et al., 2015; Tian et al., 2023a; van Manen et al., 2022). On the other side of the continent, the Weddell Sea (WS) is situated in the western part of the predominantly wind-driven cyclonic Weddell Gyre (WG) that plays a vital role in global oceanic circulation, as it is the primary source of global deep-water masses (Orsi et al., 1999, 2002). In the southern and western WS, extensive sea ice formation coupled with brine rejection in winter, results in the formation of dense, saline, and relatively cold shelf water that subsequently descends along the continental slope (Nicholls et al., 2009; Orsi et al., 2002). Ultimately the descending dense water exits the WS through the Scotia Sea, forming equatorward Antarctica Bottom Water (AABW) as it enters the lower part of the global ocean conveyor belt (Jullion et al., 2014; Orsi et al., 1999; Orsi et al., 2002; Vernet et al., 2019). Since about 50% of AABW is formed in the WS (Beckmann et al., 1999), the WS plays a critical role in global climate pathways and global thermohaline circulation (Fahrbach et al., 1994; Foldvik et al., 1985; Marinov et al., 2006), and potentially global nutrient cycling.

Given the diverse characteristics of the AS and the WS, as well as the biogeochemical functions of Zn and Cd, it is conceivable that both regions may exhibit spatial variability in the cycling and distribution of both metals, with potential impacts at the global scale. To date, compared to other Southern Ocean regions, there is a limited number of studies investigating Zn and Cd isotopic compositions in the AS and the WS. In the WS, within the framework of the International Polar Year (IPY 2007-2008) and the International GEOTRACES program, Zhao et al. (2014), and Abouchami et al. (2014) and Abouchami et al. (2011) presented vertical profiles of δ^{66}Zn and δ^{114}Cd, respectively, from a transect in the eastern WG along the Greenwich Meridian, while Xue et al. (2013) presented vertical profiles of δ^{114}Cd from two selected stations located in the western WG, adjacent to the tip of the Antarctic Peninsula. In contrast, no studies have investigated either δ^{66}Zn or δ^{114}Cd in the AS thus far. In this study, we present the first combined dataset of [dZn], [dCd], δ^{66}Zn, and δ^{114}Cd from transects in the AS (near Dotson Ice Shelf and Getz Ice Shelf) and the WS (from Antarctic Peninsula towards the central WG) to investigate the

sources, cycling, and biogeochemistry of Zn and Cd in coastal Antarctica.

4.2 Materials and methods

4.2.1 Shipboard sampling

Two GEOTRACES process studies (ID-expedition: GPpr12-ANA08B and GApr12-PS117) were conducted onboard the Korean icebreaker R/V Araon and German icebreaker R/V Polarstern during Austral Summer (December 2017 to February 2018 and December 2018 to February 2019), respectively. Dissolved and particulate Cd and Zn concentrations were previously published for GPpr12 by Tian et al. (2023b), dissolved Fe and Mn concentrations by van Manen et al. (2022), and dissolved Fe isotope ratios by Tian et al. (2023a). The sampling procedure for water samples on these cruises has been described previously (Tian et al., 2023a). The only notable difference in sampling between the two cruises is the filter used for sample collection; samples in the WS were collected through AcroPak-400 filters (VWR, precleaned with HCl and stored in MQ before used), whereas in the AS Sartobran-300 filters (Sartorius, only rinsed with MQ) were used. Just prior to use, all filters were rinsed with sample seawater, as were the used sampling containers.

For the ANA08B expedition, filtered seawater samples (4 L and 1 L, 4 L for near surface samples) were collected in the AS (71-74ºS, 112-128ºW) from two transects – the Dotson Ice Shelf (DIS) transect (10 stations, Stns 53, 52, 50, 49, 48, 45, 42, 36, 34, and 33) that follows the pathway of mCDW inflow towards and outflow emitted from the DIS, and the Gets Ice Shelf (GIS) transect (3 stations, Stns 55, 24, 57) that follows the mCDW inflow. These transects are referred to as the DIS transect and the GIS transect in this study, respectively (Fig. 4.1). Here, and in another publication emerging from this expeditions data set (Tian et al., 2023b), we group stations by geographical location – the open ocean station (Stn 53), the off-shelf station (Stn 55), the shelf break stations (Stns 52 and 24), the mCDW inflow stations (Stns 50, 49, 48, 45, 42), and the mCDW outflow stations (Stns 36, 34, 33) (Fig.

4.1). For the PS117 expedition, seawater samples (4 L and 1 L) were collected from a transect in the western WS (63-66ºS, 36-54ºW, referred to as the WS transect in this study) (Fig. 4.1) in which 12 stations are grouped into the shelf stations (Stns 95, 93, and 91), the continental shelf slope stations (Stns 82, 85, 75, 73, 70, and 67), and the off-shore stations (Stns 65, 61, and 56) (Fig. 4.1).

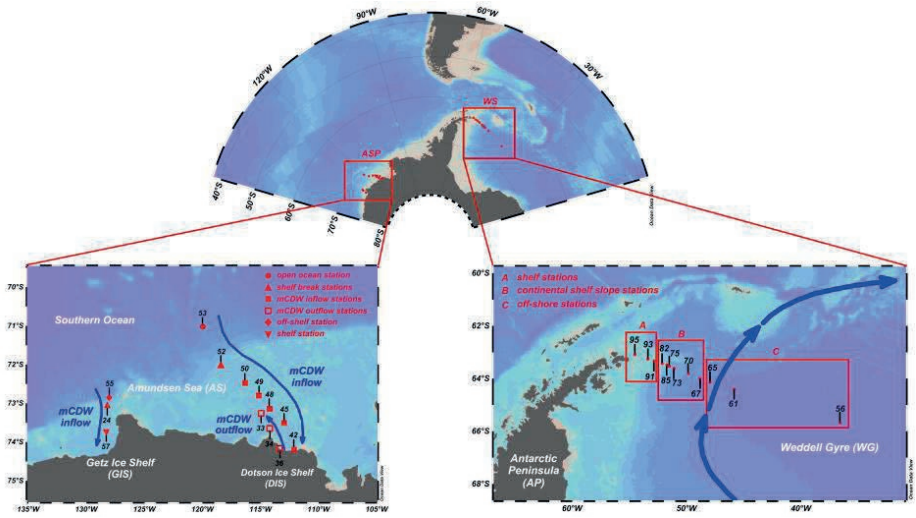

Figure 4.1 Sampling stations of expedition ANA08B (the Amundsen Sea) and PS117 (the Weddell Sea). Samples were collected during Austral Summer (December 2017 to February 2018 and December 2018 to February 2019), respectively. Expedition ANA08B comprised two transects – the DIS transect (Stns 53, 52, 50, 49, 48, 45, 42, 36, 34, and 33) and the GIS transect (Stns 55, 24, and 57), whereas expedition PS117consist of one transect – the WS transect (Stns 95, 93, 91, 82, 85, 75, 73, 70, 67, 65, 61, and 56).

4.2.2 Sample processing for isotopic analysis

All seawater samples were acidified shipboard to pH ~1.8 with 0.024 M HCl in an ISO class 5 laminar flow hood as described for the concentration samples (Tian et al., 2023b; van Manen et al., 2022). Thereafter, samples were transported to the clean room (ISO class 7, ISO class 5 in working hoods) at the Royal Netherlands Institute (NIOZ), where all further processing was done. All water used was

ultrapure water (MQ, <18.2 MΩ cm^{-1}) and all reagents were of ultrapure quality (Tian et al., 2023a; Tian et al., 2023b).

4.2.2.1 Pretreatment (extraction and purification)

Extraction and purification procedures used in this study (see Table 3.1, Chapter 3) were modified from Conway et al. (2013) and Sieber et al. (2019a), and have been described in detail by Tian et al. (2023a). Prior to processing natural samples, a series of tests (procedural blank and recovery) were conducted to validate the modified method for Zn and Cd isotopic analysis.

4.2.2.2 Procedural blank and recovery

The procedural blank for the methods was tested by processing acidified MQ (pH ~1.8 with 0.024 M HCl) through either extraction or purification portions of the method. For Zn, extraction and purification blanks are 0.08±0.07 ng (n=12) and 0.12±0.10 ng (n=6), respectively, whereas for Cd the blanks are 0.012±0.001 ng (n=12) and 0.0030±0.0021 ng (n=6), respectively. Such low combined blank values (0.2 ng for Zn and 0.009 ng for Cd) are several orders of magnitude lower than natural concentrations of dissolved samples in this study. To test the efficiency of the extraction method, multiple AAS single element standards (LabKings, AA grade) together with a lutetium (Lu) – indium (In) spike (internal standard) were added to both acidified metal-free seawater (pre-cleaned by Nobias PA1 resin) with varying dissolved concentrations in a range of natural concentrations in seawater (Middag et al., 2015). Seawater with standard added was then processed using the extraction procedure and measured by Inductively Coupled Plasma Mass Spectrometry (ICP-MS) on a Thermo Scientific Sector Field High Resolution Element 2 at NIOZ, whereas a suit of 3M HNO_3 with the same standard added for metal-free seawater (but with higher metal concentrations) were directly measured for dissolved concentrations by ICP-MS. Following Middag et al. (2015), the recovery of extraction was calculated using the seawater and HNO_3 calibration lines after normalisation to the

internal standards – the recovery for Zn and Cd was ~105% and ~98%, respectively. To test the purification procedure, a 7 M HCl solution with added metal (Ca, Ni, Pb, Co, Cu, Fe, Mo, Zn, Cd) in the expected concentration range for extracted samples, was put through the purification procedure for which the elution profile is shown in Fig. 4.2 and the overall recovery for Zn and Cd was ~98% and ~90%, respectively.

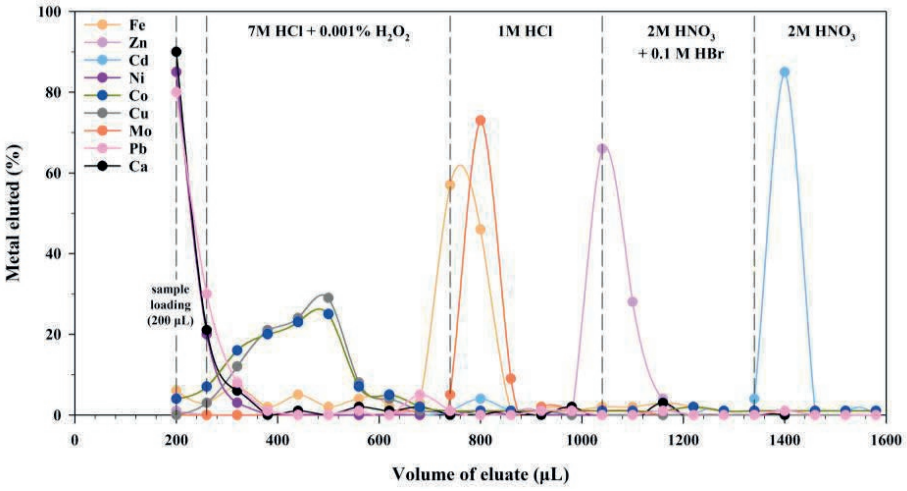

Figure 4.2 Elution profile and recovery of the purification procedure modified from Conway et al., 2013 (detailed in Table 3.1, Chapter 3). Test sample was prepared by spiking single element standards with post-extraction concentrations after pre-concentration (factor of ~20000, i.e., 4 L samples concentrated in 200 μL^{-1}) based on natural concentrations (~4 L, Fe: 0.5, Zn: 1, Cd: 0.8, Cu: 2, Cr: 3, Ni: 9, Pb: 0.04, Mo: 100 nmol L^{-1}) in 200 µL 7 M HCl. To test the recovery, a subsample of mimic sample was diluted and measured on an Element 2 ICPMS at NIOZ (referred to as initial sample). Subsequently, subsamples (eluate, every 60 µL) was collected during purification, and diluted and measured on an Element 2 ICPMS. The recovery was then calculated based on individual eluate relative to initial sample, taking the dilution factors into account.

4.2.2.3 Antarctic seawater samples

Filtered seawater samples (4 L and 1 L) were spiked with ^{64}Zn-^{67}Zn and ^{111}Cd-^{113}Cd double-spike with a sample-to-spike ratio of 1:1 (Sieber et al., 2019a, 2020), at least 48 hours prior to further treatment, guided by dissolved concentrations measured independently by a SeaFAST system and ICP-MS as reported previously (Tian et al., 2023b; van Manen et al., 2022). Samples were then processed using the method shown in Table 3.1, Chapter 3.

4.2.3 Double spike preparation and analysis with Multi-Collector ICPMS (MC-ICPMS)

Zn and Cd isotope analysis was carried out using a double-spike technique on a Thermo Neptune Plus Multi-collector ICPMS (MC-ICPMS) at NIOZ (Siebert et al., 2001). Double spike solutions (^{64}Zn-^{67}Zn and ^{111}Cd-^{113}Cd) were prepared separately from single spikes – ^{64}Zn (0.9910%), ^{67}Zn (0.8960%), ^{111}Cd (0.9590%), and ^{113}Cd (0.9330%) purchased from Isoflex USA. Single spikes were dissolved separately in 7 M HNO_3 and diluted with MQ. The single spikes were mixed with approximate ratios of 60:40 and 62:38 for ^{64}Zn-^{67}Zn and ^{111}Cd-^{113}Cd, respectively to match the optimal double spike ratios previously described for Zn (Bermin et al., 2006) and for Cd (Sieber et al., 2019a; Xue et al., 2012).

The prepared double-spikes were then purified from impurities using a scaled-up version of column purification used for samples as shown in Table 3.1 (Chapter 3, also described in Tian et al., 2023a). After purification, pure double-spikes and pure primary standards (IRMM-3702 for Zn and NIST-3108 for Cd) together with a suite of mixtures of spike – primary standard (with mixing ratios from 1:10 to 10:1), were used to calibrate the isotopic compositions of double-spikes (Siebert et al., 2001). The calibrated isotopic compositions for ^{64}Zn-^{67}Zn double-spike are $^{66}Zn/^{64}Zn$=0.03028; $^{67}Zn/^{64}Zn$=0.58562; $^{68}Zn/^{64}Zn$=0.03376; whereas for ^{111}Cd-^{113}Cd double spike are $^{112}Cd/^{111}Cd$=0.03726; $^{113}Cd/^{111}Cd$=0.57566; $^{114}Cd/^{111}Cd$=0.01347. The concentrations of double-spike were determined using reverse

isotope dilution against AAS single element (Zn and Cd) standards (LabKings, AA grade).

The details of the instrumental settings, including introduction system, cones, and cup configuration are described in Table 4.1. Here, we express Zn and Cd isotope ratios in typical delta notations relative to their commonly accepted zero standards for Zn (JMC-Lyon) and Cd (NIST-3108) respectively:

$$\delta^{66}Zn\ (‰) = \left[\frac{(^{66}Zn/^{64}Zn)_{sample}}{(^{66}Zn/^{64}Zn)_{JMC-Lyon}} - 1\right] \times 1000$$

and

$$\delta^{114}Cd\ (‰) = \left[\frac{(^{114}Cd/^{110}Cd)_{sample}}{(^{114}Cd/^{110}Cd)_{NIST-3108}} - 1\right] \times 1000$$

Table 4.1 Instrumental settings for Zn and Cd isotopic analysis on Thermo Neptune Plus Multi-Collector ICPMS at NIOZ.

Faraday cup configuration	L4	L2	L1	C	H1	H2	H3
For δ^{66}Zn (low resolution)	^{62}Ni	^{64}Zn	^{65}Cu	^{66}Zn	^{67}Zn	^{68}Zn	^{70}Zn
For δ^{114}Cd (low resolution)	^{110}Cd	^{111}Cd	^{112}Cd	^{113}Cd	^{114}Cd	^{115}In	^{116}Cd
Introduction system: Apex-Omega (ESI)							
Sampler cone: H (Thermo Scientific)							
Skimmer cone: H (Thermo Scientific)							

However, since the JMC-Lyon standard has nearly run out, we use IRMM-3702 as a primary standard, and convert $\delta^{66}Zn_{IRMM-3702}$ to $\delta^{66}Zn_{JMC-Lyon}$ by +0.29‰ (Archer et al., 2017; Moeller et al., 2012). As such, all δ^{66}Zn results reported in this study are relative to $\delta^{66}Zn_{JMC-Lyon}$.

Accuracy and external precision of MC-ICPMS analysis for $\delta^{66}Zn$ and $\delta^{114}Cd$ was assessed using the long-term delta value and precision of secondary isotope standards. For Zn, this was AA ETH (obtained from ETH Zürich) and for Cd this was BAM-I012 (purchased from BAM Federal Institute for Materials Research and Testing). Our long-term values were $\delta^{66}Zn$ of +0.27±0.04‰ and $\delta^{114}Cd$ of –1.33±0.05‰ (mean±2 SD, n=71, 15 analytical sessions for Zn and n= 66, 14 analytical sessions for Cd) for AA ETH and BAM I012 respectively; both values agree well with previously reported values (summarized in Fig. 4.3). Consequently, we consider 0.04‰ and 0.05‰ to be conservative estimates of uncertainty for $\delta^{66}Zn$ and $\delta^{114}Cd$, respectively, and apply these to all samples, except for those with 2 SE of an individual analysis larger than those values, in which case we use 2 SE as a measure of uncertainty (following Sieber et al., 2019a).

The accuracy of the modified extraction and purification procedure was also tested by doping the same secondary standards into either metal-free seawater or acidified MQ (pH ~1.8 with 0.024 M HCl) that was processed as a sample and measured alongside natural samples. The average $\delta^{66}Zn$ and $\delta^{114}Cd$ obtained from these tests were +0.26±0.05‰ (n=4, 2 for seawater, 2 for MQ) and –1.32±0.01‰ (n=4, 2 for seawater, 2 for MQ), respectively, in agreement with the expected values (Fig. 4.3). As a test of the accuracy of the dissolved concentration measurements, concentrations derived from the isotope dilution technique using Neptune ICPMS agree well with concentrations obtained from the SeaFAST-based measurements on the Element 2 ICPMS (slopes: 0.9982 and 0.9992 for Zn and Cd, respectively, Fig. 4.4). In this study, since there is good agreement between the two methods for dZn and dCd for most samples, we use the mean dissolved concentrations calculated for each sample in the discussion.

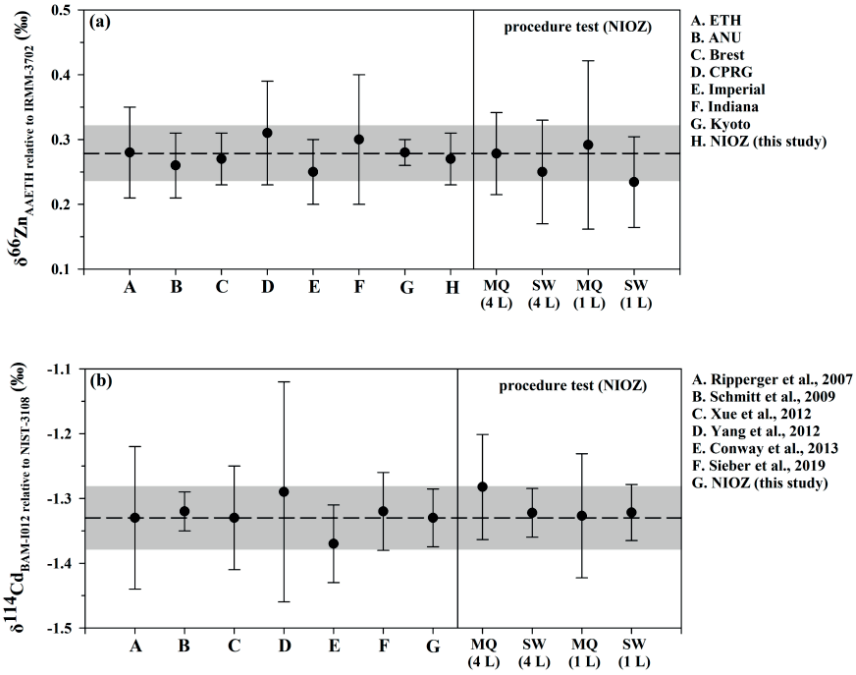

Figure 4.3 Procedural test of extraction and purification for (a) Zn and (b) Cd isotopic analysis and comparison with reported values. For the procedural test, a secondary isotope standard (Zn: AAETH; Cd: BAM-I12) was spiked in metal-free seawater (Zn: ~0.08 nmol L^{-1}, Cd: ~0.003 nmol L^{-1}, per-extracted by Nobais PA1 following the same extraction steps) and acidified MQ, both in 4 L (n=1) and 1 L (n=2), processed by the extraction and purification procedure (Table 1). Averages of all the samples mentioned above are calculated as a whole for both $\delta^{66}Zn$ and $\delta^{114}Cd$ values reported. For the comparison of $\delta^{66}Zn$ values obtained for AAETH, previous reported values are compiled from an inter-comparison study by Archer et al., (2017), whereas for $\delta^{114}Cd$ values of BAM-I012 are compiled from individual studies. The black dashed line and grey shading represent the means and 2 standard deviation (SD), respectively, of previously reported values (i.e., A-G). All error bars reported here (including the values for this study) are 2 SD.

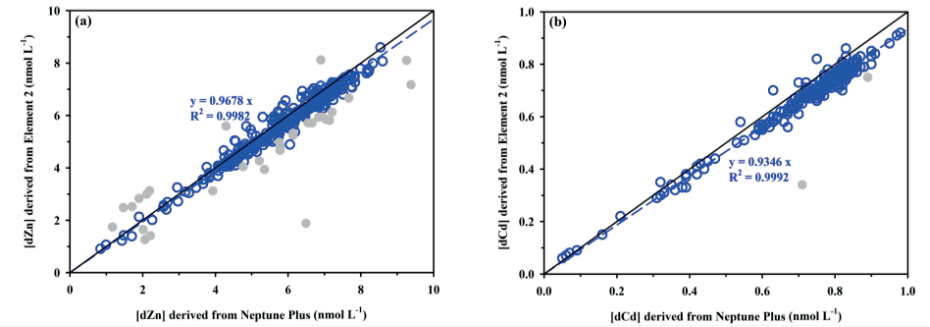

Figure 4.4 Linear regression of dissolved metal concentrations derived from ICPMS (Element 2) versus concentrations derived from ICPMS (Neptune Plus) for (a) [dZn] and (b) [dCd]. The blue-dashed line and the black solid line represents the regression line and 1:1 line. Note that the intercept of regression is set to 0. Dissolved metal concentrations used in this study are means of two measurements. However, for samples that showed a large absolute difference of concentrations between two measurements – namely, the absolute difference is larger than 0.2 nmol L^{-1} plus 10% of Element 2-derived [dZn] or larger than 0.05 nmol L^{-1} plus 10% of Element 2-derived [dCd] – [dZn] and [dCd] are selected based on oceanic consistency; these data is highlighted in grey. If only the Element 2-derived concentration was selected (i.e., the Neptune Plus-derived concentration was excluded), the isotopic value was also not included in this study. In contrast, if only Neptune Plus-derived concentration was selected (i.e., Element 2-derived concentration was excluded), the isotopic composition was included.

4.2.4 Auxiliary parameters, macronutrients, and oxygen isotopic composition ($\delta^{18}O$)

4.2.4.1 Auxiliary parameters (salinity, temperature, depth) and fluorescence calibration

A calibrated CTD (Seabird SBE 911+) with auxiliary sensors was mounted on the Titan sampling system to measure salinity (conductivity), temperature, depth (pressure), and fluorescence. The CTD-derived fluorescence was subsequently calibrated by measured total chlorophyll a concentrations. Briefly, particulate samples for pigment-based phytoplankton taxonomic composition were collected through a GF/F glass fiber filter (45 mm diameter; Whatman, Cytiva, Marlborough, USA) at 1 ˚C, using a vacuum pump (200 mbar; Pal, Port

Washington, NY, USA). Filters were double-wrapped in aluminium foil, snap-frozen in liquid nitrogen and stored at –80 ˚C. Further, filters were freeze dried and pigments were dissolved in acetone (van Leeuwe et al., 2006), and measured on High-performance liquid chromatography (HPLC). The detailed procedure of this analysis is described in van Manen et al. (2022). The correlation between CTD-derived fluorescence and measured total chlorophyll a concentrations is used to derive calibrated total chlorophyll a concentrations ([chl a]):

ANA08B: [chl a] ($\mu g\ L^{-1}$)=0.9584×fluorescence (arb);

PS117: [chl a] ($\mu g\ L^{-1}$)=0.7735×fluorescence (arb)

4.2.4.2 Macronutrients (PO_4 and $Si(OH)_4$)

Nutrient data for the ANA08B expedition were published by Tian et al. (2023b). For the PS117 expedition, unfiltered seawater samples (~50 mL) were collected for inorganic nutrient analysis, including phosphorus (PO_4) and silicic acid ($Si(OH)_4$). In the NIOZ shipboard analytical container, the nutrient samples were transferred into 5 ml polyethylene vials (ponyvials) after rinsing three times with the sample before being capped and stored in the refrigerator at 4°C. Prior to analysis, all samples and standards were brought to room temperature (~21-21.5°C) within two hours in a dark drawer. The caps were then removed and the ponyvials covered with parafilm against evaporation and placed in the sampler. Subsequently, these nutrients were analysed on a Bran and Luebbe trAAcs 800 Autoanalyzer. All analyses were generally made within four to five hours after sampling. A detailed protocol has been described in Gerringa et al. (2019). The accuracy and precision for the PO_4 and $Si(OH)_4$ measurements were determined by measuring a natural sterilized reference material nutrient sample (CA, Kanso, Japan) at 21.5 °C for which values of 1.458±0.008 and 36.899±0.172 $\mu mol\ L^{-1}$, respectively (n=196).

4.2.4.3 Oxygen isotopic composition ($\delta^{18}O$)

Oxygen isotope analysis of ANA08B expedition was published in Tian et al. (2023b). For the PS117 expedition, dissolved seawater samples for $\delta^{18}O$ were collected in 2 mL glass vials with polypropylene caps and polypropylene-coated inserts. The glass vial was then stored in refrigerators at 4°C until analysis. The $\delta^{18}O$ samples were measured using Liquid Water Isotope Analyzer (LWIA) (Los Gatos Research) at NIOZ. The precision of the analysis was estimated to be 0.16‰ (n=13) based on duplicated measurements of in-house standard (North Sea seawater-2018) over 13 analytical sessions. The stable oxygen isotope ratio in this study is expressed as $\delta^{18}O$ with respect to Vienna Standard Mean Ocean Water (VSMOW, International Atomic Energy Agency).

4.2.5 Phytoplankton pigment composition analysis

Samples were taken for pigment-based phytoplankton taxonomic composition analysis at one depth in the upper few tens of meters at selected stations in the AS (Stns 33, 34, 36, 42, 45, 49, 55, 24 and 57), whereas in the WS samples were taken at every station. The details of taxonomic composition analysis are described in Tian et al. (2023b).

4.3 Results

4.3.1 Oceanographic setting

In the AS, three main water masses are characterised – mCDW, Winter Water (WW), and Antarctic surface water (AASW) based on potential temperature (referred to as θ hereafter) and salinity (referred to as S hereafter) (Fig. 4.5a), as previously defined (e.g., Randall-Goodwin. et al., 2015). Following the intrusion to the AS, mCDW at the least modified sites (below 200-400 m at the open ocean station and the off-shelf station) is characterized by θ of >1°C and S of >34.5 (Figs 4.5a, 4.5b, and 4.5c). As the inflowing mCDW (~200 m above the mCDW inflow stations) moves towards the DIS, θ and S gradually decrease and reach ~–0.2°C and 34.3, respectively, due to mixing with overlying waters, before flowing underneath the DIS (Fig. 4.5a). The outflowing

mCDW emitted from the DIS (below 200 m at Stn 36, Tian et al., 2023b) exhibits an even lower θ (~–0.2 to –0.85°C) and S (~34.1) (Fig. 4.5a). As a remnant of waters formed via sea ice formation and brine rejection in winter, WW is generally situated between AASW and mCDW with a θ minimum as low as –1.8°C and S between 34 and 34.2 (Figs 4.5a, 4.5b, and 4.5c). Within the surface and ~70 m (Stns 50, 49, 48, 45, 34, and 33), due to enhanced irradiation and melting of sea ice, AASW exhibits elevated θ (>1.8°C) and decreases S (<34) relative to WW along the DIS transect, whereas AASW along the GIS transect was located over a shallower depth interval (~25 m).

In the WS, five water masses – AASW (θ>–1.7°C; S< 34.3), WW (θ minimum below AASW), Warm Deep Water (WDW, 0>θ>0.8°C, 34.64<S<34.72), Weddell Sea Deep Water (WSDW, –0.7°C<θ<0°C, 34.64<S< 34.68) and a precursor of Weddell Sea Bottom Water (pre-WSBW, θ<–0.7°C at depth) – are identified (Fig. 4.5a) (e.g., Fahrbach et al., 2004; Klatt et al., 2005). AASW and WW are situated in the upper ~70 m and upper ~70-250 m, respectively. In the eastern WS, CDW travels through the Antarctic Circumpolar Current (ACC) at mid-depth and enters the WG at its eastern edge following the gyre circulation (e.g., Donnelly et al., 2017; Reeve et al., 2016), resulting in WDW (situated at 230-1800 m) via mixing of CDW and other WS water masses (AASW and WW). Subsequently, mixing of WDW and uplifting WSBW generates WSDW at >1500 m (Fig. 4.5c) (Foster and Carmack, 1976). In the western WS, dense and saline shelf water forms via surface cooling and brine rejection on the continental shelf of the Antarctic Peninsula (i.e., the shelf stations) in winter. During summer (sampling period of GApr12-PS117), waters on the continental shelf stratify due to elevated temperature near the surface (AASW) (Figs 4.5a and 4.5d). For clarity, the term “dense shelf water” refers to the dense and cold water formed in winter (this process is not observed during sampling in summer), whereas the term “WS shelf water” refers to the shelf water observed at the shelf stations (deeper than AASW) in this study. Subsequently, dense shelf water descends and interacts with multiple water masses (WDW and WSDW) along the slope and eventually forms WSBW (Foster and Carmack, 1976; Vernet et al., 2019), therefore, we characterise this descending water mass

(also observed in summer) as the precursor of WSBW (pre-WSBW, θ<–0.7°C, 150-200 m above the continental shelf slope sediments, Figs 4.5a and 4.5d) in this study. Ultimately, the mixture of pre-WSBW, WDW, and WSDW in the southern and western WS leaves the WS at north-western site, becoming a main source of global deep waters (i.e., AABW) (Orsi et al., 1999). It should be noted that WSBW is usually situated deeper than 4000 m in this region (Middag et al., 2013), which it is not observed in this study since most stations were located closer to the Antarctic Peninsula with shallower depths (Fig. 4.5d).

4.3.2 Weighted average of chlorophyll a concentration ([chl a] $_{wt.avg}$)

The calibrated chlorophyll a concentration ([chl a]) increases from the surface to ~70 m and ~90 m where the maximum was observed, in the AS and the WS, respectively. In this study, we define this layer (from the surface to the depth of [chl a] maximum) as the surface layer. Further, to represent the productivity in the surface layer, we calculated the weighted average of [chl a] ([chl a]$_{wt.avg}$) based on the samples located in the surface layer (Fig 4.6a). Generally, [chl a]$_{wt.avg}$ is much higher in the AS (3.48±2.89 µg L^{-1}) than in the WS (0.13±0.09 µg L^{-1}). In the ASP, most stations exhibit [chl a]$_{wt.avg}$ >2 µg L^{-1}, except the open ocean station and the shelf break station (i.e., Stn 52). Therefore, for the discussion of biological activity, we refer the stations with [chl a]$_{wt.avg}$ >2 µg L^{-1} as bloom stations including the DIS bloom stations (Stns 50, 49, 48, 45, 42, 36, 34, and 33) and GIS bloom stations (Stns 55, 24, 57), whereas the stations with homogeneously low [chl a]$_{wt.avg}$ in the WS are simply referred to as the WS stations (Fig. 4.6a).

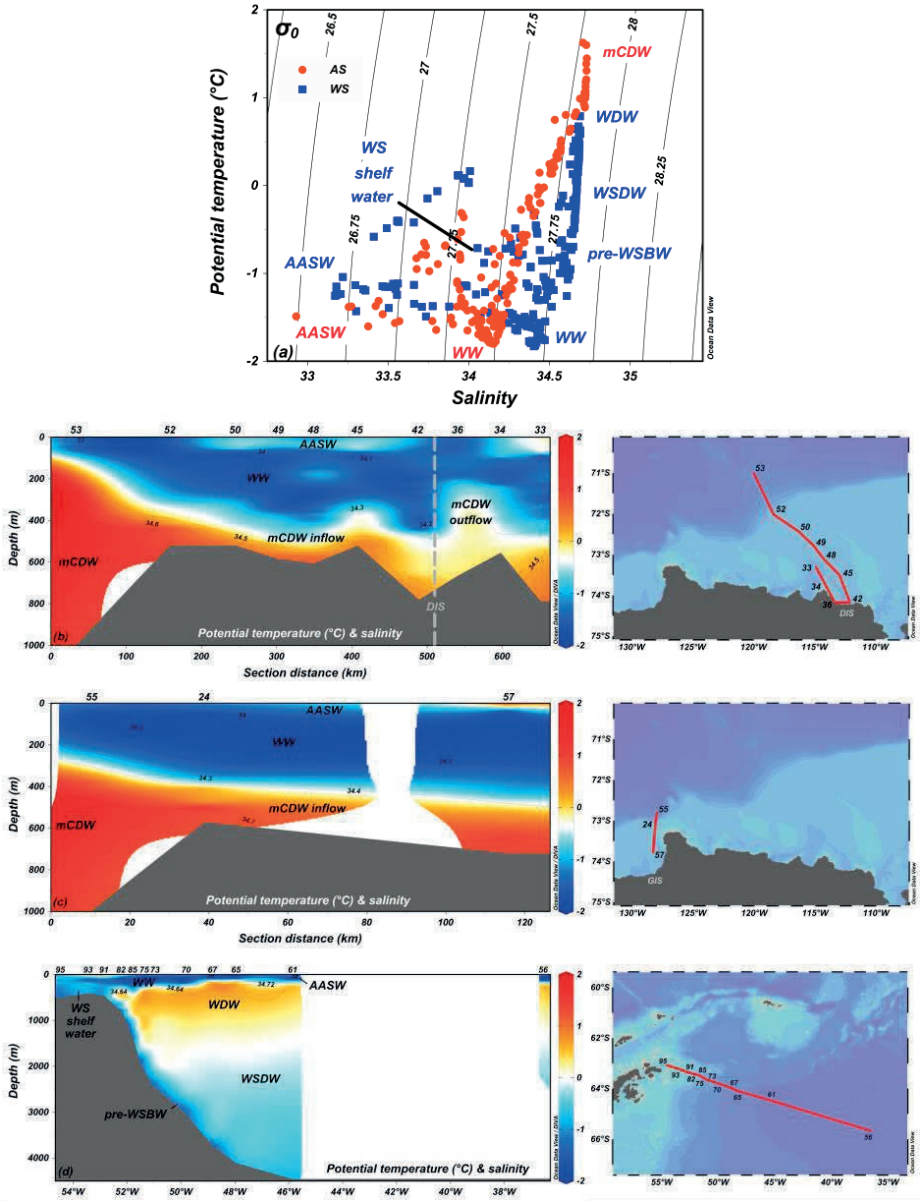

Figure 4.5 (a) Potential temperature (θ)-salinity (S) diagram of all ANA08B (the Amundsen Sea) and PS117 (the Weddell Sea) stations, and section profiles of θ and S of (b) the Dotson Ice Shelf (DIS) transect, (c) the Getz Ice Shelf (GIS) transect, and (d) the WS transect. The color grading and density isocline in (b) to (d) represent θ and S, respectively.

4.3.3 Phytoplankton community composition

In the AS, the phytoplankton community composition along the DIS transect was dominated by haptophytes (59% to almost 100%) with highest contributions at Stn 45 and Stn 49 (99.98 and 99.36%, respectively), whereas the Getz stations were dominated by diatoms (54-91%), especially at Stn 55 (91.3%) and Stn 24 (87.9%) (Tian et al., 2023b, Fig. 4.6b). In contrast, along the WS transect, the phytoplankton community composition was not dominated by either species – dinoflagellates, cryptophytes, chlorophytes, and pelagophytes also accounted for up to ~21% to ~59% (Fig. 4.6b).

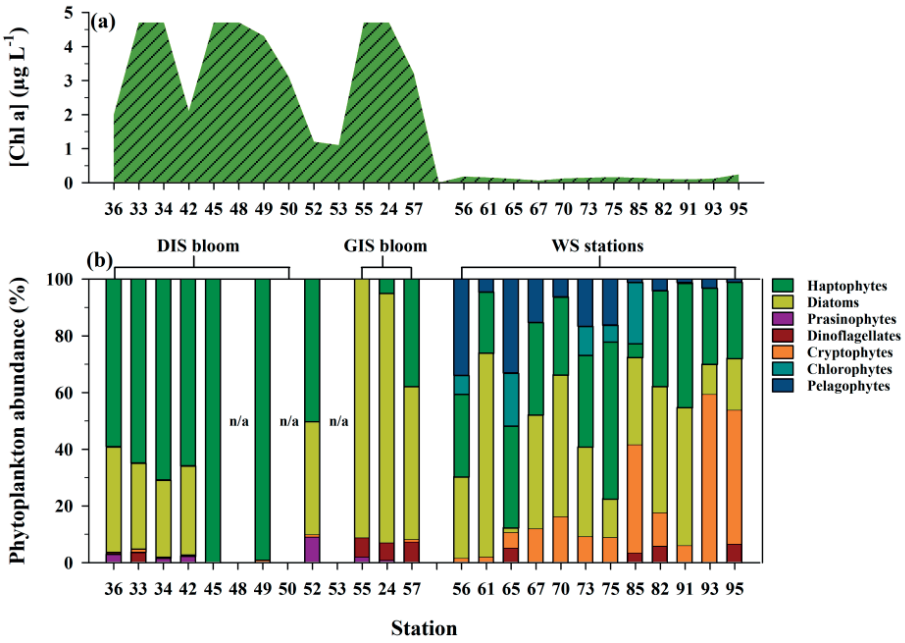

Figure 4.6 (a) Weighted average of [chl a] ([chl a]$_{wt.avg}$) and (b) phytoplankton community composition of all (the Amundsen Sea) and PS117 (the Weddell Sea) stations. [chl a]$_{wt.avg}$ is calculated based on depths within the surface layer.

4.3.4 Freshwater input ($\delta^{18}O$)

In this study, we use $\delta^{18}O$ to estimate freshwater input which includes sea-ice melt and meteoric water (e.g., ice sheet melt or iceberg melt). Previously, the fraction of sea-ice melt and meteoric water were estimated for the AS (Tian et al., 2023b), using a three-component mass balance model as described in Randall-Goodwin. et al. (2015) . Since the WS shelf stations are located near Antarctic Peninsula where large ice shelves are situated (e.g., Larsen Ice shelf, Nicholls et al., 2009), meltwater from the ice shelf may have biogeochemical impacts on these shelf stations. Here, we modified the mass balance model used in Tian et al. (2023b) to estimate the fraction of meteoric water in the WS shelf region:

$$f_{met} + f_{sim} + f_{ww} = 1 \ldots \text{(Eq. 1)}$$

$$f_{met} \times \delta^{18}O_{met} + f_{sim} \times \delta^{18}O_{sim} + f_{ww} \times \delta^{18}O_{ww} = \delta^{18}O_{observed} \ldots \text{(Eq. 2)}$$

$$f_{met} \times S_{met} + f_{sim} \times S_{sim} + f_{ww} \times S_{ww} = S_{observed} \ldots \text{(Eq. 3)}$$

Where sim, met, ww, and $observed$, denote sea ice melt, meteoric water, WW, and observed values, respectively, and f and S represent fraction and salinity, respectively. The rationale for designating WW as the ocean endmember is because WW, as the remnant water mass from winter, can best represent the initial water prior to mixing with ice shelf meltwater. To derive f_{met}, S and $\delta^{18}O$ of sea ice melt, meteoric water, and WW need to be constrained. Previously, Brown et al. (2014) used a four-components mixing model – fraction, salinity, $\delta^{18}O$ and a fourth tracer PO' that is derived from dissolved oxygen and PO_4 concentrations– to estimate f_{met} in the WS (2.5-3% in upper 100 m close to the tip of Antarctic Peninsula). However, due to a malfunctioning of the oxygen sensor on the Titan system, oxygen is not available and so we can only use a three-component mass balance model. Following the rationale of endmember choice described in

Brown et al. (2014), we assign 0, –18‰, 5, and 1.8‰ for S_{met}, $\delta^{18}O_{met}$, S_{sim}, and $\delta^{18}O_{sim}$, respectively. Using these endmembers, the estimated f_{met} in the upper 250 m at the shelf stations ranged from 0.3% to 4.8%, in agreement with estimates by Brown et al. (2014), where the highest f_{met} estimates were found close to the shore (i.e., Stn 95) with lower values towards offshore (i.e., Stn 91) (Fig. 4.7).

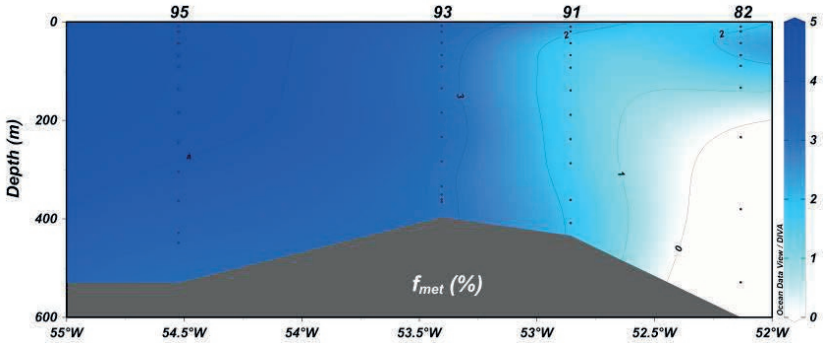

Figure 4.7 Estimated fraction of meteoric water (f_{met}) of the shelf stations along the WS transect.

4

4.3.5 Dissolved Zn and Cd concentrations and isotopic compositions

4.3.5.1 The AS

The dissolved Zn and Cd concentrations ([dZn] and [dCd]) for the AS from this cruise were previously described in depth by Tian et al. (2023b). As such, we just provide a simple overview here and focus more strongly on the isotope ratios. In the AS, [dZn] and [dCd] ranged from 0.87 to 7.67 nmol L^{-1} and from 0.05 to 0.87 nmol L^{-1}, respectively (Fig. 4.8). The lower end of this range was generally observed in the surface layer of the bloom stations whereas concentrations were higher in surface waters at non-bloom stations (i.e., Stns 53 and 52), except for two bloom stations near the DIS (i.e., Stns 42 and 36); [dZn] and [dCd] in the surface layer of the GIS bloom stations (0.87 to 5.47

nmol L^{-1} and 0.05 to 0.71 nmol L^{-1}, respectively) were lower than at DIS bloom stations (1.33 to 6.80 nmol L^{-1} and 0.30 to 0.77 nmol L^{-1}, respectively) (Fig. 4.8). Generally, both [dZn] and [dCd] increased with increasing with depth – highest [dZn] (>7 nmol L^{-1}) and [dCd] (>0.8 nmol L^{-1}) were observed close to the seafloor of the continental shelf (where the mCDW inflow was observed) and in the deep waters of the open ocean and off-shelf station where the least modified CDW was located (based on higher T at these stations relative to the other stations) (Fig. 4.8).

Dissolved Zn and Cd isotopic compositions (δ^{66}Zn and δ^{114}Cd) in the AS ranged from +0.35 to +0.64‰ and +0.11 to +0.95‰, respectively (Fig. 4.8). The heaviest isotopic signatures in these ranges for both metals were observed in the surface layer of GIS bloom stations, whereas at DIS bloom stations the values were lower for both (δ^{66}Zn: ~+0.44‰; δ^{114}Cd ~+0.65‰) (Fig. 4.8). Most δ^{114}Cd values decreased with increasing depth and became relatively constant (+0.21±0.07‰) below ~100 m, whereas for δ^{66}Zn the decreasing trend (from the surface to ~100 m) was only apparent at GIS bloom stations, the open ocean/shelf break/off-shelf stations and two of the mCDW outflow stations (i.e., Stns 34 and 33); the other stations were characterised by relatively homogeneous δ^{66}Zn from the surface to the deep ocean (+0.45±0.05‰) (Fig. 4.8).

4.3.5.2 The WS

In the WS, [dZn] and [dCd] ranged from 3.56 to 8.57 nmol L^{-1} and from 0.56 to 0.64 nmol L^{-1}, respectively (Fig. 4.9). δ^{66}Zn and δ^{114}Cd ranged from +0.34 to +0.50‰ and +0.07 to +0.44‰, respectively, smaller ranges than that for the AS (Fig. 4.9). The lowest [dZn] and [dCd] and the highest isotope ratios were typically observed in the upper 50 m of the surface layer. Generally, [dZn] and [dCd] increased (and isotopic ratios decreased) with increasing depth below the surface layer. The vertical profiles varied with station type going offshore:

Shelf stations (Stn 91, 93, and 95): at Stns 93 and 91, [dZn] and [dCd] reached maximum values of 5.63±0.39 nmol L^{-1} and 0.76±0.02 nmol L^{-}

^{1}, respectively, below 100-150 m; whereas Stn 95 exhibited relatively constant and lower [dZn] (4.58±0.29 nmol L^{-1}) and [dCd] (0.69±0.02 nmol L^{-1}) throughout the water columns (Fig. 4.9). At all three stations, δ^{66}Zn was relatively homogeneous from the surface to ~450 m (+0.42±0.04‰), whereas δ^{114}Cd decreased from ~+0.41‰ at the surface to ~+0.20 to +0.30‰ at ~100 m and became homogeneous below 100 m (+0.27±0.04‰) (Fig. 4.9), except two samples that exhibited much lower δ^{114}Cd (+0.13‰ and +0.17‰ at 20 m and 40 m at Stn 95, respectively).

Continental shelf slope stations (Stn 67, 70, 73, 75, 82, and 85): compared to the shelf stations, the increasing trends of [dZn] and [dCd] with depth stopped around 100-150 m above the sediments of the continental shelf slope where descending pre-WSBW was located with lower [dZn] (5.73±0.39 nmol L^{-1}) and [dCd] (0.75±0.01 nmol L^{-1}) (Fig. 4.9). Across the shelf slope stations, δ^{66}Zn were homogeneous in the upper ~500 m (+0.41±0.05‰), except for Stn 75 where δ^{66}Zn decreased from ~+0.50‰ at the surface to ~+0.35‰ at ~125 m and then increased to ~+0.45‰ at ~500 m. Below 500 m, δ^{66}Zn (+0.45±0.04‰) was relatively homogeneous with higher values than in the upper 500 m until near bottom depths within 100-150 m above the continental shelf slope sediments where δ^{66}Zn became slightly lower (+0.43±0.04‰) (Fig. 4.9). In contrast to δ^{66}Zn, δ^{114}Cd was as high as ~+0.40‰ in the surface layer of several continental shelf slope stations (i.e., Stns 82, 85, 75, and 73), whereas the other two stations were relatively lower (+0.23±0.09‰). These high δ^{114}Cd values decreased with increasing depth. Below 500 m, δ^{114}Cd at all continental shelf slope stations was homogeneous (+0.24±0.05‰), except for Stn 82 where δ^{114}Cd reached +0.15 within 100-150 m above the continental shelf slope sediments (Fig. 4.9).

Off-shore stations (Stn 56, 61, and 65): here, [dZn] and [dCd] reached maximum concentrations (as high as 8.34 nmol L^{-1} and 0.94 nmol L^{-1}) around ~500 m and ~250 m, respectively. Below these depths, both [dZn] and [dCd] decreased with increasing depth to values of ~7.10 nmol $L^{-1}$and 0.80 nmol L^{-1}, respectively (Fig. 4.9). At these stations, δ^{66}Zn was homogeneous from the surface to the bottom

(+0.42±0.04‰) and slightly increased to +0.45±0.07‰ below 500 m. For $\delta^{114}Cd$, although values decreased with increasing depth at all three off-shore stations, the minimum $\delta^{114}Cd$ was reached at different depths. A minimum of +0.13‰ was observed at ~40 m at Stn 65 and gradually increased to homogeneous values below 500 m (+0.23±0.03‰). In contrast, a minimum of +0.07‰ was observed at ~230 m at Stns 61 and 56 followed by a slight increase to +0.12-+0.17‰ in the deepest part of the water column (Fig. 4.9).

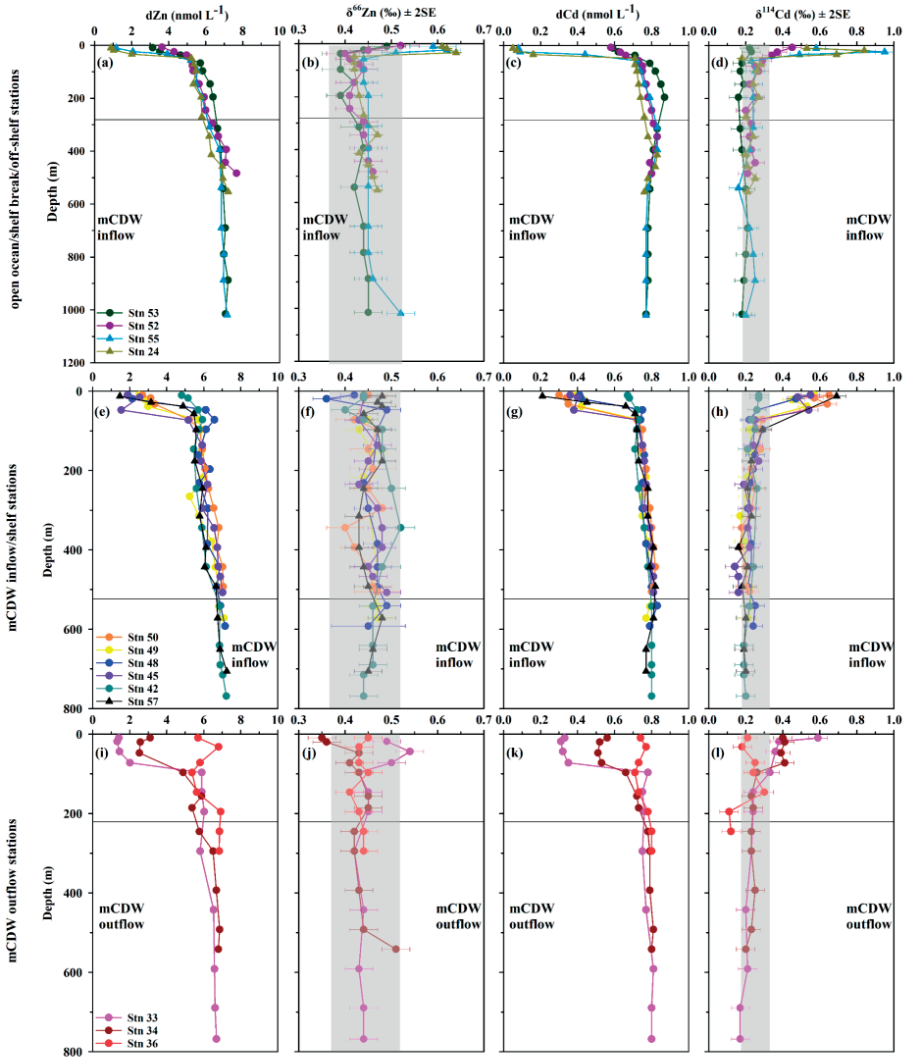

Figure 4.8 Dissolved metal concentrations ([dZn] and [dCd]) and isotopic compositions (δ^{66}Zn and δ^{114}Cd) of all Amundsen Sea (ANA08B) stations. (a) to (d) the open ocean/shelf break/off-shelf stations; (e) to (h) the mCDW inflow stations; (i) to (l) the mCDW outflow stations. The grey shadings indicate the deep-water signature of δ^{66}Zn (+0.44±0.08‰, Bermin et al., 2006; Conway and John, 2014b; Lemaitre et al., 2020; Sieber et al., 2020) and of δ^{114}Cd (+0.25±0.06‰, Abouchami et al., 2014; Conway and John, 2015; George et al., 2019; Xie et al., 2017). The error bars for δ^{66}Zn and δ^{114}Cd are two standard deviations.

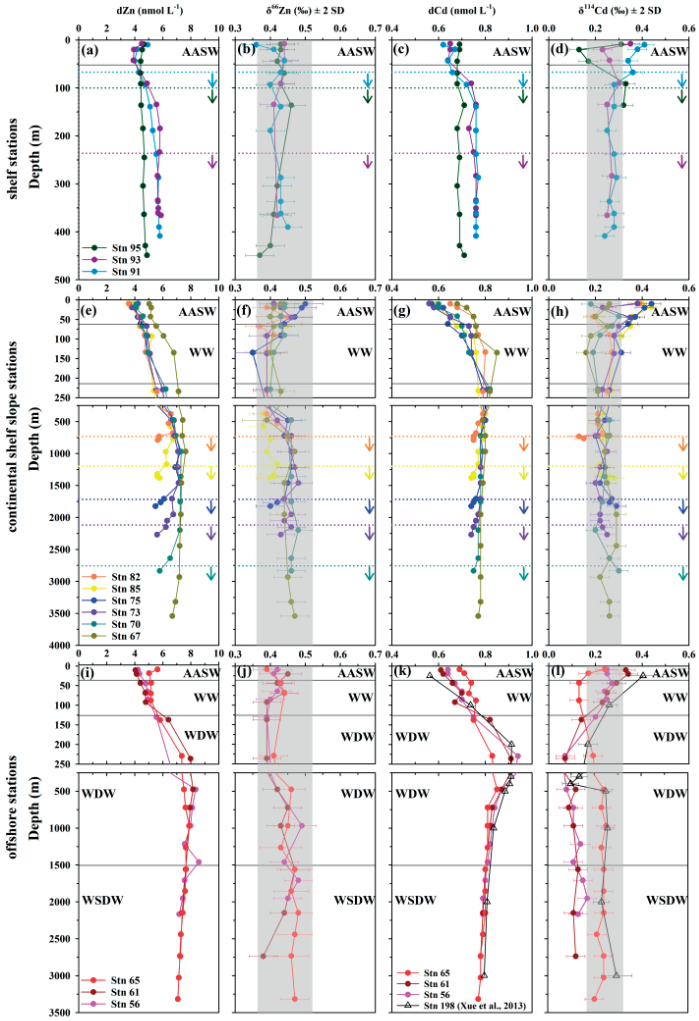

Figure 4.9 Dissolved metal concentrations ([dZn] and [dCd]) and isotopic compositions (δ^{66}Zn and δ^{114}Cd) of all Weddell Sea (PS117) stations. (a) to (d) the shelf stations; (e) to (h) the continental shelf slope stations; (i) to (l) the off-shore stations. The grey shadings indicate the deep-water signature of δ^{66}Zn (+0.44±0.08‰) and of δ^{114}Cd (+0.25±0.06‰). The dotted lines and arrows in (a) to (d) indicate the layers of WS shelf water defined based on a neutral density of <28.0 kg m^3 and θ<–0.7 ºC at the shelf stations, whereas the dotted lines and arrows in (e) to (h) indicate the layers of pre-WSBW defined based on θ<0.7 ºC. In (k) and (l), the open symbols represent the data obtained from a station previously reported by Xue et al. (2013), which was close to the offshore stations in this study. The error bars for δ^{66}Zn and δ^{114}Cd are 2 standard deviations.

4.4 Discussion

4.4.1 $\delta^{66}Zn$ and $\delta^{114}Cd$ signatures of potential external sources previously identified

The inward flow of nutrient-rich mCDW supplies most of the dissolved Zn and Cd to the AS, with only a small component from local margin sources (Sherrell et al., 2015; Tian et al., 2023b). In this study, the isotopic compositions of the least modified CDW ($\delta^{66}Zn$: +0.44±0.03‰; $\delta^{114}Cd$: +0.20±0.03‰, Figs 4.8b and 4.8d) are equivalent to homogeneous global deep-water signals for $\delta^{66}Zn$ (+0.44±0.08‰, Bermin et al., 2006; Conway and John, 2014b; Lemaitre et al., 2020; Sieber et al., 2020; Takano et al., 2017) and for $\delta^{114}Cd$ (+0.25±0.06‰, Abouchami et al., 2014; Conway and John, 2015; George et al., 2019; Xie et al., 2017). These signatures did not change significantly (overlapping within uncertainty) over the continental shelf (i.e., the shelf break stations, the mCDW inflow stations, and the shelf station) within 200 m above the seafloor ($\delta^{66}Zn$: +0.46±0.04‰; $\delta^{114}Cd$: +0.21±0.06‰) (Figs 4.8f and 4.8h), consistent with the notion that mCDW provides the dominant supply of dissolved Zn and Cd to the AS (Tian et al., 2023b).

As mCDW flows over the continental shelf into the AS it acquires Zn and Cd from shelf sediments, with Tian et al. (2023b) estimating that shelf sediments supply around 0.42 nmol L^{-1} and 0.03 nmol L^{-1} of [dZn] and [dCd], respectively, to the overlying water. This sediment source is a minor contribution to dZn and dCd, corresponding to 7% and 4% of observed [dZn] and [dCd], respectively, based on a binary mixing model of dissolved metal concentrations and S (Tian et al., 2023b). Reported isotopic compositions in marginal sediments and lithogenic sources ($\delta^{66}Zn$: –0.72 to +0.32‰, compiled by Conway and John, 2014b; Little et al., 2016; $\delta^{114}Cd$: –0.01±0.04‰, Rehkämper et al., 2012; Schmitt et al., 2009) are often lower than deep-water signatures – a sedimentary input of both metals might thus be expected to lead to lighter dissolved isotopic signatures relative to the deep ocean. However, the homogeneity of isotopic signatures in mCDW suggests that either the external sedimentary input either are similar to the

deep-water signals, or more likely, the magnitude of addition is too small to leverage changes to mCDW isotopic signatures. Taken together with observations by Tian et al. (2023b), our isotopic data suggests a minor sedimentary supply for Zn and Cd in the AS with a signature that is likely on the heavy end of the previously reported spectrum for sedimentary input. However, this would need to be confirmed in future research by taking sediment and porewater samples on the Antarctic continental shelf for isotopic analysis.

To date, there is limited constraints of glacially-derived δ^{66}Zn and ^{114}Cd – Sieber et al. (2020) speculated that glacial meltwater may supply isotopically light Zn to the surface water (within tens of meters) near the Mertz Glacier (East Antarctica), whereas for Cd there is no evidence that glaciers are an isotopically light source; we might also expect both to have lithogenic isotopes signatures (+0.3‰ and 0‰ for δ^{66}Zn and ^{114}Cd, respectively; Horner et al., 2021). Previously, we showed that ice shelf meltwater only supplies a small amount of dZn and dCd to the outflowing mCDW, and conservative mixing of the mCDW outflow, shelf waters, and ice shelf meltwater plays the primary role in regulating metal concentrations in the outflowing water (Tian et al., 2023b; van Manen et al., 2022). The shelf water endmember used in previous studies was defined as a water mass geographically adjacent to the ice shelf (with similar θ and S to WW) that mixes with the mCDW inflow (Tian et al., 2023a). In this study, to distinguish this shelf water from shelf water observed in the WS (i.e., WS shelf water), we refer it to as ASP shelf water. The results show that, although the mean δ^{66}Zn and ^{114}Cd in the mCDW inflow and ASP shelf water seem slightly higher than in the mCDW outflow, there is no statistically significant difference between the three water masses (Table 4.2). The homogeneity in the isotopic compositions of the mCDW inflow and outflow observed in this study confirms that the DIS is a negligible source of Zn and Cd as suggested before (Tian et al., 2023b), and as such, conservative mixing is likely the main process driving the changes in [dZn] and [dCd].

Table 4.2 δ^{66}Zn and δ^{114}Cd in the mCDW outflow, the mCDW outflow, and ASP shelf water along the DIS transect. For the mCDW inflow, following the path of the inflow (Fig.4.5, δ^{66}Zn and δ^{114}Cd within 100 m above the seafloor at st. 45 were selected (Tian et al., 2023a; Tian et al., 2023b) as Stn 45 is expected to represent the mCDW inflow better than Stn 42 that is closer to the DIS due to potential lithogenic material input at Stn 42 (van Manen et al., 2022). For the mCDW outflow, δ^{66}Zn and δ^{114}Cd between 195 to 295 m at Stn 36 were selected, based on potential temperature (>−1˚C) and salinity (S>34.1). The outflow was located at a similar depth as previously reported for the core of mCDW outflow (200 to 400 m, Miles et al., 2016; Randall-Goodwin. et al., 2015). For the ASP shelf water, to represent the ambient waters located around the DIS, δ^{66}Zn and δ^{114}Cd were selected from the closest station (i.e., Stn 42) to the DIS within the depth (145 to 300 m) of mCDW outflow (Tian et al., 2023b).

	station	depth (m)	δ^{66}Zn±2 SD (‰)	δ^{114}Cd±2 SD (‰)
mCDW inflow	45	442	+0.45±0.03	+0.14±0.05
		467	+0.46±0.03	+0.16±0.05
		507	+0.49±0.03	+0.16±0.05
		mean±2 SD	+0.47±0.04	+0.15±0.02
ASP shelf water	42	145	+0.48±0.03	+0.21±0.05
		245	+0.50±0.03	+0.26±0.05
		344	+0.52±0.03	n/a
		mean±2 SD	+0.50±0.05	+0.20±0.08
mCDW outflow	36	195	+0.43±0.03	+0.11±0.05
		245	+0.44±0.03	+0.12±0.05
		294	+0.44±0.03	n/a
		mean±2 SD	+0.44±0.01	+0.11±0.01

4.4.2 Isotopic signatures of Zn and Cd in the WS

In contrast to the AS where mCDW intrusion plays a critical role in trace metal biogeochemistry, the WS is characterised by a gyre circulation and the formation of the pre-WSBW that eventually flows northward and enters the main basins of the global ocean along with WSDW (reviewed by Vernet et al., 2019). Therefore, the trace metal biogeochemistry in the WS may influence regional and global cycling of trace metals via export of the WS seawaters into global deep waters. In the following section, we discuss 1) the role of glacial meltwater input in the WS; 2) isotopic compositions in different water masses and pre-WSBW; 3) observed differences between the inner and outer WG.

4.4.2.1 The shelf station (Stn 95): glacial meltwater input?

At the shelf stations, meteoric water input (f_{met}) is greatly elevated at Stn 95 (up to 4.8% above ~250 m) and gradually decreases towards the central WS basin (Fig. 4.7), which is much higher than the f_{met} (~0.64%) estimated in the mCDW outflow in the AS (Tian et al., 2023b). Since glacier-derived dZn and dCd in the surface layer (approximately in the upper 90 m) may be modulated by biological activity such as biological uptake, it is more sensible to assess samples below the surface layer (~90 m), where meltwater fractions are still high, in order to evaluate meltwater influence. Within this depth range (90 to 250 m), homogeneously lower [dZn] (4.57±0.23 nmol L^{-1}) and [dCd] (0.69±0.04 nmol L^{-1}) are observed at Stn 95 compared to the other two shelf stations with lower meltwater contributions ([dZn]: 5.50±0.55; [dCd]: 0.75±0.02 nmol L^{-1}) (Figs 4.9a and 4.9c), implying glacial meltwater may actually not supply a significant amount of dZn and dCd. Despite the resolvable difference in dissolved concentrations between Stn 95 and the other two shelf stations, δ^{66}Zn (+0.42±0.05‰) and δ^{114}Cd (+0.27±0.06‰) show values indistinguishable from deep-water signals at all three shelf stations within the 90-250 m depth range (Figs 4.9b and 4.9d). Taken together, our result suggest that glacial meltwater is not enriched in dZn and dCd relative to the ambient seawater, and thus that glacial meltwater may essentially only supply a negligible amount that is not sufficient to be reflected in the observed isotopic compositions. Instead, conservative mixing of shelf waters (low [dZn] and [dCd]) with offshore water masses (high [dZn] and [dCd], e.g., WDW) may result in the observed variability in concentrations between shelf stations (Fig. 4.9). Indeed, a strong linear relationship ($p<0.001$) of S and [dZn] and [dCd] between WS shelf water and WDW indicates the increase in dissolved concentrations results from conservative mixing between water masses, explaining the increase of [dZn] and [dCd] in the other two shelf station compared to Stn 95, whilst isotopic compositions remain homogeneous between water masses (Fig. 4.9e and 4.9f).

4.4.2.2 The continental shelf slope stations: isotopic compositions in different water masses and pre-WSBW

At the continental shelf slope stations, although most $\delta^{66}Zn$ and $\delta^{114}Cd$ values throughout the water column are equivalent to deep-water composition, there is variability from the surface to the deep, indicating biogeochemical processes (Fig. 4.9). A decrease in $\delta^{66}Zn$ and $\delta^{114}Cd$ together with increasing [dZn] and [dCd] is observed in WW (~60-220 m), compared to AASW (the upper 60 m) (Figs 4.9e, 4.9f, 4.9g, and 4.9h), implying less biological uptake and/or increased preferential regeneration of light isotopes that are assimilated in the surface (e.g., Bermin et al., 2006; Conway and John, 2015; Sieber et al., 2020; Zhao et al., 2014). This is supported by the strong linearity of the relationship of dZn and dCd with PO_4 – dZn and dCd increase with PO_4 from the surface towards the deep (Fig. 4.10), indicating uptake in the surface and subsequent remineralization of organic particles over depth in WW. Additionally, the linear relationship between Zn and Si as well as Cd and PO_4 has been observed in the deep Southern Ocean (Zn/Si=0.064 mmol mol^{-1}, Middag et al., 2019; Sieber et al., 2020; Vance et al., 2017); Cd/PO_4=0.35 mmol mol^{-1}, Middag et al., 2018; Sieber et al., 2019a). At the continental shelf slope stations, despite the strong linearity of the relationship between Zn and Si, minor but apparent changes are observed – samples in AASW plot below the deep Southern Ocean Zn-Si trend (Fig. 4.10a); whereas in WW most samples plot above the trend, suggesting a higher uptake of Zn in the surface and shallower regeneration of Zn, compared to Si (e.g., Sieber et al., 2020). At depth, dZn reached a maximum of ~7.5 nmol L^{-1} and remained relative constant in WDW and WDW while Si continued to increase (Fig. 4.10a). In the case of Cd and PO_4, most samples plotted below the deep Southern Ocean Cd-PO_4 trend (Fig. 4.10c), likely due to a lower Cd uptake relative to PO_4 in the surface (e.g., different phytoplankton community) and subsequent regeneration of both elements (with lower Cd/PO_4 ratio than reported value) over depth.

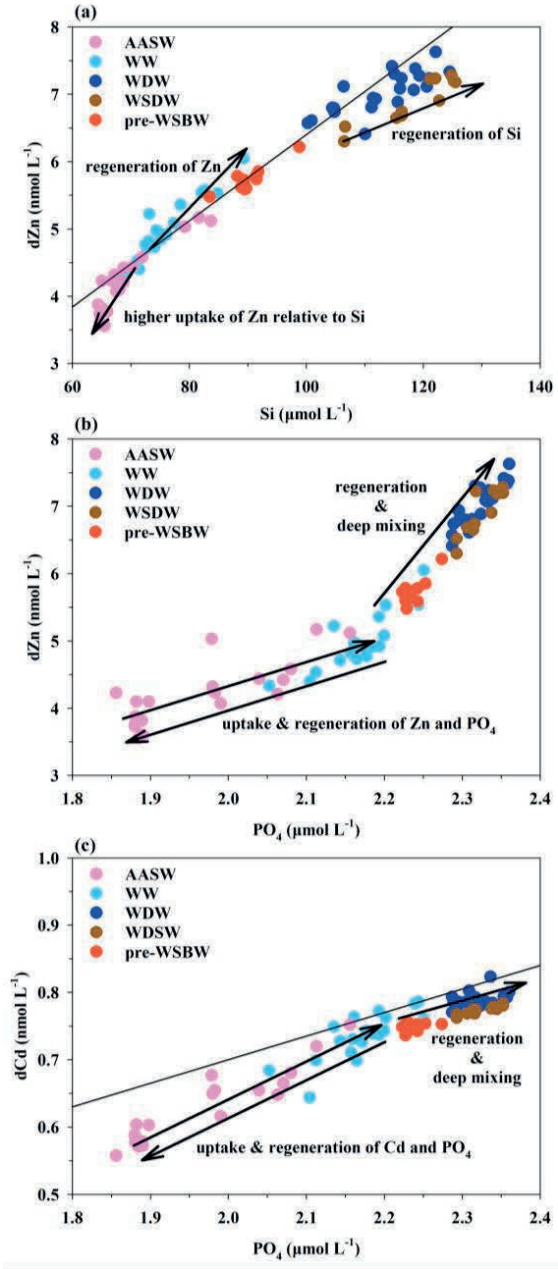

Figure 4.10 Zn-Si, Zn-PO_4, and Cd-PO_4 relationships at the continental shelf slope stations. The solid lines in (a) and (b) represent the deep Southern Ocean trends for Zn-Si (0.064 mmol mol^{-1}, Middag et al., 2019; Sieber et al., 2020; Vance et al., 2017) and Cd-PO4 (0.35 mmol mol^{-1}, Middag et al., 2018; Sieber et al., 2019a).

In WDW, homogeneous $\delta^{66}Zn$ (+0.44±0.05‰) and $\delta^{114}Cd$ (+0.23±0.04‰) and relatively elevated [dZn] (7.03±0.62 nmol L^{-1}) and [dCd] (0.79±0.02 nmol L^{-1}) are comparable to the values in the least modified CDW observed in the AS in this study ($\delta^{66}Zn$: +0.45±0.04‰, [dZn]: 6.89±0.50 nmol L^{-1}; $\delta^{114}Cd$: +0.20±0.06‰, [dCd]: 0.79±0.05 nmol L^{-1}) (Fig. 4.8). This observation suggests that both $\delta^{66}Zn$ and $\delta^{114}Cd$ in WDW (also known as the WS version of CDW) are not noticeably affected by biogeochemical processes (e.g., remineralization or scavenging) or input from external sources during the transport in the WS, and that the observed [dZn] and [dCd] maximum in WDW is essentially driven by CDW.

Since the WS exports a major component of northwards-advecting AABW (formed from WSDW and WSBW) into the global ocean (e.g., Huhn et al., 2008; Orsi et al., 1999; Vernet et al., 2019), one of the objectives of this study was to investigate any evolution of [dZn], [dCd], $\delta^{56}Zn$, and $\delta^{114}Cd$ during WSBW formation. Pre-WSBW is characterised by a slightly elevated [dZn] and [dCd] compared to WS shelf water (Figs 4.9a and 4.9c), implying an external source (e.g., sediments) along the slope or mixing with metal-rich water masses (i.e., WDW or WSDW). The linear relationship of S and dissolved metal concentrations between WS shelf water, pre-WSBW, WDW (Stns 82 to 67), and WSDW (Stns 75 to 67) suggest that physical mixing is actually the main driver for the increase of dissolved metal concentrations during the development and advection of pre-WSBW (Figs 4.11a and 4.11d). However, a few samples at shallower depths (90 to 190 m) with high [dCd] (0.72 to 0.76 nmol L^{-1}) at lower S (34.43 to 34.53) do not follow the general mixing trend; these may result from shallow remineralization since PO_4 is also elevated in these samples (Figs 4.11d and 4.11e) (e.g., Sieber et al., 2019b).

In contrast to [dZn] and [dCd], $\delta^{66}Zn$ and $\delta^{114}Cd$ are homogeneous in abovementioned water masses and hence there is also no relationship between S and isotopic compositions (Figs 4.11c and 4.11f). The consistent $\delta^{66}Zn$ and $\delta^{114}Cd$ signatures observed from the continental shelf to the continental shelf slope also imply that there is little input of metals from sediments along the continental slope as this should

have resulted in a lighter isotopic composition in the dissolved pool (e.g., Conway and John, 2014b; Liao et al., 2020; Little et al., 2016; Rehkämper et al., 2012; Schmitt et al., 2009); this observation in the WS is consistent with that in the AS (section 4.4.1). Unfortunately, we do not have data of pre-WSBW (or WSBW) available in the stations further into the basin (Stns 67, 65, 61, and 56) that could allow us to track whether these consistent isotopic signatures change before the deep water eventually is exported from the WS. Nevertheless, a comparison of δ^{66}Zn and δ^{114}Cd in the water masses with values previously reported for WSBW and WSDW in the WS (Abouchami et al., 2014; Xue et al., 2013; Zhao et al., 2014) as well as AABW further north in the global basin (Conway and John, 2014b, 2015; John et al., 2018) shows that most samples exhibit nearly identical δ^{66}Zn and δ^{114}Cd among different deep-water masses (Figs 4.11c and 4.11f), suggesting that the universal homogeneous isotopic compositions of Zn and Cd in deep water is already present in forming AABW (i.e., dense shelf water and pre-WSBW) and remains unaltered during its transport pathway as it flows into the deep global ocean, whereas the dissolved concentrations may change via conservative mixing between different deep-water masses. This is in agreement with previous observations that showed fresh ventilated deep water can preserve the signals of relatively low dissolved macro/micronutrients concentrations (e.g., Middag et al., 2013) as well as its δ^{114}Cd signature (Xue et al., 2013), and transports such signals into the deep WS basin, suggesting that biogeochemical features (e.g., uptake in the surface and regeneration over depth) on the shelf predominantly set the isotopic signatures for deep waters.

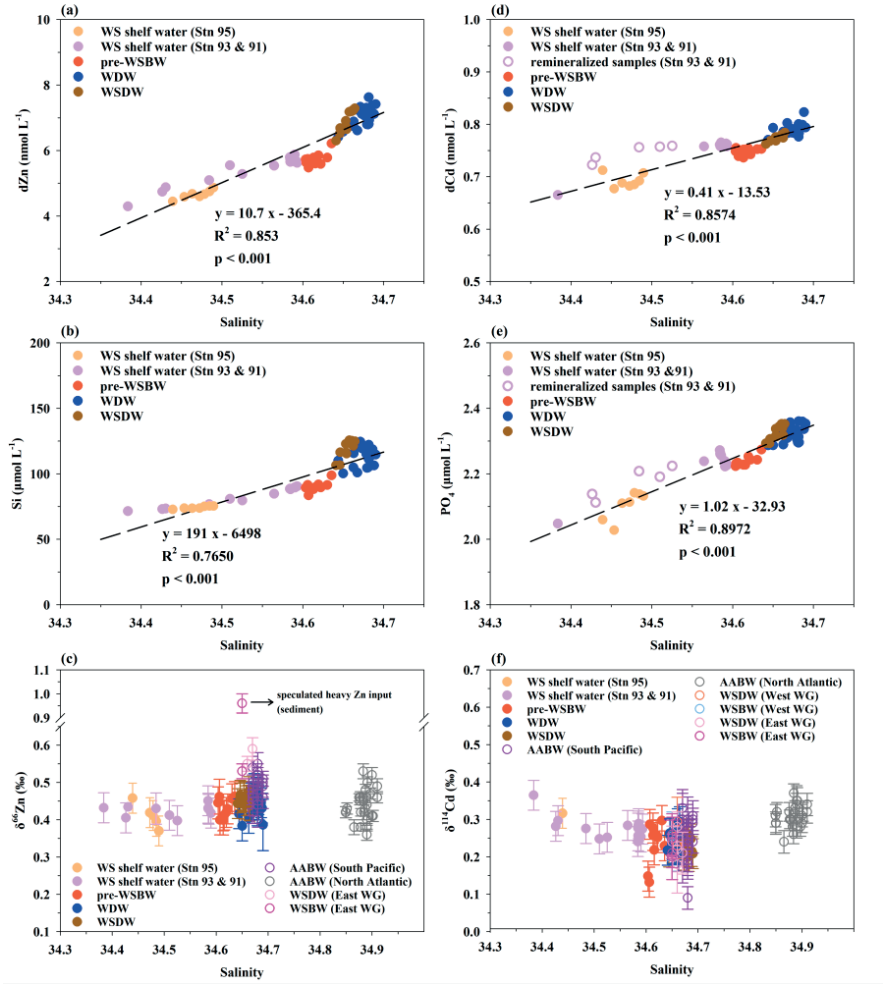

Figure 4.11 Correlations of salinity with (a) [dZn]; (b) [Si]; (c) δ^{66}Zn; (d) [dCd]; (e) [PO_4]; (f) δ^{114}Cd in different water masses observed along the Weddell Sea transect (dense shelf water, pre-WSBW, WDW, and WSDW). For (d) and (e), the open symbols indicate the samples with shallow remineralization signals; the correlation does not include these samples. For (c), open symbols represent the previously reported δ^{66}Zn values (±2 SD) in AABW (South Pacific: John et al., 2018; North Atlantic: Conway and John, 2015), WSDW and WSBW (East WG: Zhao et al., 2014). For (f), the open symbols represent the previously reported δ^{114}Cd values (±2 SD) in AABW (South Pacific: John et al., 2018; North Atlantic: Conway and John, 2015), WSDW and WSBW(East WG: Xue et al., 2013; West WG: Abouchami et al., 2014).

4.4.2.3 The offshore stations: difference between the outer and inner WG

At the offshore stations, akin to the continental shelf slope stations, $\delta^{66}Zn$ remains within the range of deep-water isotopic composition (Fig. 4.9j). On the other hand, a striking feature is observed for $\delta^{114}Cd$ at both offshore Stns 61 and 56 where $\delta^{114}Cd$ is extremely low (as low as +0.07‰) between ~250 m and ~1500 m and gradually increases towards (but not fully, ~+0.17‰) the global deep-water signal below 1000 m, whereas Stn 65 exhibits homogeneous $\delta^{114}Cd$ below ~250 m (+0.23±0.04‰) (Fig. 4.9l). Previously at a nearby location, Xue et al. (2013) observed a similar low $\delta^{114}Cd$ signal (~+0.10‰) between 200 m and 400 m at a station in the WS (i.e., their station 198, ~65°S, ~36°W) for samples collected around eleven years prior to the current samples, but $\delta^{114}Cd$ abruptly returned to global deep-water signature below 400 m (Fig. 4.9l). Using a mass balance model, they concluded that such low $\delta^{114}Cd$ values may result from remineralization of biomass with isotopically light Cd produced in the surface, which agrees with our observation that [dCd] reaches a maximum at ~250 m, coinciding with the lowest $\delta^{114}Cd$. However, this theory can only explain the isotopically light signature between 200 m and 400 m (Xue et al., 2013). Here, we speculate there may be a continuation of such light signature from 400 m to ~1500 m due to slow ventilation in the inner gyre (i.e., Stns 61 and 56) compared to the outer gyre (i.e., Stn 65) (Fig. 4.1). Specifically, apparent oxygen utilization (AOU) is higher between 250 m to 1500 m in the inner gyre (i.e., Stn 61, AOU data in Stn 56 is unfortunately not available) than the outer gyre (Fig. 4.12a), implying older water with a stronger remineralization signal at the former station down to at least 1500 m. Below 1500 m, $\delta^{114}Cd$ gradually increases, likely due to reduced influence of remineralization and mixing with underlying WSDW. Furthermore, the highest potential temperature (>0.75°C) is observed between 200 m and 400 m near the outer gyre (Stn 65, 64°S, 48°W), compared to relatively low temperatures (<0.75°C) at the inner gyre (Stns 61 and 56) at similar depth (Fig. 4.12b), indicating the western boundary current (southwest-northeast ward) of the WG likely separates Stn 61

and 56 from the remainder of the WS stations. This temperature gradient has been described before and is attributed to the gyre structure of the western WG (e.g., Fahrbach et al., 1994). Additionally, the location of the western boundary of the WG (i.e., between Stns 65 and 61) is in agreement with previous Argo float data that showed the north-eastward limb of the WG was situated between ~63-65ºS and ~40-50°W (Reeve et al., 2016). We suggest that the relatively slow ventilation of waters inside the central gyre results in relatively isolated water that, with time, is subject to accumulative remineralization as deep as ~1500 m (with a resulting isotopically light Cd signature), whereas waters towards the edge of the gyre are likely more affected by the lateral circulation of WDW. Overall, the difference in δ^{114}Cd between Stns 61 and 56 and Stn 65 may thus indicate distinct biogeochemical features between the inner and outer WG.

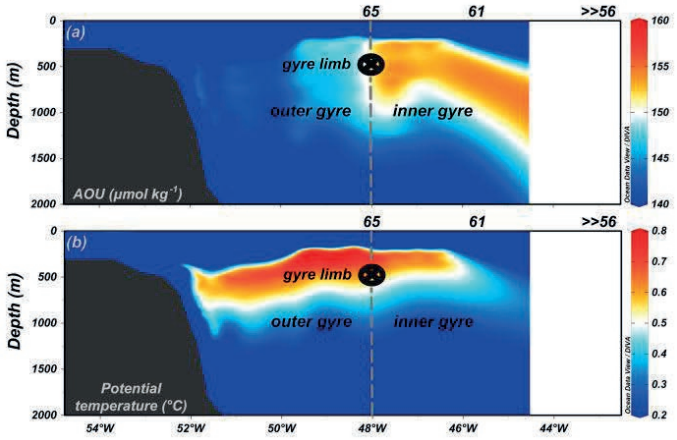

Figure 4.12 (a) Apparent oxygen utilization (AOU) and (b) potential temperature (θ) at the offshore stations along the Weddell Sea transect. AOU is converted by Ocean Data View (ODV version 5.3.0, Schlitzer, 2020), using dissolved oxygen data obtained from oxygen sensor installed on the regular CTD deployed by the research team of Alfred Wegener Institute for Polar and Marine Research, at stations close to the trace metal stations (where the Titan CTD system without functioning oxygen sensor was used). The dashed lines indicate Stns 65 and 61 (AOU at Stn 56 is not available). The location of the gyre limb is determined based on the observation of Reeve et al., (2019) and the section profiles of AOU and θ. The black cross and circle indicate the direction (pointing into the screen) of the WG.

Conversely, in the case of Zn, there is no apparent difference in δ^{66}Zn between the inner and outer gyre (Fig. 4.9j). We postulate that this observation of δ^{66}Zn may results from a larger analytical uncertainty than any isotopic effects of remineralization (Fig. 4.9j) since Zn is characterised by a much smaller and much less unidirectionally clear isotopic fractionation during uptake, for instance, a more complex interaction of surface processes that sets the δ^{66}Zn in particulate materials (e.g., frustule, organic tissues, or adsorbed), and that perhaps a mixture of phases of Zn that is regenerating over depth. Nevertheless, since δ^{66}Zn data in the WG are relatively scarce (Zhao et al. (2014) in the east WG and this study at the west WG) compared to δ^{114}Cd, we note that this speculation requires further investigation, for example, particulate Zn isotopic compositions may provide valuable information on whether speciation, scavenging (John and Conway, 2014; Sieber et al., 2023b; Weber et al., 2018) or remineralization drive δ^{66}Zn in both the inner and outer WG.

4.4.3 Variability in isotopic signatures in the surface water of the AS and the WS

Previously, it was observed that biological assimilation plays a critical role in regulating the dissolved pool of Zn and Cd in coastal Antarctica surface waters such as the AS and the WS (Abouchami et al., 2014; Sherrell et al., 2015; Tian et al., 2023b; Zhao et al., 2014). Since biological uptake for both metals has been found to result in isotopic fractionation in seawater (Conway and John, 2014b; Köbberich and Vance, 2019; Lacan et al., 2006; Ripperger et al., 2007; Samanta et al., 2018), dissolved δ^{66}Zn and δ^{114}Cd in the AS and the WS provide the potential to further investigate uptake of Zn and Cd by phytoplankton in both regions, as well as the potential mechanisms that control the isotopic systematics of both metals. In this section, we focus on data in the surface layer (i.e., between the surface and [chl a] maximum depth) for both the AS bloom stations (except Stns 36 and 42 as elevated surface [dZn] and [dCd] suggests terrestrial input that may hinder the investigation of biological uptake processes, Fig. 4.8) and the WS stations.

4.4.3.1 δ^{114}Cd systematics in the surface layer: biological uptake predominantly drives δ^{114}Cd

In the case of Cd, the effect of biological uptake clearly dominates surface δ^{114}Cd signatures; δ^{114}Cd in the surface layer ranges from +0.25 to +0.95‰ and +0.13 to +0.44‰ in the AS bloom stations and the WS stations (relative to a deep ocean of +0.25‰), respectively, with the lowest [dCd] corresponding to the higher end of the above ranges for most samples (Figs 4.13d, 4.13e, and 4.13f), indicating preferential uptake of isotopically lighter Cd in the surface as reported before (e.g., Conway and John, 2014b; Lacan et al., 2006; Sieber et al., 2019b). There is an inverse relationship between [dCd] and δ^{114}Cd that follows Rayleigh fractionation trends (closed system) with fractionation factors (α, where $\alpha = R_{biomass}/R_{seawater}$) ranging from 0.99930 to 0.99995 in the AS and 0.99800 to 0.99950 in the WS (Figs 4.13d, 4.13e, and 4.13f), in good agreement with previous observations in the Southern Ocean (0.99955±0.00002, Abouchami et al., 2011; Sieber et al., 2019a; Xue et al., 2013) and culture experiments (0.99974±0.00005, Horner et al., 2013). Furthermore, by assuming WW preserves the initial conditions prior to seasonal biological uptake, the removal of dCd and the change in δ^{114}Cd ($\Delta\delta^{114}$Cd) display a strong correlation in which the highest dCd removal and largest δ^{114}Cd difference relative to WW correspond to the highest $[\text{chl a}]_{wt.avg}$ (Figs 4.6 and 4.14). This indicates that biological uptake predominantly controls both [dCd] and δ^{114}Cd in the surface layer (e.g., Conway and John, 2015) as there is no evidence for an influence of other sources (Tian et al., 2023b) to the surface layer. Data from the AS follows Rayleigh fractionation trends even more closely (i.e., less scattered data) with higher fractionation factors than in the WS (Figs 4.13d, 4.13e, and 4.13f), implying distinct biological fractionation effects between these regions.

There are two possible explanations for this (or a combination of the two): 1) uptake of a smaller fraction of the dissolved Cd pool by phytoplankton in the WS compared to the AS due to relatively lower productivity would mean less overall isotopic fractionation (i.e., remnant dCd pool is closer-to-deep ocean signal) for δ^{114}Cd in the

surface of the WS (Figs 4.13), and a greater degree of uptake of Cd should result in a heavier remnant dissolved pool, as observed in the AS (Fig. 4.13). This is supported by higher surface $[chl\ a]_{wt.avg}$ (4.32±1.36 μg L^{-1}) in the AS bloom stations compared to the WS (0.13±0.09 μg L^{-1}) (Fig. 4.6), and the degree of removal of PO_4 and Cd in the surface layer was generally larger in the AS (Fig. 4.14). Alternatively, and/or additionally, 2) variable fractionation factors between phytoplankton species and groups could affect the overall magnitude of fractionation (Abouchami et al., 2011). Indeed, in this study, the composition of the phytoplankton community was different between the AS and the WS – haptophytes (DIS bloom) and diatoms (GIS bloom) were the main dominant species (more than 50% of bulk phytoplankton composition) in the AS, whereas a more diverse phytoplankton community was observed in the WS (Fig. 4.6b). Interestingly, this more uniform phytoplankton community in the AS blooms is coincident with data that follows Rayleigh trends more closely than the mixed phytoplankton community in the WS where much more scatter is seen – this may imply that different species do indeed have different biological fractionation factors. Further evidence for this idea is found within the AS, where fractionation factors in the haptophyte bloom (0.99930 to 0.99960; α derived after excluding two datapoints from Stn 33 that deviated) are different – lower than in the diatom bloom (0.99970 to 0.99990) (Figs 4.13d and 4.13e).

To date, there are only a handful of culturing studies investigating the fractionation effect of Cd uptake by distinct species - freshwater algae *Chlamydomonas reinhardtii* and *Chlorella* (Lacan et al., 2006) and marine flagellate *Dunaliella tertiolecta* (John and Conway, 2014), and heterotrophic bacteria *Escherichia coli* (Horner et al., 2013). Although these selected species from both marine and freshwater environments generated similar isotopic fractionation effects for Cd uptake (John and Conway, 2014; Lacan et al., 2006), John and Conway (2014) speculated that phytoplankton species with different uptake pathways may drive variable Cd isotopic fractionation. In contrast, Horner et al. (2013) proposed a 'non-specific uptake' of Cd into cell membranes, regardless of the species and their ability to use Cd.

Therefore, this 'non-specific uptake' should yield similar isotopic fractionation factors between species. Since the uptake of Cd by phytoplankton is known to occur through various transport systems (e.g., divalent metal transporters) induced depending on the expression of other trace metal transporters (e.g., Mn and Zn) (Lane et al., 2008; Sunda and Huntsman, 1998a, 2000), and inter-species have distinct metal requirements under different environmental conditions (e.g., Fe-replete/deplete) (e.g., Twining and Baines 2013 Ho et al., 2003; Twining et al., 2003), we deem it likely the difference in Cd isotopic fractionation in the surface layer of the ASP may result from the use of different transporters of Cd or pathways employed by haptophytes and diatoms, as speculated for Fe in the same region (Tian et al., 2023a). On the other hand, the less clear Rayleigh fractionation trend in the WS may imply a relatively reduced uptake of Cd that is supported by lower $[\text{chl a}]_{\text{wt.avg}}$ (Fig. 4.6) and/or a more complex environment where other surface processes (e.g., ligand complexation) and external sources that interact with biological uptake (Horner et al., 2021), could lead to a "muted" fractionation in the surface water as previously observed elsewhere (e.g., Gault-Ringold et al., 2012; George et al., 2019; Sieber et al., 2019a). However, although diatoms and haptophytes are the most commonly dominant phytoplankton species in the Southern Ocean, there is a relatively limited number of studies investigating the variability in biological fractionation of Cd between these two species, either from in-situ observations or culturing experiments. Hence, to understand the biological fractionation of Cd by these two species groups and the subsequent influence on Cd cycling in the surface Southern Ocean, further investigation and culturing experiments are required to support our in-situ observations.

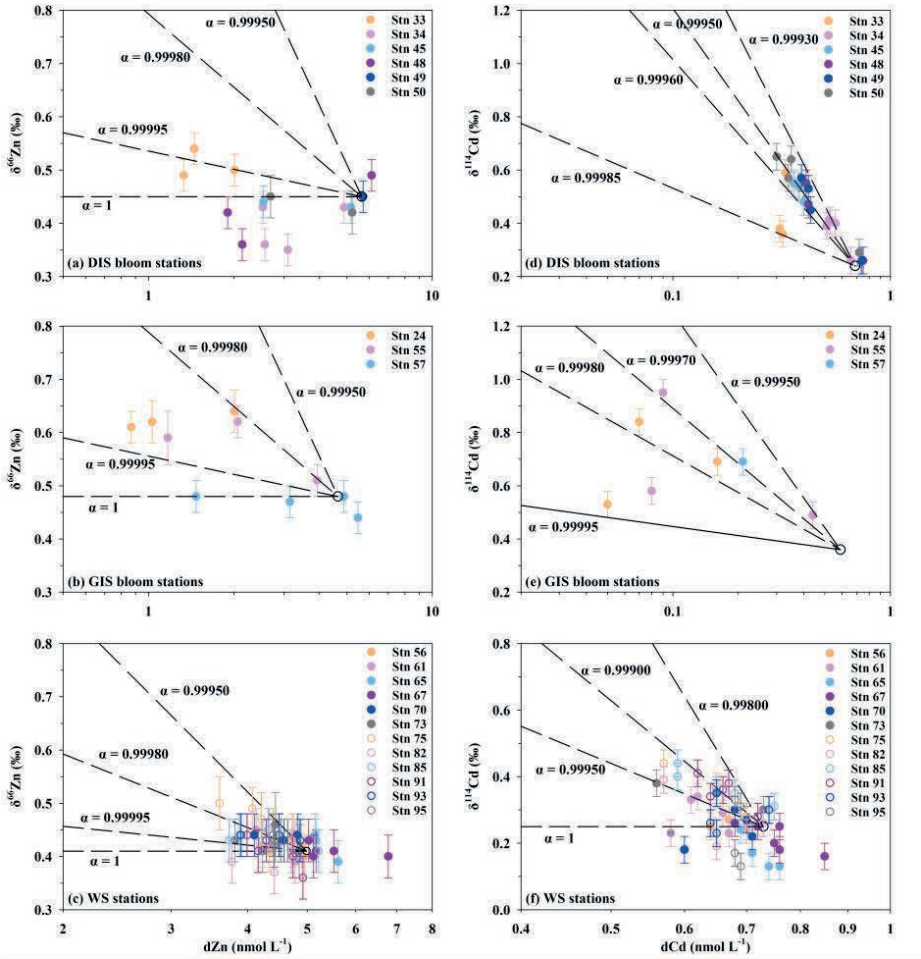

Figure 4.13 Isotopic systematics of δ^{66}Zn and δ^{114}Cd in the surface layer of the bloom stations of the ANA08B expedition and the WS stations of the PS117 expedition. (a) and (d) DIS bloom stations; (b) and (e) GIS bloom stations; (c) and (f) the WS stations. The dashed lines represent closed-system Rayleigh fractionation trends with $\alpha=R_{biomass}/R_{seawater}$, which are modelled by setting δ^{66}Zn and δ^{114}Cd values in WW as starting points (black open circle). The error bars for δ^{66}Zn and δ^{114}Cd are 2 SD.

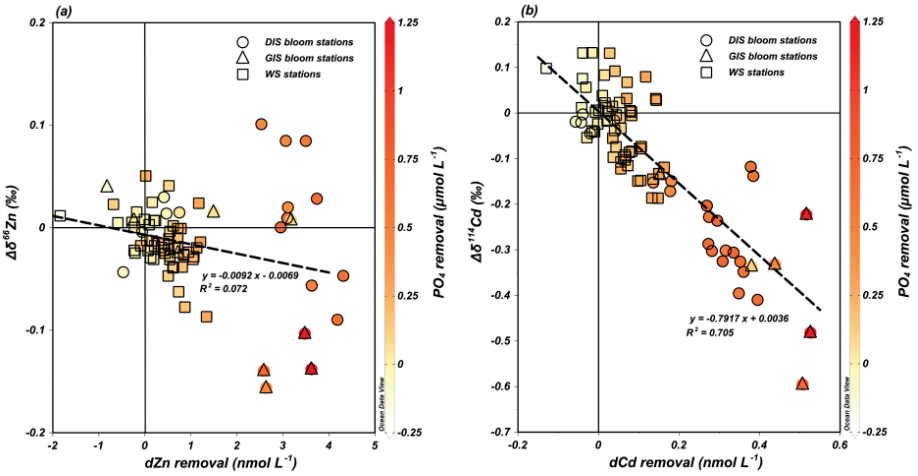

Figure 4.14 Correlations of the removal of metals with the change of isotopic composition in the surface layer at the bloom stations (ANA08B expedition) and the WS stations (PS117 expedition). Both the removal of metals (concentrations) and the change in isotopic composition are calculated as follows: the removal (or change) = observed values – WW values. In the same manner, the color grading shows the removal of PO_4. The dashed lines represent the correlations for all stations combined.

4

4.4.3.2 δ^{66}Zn systematics in the surface layer: interplay of multiple biogeochemistry processes

In the case of Zn, the variation in δ^{66}Zn is similar for the AS bloom stations (+0.35 to +0.64‰) and the WS stations (+0.36 to +0.50‰) (Figs 4.13a, 4.13b, and 4.13c). However, in contrast to Cd, highest δ^{66}Zn does not always correspond to lowest [dZn]. Furthermore, the removal of Zn and the change in δ^{66}Zn ($\Delta\delta^{66}$Zn) are not as well correlated as for Cd (Fig. 4.14), even though the drawdown of dZn often exceeds 60% of the dissolved Zn pool in the surface layer (relative to WW). Together, these patterns suggest that δ^{66}Zn values in the surface layer are likely not predominantly controlled by simple fractionation during biological uptake. This result is also supported by the isotopic systematics where most data do not follow a clear Rayleigh fractionation trend in both regions and both [dZn] and δ^{66}Zn are within a very narrow range (Figs 4.13a, 4.13b, and 4.13c), except

for Stn 33 in the DIS bloom and Stns 55 and 24 in the GIS bloom with only small fractionation factors around 0.99995 and between 0.99980 to 0.99995, respectively, when compared to Cd. These values are comparable to previously reported values associated with biological uptake in the surface Southern Ocean (0.99995±0.00001, Sieber et al., 2020; Wang et al., 2019) and these authors suggested that the uptake of Zn by phytoplankton only causes slight isotopic fractionation in the Southern Ocean, as supported by culturing experiments (John et al., 2007; Köbberich and Vance, 2017, 2019). Nevertheless, despite the presumably small isotopic fractionation induced by biological uptake, the consistent fractionation factors observed at Stn 33 in the DIS bloom and the GIS bloom stations may suggest that Zn assimilation by haptophytes and diatoms potentially exhibit a similar isotopic fractionation effect.

The absence of Rayleigh fractionation trends for Zn in most DIS bloom stations and WS stations could result from interactions of multiple processes besides biological uptake. For example, Köbberich and Vance (2017) noted that the common organic chelator (EDTA) used in culturing media preferentially binds isotopically heavy Zn, resulting in an overestimation of biological uptake fractionation. Such fractionation induced by ligand complexation may sometimes be larger than the effect of biological uptake (Köbberich and Vance, 2019; Vance et al., 2019). Moreover, Weber et al. (2018) and Sieber et al. (2023b) proposed that ligand complexation in conjunction with reversible scavenging of Zn play a role in controlling the distribution of δ^{66}Zn in the Oceans, potentially explaining the light isotope excursions seen in the subsurface of the North Pacific. Either of these might play a role in muting any apparent isotopic fractionation from biological uptake or resulting in lower δ^{66}Zn. However, in this study, all δ^{66}Zn was within uncertainty of the 2 SD of the deep ocean mean, suggesting little need for adsorption effects to explain isotope distributions. Unfortunately, measurements of Zn speciation are not available in this study. Further investigation including the speciation of Zn, notably the complexation of Zn by organic ligands, as well as the fractionation induced by various organic ligands could be helpful to evaluate the influence of ligand complexation on the isotopic

composition of Zn in coastal Antarctica. Nevertheless, our results suggest that the biogeochemistry of Zn and its isotopic systematics are not predominantly driven by biological uptake in the surface layer, neither in the significantly productive ASP nor in the less productive WS, implying the importance of other processes such as ligand complexation in coastal Antarctic regions.

4.5 Conclusions

In this study, we present the first combined investigations of δ^{66}Zn and δ^{114}Cd to assess the sources of Zn and Cd as well as the biogeochemical and physical processes affecting their distributions in two distinct coastal Antarctic systems. Firstly, in the AS, mCDW is a known primary source of Zn and Cd and this inflowing water mass is characterised by δ^{66}Zn and δ^{114}Cd values that are identical to global deep-water signatures. This mCDW signature stays constant during the transport of mCDW over the continental shelf in the inflow and outflow into and out of the ice shelf cavity, confirming that both shelf sediments and ice shelf meltwater only supply a minor amount of Zn and Cd (that is not sufficient to affect isotopic compositions), agreeing with previous observations based on [dZn] and [dCd] (Tian et al., 2023b). Secondly, in the WS, compared to other stations, the shelf station near the ice sheet exhibits uniformly-lower [dZn] and [dCd] with homogeneous δ^{66}Zn and δ^{114}Cd that are indistinguishable from deep-water signals in the upper 250 m, implying that meltwater is not a significant Zn and Cd source. A strong correlation between dissolved concentrations and salinity in dense shelf water, pre-WSBW, WDW, and WSDW suggests physical mixing with metal-rich water masses as pre-WSBW descends. Nearly identical δ^{66}Zn and δ^{114}Cd compared to deep-water signatures observed among these water masses and AABW suggest that universal deep-water signatures are set early in the WSBW formation and remain constant as it enters the global ocean. Furthermore, based on the notable δ^{114}Cd vertical profile disparities between the outer and inner WG, the inner WG appears to have unique biogeochemical settings, exhibiting a considerably lighter Cd isotopic signature (+0.07‰) between 250 m and 1500 m,

compared to the outer WG (+0.23‰). We postulate that this difference is likely due to the reduced ventilation of waters within the gyre. Lastly, in the surface layer, clear closed-system Rayleigh fractionation trends for $\delta^{114}Cd$ indicate that $\delta^{114}Cd$ is predominantly controlled by biological uptake, whereas such trends for $\delta^{66}Zn$ are less apparent, likely due to the interplay of biological uptake, ligand complexation, and adsorption. Furthermore, modelled fractionation factors (α) for $\delta^{114}Cd$ in the haptophyte bloom (0.99930 to 0.99960) are lower than in the diatom bloom (0.99970 to 0.99990), potentially due to varying Cd transporters or pathways utilized by haptophytes and diatoms. Conversely, $\delta^{66}Zn$ in the surface layer may be regulated by multiple processes, but similar α values observed at one station in the haptophyte bloom (0.99995) and the diatom bloom (0.99980 to 0.99995) suggest that Zn assimilation by both haptophytes and diatoms yields similar isotopic fractionation effects. Overall, our findings suggest that (global change induced) increasing glacial melt as such will not contribute substantial amounts of dissolved Cd and Zn to coastal Antarctica, nor is it likely to substantially affect the isotopic compositions. However, coinciding changes in circulation, ventilation, biological activity, or particle loading (and thus scavenging intensity) could influence the biogeochemistry of Cd and Zn. The current data set provides a first baseline to assess any future consequences of such interactive effects that are inherently difficult to predict.

CHAPTER 5

ISOTOPIC COMPOSITION OF DISSOLVED IRON IN THE WEDDELL SEA: FATE OF SEDIMENTARY IRON AND EVIDENCE FOR ITS TRANSPORT

Hung-An Tian, Mathijs van Manen, Zach B. Bunnell,
Gert-Jan Reichart, Tim M. Conway, Rob Middag

In preparation

Abstract

The Weddell Sea (WS) in the Southern Ocean is a key hub in ocean circulation and hence biogeochemical cycling. Processes such as external sources and biological cycling that occur within the WS affect trace metal concentrations with consequences for the wider Southern Ocean via ocean currents and formation of deep waters. As such, the WS plays a crucial role in both regional and global elemental cycling of bio-essential trace metals such as Fe. The concentrations of dissolved Fe ([dFe]) combined with the isotopic composition (δ^{56}Fe) in the western WS (south of 60°S), provide insights into the underlying processes. We observed an increase in [dFe] associated with glacial melting and negative Fe isotopic signatures in the upper 250m towards the Antarctic Peninsula, implying that glacial meltwater is a significant Fe source that potentially advects along a isopycnal near the surface towards the central WS. Additionally, within ~200 m above the seafloor of the continental shelf, sedimentary processes including reductive dissolution (RD) supply isotopically light Fe to the overlying shelf water (–1.25 to –1.37‰), with up to 90% of Fe estimated to be derived from RD. This primary light signature subsequently evolves towards heavier compositions as this water descends along the continental shelf slope, likely due to physical mixing with Warm Deep Water (WDW) and Weddell Sea Deep Water (WSDW). Lastly, we also noted a persistent δ^{56}Fe minimum (–0.66 to –0.34‰) at intermediate depths (~200-300 m), consistent with previous Southern Ocean observations close to the WS (north of 60°S). Our results suggest long-distance transport of reductive Fe derived either from the Peninsula shelf sediments and/or other regions where WDW carries this sedimentary-derived Fe along the pathway of the circulation within the Weddell Gyre.

5.1 Introduction

Marine phytoplankton are responsible for about 40-50% of total carbon fixation on Earth (Morel and Price, 2003); as such, marine primary productivity has significant impacts on the changing global climate (e.g., Behrenfeld et al., 2006). As the most abundant metal found in most marine biogenic particles (e.g., phytoplankton) (Twining and Baines, 2013; Twining et al., 2004), iron (Fe) is known to operate in various electron transport systems associated with multiple metabolic processes of marine phytoplankton, such as photosynthesis, respiration, and nitrogen fixation (Morel and Price, 2003; Twinging et al., 2013 Twining and Baines, 2013). Consequently, the availability of Fe in oceans plays a critical role in phytoplankton growth and, in turn, CO_2 exchange over the air-sea interface. In the Southern Ocean, the largest high-nutrient and low-chlorophyll (HNLC) zone in the global ocean, where nearly 40% of anthropogenic CO_2 uptake by ocean takes place (Landschützer et al., 2015; Sabine et al., 2004), depletion of bioavailable Fe and scarce availability of light are found to be the two primary limiting factors to phytoplankton growth over a large range of the surface Southern Ocean, while macronutrients such as PO_4 and NO_3 remain replete (Boyd et al., 2001; Mitchell et al., 1991 Boyd et al., 2007; de Baar et al., 1995; de Baar et al., 1999; Martin et al., 1990). Over the past decades, multiple external Fe sources have been suggested that can supply Fe and trigger phytoplankton growth as well as cause spatial variation of primary productivity in the surface Southern Ocean (e.g., Sohrin et al., 2000; Tagliabue et al., 2014a) including upwelling of Fe-rich deep waters (de Baar et al., 1995; Klunder et al., 2011; Sieber et al., 2021; van Manen et al., 2022); continental sediments (Tagliabue et al., 2009; Tian et al., 2023a, Chapter 3), drifting iceberg melting (Lin et al., 2011; Raiswell, 2011), sea ice melting (Lannuzel et al., 2007; Lannuzel et al., 2010), glacial melting (Gerringa et al., 2012, 2020b), and hydrothermal venting (Sieber et al., 2021; Tagliabue et al., 2010). Nevertheless, the exact constraints of these sources as well as their influence on Fe cycling and the response from the marine ecosystem in the Southern Ocean are still poorly known.

The Weddell Sea (WS), located in the Atlantic sector of the Southern Ocean, is essential to understanding global oceanic circulation and climate dynamics. Its key feature, the Weddell Gyre (WG), is a wind-driven cyclonic system around 50°S, between ~60°W and ~20ºE (Deacon, 1979; Park et al., 2001). Flowing along with the southern part of the eastward Antarctic Circumpolar Current (ACC), Circumpolar Deep Water (CDW, also called Warm Deep Water – WDW – within the gyre) enters the WG east of 20-30ºE and is further transported along the southern limb of the WG to the western boundary of the WG (50°W) bordered by the Antarctic Peninsula (Deacon, 1979; Gouretski and Danilov, 1993). After turning from a westward to a northward path along the Antarctic Peninsula, the WG circulation is completed by eastward movement along the northern boundary (55-60°S) bordered by the frontal structure of the southern ACC. This overall cyclonic circulation facilitates the exchange of the Southern Ocean water masses with the WS waters and promotes the transport of waters within the WS (reviewed by Vernet et al. (2019)).

Another significant feature is the formation of global deep waters, particularly in the southern and western WS (e.g., Filchner-Ronne Ice Shelf) during winter due to extensive sea ice production and brine rejection (Nicholls et al., 2009; Orsi et al., 2002). As a result, Weddell Sea Bottom Water (WSBW) forms by highly saline and dense shelf water descending along the shelf floor and the continental shelf slope in the western and southern WS that is modified by mixing with WDW and its underlying water, Weddell Sea Deep Water (WSDW) (Foldvik et al., 1985; Foster and Carmack, 1976). This resultant mixture is then transported northward and subsequently overflows into the Scotia Sea (e.g., Wilchinsky and Feltham, 2009) and eventually enters the Atlantic sector of the Southern Ocean as part of Antarctic Bottom Water (AABW) which fills the deepest layer of the global ocean, playing a critical role in the global ocean circulation (Orsi et al., 1999 Orsi et al., 1999). As a major site of AABW formation – a numerical modelling result shows that ~50% of global AABW is supplied by an Atlantic source (Beckmann et al., 1999) – the WS contributes extensively to global thermohaline circulation (‘global conveyor belt’), which is crucial for the distribution of heat and nutrients across the

world's oceans, affecting both regional climates and marine ecosystems.

Over the past 15 years, the international GEOTRACES program has promoted the utilization of dissolved Fe isotopic composition (δ^{56}Fe) for constraining the external sources of Fe to the ocean and investigating internal biogeochemical processes that affect the distribution and cycling of Fe in the oceans (Conway et al., 2021; Fitzsimmons and Conway, 2023; Schlitzer et al., 2018). Taking advantage of distinct isotopic signatures that result from different isotopic fractionation effects (Dauphas et al., 2017), δ^{56}Fe enables us to gain further insights into internal biogeochemistry processes such as biological assimilation (Ellwood et al., 2020; Ellwood et al., 2015), adsorption (Crosby et al., 2007; Labatut et al., 2014; Radic et al., 2011); remineralization (Abadie et al., 2017; Sieber et al., 2021), and ligand complexation (Dideriksen et al., 2008; Fitzsimmons et al., 2015; Morgan et al., 2010), improving our understandings of how these processes play a role in marine Fe cycling (König and Tagliabue, 2023; Sieber et al., 2021). Furthermore, distinct δ^{56}Fe signatures from different external sources, including atmospheric deposition, continental margins, rivers, hydrothermal vents, upwelling of Fe -rich deep waters, and cryosphere (sea ice/icebergs/ice shelves and glaciers), also help us to constrain the input of Fe to the oceans (recently reviewed by Fitzsimmons and Conway (2023)) and to estimate their relative contributions (e.g., Conway and John, 2014a), as well as to trace the transport of Fe in the oceans (e.g., Abadie et al., 2017; Sieber et al., 2021).

Although there is a relatively large number of studies investigating the dissolved Fe concentrations in the WS (de Baar et al., 1990; Klunder et al., 2011; Klunder et al., 2014; Lannuzel et al., 2008; Lin et al., 2011; Sanchez et al., 2019; Sañudo-Wilhelmy et al., 2002; Shaw et al., 2011), to date, there is a lack of investigation of dissolved δ^{56}Fe in the inner WS (~south of 60°S), and only a handful of studies of δ^{56}Fe in the northern outer WS (north of 60°S, e.g., Abadie et al., 2017; Sieber et al., 2021). The scarcity of δ^{56}Fe data in the WS hinders our interpretation of the biogeochemistry and cycling of Fe in such an

extensive gyre system with interactions and connections to the Southern Ocean and Antarctic ice sheets. For example, based on δ^{56}Fe data collected from a few stations located in the north-east WG, Abadie et al. (2017) and Sieber et al. (2021) suggested that Fe could be derived from subsurface remineralization or sediments on the Antarctic Peninsula shelf, respectively, and that this Fe could be further transported into the WG and Southern Ocean following the ACC, and ultimately the South Atlantic via the upper Circumpolar Deep Water (UCDW) and Antarctic Intermediate Water (AAIW). Those studies also noted crustal Fe isotope signatures in AABW, which is at least partially derived from deep water formation in the WS. These studies imply that regional biogeochemical processes and sources of Fe in the Weddell Gyre may subsequently impact regional Fe cycling at a range of depths in the wider oceans.

In this study, we present the first dissolved δ^{56}Fe dataset for the inner WS, from a transect in the western WS, extending from the east of the Antarctic Peninsula shelf towards the central WS basin, where previous studies have identified Fe enrichment linked to sediments (Hatta et al., 2013; Klunder et al., 2014; Sieber et al., 2021). This transect covers the continental shelf of the Antarctic Peninsula (eastern side), the continental shelf slope, as well as the off-shore region in the deep basin, allowing us to investigate the potential sources of Fe, the transport of Fe within the WS, and the processes that affect dissolved Fe concentrations and isotopic composition during the formation of WSBW.

5.2 Materials and methods

5.2.1 Study area and shipboard sampling

GEOTRACES process study (ID: GApr12; expedition: PS-117) was conducted on the German icebreaker R/V Polarstern during Austral Summer (December 2018 to February 2019) in the western WS (63-66ºS, 36-54ºW). Seawater samples (4 L and 1 L, 4 L for near surface samples) were collected from 12 stations that are grouped into the shelf stations (Stns 95, 93, and 91), the continental shelf slope stations

(Stns 82, 85, 75, 73, 70, and 67), and the off-shore stations (Stns 65, 61, and 56), based on their geographical location (Fig. 5.1). The detailed sampling procedure for dissolved metal concentrations and isotopic compositions was as previously reported by van Manen et al. (2022) and Chapter 4). Briefly, samples for dissolved Fe isotope analysis were collected using the Royal Netherlands Institute for Sea Research (NIOZ) "Titan" ultra-clean sampling system, mounted with multiple auxiliary sensors for basic parameters (Seabird SBE 911+, e.g., salinity, temperature, and fluorescence,) (de Baar et al., 2008; Rijkenberg et al., 2015). Filter cartridges (0.2 µm, AcroPak-400, VWR, precleaned with HCl and stored in MQ water before used) were used to filtered seawater into 4 L LDPE cubitainers (for surface samples) and 1L LDPE bottles. The filtered samples were subsequently acidified to reach 0.024 M of HCl (pH of ~1.8) using 12 M ultrapure concentrated HCl (Baseline, Seastar Chemicals Inc.). Finally, acidified samples were stored at room temperature for over five months before performing analysis for dissolved Fe concentration and isotopic composition at NIOZ.

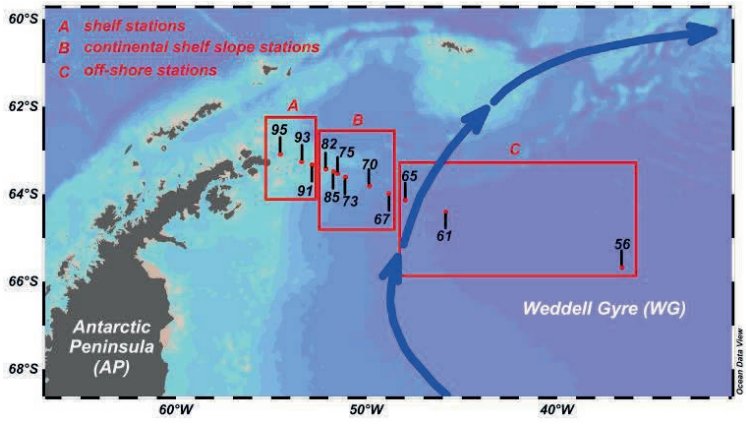

Figure 5.1 Sampling stations of expedition PS117. Samples were collected during Austral Summer (December 2018 to February 2019) from 12 stations that consist of the shelf stations (Stns 95, 93, and 91), the continental shelf slope stations (Stns 82, 85, 75, 73, 70, and 67), and the off-shore stations (Stns 65, 67, and 61). The blue arrows indicate the Weddell Gyre circulation based on Reeve et al., 2016 and Chapter 4).

5.2.2 Analysis of macronutrients and oxygen isotopic composition ($\delta^{18}O$)

5.2.2.1 Macronutrients

Nutrient analysis for phosphate, silicate, nitrite, and nitrate with nitrite was performed in the NIOZ shipboard analytical container during PS-117 (Chapter 4). A detailed protocol has been described by Gerringa et al. (2019). Briefly, unfiltered seawater samples (~50 mL) were collected from Titan and transferred into 5 ml polyethylene vials (ponyvials) after rinsing three times with the sample before being capped and stored in the refrigerator at 4°C. Prior to analysis, all samples and standards were placed in a dark drawer for up to two hours to let them warm up to room temperature (~21 to 21.5°C). After that, the ponyvials were uncapped and covered with parafilm against evaporation while in the sampler, ready for measurements on a Bran and Luebbe trAAcs 800 Autoanalyzer. All analyses were generally performed within four to five hours after sampling. In this study, phosphate (PO_4) was used to aid in the data interpretation. The precision for the PO_4 measurements was determined (1.5±0.018 µmol L^{-1}, n=196) by measuring a natural sterilized reference material nutrient sample (CA, Kanso, Japan) (at 1.5 µmol L^{-1}, 2 SD=±0.018 µmol L^{-1}, n=196). The accuracy was determined by measuring a NIOZ-made 'cocktail' standard which contains all the nutrients listed above in quadruplicate in every analytical run. The values for PO_4 is 2.395±0.028 µmol L^{-1} (n= 256). The cocktail measurements showed that there were no trends observe during the analytic session, thus concluding that the calibration standards were stable during the expedition.

5.2.2.2 Oxygen isotopic composition ($\delta^{18}O$)

Dissolved seawater samples for $\delta^{18}O$ were collected in 2 mL glasses vial with a polypropylene cap and polypropylene-coated insert. Samples were collected alongside dissolved trace metal samples. The glass vials were then stored in refrigerators at 4°C until analysis. The $\delta^{18}O$ samples were measured using a Liquid Water Isotope Analyzer

(LWIA) (Los Gatos Research, model 912-0008) at NIOZ. The precision of the analysis was estimated to be 0.16‰ (n=13) based on duplicated measurements of in-house standard (North Sea seawater-2018) over 13 analytical sessions. The stable oxygen isotope ratio in this study is expressed as $\delta^{18}O$ with respect to Vienna Standard Mean Ocean Water (VSMOW, International Atomic Energy Agency).

5.2.3 Analysis of dissolved Fe isotopic composition

The analysis of Fe isotopic composition has been previously reported by Tian et al. (2023a) and Chapter 3. Prior to chemical pretreatment (extraction and purification), acidified seawater samples were spiked with a ^{57}Fe-^{58}Fe double spike at least 48 hours prior to analysis with a sample-to-spike ratio of 1:2 (Sieber et al., 2021), guided by sample dissolved Fe concentrations ([dFe]) previously measured by a SeaFAST system and Element 2 ICPMS. After reaching sample-spike equilibrium, samples were processed by extraction and purification steps, following Chapter 3.

5.2.4 Measurements by Multi-Collector ICPMS (MC-ICPMS)

Dissolved Fe isotopic compositions ($\delta^{56}Fe$) were determined by Thermo Neptune Plus multi-collector ICPMS (MC-ICPMS) in the Tampa Bay Plasma Facility at the University of South Florida (USF), using a double spike analytical technique modified from Conway et al. (2013) after initial chemical processing of samples at NIOZ (ISO class 7, ISO class 5 in working hoods), with subsequent purification and analysis at the USF (ISO class 6). The details of the instrumental settings, including introduction system, cones, cup configuration, mass bias correction, and double spike technique performance, are identical to those described by Sieber et al. (2021) and Tian et al. (2023a), and Chapter 3. Here, we express dissolved Fe isotopic compositions in typical delta notations relative to the IRMM-014 standard:

$$\delta^{56}Fe\ (‰) = \left[\frac{(^{56}Fe/^{54}Fe)_{sample}}{(^{56}Fe/^{54}Fe)_{IRMM-014}} - 1\right] \times 1000$$

5.2.4.1 Procedural blank

An estimation of the procedural blank for the method was determined by processing acidified ultrapure water through the same method used for natural samples (Tian et al., 2023a and Chapter 3). The total procedural blank is ~0.66 ng, which is generally two orders of magnitude lower than natural [dFe] in our samples after the pretreatment, as well as being too small to measure δ^{56}Fe; as such we follow Sieber et al. (2021) and do not apply blank corrections to [dFe] or δ^{56}Fe.

5.2.4.2 Analytical precision and accuracy

As described in Chapter 3, external precision of δ^{56}Fe measurements at USF is determined by the long-term instrumental precision on the secondary NIST SRM 3126a, with a value of +0.36±0.05‰ (mean±2SD, n=524) obtained over 37 sessions (Hunt et al., 2022), which agrees with literature values (Conway et al., 2013; +0.35±0.08‰; +0.39±0.13‰, Rouxel and Auro, 2010; +0.32±0.02‰, Sun et al., 2021). Consequently, we assign 0.05‰ to be the overall analytical uncertainty and apply this to all samples, except for those where the two standard errors (2 SE) of an individual analysis is larger, in which case we use this as measure of uncertainty. The accuracy of the applied method was tested by doping the same secondary Fe standard (NIST-3126a) into acidified MQ that was processed as a sample and measured alongside natural samples. The average δ^{56}Fe of +0.35±0.02‰ (2 SD, n=3) of this test agrees with the expected value.

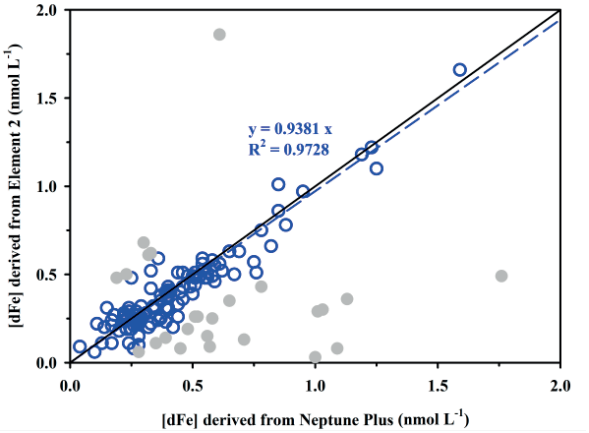

Figure 5.2 Linear regressions of dissolved Fe concentrations ([dFe]) derived from ICPMS (Element 2) versus concentrations derived from ICPMS (Neptune Plus) for PS117 expedition. Measurements from both expeditions were conducted at NIOZ (Element 2) and the USF (Neptune Plus). The blue-dashed line and the black solid line represents the regression line and 1:1 line. Note that the intercept of regression is set to 0. [dFe] used in this study are means of two measurements. However, for samples that showed large absolute difference of concentrations between two measurements – namely, the absolute difference is larger than 0.1 nmol L^{-1} plus 10% of Element 2-derived [dFe] – [dFe] are selected based on oceanic consistency; these data is highlighted in grey. If only the Element 2-derived [dFe] was selected (i.e., the Neptune Plus-derived [dFe] was excluded), the δ^{56}Fe value was also not included in this study. In contrast, if only Neptune Plus-derived [dFe] was selected (i.e., Element 2-derived [dFe] was excluded), the δ^{56}Fe value was still included.

[dFe] derived from the isotope dilution technique after measurement using the Neptune Plus MC-ICPMS agreed well with [dFe] obtained from the SeaFAST based measurements on the Element 2 ICPMS. In this study, since there is good agreement between the two methods for dFe in most samples (detailed in Fig. 5.2 and Fig. 3.2, Chapter 3), we use the mean [dFe] calculated for each sample from the two methods.

5.3 Results

5.3.1 Oceanographic setting

Based on potential temperature (referred to as θ hereafter) and salinity (referred to as S hereafter) diagram (Fig. 5.3a) and previous observations (e.g., Fahrbach et al., 2004; Klatt et al., 2005; Middag et al., 2013), there are five primary water masses identified along the transect in this study, including Antarctic Surface Water (AASW), Winter Water (WW), Warm Deep Water (WDW), Weddell Sea Deep Water (WSDW), and precursor of Weddell Sea Bottom Water (pre-WSBW) (Fig. 5.3b).

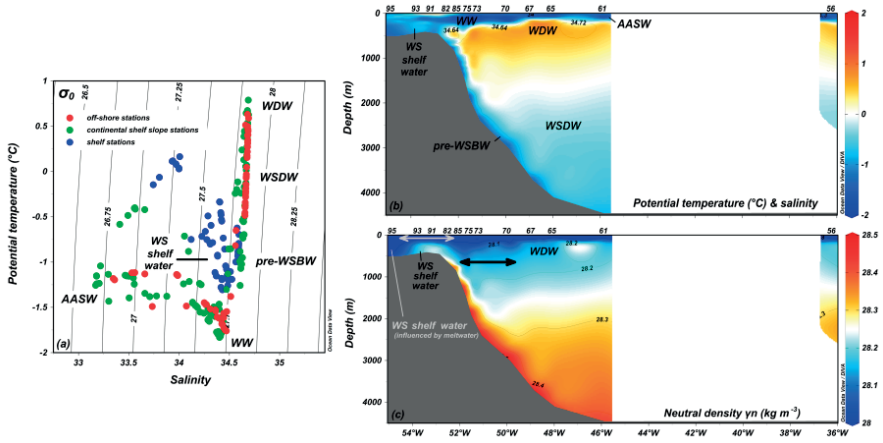

Figure 5.3 (a) Potential temperature (θ)-salinity (S) diagram of all PS117 stations; (b) section profile of θ and S, and (c) section profile of neutral density (γn). In (c), the grey double-head arrow indicates the density isocline of <28.0 kg m^{-3}, whereas the black double-head arrow indicate the density isocline of 28.1-28.2 kg m^{-3}.

AASW (~upper 70, θ>−1.7°C; S<34.3) is generally situated above WW (~70-250 m, θ minimum below AASW) since the former is a result of the latter experiencing heating and ice melting during summer and eventually becomes warmer and less saline (Figs 5.3a and 5.3b). Below WW, WDW is situated between ~230 and 1800 m with warmer features (0>θ>0.8°C, 34.64<S<34.72) than overlying WW since it is originally derived from CDW (Donnelly et al., 2017; Reeve et al., 2016).

Situated deeper than ~1500 m, WSDW (–0.7<θ<0°C, 34.64<S<34.68) is a result of WDW mixing with uplifting WSBW (Fig. 5.3b) (Foster and Carmack, 1976). The latter is formed on the shelf of the Antarctic Peninsula, where dense and cold shelf water forms via sea ice production and brine rejection during winter (Orsi et al., 2002). Given its dense characteristic, extensive vertical mixing leads to a homogeneous water mass on the shelf; in this study we refer to this water as to dense shelf water which subsequently descends along the continental shelf slope and eventually forms WSBW in the deep basin while mixing with WDW and WSDW along the pathway (Fig. 5.3b). The descending water mass situated along the continental shelf slope is referred to as pre-WSBW and is defined based on WSBW characteristics (i.e., θ<–0.7°C, Fahrbach et al., 2004). It should be noted that WSBW is usually situated deeper than 4000 m in this region (Middag et al., 2013) and is not observed in this study since most stations were located closer to the Antarctic Peninsula with shallower depths (Fig. 5.3b). During summer (i.e., the sampling period of this study), waters on the continental shelf stratify due to elevated θ near the surface, leading to a less dense water mass (relative to dense shelf water), located below AASW, that we refer to as WS shelf water (Fig. 5.3b and 5.3c). Essentially, WS shelf water and pre-WSBW exhibit similar θ (θ<–0.7°C, Fig. 5.3a). For clarity, the term “dense shelf water” refers to the dense shelf water formed in winter (not observed during sampling in summer), whereas the term “WS shelf water” refers to the shelf water observed at the shelf stations (deeper than AASW) in this study.

5.3.2 Freshwater input ($\delta^{18}O$)

In this study, we employ seawater $\delta^{18}O$ to estimate input of meteoric freshwater (e.g., glacial melting) and sea ice melting, using a three-component mass balance model (i.e., meteoric water, sea ice melt, and WW) modified from a method used in Randall-Goodwin. et al. (2015):

$$f_{met} + f_{sim} + f_{ww} = 1 \ldots \text{(Eq. 1)}$$

$$f_{met} \times \delta^{18}O_{met} + f_{sim} \times \delta^{18}O_{sim} + f_{ww} \times \delta^{18}O_{ww} = \delta^{18}O_{observed} \ldots \text{(Eq. 2)}$$

$$f_{met} \times S_{met} + f_{sim} \times S_{sim} + f_{ww} \times S_{ww} = S_{observed} \ldots \text{(Eq. 3)}$$

Here, met, sim , ww, and $observed$, denote meteoric water, sea ice melt, WW, and observed values respectively, whereas f and S denote fraction and salinity respectively. The details of the calculation and assignment of endmembers have been reported in Chapter 4. The fraction of meteoric water (f_{met}) in the upper 500 m showed an increasing gradient from the central WS basin (the off-shore stations) towards the Antarctic Peninsula (the shelf stations) (Fig. 5.4a).

The highest f_{met} was estimated in the upper 250 m at Stn 95 (>4%), whereas at Stns 93 and 91 it decreased to 2-3% (Fig. 5.4a). The fraction of sea ice melt (f_{sim}) was generally elevated in the upper 20 m relative to greater depths, with over 5% estimated in the upper 10 m at some continental shelf slope stations (Stns 70 and 67) and the off-shore stations (Fig. 5.4b). At the shelf stations, f_{sim} show negative features (indicative of sea ice formation rather than melting) in the upper 20 m, with values decreasing from 0% (Stn 91) to –4.4% (Stn 95) (Fig. 5.4b).

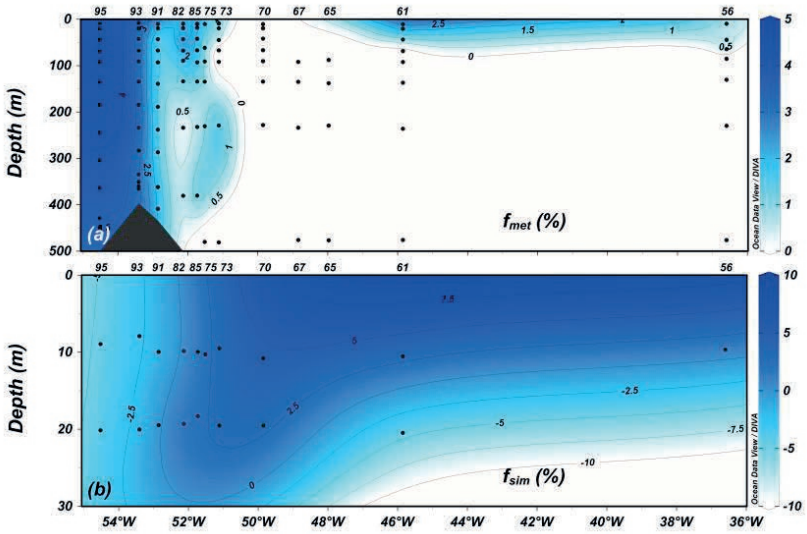

Figure 5.4 Estimated fraction of meltwater input of (a) meteoric water (f_{met}, upper 500 m) and (b) sea ice melting (f_{sim}, upper 30 m). The fractions were estimated using Oxygen isotopic composition ($\delta^{18}O$) following a three-component mass balance model described in Randall-Goodwin. et al. (2015) and Chapter 4.

5.3.3 Dissolved Fe concentrations and isotopic compositions

At the shelf stations, [dFe] generally increased from the surface to greater depths and ranged from 0.05 to 1.32 nmol L^{-1} and from 1.20 to 7.14 nmol L^{-1} in the upper 20 m and the near-bottom samples, respectively (Fig. 5.5a). Although the shelf stations (Stns 95, 93, and 91) generally exhibited a similar vertical [dFe] profile (Fig. 5.5), Stn 95 (the most shelf proximal station) showed higher [dFe] throughout the water column, compared to the other two shelf stations (Fig. 5.5a). These [dFe] vertical profiles are mirrored by $\delta^{56}Fe$ (i.e., decreasing [dFe] accompanied by increasing $\delta^{56}Fe$), around –0.19‰ in the upper 20 m and ranged from –1.38 to –1.25‰ in the near-bottom samples, except for two samples at Stn 95 (upper 20 m) that exhibit relatively low $\delta^{56}Fe$ values (~–1.24‰) (Fig. 5.5b). All $\delta^{56}Fe$ values observed at the shelf stations were lower than 0‰.

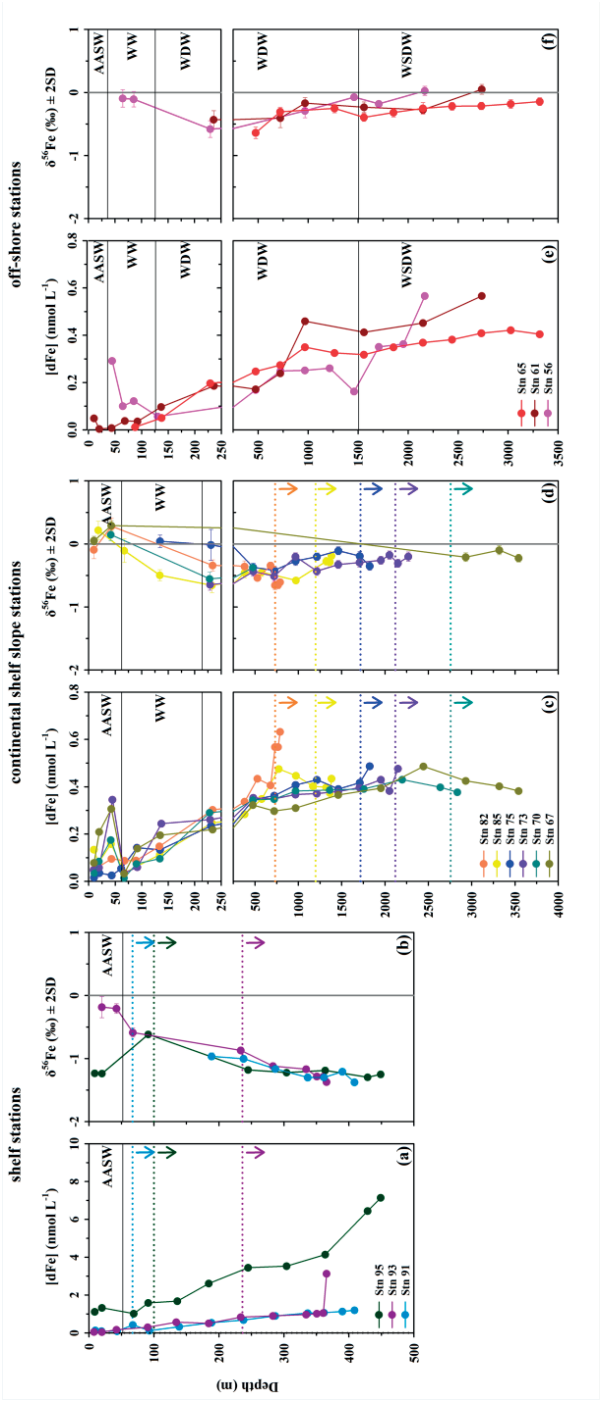

Figure 5.5 profiles of dissolved Fe concentrations ([dFe]) and isotopic ratios (δ^{56}Fe). (a) and (b) the shelf stations; (c) and (d) the continental shelf slope stations; (e) and (f) the off-shore stations. The grey solid lines indicate the crustal δ^{56}Fe (~0‰, Beard et al., 2003). The dotted lines and arrows in (a) and (b) indicate the layers of WS shelf water defined based on the neutral density <28.0 kg m^3 and θ<–0.7 ºC at the shelf stations, whereas the dotted lines and arrows in (c) and (d) indicate the layers of pre-WSBW defined based on θ<0.7ºC. The error bars for δ^{56}Fe are 2 standard deviations.

At the continental shelf slope stations, analogously to the shelf stations, [dFe] show a general increasing trend from the upper 20 m (ranging from 0.02 to 0.21 nmol L^{-1}) to greater depths (ranging from 0.37 to 0. 63 nmol L^{-1}) (Fig. 5.5c). It should be pointed out that [dFe] at the higher end of the range at greater depths (i.e., 0.63 nmol L^{-1}) is observed in one near-bottom sample (Stn 82) collected near to the shelf stations; the other near-bottom samples at the continental shelf slope stations exhibited relatively homogeneous [dFe] (~0.30 to 0.40 nmol L^{-1}) (Fig. 5.5c). $\delta^{56}Fe$ did not show mirrored profiles for the continental slope station, in contrast to the shelf stations – a $\delta^{56}Fe$ minimum (–0.66 to –0.34‰) is observed between 200 to 300 m, whereas higher $\delta^{56}Fe$ values are observed in the upper 20 m (–0.09 to –0.22‰) and near-bottom (–0.35 to –0.19‰) except for one relatively low $\delta^{56}Fe$ observation (–0.61‰, near-bottom) with elevated [dFe] at Stn 82 (Figs 5.5c and 5.5d).

At the off-shore stations, akin to the other station groups, [dFe] generally decreased from the surface to depth, with values around 0.05 nmol L^{-1} in the upper 20 m and values ranging from 0.40 to 0.57 nmol L^{-1} at greater depths (2100 to 3300 m) (Fig. 5.5e). However, much lower [dFe] is observed in the upper ~750 m (< 0.3 nmol L^{-1}), compared to the other station groups. For $\delta^{56}Fe$, a minimum (–0.64 to –0.43‰) similar to the continental shelf slope stations is also observed at the intermediate depths (200-500 m), whereas ~0‰ of $\delta^{56}Fe$ is observed both shallower and deeper (Fig. 5.5f).

5.4 Discussion

In this study, we aim to investigate the cycling of Fe using the first observational transect data of the Fe isotopic composition reported for the WS. First, we evaluate the potential Fe sources to the WS, including glacial melting and continental shelf sediments. Second, we discuss the processes that result in a transition of the $\delta^{56}Fe$ signature between WS shelf water and pre-WSBW as the precursor of AABW (i.e., WSBW and WSDW) forms. Finally, combined with $\delta^{56}Fe$ observations in the Southern Ocean, we provide evidence for long-

distance transport of sedimentary Fe derived from the Antarctica Peninsula shelf sediments.

5.4.1 External sources of dissolved Fe in the WS

5.4.1.1 Glacial melting

At the shelf stations, relatively high f_{met} (>4%) is estimated in the upper ~250 m at Stn 95 and this fraction gradually decreases towards the central WG (Fig. 5.4a), indicating glacial meltwater input from the tip of the peninsula that is transported offshore. Coincidently, over the same depth interval, increasing [dFe] from Stn 91 (ranged from 0.10 to 0.68 nmol L^{-1}) to Stn 95 (ranged from 1.02 to 3.50 nmol L^{-1}) suggests a supply of Fe from glacial melting (Figs. 5.5) (Annett et al., 2015; Gerringa et al., 2012, 2020b). This is also supported by a significant correlation ($p<0.05$) between [dFe] and f_{met} in the upper 250 m at the shelf stations (Fig. 5.6b).

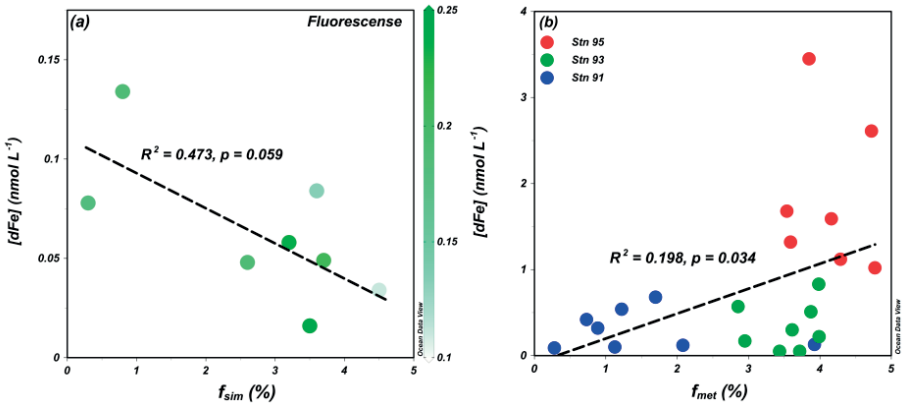

Figure 5.6 Linear relationships between dissolved Fe concentration ([dFe]) and (a) fraction of sea ice melting (f_{sim}) and (b) meteoric water fraction (f_{met}). In (a), samples with positive f_{sim} in the upper 20 m of all stations are shown; the colour grading represent fluorescence. In (b), samples in the upper 250 m of the shelf stations are shown.

Fe isotopic compositions in the upper 250 m at the shelf stations were generally lower than the crustal signal (+0.1±0.1‰, Beard et al., 2003;

Conway et al., 2019), especially two depths at the very surface (~20 m) at Stn 95 (the most proximal station to the glacier) exhibit a minimum of δ^{56}Fe value (–1.24±0.01‰) (Fig. 5.5b). Such a light signal potentially results from reductive dissolution of Fe or other microbially mediated redox reactions that reduce Fe^{3+} to Fe^{2+} in subglacial discharge (Henkel et al., 2018). Analogously, low δ^{56}Fe (–2.6‰) was reported in Blood Falls beneath the Taylor Glacier, East Antarctica, which was attributed to microbial reducing activity and reductive dissolution that promotes Fe^{2+} liberation (Mikucki et al., 2004). However, while our δ^{56}Fe data implies that Fe in glaciers indeed may experience (microbial) redox reactions prior to entering the coastal waters, it should be noted that δ^{56}Fe in subglacial discharge is subject to subglacial conditions (e.g., the intensity of chemical weathering, particle loading, Fe speciation, and saturation of Fe-binding ligands) (Henkel et al., 2018; Krisch et al., 2021; Stevenson et al., 2017; Tian et al., 2023a, Chapter 3). Therefore, we suggest that, to constrain δ^{56}Fe in glacial meltwaters, it is necessary to take geochemical settings in corresponding subglacial systems into account. Nevertheless, in this study increasing [dFe] and elevated f_{met} close to the peninsula, together with generally low δ^{56}Fe values, suggest glacial meltwater input is an important source of Fe to the shelf region. This input could advect between the shelf region and the central WS basin following isopycnals along the surface (<28.0 kg m^{-3}), potentially supplying dFe to the surface due to reduced density (Fig. 5.3c).

5.4.1.2 Continental shelf sediment

To date, two main mechanisms have been identified that can supply Fe from sediments to seawater. First, reductive dissolution (RD) of Fe oxyhydroxide minerals catalysed by microbial respiration within sediments, leads to [dFe] (mostly Fe^{2+}) several orders of magnitude higher in porewaters then overlying waters which subsequently diffuses to into the overlying seawater (Elrod et al., 2004; Jung et al., 2019; Radic et al., 2011). Second, abiotic non-reductive dissolution (NRD) can release Fe from lithogenic particles via dissolution or

desorption of sediments (Abadie et al., 2017; Homoky et al., 2013; Radic et al., 2011). Recently, it has also been suggested that Fe colloids resulting from lithogenic weathering in oxic sediments can be an dominant form of sedimentary Fe in porewaters (Homoky et al., 2021). In the present study, elevated [dFe] towards the seafloor is observed at the shelf stations, with highest values near the bottom (~1 to 7 nmol L^{-1}) (Fig. 5.5a). Furthermore, decreasing beam transmission (%) towards the seafloor (within ~200 m above the seafloor) implies bottom resuspension that could supply sedimentary Fe from continental shelf sediments (Fig. 5.7). Assuming bottom resuspension is the main transfer pathway for Fe from sediments to overlying waters, the elevation of seawater dFe would likely be an integral signal of Fe from both porewater and particle desorption (Elrod et al., 2004, Chapter 3).

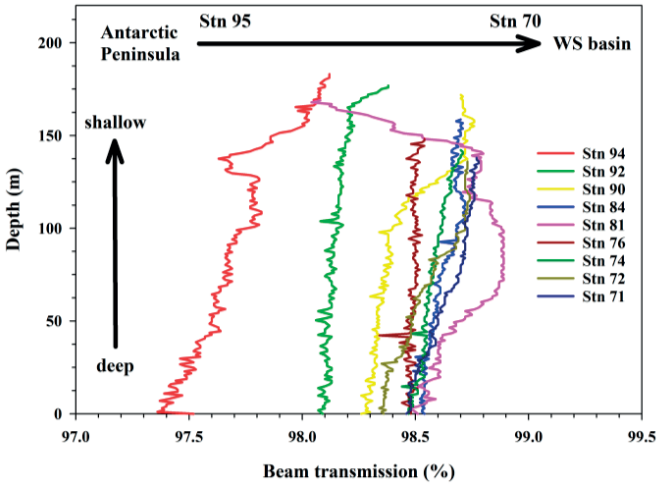

Figure 5.7 Beam transmission (%) within 200 m above the seafloor. The measurement at 0 m indicate the near-bottom measurement (~20 to 30 m above the seafloor). Note that data were obtained from transmissometer installed on the regular CTD deployed by the research team of Alfred Wegener Institute for Polar and Marine Research. Therefore, the station numbers do not match with trace metal stations. Here we show the measurements at nearby stations relative to trace metal stations.

The Fe isotopic signatures for the abovementioned processes have been reported – RD induced by bacterial reduction results in porewater δ^{56}Fe spanning from –3.5 to –1.5‰ (Fitzsimmons and Conway (2023)), whereas NRD and Fe colloids formed via lithogenic weathering have a near-crustal signal (~+0.1‰, Conway and John, 2014a; Homoky et al., 2021). Here, δ^{56}Fe within ~200 m above the seafloor at all three shelf stations shows a decreasing trend towards the seafloor, with lowest values observed at the near-bottom samples (–1.37 to –1.25‰) (Fig. 5.5b). Given that continental sediment in the western WS has been suggested to be reducing (Howe et al., 2007; Middag et al., 2013), these light values imply the release of dFe from RD via redox reactions within shelf sediments (Jung et al., 2019; Sieber et al., 2021). However, since these δ^{56}Fe values are between the higher end of the reported range for RD δ^{56}Fe (up to –1.5‰) and NRD δ^{56}Fe (~+0.1‰), we cannot exclude the possibility of NRD. Assuming that RD and NRD both supply Fe to the overlying water, we can then estimate the relative contributions of each component with a two-component mass-balance model, taking the range of reported RD δ^{56}Fe (i.e., –3.5 and –1.5‰), NRD δ^{56}Fe (i.e., +0.1‰), and a mean of δ^{56}Fe of the near-bottom water from all shelf stations (–1.33‰) into account. As such, a contribution of ~40 to 90% of Fe from RD was estimated, with Fe from NRD decreasing from ~60 to 10%, using the upper and lower bound for the RD endmember, respectively. Although there are no porewater δ^{56}Fe measurements available from this region to directly determine the actual endmember for RD, our δ^{56}Fe data suggest that RD is an important process in supplying dFe in the western WS. This is in agreement with previous observation near West Antarctic Peninsula (WAP) (Annett et al., 2015; de Jong et al., 2012; Jiang et al., 2019; Sherrell et al., 2015; Sieber et al., 2021), indicating that both WAP and East Antarctic Peninsula (EAP) are significant contributors of sedimentary light Fe. In the following section, we further discuss whether this sedimentary Fe is transported from the shelf to the central basin, following the gyre circulation.

5.4.1.3 Sea ice melting?

Sea ice melting has been proposed to be an important source of Fe to Fe-deplete surface waters in the western WS – Fe trapped in brine pockets during sea ice formation is released to underlying seawater in spring/summer, fertilizing the surface ocean of coastal Antarctica (Lannuzel et al., 2007; Lannuzel et al., 2008). Given that the majority of the WS is covered by multiyear ice (Parkinson and Cavalieri, 2012; Turner et al., 2020), long-term dust deposition accumulated on sea ice could potentially serve as a source of Fe to the WS, as suggested for aluminium in the same region (Middag et al., 2013).

In the present study, most stations (except the shelf stations) exhibit positive f_{sim} in the upper 20 m, indicating sea ice melting (Fig. 5.4b). However, increasing f_{sim} corresponds with decreasing [dFe], suggesting that either surface [dFe] is mainly controlled by biogeochemical processes (e.g., biological uptake and/or scavenging) or sea ice melting is not a significant source of Fe. Indeed, samples with high f_{sim} generally coinciding with elevated fluorescence (except for Stn 70) implies that low observed [dFe] is a result of biological uptake (Fig. 5.6a). Therefore, if there were any Fe released from sea ice melting, it is likely quickly removed from seawater by biological uptake, leading to a very short residence time for Fe in the surface water of the Southern Ocean as suggested previously (Ellwood et al., 2020; Sieber et al., 2021). This observation – high f_{sim} coinciding with low [dFe] – was also previously observed in the Amundsen Sea (AS) for Fe (van Manen et al., 2022) and for other bioavailable metals such as zinc and cadmium (Tian et al., 2023b), where the chlorophyll concentration in the surface layer (i.e., surface to the depth of chlorophyll maximum) was ~25 times higher than in this study (Chapter 4). Furthermore, in the upper 20 m, the WS exhibits higher f_{sim} (~2.8%) than the AS (~0.34%) (van Manen et al., 2022), however, higher f_{sim} does not correspond with higher [dFe] (WS: 0.07±0.10 nmol L^{-1}; AS: 0.26±0.15 nmol L^{-1}). Taken together, the comparable relationships of f_{sim} and [dFe] from two regions characterized with distinct primary productivity, as well as no observed elevated [dFe] associated with higher f_{sim}, suggest that sea ice melt may not be a

significant Fe source and biological uptake is likely the main process controlling [dFe] in the surface water of the WS (van Manen et al., 2022). Unfortunately, among all the stations characterised by positive f_{sim}, due to extremely low [dFe], only three surface samples in the upper 20 m had sufficient signals allowing δ^{56}Fe analysis, with δ^{56}Fe value (–0.09 to 0.22‰) close to the crustal signature (~0‰, Beard et al., 2003). Nevertheless, these signals may reflect biological uptake rather than lithogenic Fe input as δ^{56}Fe is higher than WW (~–0.22‰, Table. 5.1), the best representative for AASW prior to uptake in spring/summer in this study.

Table 5.1 Dissolved Fe concentrations ([dFe]) and isotopic ratios (δ^{56}Fe) of water masses identified in this study. The definition – potential temperature (θ) and salinity (S) for each water mass follows Fahrbach et al., 2004. Abbreviation: Antarctic Surface Water (AASW), Winter Water (WW), Warm Deep Water (WDW), Weddell Sea Deep Water (WSDW), precursor of Weddell Sea Bottom Water (pre-WSBW), and WS shelf water.

	Definition		[dFe]±2 SD (nmol L^{-1})	δ^{56}Fe±2 SD (‰)
	S	θ (°C)		
AASW	S<34.3	θ>–1.7	0.18±0.61	–0.20±1.15
WW		θ Minimum below AASW	0.11±0.18	–0.22±0.50
WDW	34.64<S<34.72	0<θ<0.8	0.32±0.16	–0.38±0.25
WSDW	34.64 <S<34.68	–0.7<θ<0	0.41±0.15	–0.18±0.20
Pre-WSBW		θ<–0.7	0.43±0.35	–0.39±0.38
WS shelf water		θ<–0.7	0.90±1.33	–1.21±0.27

5.4.2 Difference in δ^{56}Fe between WS shelf water and pre-WSBW: physical mixing

In WS shelf water, [dFe] exhibits great spatial variation – it decreases vertically towards the surface and horizontally offshore – over a large concentration range (0.12 to 7.14 nmol L^{-1}, Fig. 5.5a). In contrast, δ^{56}Fe remains consistently low in WS shelf water (–1.22±0.23‰) (Fig. 5.5b). This light isotope signature, which we attribute to reductive dissolution (RD) supplied from and shelf sediments (near bottom)

and/or glacial melting (the upper 250 m) (section 4.1), might be expected to be attenuated during oxidation/precipitation as Fe^{2+} enters the water column (Dauphas et al., 2017). However, our data – near homogenous light $\delta^{56}Fe$ values over the shelf stations – suggests that the local RD $\delta^{56}Fe$ signature is preserved over the continental shelf over a range of dFe concentrations, and as such with little fractionation effects due to loss of dFe in the water column. This finding, as well as providing a distinct endmember for tracing sediment derived $\delta^{56}Fe$ away from the shelf, adds weight to the use of $\delta^{56}Fe$ as tracers of sediment supply to the open ocean (e.g. Conway and John, 2014a). This result also supports the conclusion by Sieber et al. (2021) that a light Fe signature associated with RD can last during long-distance transport, making $\delta^{56}Fe$ a useful tracer for tracking sedimentary derived Fe.

Assuming the sedimentary Fe flux is similar between dense shelf water (formed in winter, not observed in this study) and WS shelf water (formed in summer, observed in this study), [dFe] and $\delta^{56}Fe$ in dense shelf water should be comparable to observed $\delta^{56}Fe$ in WS shelf water. As such, in the following discussion, WS shelf water is used to represent the descending dense shelf water, despite forming in different seasons. Based on this assumption, the increase of $\delta^{56}Fe$ and decrease of [dFe] observed in pre-WSBW relative to WS shelf water (Figs 5.5 and 5.8a), suggests a transition of $\delta^{56}Fe$ and [dFe] as WS shelf water descends along the continental shelf slope during the cold season, forming pre-WSBW (Figs 5.3b and 5.8b). Taking the near-bottom water at Stn 91 as a starting point ([dFe]: 1.20 nmol L^{-1}; $\delta^{56}Fe$: –1.38‰) representing pre-descending conditions, there is a ~65% of decrease in [dFe] and a change of (~+1.11‰) in $\delta^{56}Fe$ as WS shelf water descends. In a systematic plot of [dFe] and $\delta^{56}Fe$ of WS shelf water and pre-WSBW (Fig. 5.8b), it seems that such moderation is controlled by one single process, following a closed Rayleigh fractionation trend. Here, two potential processes can cause this – adsorption of Fe onto particles and/or mixing with waters with low dFe and high $\delta^{56}Fe$.

First, particle adsorption has been discovered to preferentially remove light Fe from seawater, leading to an isotopically heavy dissolved pool, with $\Delta\delta^{56}Fe_{dissolved\text{-}particulate}$ ranging from +0.02 to +0.67% (Ellwood et al., 2015; Labatut et al., 2014; Radic et al., 2011). However, the observed change of $\delta^{56}Fe$ (+1.11‰) between WS shelf water and pre-WSBW in this study exceeds this reported range, indicating that scavenging may not be the only process leading to the transition of $\delta^{56}Fe$. Further, increasing beam transmission along the continental shelf slope suggest less resuspension of particles compared to the shelf (Fig. 5.7), making particle adsorption unlikely.

Alternatively, physical mixing with WW, WDW, and WSDW as WS shelf water transforms into pre-WSBW can also lead to the transition of $\delta^{56}Fe$ since WW, WDW, and WSDW all exhibit lower [dFe] and higher $\delta^{56}Fe$ relative to WS shelf water (Table 5.1). Taking the means of [dFe] and $\delta^{56}Fe$ in each water mass as endmembers (Table 5.1), the decrease of [dFe] and the transition of $\delta^{56}Fe$ appears to follow the mixing lines between water masses (Fig. 5.8b). In detail, samples from Stn 91 follow a mixing line between WW and the near-bottom sample, implying conservative mixing between two endmembers. Conversely, samples in pre-WSBW follow a mixing line between the near-bottom sample at Stn 91 and WDW (and WSDW), suggesting physical mixing as dense shelf water descends along the slope. This observation is also supported by a significant correlation between salinity and dFe (Fig. 5.8c). This does not imply particle scavenging and/or any input from the slope sediments do not play a role in altering $\delta^{56}Fe$. However, the net effect seems to be mainly controlled by physical mixing.

Based on these observations, we propose that physical mixing is the main mechanism driving the transition of $\delta^{56}Fe$ when downward dense shelf water transforms into pre-WSBW. Given that WSBW is one of the precursors of AABW that is found in different oceanic basins, a sediment-derived isotopic signature is likely lost for AABW due to mixing and any sediment-derived contribution is too small to be quantified in the AABW exiting this region. Instead, due to mixing, a lot of this sediment-derived Fe remains in the region (diluted into WDW or WSDW), either eventually removed by scavenging during the

circulation or potentially supplied to the surface for phytoplankton growth via upwelling.

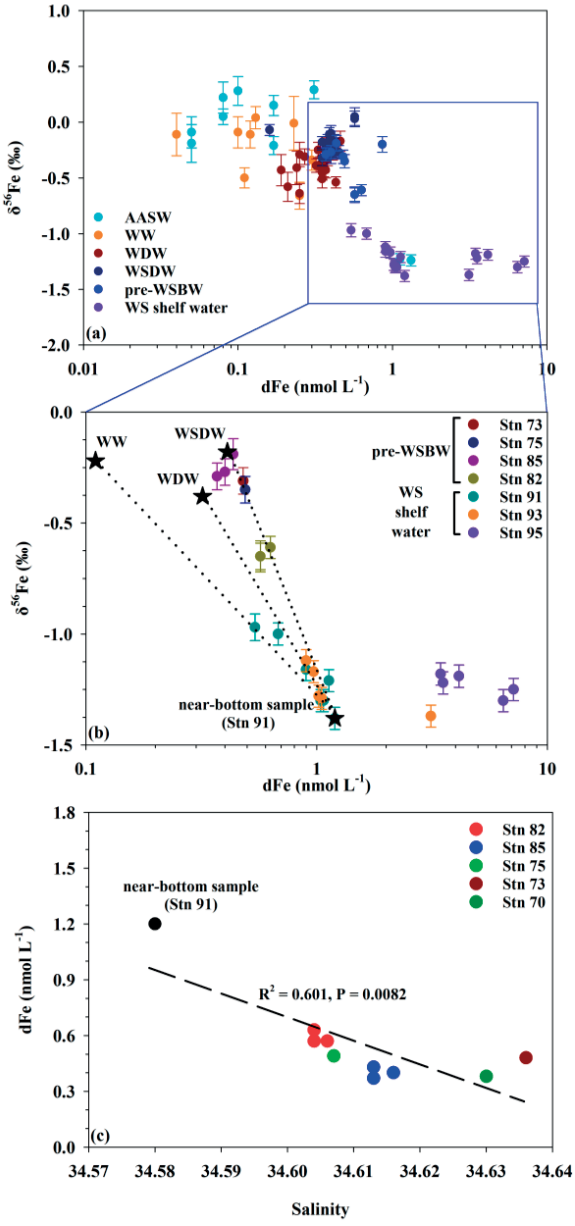

Figure 5.8 Isotopic systematics of dissolved Fe concentrations ([dFe]) isotopic ratios (δ^{56}Fe) in (a) water masses identified in this study (Antarctic Surface Water (AASW), Winter Water (WW), Warm Deep Water (WDW), Weddell Sea Deep Water (WSDW), precursor of Weddell Sea Bottom Water (pre-WSBW), and WS shelf water) and (b) WS shelf water and pre-WSBW. In (b), four endmembers (marked with star signs) are selected for the physical mixing lines (marked with dotted lines) – WW (0.11 nmol L^{-1}; –0.22‰); WDW (0.32 nmol L^{-1}; –0.38‰); WSDW (0.41 nmol L^{-1}; –0.18‰); and the near bottom sample of Stn 91 (1.20 nmol L^{-1}; –1.38‰).

5.4.3 δ^{56}Fe minimum in WDW: evidence for sedimentary Fe transport

Another remarkable feature of our dataset is the δ^{56}Fe minimum (–0.66 to –0.34‰) observed at the intermediate depth (~200-300 m) at most continental shelf slope stations and the offshore stations where upper WDW is located (Fig. 5.5). This δ^{56}Fe minimum is accompanied by elevated [dFe] (up to 0.35 nmol L^{-1}), and is consistent with the observations close to the north-eastern WG by both Abadie et al. (2017) and Sieber et al. (2021). However, there are two different hypotheses put forward to explain the δ^{56}Fe minimum at intermediate depth. Abadie et al. (2017) firstly observed a δ^{56}Fe minimum (–0.74 to –0.17‰) around ~200-800 m in the Atlantic sector (meridional) of the Southern Ocean, including UCDW and AAIW. They attributed these light signals to remineralization in UCDW that originated from Drake Passage and advected with the ACC. Furthermore, based on a similar δ^{56}Fe minimum observed at one station located on the north-eastern WG, they postulated that this minimum could potentially be modulated by similar remineralization occurring in the Southern Ocean, although there was no robust evidence for remineralization (e.g., apparent oxygen utilization) available at this station. Conversely, Sieber et al. (2021) suggested that the isotopically light Fe signal at subsurface (100-300 m) originates from sedimentary input along the Antarctic Peninsula shelf and nearby islands, rather than remineralization. In their data, the δ^{56}Fe minimum (as low as –1.0‰) was accompanied by elevated [dFe] (~0.5 nmol L^{-1}), observed within 100-300 m at the Antarctic Peninsula shelf; and this isotopic signal was further observed at similar depths (100-150 m) at stations close to the north-eastern WG (~–0.5 to –0.75‰), implying a long-distance transport of sedimentary Fe originating from the Antarctic Peninsula into the WS (Hatta et al., 2013; Sieber et al., 2021).

Here, our isotopic data favours the hypothesis that this δ^{56}Fe minimum is indicative of a long-distance sedimentary Fe signal, rather than remineralisation. Firstly, based on the distribution of AOU and PO_4, the most prominent remineralization occurs between 200 and 700 m at stations towards the central WS (i.e., Stns 61 and 56)

compared to at stations towards the shelf (i.e., Stns 75, 73, 70, 67, and 65) (Figs 5.9c and 5.9d). Assuming remineralization is the dominant process as previously purposed, a strong remineralization (i.e., higher AOU) should coincide with high [dFe] and low δ^{56}Fe (Radic et al., 2011). However, our observations do not support this – lower [dFe] corresponded with elevated AOU at 200-500 m towards the central WS, (Figs 5.9a and 5.9d), whilst δ^{56}Fe remains consistently low (–0.50±0.24‰) throughout the stations from the continental shelf slope towards the central WS (Figs 5.9b and 5.5). Consequently, this suggests that, while remineralization can potentially lead to low δ^{56}Fe in seawater (Abadie et al., 2017; Radic et al., 2011), it cannot explain the subsurface δ^{56}Fe minimum, instead there are other process or external input overprinting its isotopic signature and concentration. Secondly, based on elevated θ between 200 and 500 m from Stn 65 towards the shelf indicate the presence of the core of WDW (southwest-northeast ward) in the western limb of WG circulation that include stations towards the shelf (i.e., Stns 75, 73, 70, 67, and 65) (Chapter 4). Since WDW is modified from CDW that receives sedimentary light Fe from the Antarctica Peninsula and islands along the pathway of ACC (Hatta et al., 2013; Klunder et al., 2014; Sieber et al., 2021), following the gyre circulation in the western WS, elevated [dFe] and low δ^{56}Fe values observed at the same depth as WDW (200-500 m) at these stations compared to stations towards the central WS (i.e., Stns 61 and 56), is potentially associated with WDW receiving isotopically light Fe from the Southern Ocean (i.e., UCDW) and sedimentary Fe derived from WS continental shelf along the circulation of WDW. Indeed, based on neutral density (Fig. 5.3c), stratification of WS shelf water may allow dFe derived from the shelf sediments and glacial melting to advect from the shelf stations towards the off-shore stations (~150 to 1000 m, Fig. 5.5) along an isopycnal (28.0 to 28.2 kg m^{-3}, ~200 to 1000 m, Fig. 5.3c), facilitating lateral transport of Fe.

Taken together, our results favour the hypothesis that sedimentary light Fe (as low as ~–1‰) derived from the Antarctic Peninsula shelves can be preserved and transported over a long distance, as proposed by Sieber et al. (2021). Furthermore, the continental shelf elsewhere

in the WS can also contribute to the observed δ^{56}Fe minimum (–0.66 to –0.34‰) at the intermediate depths (~200-300 m) in the WS. Although we cannot disentangle the source (i.e., sedimentary Fe transported with UCDW versus sedimentary Fe derived from the WS continental shelf), this dataset indicates long distance transport of reductively derived Fe from the sediment (Homoky et al., 2009; John and Adkins, 2012; Jung et al., 2019; Sieber et al., 2021).

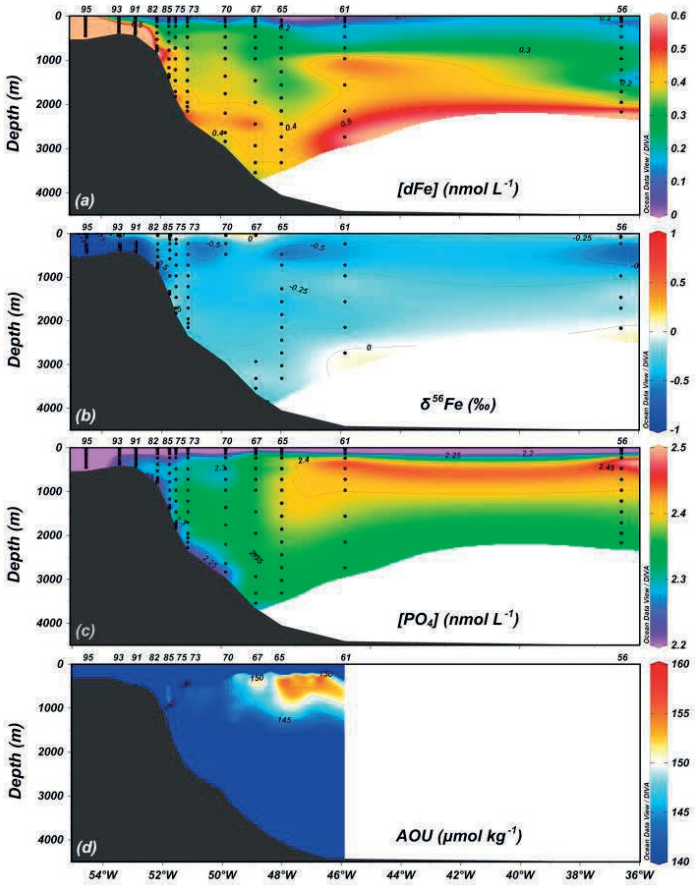

Figure 5.9 Section profile of (a) dissolved Fe concentration ([dFe]), (b) dissolved Fe isotopic ratio (δ^{56}Fe); (c) phosphate (PO_4); and (d) apparent oxygen utilization (AOU). The AOU is derived from Ocean Data View (ODV version 5.3.0, Schlitzer, 2020) using dissolved oxygen data obtained from oxygen sensor installed on the regular CTD deployed by the research team of Alfred Wegener Institute for Polar and Marine Research.

5.5 Conclusions

In this study, we present the first observational transect with $\delta^{56}Fe$ data in the western WS, investigating potential sources of Fe and processes that affect the [dFe] and $\delta^{56}Fe$ during formation of WSBW, and found indications of transport of sedimentary Fe within the WS.

An increasing [dFe] (from 0.68 to 3.5 nmol L^{-1}) corresponding with elevated f_{met} (>4%) in the upper 250 m towards the Antarctic Peninsula suggests glacial meltwater is an significant Fe source to the shelf water. These samples are all characterized by negative Fe isotopic signatures, implying that glacial Fe may be derived from reduction of Fe^{3+} to Fe^{2} induced by microbially redox reactions in subglacial discharge system and potentially supply to the surface following isopycnals (<28.0 kg m^{-3}). Furthermore, sedimentary process also play a critical role in supplying Fe to the overlying water, with generally over 1 nmol L^{-1} of [dFe] and low $\delta^{56}Fe$ values (–1.37 to –1.25‰) observed near the bottom at the shelf stations. Based on reported ranges of constraints of $\delta^{56}Fe$ for sedimentary processes (RD and NRD), a contribution of ~40 to 90% of Fe from RD to the overlying shelf water is estimated, with 10 to 60% from NRD, suggesting that RD is a more prominent process supplying Fe over the Antarctic Peninsula continental shelf. While [dFe] at depth shows a horizontally decreasing trend away from the Antarctic Peninsula (from 7 to 1 nmol L^{-1}), consistently low $\delta^{56}Fe$ (–1.22±0.23‰) over the shelf supports the hypothesis postulated previously that Fe from RD can be preserved and transported over a relatively long distance. On the other hand, elevated f_{sim} does not correspond with elevated [dFe] near the surface (upper 20 m), implying sea ice melting is not a significant source of Fe in this region. The $\delta^{56}Fe$ values within this depth range are most likely modulated by biological uptake.

On the Antarctic Peninsula continental shelf, as dense shelf water forms during cold seasons, it sinks to greater depths on the shelf and receives isotopically light Fe from sediments. However, we found that this light signature gets heavier (~+1.11‰) as [dFe] decreases (~65% of Fe decrease) while dense shelf water descends along the

continental shelf slope (i.e., pre-WSBW). This transition of δ^{56}Fe as well as the [dFe] decrease most likely results from physical mixing of descending water with WDW and WSDW, implying a dilution of the sediment derived signature and transfer of sediments-derived Fe from pre-WSBW to WDW and WSDW. In contrast to the loss of this signature, over the continental shelf slope and in the offshore region, a general δ^{56}Fe minimum (–0.66 to –0.34‰) is observed at the intermediate depth (~200-300 m), consistent with previous observations in the Atlantic sector of the Southern Ocean. As such, our results suggest that sedimentary light Fe is potentially transported within the intermediate depths both from Antarctic Peninsula sediments and sedimentary sources elsewhere in the Southern Ocean via the gyre. Overall, this study suggests that Fe biogeochemistry in the Southern Ocean, notable at intermediate depths, may have large impacts on Fe cycling in and supply to the WS.

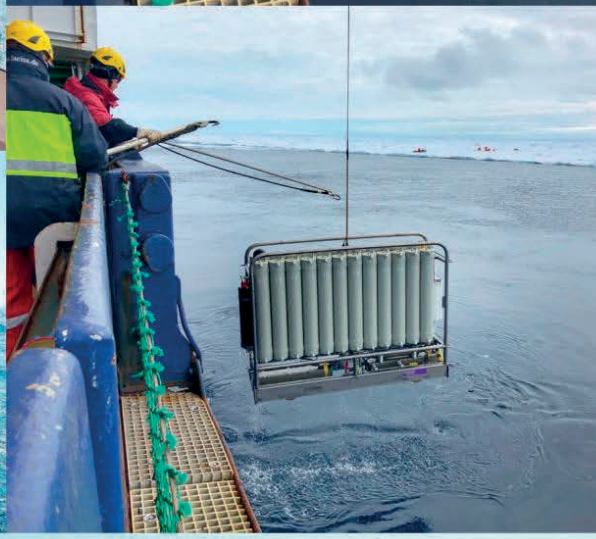

REFERENCES

Abadie C., Lacan F., Radic A., Pradoux C. and Poitrasson F. (2017) Iron isotopes reveal distinct dissolved iron sources and pathways in the intermediate versus deep Southern Ocean. *Proceedings of the National Academy of Sciences* **114**, 858-863.

Abouchami W., Galer S. J. G., de Baar H. J. W., Alderkamp A. C., Middag R., Laan P., Feldmann H. and Andreae M. O. (2011) Modulation of the Southern Ocean cadmium isotope signature by ocean circulation and primary productivity. *Earth and Planetary Science Letters* **305**, 83-91.

Abouchami W., Galer S. J. G., de Baar H. J. W., Middag R., Vance D., Zhao Y., Klunder M., Mezger K., Feldmann H. and Andreae M. O. (2014) Biogeochemical cycling of cadmium isotopes in the Southern Ocean along the Zero Meridian. *Geochimica et Cosmochimica Acta* **127**, 348-367.

Alderkamp A.-C., Mills M. M., van Dijken G. L., Laan P., Thuróczy C.-E., Gerringa L. J. A., de Baar H. J. W., Payne C. D., Visser R. J. W., Buma A. G. J. and Arrigo K. R. (2012) Iron from melting glaciers fuels phytoplankton blooms in the Amundsen Sea (Southern Ocean): Phytoplankton characteristics and productivity. *Deep Sea Research Part II: Topical Studies in Oceanography* **71-76**, 32-48.

Alderkamp A.-C., van Dijken G. L., Lowry K. E., Connelly T. L., Lagerström M., Sherrell R. M., Haskins C., Rogalsky E., Schofield O., Stammerjohn S. E., Yager P. L. and Arrigo K. R. (2015) Fe availability drives phytoplankton photosynthesis rates during spring bloom in the Amundsen Sea Polynya, Antarctica. *Elementa: Science of the Anthropocene* **3**, 000043.

Alexander H., Rouco M., Haley S. T., Wilson S. T., Karl D. M. and Dyhrman S. T. (2015) Functional group-specific traits drive phytoplankton dynamics in the oligotrophic ocean. *Proceedings of the National Academy of Sciences* **112**, E5972-E5979.

Andersen M. B., Vance D., Archer C., Anderson R. F., Ellwood M. J. and Allen C. S. (2011) The Zn abundance and isotopic composition of diatom frustules, a proxy for Zn availability in ocean surface seawater. *Earth and Planetary Science Letters* **301**, 137-145.

Anderson P. S. (1993) Evidence for an Antarctic winter coastal polynya. *Antarctic Science* **5**, 221-226.

Annett A. L., Skiba M., Henley S. F., Venables H. J., Meredith M. P., Statham P. J. and Ganeshram R. S. (2015) Comparative roles of upwelling and

glacial iron sources in Ryder Bay, coastal western Antarctic Peninsula. *Marine Chemistry* **176**, 21-33.

Archer C., Andersen M. B., Cloquet C., Conway T. M., Dong S., Ellwood M., Moore R., Nelson J., Rehkämper M., Rouxel O., Samanta M., Shin K.-C., Sohrin Y., Takano S. and Wasylenki L. (2017) Inter-calibration of a proposed new primary reference standard AA-ETH Zn for zinc isotopic analysis. *Journal of Analytical Atomic Spectrometry* **32**, 415-419.

Ardelan M. V., Holm-Hansen O., Hewes C. D., Reiss C. S., Silva N. S., Dulaiova H., Steinnes E. and Sakshaug E. (2010) Natural iron enrichment around the Antarctic Peninsula in the Southern Ocean. *Biogeosciences* **7**, 11-25.

Ardiningsih I., Krisch S., Lodeiro P., Reichart G.-J., Achterberg E. P., Gledhill M., Middag R. and Gerringa L. J. A. (2020) Natural Fe-binding organic ligands in Fram Strait and over the northeast Greenland shelf. *Marine Chemistry* **224**, 103815.

Arneborg L., Wåhlin A. K., Björk G., Liljebladh B. and Orsi A. H. (2012) Persistent inflow of warm water onto the central Amundsen shelf. *Nature Geoscience* **5**, 876-880.

Arrigo K. R. and van Dijken G. L. (2003) Phytoplankton dynamics within 37 Antarctic coastal polynya systems. *Journal of Geophysical Research: Oceans* **108**, 3271.

Arrigo K. R., van Dijken G. L. and Bushinsky S. (2008) Primary production in the Southern Ocean, 1997–2006. *Journal of Geophysical Research: Oceans* **113**, C08004.

Arrigo K. R., Lowry K. E. and van Dijken G. L. (2012) Annual changes in sea ice and phytoplankton in polynyas of the Amundsen Sea, Antarctica. *Deep Sea Research Part II: Topical Studies in Oceanography* **71-76**, 5-15.

Arrigo K. R., Worthen D. L., Lizotte M. P., Dixon P. and Dieckmann G. (1997) Primary Production in Antarctic Sea Ice. *Science* **276**, 394.

Assmann K. M., Jenkins A., Shoosmith D. R., Walker D. P., Jacobs S. S. and Nicholls K. W. (2013) Variability of Circumpolar Deep Water transport onto the Amundsen Sea Continental shelf through a shelf break trough. *Journal of Geophysical Research: Oceans* **118**, 6603-6620.

Baars O. and Croot P. L. (2011) The speciation of dissolved zinc in the Atlantic sector of the Southern Ocean. *Deep Sea Research Part II: Topical Studies in Oceanography* **58**, 2720-2732.

Baars O., Abouchami W., Galer S. J. G., Boye M. and Croot P. L. (2014) Dissolved cadmium in the Southern Ocean: Distribution, speciation, and relation to phosphate. *Limnology and Oceanography* **59**, 385-399.

Beard B. L. and Johnson C. M. (2004) Fe Isotope Variations in the Modern and Ancient Earth and Other Planetary Bodies. *Reviews in Mineralogy and Geochemistry* **55**, 319-357.

Beard B. L., Johnson C. M., Skulan J. L., Nealson K. H., Cox L. and Sun H. (2003) Application of Fe isotopes to tracing the geochemical and biological cycling of Fe. *Chemical Geology* **195**, 87-117.

Beckmann A., Hellmer H. H. and Timmermann R. (1999) A numerical model of the Weddell Sea: Large-scale circulation and water mass distribution. *Journal of Geophysical Research: Oceans* **104**, 23375-23391.

Behrenfeld M. J., Bale A. J., Kolber Z. S., Aiken J. and Falkowski P. G. (1996) Confirmation of iron limitation of phytoplankton photosynthesis in the equatorial Pacific Ocean. *Nature* **383**, 508-511.

Behrenfeld M. J., O'Malley R. T., Siegel D. A., McClain C. R., Sarmiento J. L., Feldman G. C., Milligan A. J., Falkowski P. G., Letelier R. M. and Boss E. S. (2006) Climate-driven trends in contemporary ocean productivity. *Nature* **444**, 752-755.

Belkin I. M. and Gordon A. L. (1996) Southern Ocean fronts from the Greenwich meridian to Tasmania. *Journal of Geophysical Research: Oceans* **101**, 3675-3696.

Bennett S. A., Rouxel O., Schmidt K., Garbe-Schönberg D., Statham P. J. and German C. R. (2009) Iron isotope fractionation in a buoyant hydrothermal plume, 5°S Mid-Atlantic Ridge. *Geochimica et Cosmochimica Acta* **73**, 5619-5634.

Berger C. J. M., Lippiatt S. M., Lawrence M. G. and Bruland K. W. (2008) Application of a chemical leach technique for estimating labile particulate aluminum, iron, and manganese in the Columbia River plume and coastal waters off Oregon and Washington. *Journal of Geophysical Research: Oceans* **113**.

Bergquist B. A. and Boyle E. A. (2006) Iron isotopes in the Amazon River system: Weathering and transport signatures. *Earth and Planetary Science Letters* **248**, 54-68.

Bermin J., Vance D., Archer C. and Statham P. J. (2006) The determination of the isotopic composition of Cu and Zn in seawater. *Chemical Geology* **226**, 280-297.

Bertrand E. M., Saito M. A., Rose J. M., Riesselman C. R., Lohan M. C., Noble A. E., Lee P. A. and DiTullio G. R. (2007) Vitamin B12 and iron colimitation of phytoplankton growth in the Ross Sea. *Limnology and Oceanography* **52**, 1079-1093.

Bertrand E. M., McCrow J. P., Moustafa A., Zheng H., McQuaid J. B., Delmont T. O., Post A. F., Sipler R. E., Spackeen J. L., Xu K., Bronk D. A., Hutchins D. A. and Allen A. E. (2015) Phytoplankton–bacterial interactions mediate micronutrient colimitation at the coastal Antarctic sea ice edge. *Proceedings of the National Academy of Sciences* **112**, 9938-9943.

Biller D. V. and Bruland K. W. (2012) Analysis of Mn, Fe, Co, Ni, Cu, Zn, Cd, and Pb in seawater using the Nobias-chelate PA1 resin and magnetic sector inductively coupled plasma mass spectrometry (ICP-MS). *Marine Chemistry* **130-131**, 12-20.

Boutin J., Merlivat L., HÉnocq C., Martin N. and SallÉe J. B. (2008) Air-sea CO2 flux variability in frontal regions of the Southern Ocean from CARbon Interface OCean Atmosphere drifters. *Limnology and Oceanography* **53**, 2062-2079.

Boyd P. W. and Ellwood M. J. (2010) The biogeochemical cycle of iron in the ocean. *Nature Geoscience* **3**, 675-682.

Boyd P. W., Crossley A. C., DiTullio G. R., Griffiths F. B., Hutchins D. A., Queguiner B., Sedwick P. N. and Trull T. W. (2001) Control of phytoplankton growth by iron supply and irradiance in the subantarctic Southern Ocean: Experimental results from the SAZ Project. *Journal of Geophysical Research: Oceans* **106**, 31573-31583.

Boyd P. W., Jickells T., Law C. S., Blain S., Boyle E. A., Buesseler K. O., Coale K. H., Cullen J. J., de Baar H. J. W., Follows M., Harvey M., Lancelot C., Levasseur M., Owens N. P. J., Pollard R., Rivkin R. B., Sarmiento J., Schoemann V., Smetacek V., Takeda S., Tsuda A., Turner S. and Watson A. J. (2007) Mesoscale Iron Enrichment Experiments 1993-2005: Synthesis and Future Directions. *Science* **315**, 612-617.

Boyle E. A. (1988) Cadmium: Chemical tracer of deepwater paleoceanography. *Paleoceanography* **3**, 471-489.

Boyle E. A., Sclater F. and Edmond J. M. (1976) On the marine geochemistry of cadmium. *Nature* **263**, 42-44.

Boyle E. A., Huested S. S. and Jones S. P. (1981) On the distribution of copper, nickel, and cadmium in the surface waters of the North Atlantic and North Pacific Ocean. *Journal of Geophysical Research: Oceans* **86**, 8048-8066.

Brown P. J., Meredith M. P., Jullion L., Naveira Garabato A., Torres-Valdés S., Holland P., Leng M. J. and Venables H. (2014) Freshwater fluxes in the Weddell Gyre: results from δ18O. *Philosophical Transactions of the Royal Society A: Mathematical, Physical and Engineering Sciences* **372**, 20130298.

Browning T. J., Achterberg E. P., Engel A. and Mawji E. (2021) Manganese co-limitation of phytoplankton growth and major nutrient drawdown in the Southern Ocean. *Nature Communications* **12**, 884.

Bruland K. W. (1980) Oceanographic distributions of cadmium, zinc, nickel, and copper in the North Pacific. *Earth and Planetary Science Letters* **47**, 176-198.

Bruland K. W., Donat J. R. and Hutchins D. A. (1991) Interactive influences of bioactive trace metals on biological production in oceanic waters. *Limnology and Oceanography* **36**, 1555-1577.

Bruland K. W., Orians K. J. and Cowen J. P. (1994) Reactive trace metals in the stratified central North Pacific. *Geochimica et Cosmochimica Acta* **58**, 3171-3182.

Bruland K. W., Middag R. and Lohan M. C. (2013) Controls of Trace Metals in Seawater. In *Treatise on Geochemistry: Second Edition.* (eds. M. J. Mottl and H. Elderfield). Saunders, Elsevier Inc, Philadelphia, USA. pp. 19-51.

Bruland K. W., Middag R. and Lohan M. C. (2014) Controls of Trace Metals in Seawater. In *Treatise on Geochemistry (Second Edition)* (eds. H. D. Holland and K. K. Turekian). Elsevier, Oxford. pp. 19-51.

Buma A. G. J., de Baar H. J. W., Nolting R. F. and van Bennekom A. J. (1991) Metal enrichment experiments in the Weddell-Scotia Seas: Effects of iron and manganese on various plankton communities. *Limnology and Oceanography* **36**, 1865-1878.

Chen X.-G., Krisch S., Al-Hashem A., Hopwood M. J., Rutgers van der Loeff M. M., Huhn O., Lodeiro P., Steffens T. and Achterberg E. P. (2022) Dissolved, Labile, and Total Particulate Trace Metal Dynamics on the Northeast Greenland Shelf. *Global Biogeochemical Cycles* **36**, e2022GB007528.

Cloquet C., Carignan J., Libourel G., Sterckeman T. and Perdrix E. (2006) Tracing Source Pollution in Soils Using Cadmium and Lead Isotopes. *Environmental Science & Technology* **40**, 2525-2530.

Coale K. H., Johnson K. S., Fitzwater S. E., Gordon R. M., Tanner S., Chavez F. P., Ferioli L., Sakamoto C., Rogers P., Millero F., Steinberg P., Nightingale P., Cooper D., Cochlan W. P., Landry M. R., Constantinou

J., Rollwagen G., Trasvina A. and Kudela R. (1996) A massive phytoplankton bloom induced by an ecosystem-scale iron fertilization experiment in the equatorial Pacific Ocean. *Nature* **383**, 495-501.

Coleman J. (1998) Zinc enzymes. *Curr Opin Chem Biol*, 222-234.

Coleman J. E. (1992) ZINC PROTEINS: Enzymes, Storage Proteins, Transcription Factors, and Replication Proteins. *Annual Review of Biochemistry* **61**, 897-946.

Connolley W. M. (1997) Variability in annual mean circulation in southern high latitudes. *Climate Dynamics* **13**, 745-756.

Conway T. M. and John S. G. (2014a) Quantification of dissolved iron sources to the North Atlantic Ocean. *Nature* **511**, 212-215.

Conway T. M. and John S. G. (2014b) The biogeochemical cycling of zinc and zinc isotopes in the North Atlantic Ocean. *Global Biogeochemical Cycles* **28**, 1111-1128.

Conway T. M. and John S. G. (2015) The cycling of iron, zinc and cadmium in the North East Pacific Ocean – Insights from stable isotopes. *Geochimica et Cosmochimica Acta* **164**, 262-283.

Conway T. M., John S. G. and Lacan F. (2016) Intercomparison of dissolved iron isotope profiles from reoccupation of three GEOTRACES stations in the Atlantic Ocean. *Marine Chemistry* **183**, 50-61.

Conway T. M., Rosenberg A. D., Adkins J. F. and John S. G. (2013) A new method for precise determination of iron, zinc and cadmium stable isotope ratios in seawater by double-spike mass spectrometry. *Analytica Chimica Acta* **793**, 44-52.

Conway T. M., Horner T. J., Plancherel Y. and González A. G. (2021) A decade of progress in understanding cycles of trace elements and their isotopes in the oceans. *Chemical Geology* **580**, 120381.

Conway T. M., Hamilton D. S., Shelley R. U., Aguilar-Islas A. M., Landing W. M., Mahowald N. M. and John S. G. (2019) Tracing and constraining anthropogenic aerosol iron fluxes to the North Atlantic Ocean using iron isotopes. *Nature Communications* **10**, 2628.

Croft M. T., Lawrence A. D., Raux-Deery E., Warren M. J. and Smith A. G. (2005) Algae acquire vitamin B12 through a symbiotic relationship with bacteria. *Nature* **438**, 90-93.

Croot P. L., Baars O. and Streu P. (2011) The distribution of dissolved zinc in the Atlantic sector of the Southern Ocean. *Deep Sea Research Part II: Topical Studies in Oceanography* **58**, 2707-2719.

Crosby H. A., Roden E. E., Johnson C. M. and Beard B. L. (2007) The mechanisms of iron isotope fractionation produced during dissimilatory Fe(III) reduction by Shewanella putrefaciens and Geobacter sulfurreducens. *Geobiology* **5**, 169-189.

Cullen J. T. (2006) On the nonlinear relationship between dissolved cadmium and phosphate in the modern global ocean: Could chronic iron limitation of phytoplankton growth cause the kink? *Limnology and Oceanography* **51**, 1369-1380.

Cullen J. T., Chase Z., Coale K. H., Fitzwater S. E. and Sherrell R. M. (2003) Effect of iron limitation on the cadmium to phosphorus ratio of natural phytoplankton assemblages from the Southern Ocean. *Limnology and Oceanography* **48**, 1079-1087.

Cuvelier M. L., Allen A. E., Monier A., McCrow J. P., Messié M., Tringe S. G., Woyke T., Welsh R. M., Ishoey T., Lee J.-H., Binder B. J., DuPont C. L., Latasa M., Guigand C., Buck K. R., Hilton J., Thiagarajan M., Caler E., Read B., Lasken R. S., Chavez F. P. and Worden A. Z. (2010) Targeted metagenomics and ecology of globally important uncultured eukaryotic phytoplankton. *Proceedings of the National Academy of Sciences* **107**, 14679-14684.

Dauphas N., John S. G. and Rouxel O. (2017) Iron Isotope Systematics. *Reviews in Mineralogy and Geochemistry* **82**, 415-510.

de Baar H. J. W. and de Jong J. T. M. (2001) Distributions, sources and sinks of iron in seawater. *The Biogeochemistry of iron in seawater*.

de Baar H. J. W. and La Roche J. (2003) Trace Metals in the Oceans: Evolution, Biology and Global Change. In *Marine Science Frontiers for Europe* (eds. G. Wefer, F. Lamy and F. Mantoura). Springer Berlin Heidelberg, Berlin, Heidelberg. pp. 79-105.

de Baar H. J. W., Saager P. M., Nolting R. F. and van der Meer J. (1994) Cadmium versus phosphate in the world ocean. *Marine Chemistry* **46**, 261-281.

de Baar H. J. W., Buma A. G. J., Nolting R. F., Cadée G. C., Jacques G. and Tréguer P. J. (1990) On iron limitation of the Southern Ocean: experimental observations in the Weddell and Scotia Seas. *Marine Ecology Progress Series* **65**, 105-122.

de Baar H. J. W., de Jong J. T. M., Bakker D. C. E., Löscher B. M., Veth C., Bathmann U. and Smetacek V. (1995) Importance of iron for plankton blooms and carbon dioxide drawdown in the Southern Ocean. *Nature* **373**, 412-415.

de Baar H. J. W., de Jong J. T. M., Nolting R. F., Timmermans K. R., van Leeuwe M. A., Bathmann U., Rutgers van der Loeff M. and Sildam J. (1999) Low dissolved Fe and the absence of diatom blooms in remote Pacific waters of the Southern Ocean. *Marine Chemistry* **66**, 1-34.

de Baar H. J. W., Timmermans K. R., Laan P., De Porto H. H., Ober S., Blom J. J., Bakker M. C., Schilling J., Sarthou G., Smit M. G. and Klunder M. (2008) Titan: A new facility for ultraclean sampling of trace elements and isotopes in the deep oceans in the international Geotraces program. *Marine Chemistry* **111**, 4-21.

de Jong J., Schoemann V., Lannuzel D., Croot P., de Baar H. and Tison J.-L. (2012) Natural iron fertilization of the Atlantic sector of the Southern Ocean by continental shelf sources of the Antarctic Peninsula. *Journal of Geophysical Research: Biogeosciences* **117**, G01029.

de Souza G. F., Khatiwala S. P., Hain M. P., Little S. H. and Vance D. (2018) On the origin of the marine zinc–silicon correlation. *Earth and Planetary Science Letters* **492**, 22-34.

Deacon G. E. R. (1959) THE ANTARCTIC OCEAN. *Science Progress (1933-)* **47**, 647-660.

Deacon G. E. R. (1979) The Weddell gyre. *Deep Sea Research Part A. Oceanographic Research Papers* **26**, 981-995.

Dideriksen K., Baker J. A. and Stipp S. L. S. (2008) Equilibrium Fe isotope fractionation between inorganic aqueous Fe(III) and the siderophore complex, Fe(III)-desferrioxamine B. *Earth and Planetary Science Letters* **269**, 280-290.

Dong S., Weiss D. J., Strekopytov S., Kreissig K., Sun Y., Baker A. R. and Formenti P. (2013) Stable isotope ratio measurements of Cu and Zn in mineral dust (bulk and size fractions) from the Taklimakan Desert and the Sahel and in aerosols from the eastern tropical North Atlantic Ocean. *Talanta* **114**, 103-109.

Donnelly M., Leach H. and Strass V. (2017) Modification of the deep salinity-maximum in the Southern Ocean by circulation in the Antarctic Circumpolar Current and the Weddell Gyre. *Ocean Dynamics* **67**, 813-838.

Duprat L., Corkill M., Genovese C., Townsend A. T., Moreau S., Meiners K. M. and Lannuzel D. (2020) Nutrient Distribution in East Antarctic Summer Sea Ice: A Potential Iron Contribution From Glacial Basal Melt. *Journal of Geophysical Research: Oceans* **125**, e2020JC016130.

Dutrieux P., De Rydt J., Jenkins A., Holland P. R., Ha H. K., Lee S. H., Steig E. J., Ding Q., Abrahamsen E. P. and Schröder M. (2014) Strong Sensitivity of Pine Island Ice-Shelf Melting to Climatic Variability. *Science* **343**, 174.

Eich C., Biggs T. E. G., van de Poll W. H., van Manen M., Tian H.-A., Jung J., Lee Y., Middag R. and Brussaard C. P. D. (2022) Ecological Importance of Viral Lysis as a Loss Factor of Phytoplankton in the Amundsen Sea, Microorganisms.

Ellwood M. J. and Hunter K. A. (2000) Variations in the Zn/Si record over the Last Interglacial Glacial Transition. *Paleoceanography* **15**, 506-514.

Ellwood M. J., Strzepek R. F., Strutton P. G., Trull T. W., Fourquez M. and Boyd P. W. (2020) Distinct iron cycling in a Southern Ocean eddy. *Nature Communications* **11**, 825.

Ellwood M. J., Hutchins D. A., Lohan M. C., Milne A., Nasemann P., Nodder S. D., Sander S. G., Strzepek R., Wilhelm S. W. and Boyd P. W. (2015) Iron stable isotopes track pelagic iron cycling during a subtropical phytoplankton bloom. *Proceedings of the National Academy of Sciences* **112**, E15-E20.

Elrod V. A., Berelson W. M., Coale K. H. and Johnson K. S. (2004) The flux of iron from continental shelf sediments: A missing source for global budgets. *Geophysical Research Letters* **31**.

Endo H., Ogata H. and Suzuki K. (2018) Contrasting biogeography and diversity patterns between diatoms and haptophytes in the central Pacific Ocean. *Scientific Reports* **8**, 10916.

Escoube R., Rouxel O. J., Sholkovitz E. and Donard O. F. X. (2009) Iron isotope systematics in estuaries: The case of North River, Massachusetts (USA). *Geochimica et Cosmochimica Acta* **73**, 4045-4059.

Escoube R., Rouxel O. J., Pokrovsky O. S., Schroth A., Max Holmes R. and Donard O. F. X. (2015) Iron isotope systematics in Arctic rivers. *Comptes Rendus Geoscience* **347**, 377-385.

Fahrbach E., Peterson R. G., Rohardt G., Schlosser P. and Bayer R. (1994) Suppression of bottom water formation in the southeastern Weddell sea. *Deep Sea Research Part I: Oceanographic Research Papers* **41**, 389-411.

Fahrbach E., Hoppema M., Rohardt G., Schröder M. and Wisotzki A. (2004) Decadal-scale variations of water mass properties in the deep Weddell Sea. *Ocean Dynamics* **54**, 77-91.

Falkowski P. G. (1997) Evolution of the nitrogen cycle and its influence on the biological sequestration of CO2 in the ocean. *Nature* **387**, 272-275.

Falkowski P. G., Barber R. T. and Smetacek V. (1998) Biogeochemical Controls and Feedbacks on Ocean Primary Production. *Science* **281**, 200-206.

Fan S., Gao Y., Sherrell R. M., Yu S. and Bu K. (2021) Concentrations, particle-size distributions, and dry deposition fluxes of aerosol trace elements over the Antarctic Peninsula in austral summer. *Atmos. Chem. Phys.* **21**, 2105-2124.

Field C. B., Behrenfeld M. J., Randerson J. T. and Falkowski P. (1998) Primary Production of the Biosphere: Integrating Terrestrial and Oceanic Components. *Science* **281**, 237-240.

Fitzsimmons J. N. and Conway T. M. (2023) Novel Insights into Marine Iron Biogeochemistry from Iron Isotopes. *Annual Review of Marine Science* **15**, 383-406.

Fitzsimmons J. N., Zhang R. and Boyle E. A. (2013) Dissolved iron in the tropical North Atlantic Ocean. *Marine Chemistry* **154**, 87-99.

Fitzsimmons J. N., John S. G., Marsay C. M., Hoffman C. L., Nicholas Sarah L., Toner B. M., German C. R. and Sherrell R. M. (2017) Iron persistence in a distal hydrothermal plume supported by dissolved–particulate exchange. *Nature Geoscience* **10**, 195-201.

Fitzsimmons J. N., Carrasco G. G., Wu J., Roshan S., Hatta M., Measures C. I., Conway T. M., John S. G. and Boyle E. A. (2015) Partitioning of dissolved iron and iron isotopes into soluble and colloidal phases along the GA03 GEOTRACES North Atlantic Transect. *Deep Sea Research Part II: Topical Studies in Oceanography* **116**, 130-151.

Fitzwater S. E., Johnson K. S., Elrod V. A., Ryan J. P., Coletti L. J., Tanner S. J., Gordon R. M. and Chavez F. P. (2003) Iron, nutrient and phytoplankton biomass relationships in upwelled waters of the California coastal system. *Continental Shelf Research* **23**, 1523-1544.

Foldvik A., Gammelsrød T. and Tørresen T. (1985) Circulation and Water Masses on the Southern Weddell Sea Shelf. In *Oceanology of the Antarctic Continental Shelf*. pp. 5-20.

Foster T. D. and Carmack E. C. (1976) Frontal zone mixing and Antarctic Bottom water formation in the southern Weddell Sea. *Deep Sea Research and Oceanographic Abstracts* **23**, 301-317.

Gao B., Zhou H., Liang X. and Tu X. (2013) Cd isotopes as a potential source tracer of metal pollution in river sediments. *Environmental Pollution* **181**, 340-343.

Gault-Ringold M., Adu T., Stirling C. H., Frew R. D. and Hunter K. A. (2012) Anomalous biogeochemical behavior of cadmium in subantarctic surface waters: Mechanistic constraints from cadmium isotopes. *Earth and Planetary Science Letters* **341-344**, 94-103.

George E., Stirling C. H., Gault-Ringold M., Ellwood M. J. and Middag R. (2019) Marine biogeochemical cycling of cadmium and cadmium isotopes in the extreme nutrient-depleted subtropical gyre of the South West Pacific Ocean. *Earth and Planetary Science Letters* **514**, 84-95.

Gerringa L. J. A., Laan P., Arrigo K. R., van Dijken G. L. and Alderkamp A. C. (2019) The organic complexation of iron in the Ross sea. *Marine Chemistry* **215**, 103672.

Gerringa L. J. A., Alderkamp A.-C., van Dijken G., Laan P., Middag R. and Arrigo K. R. (2020a) Dissolved Trace Metals in the Ross Sea. *Frontiers in Marine Science* **7**, 874.

Gerringa L. J. A., Alderkamp A.-C., Laan P., Thuróczy C.-E., De Baar H. J. W., Mills M. M., van Dijken G. L., Haren H. v. and Arrigo K. R. (2012) Iron from melting glaciers fuels the phytoplankton blooms in Amundsen Sea (Southern Ocean): Iron biogeochemistry. *Deep Sea Research Part II: Topical Studies in Oceanography* **71-76**, 16-31.

Gerringa L. J. A., Alderkamp A.-C., Laan P., Thuróczy C.-E., De Baar H. J. W., Mills M. M., van Dijken G. L., Haren H. v. and Arrigo K. R. (2020b) Corrigendum to “Iron from melting glaciers fuels the phytoplankton blooms in Amundsen Sea (Southern Ocean): iron biogeochemistry” (Gerringa et al., 2012). *Deep Sea Research Part II: Topical Studies in Oceanography* **177**, 104843.

Girton J. B., Christianson K., Dunlap J., Dutrieux P., Gobat J., Lee C. and Rainville L. Buoyancy-adjusting Profiling Floats for Exploration of Heat Transport, Melt Rates, and Mixing in the Ocean Cavities Under Floating Ice Shelves. *OCEANS 2019 MTS/IEEE SEATTLE*.

Gledhill M. and van den Berg C. M. G. (1994) Determination of complexation of iron(III) with natural organic complexing ligands in seawater using cathodic stripping voltammetry. *Marine Chemistry* **47**, 41-54.

Gordon L. I., Jennings J. C. and Ross A. A. A Suggested Protocol for Continuous Flow Automated Analysis of Seawater Nutrients Using the Alpkem Flow Solution IV System (Phosphate, Nitrate, Nitrite,

Silicic Acid and Ammonia) chemical protocols used in the WOCE Hydrographic Program and the Joint Global Ocean Fluxes Study.

Gouretski V. V. and Danilov A. I. (1993) Weddell Gyre: structure of the eastern boundary. *Deep Sea Research Part I: Oceanographic Research Papers* **40**, 561-582.

Gourmelen N., Goldberg D. N., Snow K., Henley S. F., Bingham R. G., Kimura S., Hogg A. E., Shepherd A., Mouginot J., Lenaerts J. T. M., Ligtenberg S. R. M. and van de Berg W. J. (2017) Channelized Melting Drives Thinning Under a Rapidly Melting Antarctic Ice Shelf. *Geophysical Research Letters* **44**, 9796-9804.

Guinoiseau D., Galer S. J. G. and Abouchami W. (2018) Effect of cadmium sulphide precipitation on the partitioning of Cd isotopes: Implications for the oceanic Cd cycle. *Earth and Planetary Science Letters* **498**, 300-308.

Ha H. K., Wåhlin A. K., Kim T. W., Lee S. H., Lee J. H., Lee H. J., Hong C. S., Arneborg L., Björk G. and Kalén O. (2014) Circulation and Modification of Warm Deep Water on the Central Amundsen Shelf. *Journal of Physical Oceanography* **44**, 1493-1501.

Halse G. R. and Syvertsen E. E. (1996) Chapter 2 - Marine Diatoms. In *Identifying Marine Diatoms and Dinoflagellates* (ed. C. R. Tomas). Academic Press, San Diego. pp. 5-385.

Hassler C., Sinoir M., Clementson L. and Butler E. (2012) Exploring the Link between Micronutrients and Phytoplankton in the Southern Ocean during the 2007 Austral Summer. *Frontiers in Microbiology* **3**.

Hatta M., Measures C. I., Selph K. E., Zhou M. and Hiscock W. T. (2013) Iron fluxes from the shelf regions near the South Shetland Islands in the Drake Passage during the austral-winter 2006. *Deep Sea Research Part II: Topical Studies in Oceanography* **90**, 89-101.

Hawco N. J., Tagliabue A. and Twining B. S. (2022) Manganese Limitation of Phytoplankton Physiology and Productivity in the Southern Ocean. *Global Biogeochemical Cycles* **36**, e2022GB007382.

Henkel S., Kasten S., Hartmann J. F., Silva-Busso A. and Staubwasser M. (2018) Iron cycling and stable Fe isotope fractionation in Antarctic shelf sediments, King George Island. *Geochimica et Cosmochimica Acta* **237**, 320-338.

Henley S. F., Cavan E. L., Fawcett S. E., Kerr R., Monteiro T., Sherrell R. M., Bowie A. R., Boyd P. W., Barnes D. K. A., Schloss I. R., Marshall T., Flynn R. and Smith S. (2020) Changing Biogeochemistry of the

Southern Ocean and Its Ecosystem Implications. *Frontiers in Marine Science* **7**.

Herbert L. C., Lepp A. P., Garcia S. M., Browning A., Miller L. E., Wellner J., Severmann S., Hillenbrand C.-D., Johnson J. S. and Sherrell R. M. (2023) Volcanogenic fluxes of iron from the seafloor in the Amundsen Sea, West Antarctica. *Marine Chemistry*, 104250.

Herraiz-Borreguero L., Lannuzel D., van der Merwe P., Treverrow A. and Pedro J. B. (2016) Large flux of iron from the Amery Ice Shelf marine ice to Prydz Bay, East Antarctica. *Journal of Geophysical Research: Oceans* **121**, 6009-6020.

Ho T.-Y., Chou W.-C., Lin H.-L. and Sheu D. D. (2011) Trace metal cycling in the deep water of the South China Sea: The composition, sources, and fluxes of sinking particles. *Limnology and Oceanography* **56**, 1225-1243.

Ho T.-Y., Quigg A., Finkel Z. V., Milligan A. J., Wyman K., Falkowski P. G. and Morel F. M. M. (2003) THE ELEMENTAL COMPOSITION OF SOME MARINE PHYTOPLANKTON1. *Journal of Phycology* **39**, 1145-1159.

Homoky W. B., John S. G., Conway T. M. and Mills R. A. (2013) Distinct iron isotopic signatures and supply from marine sediment dissolution. *Nature Communications* **4**, 2143.

Homoky W. B., Severmann S., Mills R. A., Statham P. J. and Fones G. R. (2009) Pore-fluid Fe isotopes reflect the extent of benthic Fe redox recycling: Evidence from continental shelf and deep-sea sediments. *Geology* **37**, 751-754.

Homoky W. B., Severmann S., McManus J., Berelson W. M., Riedel T. E., Statham P. J. and Mills R. A. (2012) Dissolved oxygen and suspended particles regulate the benthic flux of iron from continental margins. *Marine Chemistry* **134-135**, 59-70.

Homoky W. B., Conway T. M., John S. G., König D., Deng F., Tagliabue A. and Mills R. A. (2021) Iron colloids dominate sedimentary supply to the ocean interior. *Proceedings of the National Academy of Sciences* **118**, e2016078118.

Horner T. J., Lee R. B. Y., Henderson G. M. and Rickaby R. E. M. (2013) Nonspecific uptake and homeostasis drive the oceanic cadmium cycle. *Proceedings of the National Academy of Sciences* **110**, 2500-2505.

Horner T. J., Little S. H., Conway T. M., Farmer J. R., Hertzberg J. E., Janssen D. J., Lough A. J. M., McKay J. L., Tessin A., Galer S. J. G., Jaccard S. L., Lacan F., Paytan A., Wuttig K. and Members G. P. B. P. W. G. (2021)

Bioactive Trace Metals and Their Isotopes as Paleoproductivity Proxies: An Assessment Using GEOTRACES-Era Data. *Global Biogeochemical Cycles* **35**, e2020GB006814.

Hosking J. S., Orr A., Marshall G. J., Turner J. and Phillips T. (2013) The Influence of the Amundsen–Bellingshausen Seas Low on the Climate of West Antarctica and Its Representation in Coupled Climate Model Simulations. *Journal of Climate* **26**, 6633-6648.

Howe J. A., Wilson C. R., Shimmield T. M., Diaz R. J. and Carpenter L. W. (2007) Recent deep-water sedimentation, trace metal and radioisotope geochemistry across the Southern Ocean and Northern Weddell Sea, Antarctica. *Deep Sea Research Part II: Topical Studies in Oceanography* **54**, 1652-1681.

Huhn O., Hellmer H. H., Rhein M., Rodehacke C., Roether W., Schodlok M. P. and Schröder M. (2008) Evidence of deep- and bottom-water formation in the western Weddell Sea. *Deep Sea Research Part II: Topical Studies in Oceanography* **55**, 1098-1116.

Hunt H. R., Summers B. A., Sieber M., Krisch S., Al-Hashem A., Hopwood M., Achterberg E. P. and Conway T. M. (2022) Distinguishing the influence of sediments, the Congo River, and water-mass mixing on the distribution of iron and its isotopes in the Southeast Atlantic Ocean. *Marine Chemistry* **247**, 104181.

Hutchins D. A., Franck V. M., Brzezinski M. A. and Bruland K. W. (1999) Inducing phytoplankton iron limitation in iron-replete coastal waters with a strong chelating ligand. *Limnology and Oceanography* **44**, 1009-1018.

Ilina S. M., Poitrasson F., Lapitskiy S. A., Alekhin Y. V., Viers J. and Pokrovsky O. S. (2013) Extreme iron isotope fractionation between colloids and particles of boreal and temperate organic-rich waters. *Geochimica et Cosmochimica Acta* **101**, 96-111.

Ito T., Woloszyn M. and Mazloff M. (2010) Anthropogenic carbon dioxide transport in the Southern Ocean driven by Ekman flow. *Nature* **463**, 80-83.

Jacobs S., Jenkins A., Hellmer H., Giulivi C., Nitsche F., Huber B. and Guerrero R. (2012) THE AMUNDSEN SEA AND THE ANTARCTIC ICE SHEET. *Oceanography* **25**, 154-163.

Jacobs S. S., Hellmer H. H. and Jenkins A. (1996) Antarctic Ice Sheet melting in the southeast Pacific. *Geophysical Research Letters* **23**, 957-960.

Jacobs S. S., Jenkins A., Giulivi C. F. and Dutrieux P. (2011) Stronger ocean circulation and increased melting under Pine Island Glacier ice shelf. *Nature Geoscience* **4**, 519-523.

Jakuba R. W., Moffett J. W. and Dyhrman S. T. (2008) Evidence for the linked biogeochemical cycling of zinc, cobalt, and phosphorus in the western North Atlantic Ocean. *Global Biogeochemical Cycles* **22**.

Janssen D. J., Abouchami W., Galer S. J. G. and Cullen J. T. (2017) Fine-scale spatial and interannual cadmium isotope variability in the subarctic northeast Pacific. *Earth and Planetary Science Letters* **472**, 241-252.

Jeandel C. (2016) Overview of the mechanisms that could explain the 'Boundary Exchange' at the land–ocean contact. *Philosophical Transactions of the Royal Society A: Mathematical, Physical and Engineering Sciences* **374**, 20150287.

Jenkins A., Dutrieux P., Jacobs S. S., McPhail S. D., Perrett J. R., Webb A. T. and White D. (2010) Observations beneath Pine Island Glacier in West Antarctica and implications for its retreat. *Nature Geoscience* **3**, 468-472.

Jensen L. T., Morton P., Twining B. S., Heller M. I., Hatta M., Measures C. I., John S., Zhang R., Pinedo-Gonzalez P., Sherrell R. M. and Fitzsimmons J. N. (2020) A comparison of marine Fe and Mn cycling: U.S. GEOTRACES GN01 Western Arctic case study. *Geochimica et Cosmochimica Acta* **288**, 138-160.

Jeon M. H., Jung J., Park M. O., Aoki S., Kim T.-W. and Kim S.-K. (2021) Tracing Circumpolar Deep Water and glacial meltwater using humic-like fluorescent dissolved organic matter in the Amundsen Sea, Antarctica. *Marine Chemistry* **235**, 104008.

Jiang M., Measures C. I., Barbeau K. A., Charette M. A., Gille S. T., Hatta M., Kahru M., Mitchell B. G., Naveira Garabato A. C., Reiss C., Selph K. and Zhou M. (2019) Fe sources and transport from the Antarctic Peninsula shelf to the southern Scotia Sea. *Deep Sea Research Part I: Oceanographic Research Papers* **150**, 103060.

John S. G. and Adkins J. F. (2010) Analysis of dissolved iron isotopes in seawater. *Marine Chemistry* **119**, 65-76.

John S. G. and Adkins J. (2012) The vertical distribution of iron stable isotopes in the North Atlantic near Bermuda. *Global Biogeochemical Cycles* **26**, GB2034.

John S. G. and Conway T. M. (2014) A role for scavenging in the marine biogeochemical cycling of zinc and zinc isotopes. *Earth and Planetary Science Letters* **394**, 159-167.

John S. G., Helgoe J. and Townsend E. (2018) Biogeochemical cycling of Zn and Cd and their stable isotopes in the Eastern Tropical South Pacific. *Marine Chemistry* **201**, 256-262.

John S. G., Geis R. W., Saito M. A. and Boyle E. A. (2007) Zinc isotope fractionation during high-affinity and low-affinity zinc transport by the marine diatom Thalassiosira oceanica. *Limnology and Oceanography* **52**, 2710-2714.

John S. G., Mendez J., Moffett J. and Adkins J. (2012) The flux of iron and iron isotopes from San Pedro Basin sediments. *Geochimica et Cosmochimica Acta* **93**, 14-29.

John S. G., Rouxel O. J., Craddock P. R., Engwall A. M. and Boyle E. A. (2008) Zinc stable isotopes in seafloor hydrothermal vent fluids and chimneys. *Earth and Planetary Science Letters* **269**, 17-28.

Johnson C., Beard B. and Weyer S. (2020) High-Temperature Fe Isotope Geochemistry. In *Iron Geochemistry: An Isotopic Perspective*. Springer Cham. pp. 85-147.

Johnson C. M., Beard B. L. and Roden E. E. (2008) The Iron Isotope Fingerprints of Redox and Biogeochemical Cycling in Modern and Ancient Earth. *Annual Review of Earth and Planetary Sciences* **36**, 457-493.

Johnson K. S., Elrod V., Fitzwater S., Plant J., Boyle E., Bergquist B., Bruland K., Aguilar-Islas A., Buck K., Lohan M., Smith G. J., Sohst B., Coale K., Gordon M., Tanner S., Measures C., Moffett J., Barbeau K., King A., Bowie A., Chase Z., Cullen J., Laan P., Landing W., Mendez J., Milne A., Obata H., Doi T., Ossiander L., Sarthou G., Sedwick P., Van den Berg S., Laglera-Baquer L., Wu J.-f. and Cai Y. (2007) Developing standards for dissolved iron in seawater. *Eos, Transactions American Geophysical Union* **88**, 131-132.

Jordan T. A., Porter D., Tinto K., Millan R., Muto A., Hogan K., Larter R. D., Graham A. G. C. and Paden J. D. (2020) New gravity-derived bathymetry for the Thwaites, Crosson, and Dotson ice shelves revealing two ice shelf populations. *The Cryosphere* **14**, 2869-2882.

Jullion L., Garabato A. C. N., Bacon S., Meredith M. P., Brown P. J., Torres-Valdés S., Speer K. G., Holland P. R., Dong J., Bakker D., Hoppema M., Loose B., Venables H. J., Jenkins W. J., Messias M.-J. and Fahrbach E. (2014) The contribution of the Weddell Gyre to the lower limb of the Global Overturning Circulation. *Journal of Geophysical Research: Oceans* **119**, 3357-3377.

Jung J., Yoo K.-C., Rosenheim B. E., Conway T. M., Lee J. I., Yoon H. I., Hwang C. Y., Yang K., Subt C. and Kim J. (2019) Microbial Fe(III) reduction as a potential iron source from Holocene sediments beneath Larsen Ice Shelf. *Nature Communications* **10**, 5786.

Kellogg M. M., McIlvin M. R., Vedamati J., Twining B. S., Moffett J. W., Marchetti A., Moran D. M. and Saito M. A. (2020) Efficient zinc/cobalt inter-replacement in northeast Pacific diatoms and relationship to high surface dissolved Co : Zn ratios. *Limnology and Oceanography* **65**, 2557-2582.

Kim S.-H., Choi A., Jin Yang E., Lee S. and Hyun J.-H. (2016) Low benthic respiration and nutrient flux at the highly productive Amundsen Sea Polynya, Antarctica. *Deep Sea Research Part II: Topical Studies in Oceanography* **123**, 92-101.

Kim T.-W., Yang H. W., Dutrieux P., Wåhlin A. K., Jenkins A., Kim Y. G., Ha H. K., Kim C.-S., Cho K.-H., Park T., Park J., Lee S. and Cho Y.-K. (2021) Interannual Variation of Modified Circumpolar Deep Water in the Dotson-Getz Trough, West Antarctica. *Journal of Geophysical Research: Oceans* **126**, e2021JC017491.

Kim T. W., Ha H. K., Wåhlin A. K., Lee S. H., Kim C. S., Lee J. H. and Cho Y. K. (2017) Is Ekman pumping responsible for the seasonal variation of warm circumpolar deep water in the Amundsen Sea? *Continental Shelf Research* **132**, 38-48.

Klar J. K., Schlosser C., Milton J. A., Woodward E. M. S., Lacan F., Parkinson I. J., Achterberg E. P. and James R. H. (2018) Sources of dissolved iron to oxygen minimum zone waters on the Senegalese continental margin in the tropical North Atlantic Ocean: Insights from iron isotopes. *Geochimica et Cosmochimica Acta* **236**, 60-78.

Klatt O., Fahrbach E., Hoppema M. and Rohardt G. (2005) The transport of the Weddell Gyre across the Prime Meridian. *Deep Sea Research Part II: Topical Studies in Oceanography* **52**, 513-528.

Klunder M. B., Laan P., Middag R., De Baar H. J. W. and van Ooijen J. C. (2011) Dissolved iron in the Southern Ocean (Atlantic sector). *Deep Sea Research Part II: Topical Studies in Oceanography* **58**, 2678-2694.

Klunder M. B., Laan P., De Baar H. J. W., Middag R., Neven I. and Van Ooijen J. (2014) Dissolved Fe across the Weddell Sea and Drake Passage: impact of DFe on nutrient uptake. *Biogeosciences* **11**, 651-669.

Köbberich M. and Vance D. (2017) Kinetic control on Zn isotope signatures recorded in marine diatoms. *Geochimica et Cosmochimica Acta* **210**, 97-113.

Köbberich M. and Vance D. (2019) Zn isotope fractionation during uptake into marine phytoplankton: Implications for oceanic zinc isotopes. *Chemical Geology* **523**, 154-161.

König D. and Tagliabue A. (2023) The Fingerprint of Climate Variability on the Surface Ocean Cycling of Iron and its Isotopes. *Biogeosciences Discuss.* **2023**, 1-23.

König D., Conway T. M., Ellwood M. J., Homoky W. B. and Tagliabue A. (2021) Constraints on the Cycling of Iron Isotopes From a Global Ocean Model. *Global Biogeochemical Cycles* **35**, e2021GB006968.

Krisch S., Hopwood M. J., Schaffer J., Al-Hashem A., Höfer J., Rutgers van der Loeff M. M., Conway T. M., Summers B. A., Lodeiro P., Ardiningsih I., Steffens T. and Achterberg E. P. (2021) The 79°N Glacier cavity modulates subglacial iron export to the NE Greenland Shelf. *Nature Communications* **12**, 3030.

Kurisu M., Takahashi Y., Iizuka T. and Uematsu M. (2016a) Very low isotope ratio of iron in fine aerosols related to its contribution to the surface ocean. *Journal of Geophysical Research: Atmospheres* **121**, 11,119-111,136.

Kurisu M., Sakata K., Uematsu M., Ito A. and Takahashi Y. (2021) Contribution of combustion Fe in marine aerosols over the northwestern Pacific estimated by Fe stable isotope ratios. *Atmos. Chem. Phys.* **21**, 16027-16050.

Kurisu M., Sakata K., Miyamoto C., Takaku Y., Iizuka T. and Takahashi Y. (2016b) Variation of Iron Isotope Ratios in Anthropogenic Materials Emitted through Combustion Processes. *Chemistry Letters* **45**, 970-972.

Kustka A. B., Allen A. E. and Morel F. M. M. (2007) Sequence analysis and transcriptional regulation of iron acquisition genes in two marine diatoms. *Journal of Phycology* **43**, 715-729.

Labatut M., Lacan F., Pradoux C., Chmeleff J., Radic A., Murray J. W., Poitrasson F., Johansen A. M. and Thil F. (2014) Iron sources and dissolved-particulate interactions in the seawater of the Western Equatorial Pacific, iron isotope perspectives. *Global Biogeochemical Cycles* **28**, 1044-1065.

Lacan F. and Jeandel C. (2005) Neodymium isotopes as a new tool for quantifying exchange fluxes at the continent–ocean interface. *Earth and Planetary Science Letters* **232**, 245-257.

Lacan F., Francois R., Ji Y. and Sherrell R. M. (2006) Cadmium isotopic composition in the ocean. *Geochimica et Cosmochimica Acta* **70**, 5104-5118.

Lacan F., Artigue L., Klar J. K., Pradoux C., Chmeleff J. and Freydier R. (2021) Interferences and Matrix Effects on Iron Isotopic Composition Measurements by 57Fe-58Fe Double-Spike Multi-Collector Inductively Coupled Plasma Mass Spectrometry; the Importance of Calcium and Aluminum Interferences. *Frontiers in Environmental Chemistry* **2**, 692025.

Lambelet M., Rehkämper M., van de Flierdt T., Xue Z., Kreissig K., Coles B., Porcelli D. and Andersson P. (2013) Isotopic analysis of Cd in the mixing zone of Siberian rivers with the Arctic Ocean—New constraints on marine Cd cycling and the isotope composition of riverine Cd. *Earth and Planetary Science Letters* **361**, 64-73.

Landschützer P., Gruber N., Haumann F. A., Rödenbeck C., Bakker D. C. E., van Heuven S., Hoppema M., Metzl N., Sweeney C., Takahashi T., Tilbrook B. and Wanninkhof R. (2015) The reinvigoration of the Southern Ocean carbon sink. *Science* **349**, 1221-1224.

Lane E. S., Jang K., Cullen J. T. and Maldonado M. T. (2008) The interaction between inorganic iron and cadmium uptake in the marine diatom Thalassiosira oceanica. *Limnology and Oceanography* **53**, 1784-1789.

Lane E. S., Semeniuk D. M., Strzepek R. F., Cullen J. T. and Maldonado M. T. (2009) Effects of iron limitation on intracellular cadmium of cultured phytoplankton: Implications for surface dissolved cadmium to phosphate ratios. *Marine Chemistry* **115**, 155-162.

Lane T. W. and Morel F. M. M. (2000) A biological function for cadmium in marine diatoms. *Proceedings of the National Academy of Sciences* **97**, 4627-4631.

Lannuzel D., Schoemann V., de Jong J., Tison J.-L. and Chou L. (2007) Distribution and biogeochemical behaviour of iron in the East Antarctic sea ice. *Marine Chemistry* **106**, 18-32.

Lannuzel D., Bowie A. R., van der Merwe P. C., Townsend A. T. and Schoemann V. (2011) Distribution of dissolved and particulate metals in Antarctic sea ice. *Marine Chemistry* **124**, 134-146.

Lannuzel D., Schoemann V., de Jong J., Chou L., Delille B., Becquevort S. and Tison J.-L. (2008) Iron study during a time series in the western Weddell pack ice. *Marine Chemistry* **108**, 85-95.

Lannuzel D., Schoemann V., de Jong J., Pasquer B., van der Merwe P., Masson F., Tison J.-L. and Bowie A. (2010) Distribution of dissolved iron in Antarctic sea ice: Spatial, seasonal, and inter-annual variability. *Journal of Geophysical Research: Biogeosciences* **115**.

Le Quéré C., Raupach M. R., Canadell J. G., Marland G., Bopp L., Ciais P., Conway T. J., Doney S. C., Feely R. A., Foster P., Friedlingstein P., Gurney K., Houghton R. A., House J. I., Huntingford C., Levy P. E., Lomas M. R., Majkut J., Metzl N., Ometto J. P., Peters G. P., Prentice I. C., Randerson J. T., Running S. W., Sarmiento J. L., Schuster U., Sitch S., Takahashi T., Viovy N., van der Werf G. R. and Woodward F. I. (2009) Trends in the sources and sinks of carbon dioxide. *Nature Geoscience* **2**, 831-836.

Lee S. H., Kim B. K., Yun M. S., Joo H., Yang E. J., Kim Y. N., Shin H. C. and Lee S. (2012) Spatial distribution of phytoplankton productivity in the Amundsen Sea, Antarctica. *Polar Biology* **35**, 1721-1733.

Lemaitre N., de Souza G. F., Archer C., Wang R.-M., Planquette H., Sarthou G. and Vance D. (2020) Pervasive sources of isotopically light zinc in the North Atlantic Ocean. *Earth and Planetary Science Letters* **539**, 116216.

Lenton A., Tilbrook B., Law R. M., Bakker D., Doney S. C., Gruber N., Ishii M., Hoppema M., Lovenduski N. S., Matear R. J., McNeil B. I., Metzl N., Mikaloff Fletcher S. E., Monteiro P. M. S., Rödenbeck C., Sweeney C. and Takahashi T. (2013) Sea–air CO₂ fluxes in the Southern Ocean for the period 1990–2009. *Biogeosciences* **10**, 4037-4054.

Li F., Ginoux P. and Ramaswamy V. (2008) Distribution, transport, and deposition of mineral dust in the Southern Ocean and Antarctica: Contribution of major sources. *Journal of Geophysical Research: Atmospheres* **113**.

Liao W.-H., Yang S.-C. and Ho T.-Y. (2017) Trace metal composition of size-fractionated plankton in the Western Philippine Sea: The impact of anthropogenic aerosol deposition. *Limnology and Oceanography* **62**, 2243-2259.

Liao W.-H., Takano S., Yang S.-C., Huang K.-F., Sohrin Y. and Ho T.-Y. (2020) Zn Isotope Composition in the Water Column of the Northwestern Pacific Ocean: The Importance of External Sources. *Global Biogeochemical Cycles* **34**, e2019GB006379.

Lin H., Rauschenberg S., Hexel C. R., Shaw T. J. and Twining B. S. (2011) Free-drifting icebergs as sources of iron to the Weddell Sea. *Deep Sea Research Part II: Topical Studies in Oceanography* **58**, 1392-1406.

Litchman E., Klausmeier C. A., Schofield O. M. and Falkowski P. G. (2007) The role of functional traits and trade-offs in structuring phytoplankton communities: scaling from cellular to ecosystem level. *Ecology Letters* **10**, 1170-1181.

Little S. H., Vance D., Walker-Brown C. and Landing W. M. (2014) The oceanic mass balance of copper and zinc isotopes, investigated by analysis of their inputs, and outputs to ferromanganese oxide sediments. *Geochimica et Cosmochimica Acta* **125**, 673-693.

Little S. H., Vance D., McManus J. and Severmann S. (2016) Key role of continental margin sediments in the oceanic mass balance of Zn and Zn isotopes. *Geology* **44**, 207-210.

Liu X. and Millero F. J. (2002) The solubility of iron in seawater. *Marine Chemistry* **77**, 43-54.

Lohan M. C., Statham P. J. and Crawford D. W. (2002) Total dissolved zinc in the upper water column of the subarctic North East Pacific. *Deep Sea Research Part II: Topical Studies in Oceanography* **49**, 5793-5808.

Lough A. J. M., Klar J. K., Homoky W. B., Comer-Warner S. A., Milton J. A., Connelly D. P., James R. H. and Mills R. A. (2017) Opposing authigenic controls on the isotopic signature of dissolved iron in hydrothermal plumes. *Geochimica et Cosmochimica Acta* **202**, 1-20.

Lumpkin R. and Speer K. (2007) Global Ocean Meridional Overturning. *Journal of Physical Oceanography* **37**, 2550-2562.

Mackey M. D., Mackey D. J., Higgins H. W. and Wright S. W. (1996) CHEMTAX - a program for estimating class abundances from chemical markers: application to HPLC measurements of phytoplankton. *Marine Ecology Progress Series* **144**, 265-283.

Mahowald N. M., Hamilton D. S., Mackey K. R. M., Moore J. K., Baker A. R., Scanza R. A. and Zhang Y. (2018) Aerosol trace metal leaching and impacts on marine microorganisms. *Nature Communications* **9**, 2614.

Maldonado M. T. and Price N. M. (1996) Influence of N substrate on Fe requirements of marine centric diatoms. *Marine Ecology Progress Series* **141**, 161-172.

Mankoff K. D., Jacobs S. S., Tulaczyk S. M. and Stammerjohn S. E. (2012) The role of Pine Island Glacier ice shelf basal channels in deep-water

upwelling, polynyas and ocean circulation in Pine Island Bay, Antarctica. *Annals of Glaciology* **53**, 123-128.

Maranger R., Bird D. F. and Price N. M. (1998) Iron acquisition by photosynthetic marine phytoplankton from ingested bacteria. *Nature* **396**, 248-251.

Maréchal C. N., Nicolas E., Douchet C. and Albarède F. (2000) Abundance of zinc isotopes as a marine biogeochemical tracer. *Geochemistry, Geophysics, Geosystems* **1**.

Margalef R. (1978) Life-forms of phytoplankton as survival alternatives in an unstable environment. *Oceanologica Acta* **1**, 493-509.

Marinov I., Gnanadesikan A., Toggweiler J. R. and Sarmiento J. L. (2006) The Southern Ocean biogeochemical divide. *Nature* **441**, 964-967.

Marsay C. M., Lam P. J., Heller M. I., Lee J.-M. and John S. G. (2018a) Distribution and isotopic signature of ligand-leachable particulate iron along the GEOTRACES GP16 East Pacific Zonal Transect. *Marine Chemistry* **201**, 198-211.

Marsay C. M., Kadko D., Landing W. M., Morton P. L., Summers B. A. and Buck C. S. (2018b) Concentrations, provenance and flux of aerosol trace elements during US GEOTRACES Western Arctic cruise GN01. *Chemical Geology* **502**, 1-14.

Marshall J. and Speer K. (2012) Closure of the meridional overturning circulation through Southern Ocean upwelling. *Nature Geoscience* **5**, 171-180.

Martin J. H., Fitzwater S. E. and Gordon R. M. (1990) Iron deficiency limits phytoplankton growth in Antarctic waters. *Global Biogeochemical Cycles* **4**, 5-12.

Martinková E., Chrastný V., Francová M., Šípková A., Čuřík J., Myška O. and Mižič L. (2016) Cadmium isotope fractionation of materials derived from various industrial processes. *Journal of Hazardous Materials* **302**, 114-119.

Masquelier S., Foulon E., Jouenne F., Ferréol M., Brussaard C. P. D. and Vaulot D. (2011) Distribution of eukaryotic plankton in the English Channel and the North Sea in summer. *Journal of Sea Research* **66**, 111-122.

McCain J. S. P., Allen A. E. and Bertrand E. M. (2022) Proteomic traits vary across taxa in a coastal Antarctic phytoplankton bloom. *The ISME Journal* **16**, 569-579.

Measures C. I., Brown M. T., Selph K. E., Apprill A., Zhou M., Hatta M. and Hiscock W. T. (2013) The influence of shelf processes in delivering

dissolved iron to the HNLC waters of the Drake Passage, Antarctica. *Deep-Sea Research Part II: Topical Studies in Oceanography* **90**, 77-88.

Meredith M. P., Venables H. J., Clarke A., Ducklow H. W., Erickson M., Leng M. J., Lenaerts J. T. M. and van den Broeke M. R. (2013) The Freshwater System West of the Antarctic Peninsula: Spatial and Temporal Changes. *Journal of Climate* **26**, 1669-1684.

Middag R., de Baar H. J. W. and Bruland K. W. (2019) The Relationships Between Dissolved Zinc and Major Nutrients Phosphate and Silicate Along the GEOTRACES GA02 Transect in the West Atlantic Ocean. *Global Biogeochemical Cycles* **33**, 63-84.

Middag R., de Baar H. J. W., Klunder M. B. and Laan P. (2013) Fluxes of dissolved aluminum and manganese to the Weddell Sea and indications for manganese co-limitation. *Limnology and Oceanography* **58**, 287-300.

Middag R., van Heuven S. M. A. C., Bruland K. W. and de Baar H. J. W. (2018) The relationship between cadmium and phosphate in the Atlantic Ocean unravelled. *Earth and Planetary Science Letters* **492**, 79-88.

Middag R., Séférian R., Conway T. M., John S. G., Bruland K. W. and de Baar H. J. W. (2015) Intercomparison of dissolved trace elements at the Bermuda Atlantic Time Series station. *Marine Chemistry* **177**, 476-489.

Mikucki J. A., Foreman C. M., Sattler B., Berry Lyons W. and Priscu J. C. (2004) Geomicrobiology of Blood Falls: An Iron-Rich Saline Discharge at the Terminus of the Taylor Glacier, Antarctica. *Aquatic Geochemistry* **10**, 199-220.

Miles T., Lee S. H., Wåhlin A., Ha H. K., Kim T. W., Assmann K. M. and Schofield O. (2016) Glider observations of the Dotson Ice Shelf outflow. *Deep Sea Research Part II: Topical Studies in Oceanography* **123**, 16-29.

Millero F. J., Yao W. and Aicher J. (1995) The speciation of Fe(II) and Fe(III) in natural waters. *Marine Chemistry* **50**, 21-39.

Mitchell B. G., Brody E. A., Holm-Hansen O., McClain C. and Bishop J. (1991) Light limitation of phytoplankton biomass and macronutrient utilization in the Southern Ocean. *Limnology and Oceanography* **36**, 1662-1677.

Moeller K., Schoenberg R., Pedersen R.-B., Weiss D. and Dong S. (2012) Calibration of the New Certified Reference Materials ERM-AE633 and ERM-AE647 for Copper and IRMM-3702 for Zinc Isotope

Amount Ratio Determinations. *Geostandards and Geoanalytical Research* **36**, 177-199.

Moore C. M., Mills M. M., Arrigo K. R., Berman-Frank I., Bopp L., Boyd P. W., Galbraith E. D., Geider R. J., Guieu C., Jaccard S. L., Jickells T. D., La Roche J., Lenton T. M., Mahowald N. M., Marañón E., Marinov I., Moore J. K., Nakatsuka T., Oschlies A., Saito M. A., Thingstad T. F., Tsuda A. and Ulloa O. (2013) Processes and patterns of oceanic nutrient limitation. *Nature Geoscience* **6**, 701-710.

Moore J. K., Doney S. C., Glover D. M. and Fung I. Y. (2001) Iron cycling and nutrient-limitation patterns in surface waters of the World Ocean. *Deep Sea Research Part II: Topical Studies in Oceanography* **49**, 463-507.

Moreau S., Lannuzel D., Janssens J., Arroyo M. C., Corkill M., Cougnon E., Genovese C., Legresy B., Lenton A., Puigcorbé V., Ratnarajah L., Rintoul S., Roca-Martí M., Rosenberg M., Shadwick E. H., Silvano A., Strutton P. G. and Tilbrook B. (2019) Sea Ice Meltwater and Circumpolar Deep Water Drive Contrasting Productivity in Three Antarctic Polynyas. *Journal of Geophysical Research: Oceans* **124**, 2943-2968.

Morel F. M. M. and Price N. M. (2003) The Biogeochemical Cycles of Trace Metals in the Oceans. *Science* **300**, 944.

Morel F. M. M., Kustka A. B. and Shaked Y. (2008) The role of unchelated Fe in the iron nutrition of phytoplankton. *Limnology and Oceanography* **53**, 400-404.

Morel F. M. M., Lam P. J. and Saito M. A. (2020) Trace Metal Substitution in Marine Phytoplankton. *Annual Review of Earth and Planetary Sciences* **48**, 491-517.

Morel F. M. M., Reinfelder J. R., Roberts S. B., Chamberlain C. P., Lee J. G. and Yee D. (1994) Zinc and carbon co-limitation of marine phytoplankton. *Nature* **369**, 740-742.

Morel F. M. M., Cox E. H., Kraepiel A. M. L., Lane T. W., Milligan A. J., Schaperdoth I., Reinfelder J. R. and Tortell P. D. (2002) Acquisition of inorganic carbon by the marine diatom <emph type="2">Thalassiosira weissflogii</emph>. *Functional Plant Biology* **29**, 301-308.

Morgan J. L. L., Wasylenki L. E., Nuester J. and Anbar A. D. (2010) Fe Isotope Fractionation during Equilibration of Fe−Organic Complexes. *Environmental Science & Technology* **44**, 6095-6101.

Mosby H. (1936) Part XIII. Physical Oceanography. *Geografiska Annaler* **18**, 20-29.

Mu L., Stammerjohn S. E., Lowry K. E. and Yager P. L. (2014) Spatial variability of surface pCO2 and air-sea CO2 flux in the Amundsen Sea Polynya, Antarctica. *Elementa: Science of the Anthropocene* **3**, 000036.

Mulholland D. S., Poitrasson F., Shirokova L. S., González A. G., Pokrovsky O. S., Boaventura G. R. and Vieira L. C. (2015) Iron isotope fractionation during Fe(II) and Fe(III) adsorption on cyanobacteria. *Chemical Geology* **400**, 24-33.

Nakamura K., Aoki S., Yoshimura K. and Kurita N. (2014) Distribution of Oxygen Isotope Ratio of Precipitation in the Atlantic-Indian Sectors of the Southern Ocean. *SOLA* **10**, 154-157.

Nasemann P., Gault-Ringold M., Stirling C. H., Koschinsky A. and Sander S. G. (2018) Processes affecting the isotopic composition of dissolved iron in hydrothermal plumes: A case study from the Vanuatu back-arc. *Chemical Geology* **476**, 70-84.

Nicholls K. W., Østerhus S., Makinson K., Gammelsrød T. and Fahrbach E. (2009) Ice-ocean processes over the continental shelf of the southern Weddell Sea, Antarctica: A review. *Reviews of Geophysics* **47**.

Nolting R. F., De Baar H. J. W., Van Bennekom A. J. and Masson A. (1991) Cadmium, copper and iron in the Scotia Sea, Weddell Sea and Weddell/Scotia Confluence (Antarctica). *Marine Chemistry* **35**, 219-243.

Ohnemus D. C., Auro M. E., Sherrell R. M., Lagerström M., Morton P. L., Twining B. S., Rauschenberg S. and Lam P. J. (2014) Laboratory intercomparison of marine particulate digestions including Piranha: a novel chemical method for dissolution of polyethersulfone filters. *Limnology and Oceanography: Methods* **12**, 530-547.

Orsi A. H., Johnson G. C. and Bullister J. L. (1999) Circulation, mixing, and production of Antarctic Bottom Water. *Progress in Oceanography* **43**, 55-109.

Orsi A. H., Smethie Jr W. M. and Bullister J. L. (2002) On the total input of Antarctic waters to the deep ocean: A preliminary estimate from chlorofluorocarbon measurements. *Journal of Geophysical Research: Oceans* **107**, 31-31-31-14.

Östlund H. G. and Hut G. (1984) Arctic Ocean water mass balance from isotope data. *Journal of Geophysical Research: Oceans* **89**, 6373-6381.

Paolo F. S., Fricker H. A. and Padman L. (2015) Volume loss from Antarctic ice shelves is accelerating. *Science* **348**, 327-331.

Park H., Song B. and Morel F. M. M. (2007) Diversity of the cadmium-containing carbonic anhydrase in marine diatoms and natural waters. *Environmental Microbiology* **9**, 403-413.

Park J., Kuzminov F. I., Bailleul B., Yang E. J., Lee S., Falkowski P. G. and Gorbunov M. Y. (2017) Light availability rather than Fe controls the magnitude of massive phytoplankton bloom in the Amundsen Sea polynyas, Antarctica. *Limnology and Oceanography* **62**, 2260-2276.

Park Y.-H., Charriaud E., Craneguy P. and Kartavtseff A. (2001) Fronts, transport, and Weddell Gyre at 30°E between Africa and Antarctica. *Journal of Geophysical Research: Oceans* **106**, 2857-2879.

Parkinson C. L. and Cavalieri D. J. (2012) Antarctic sea ice variability and trends, 1979–2010. *The Cryosphere* **6**, 871-880.

Parry G. D. (1981) The meanings of r- and K-selection. *Oecologia* **48**, 260-264.

Pease C. H. (1987) The size of wind-driven coastal polynyas. *Journal of Geophysical Research: Oceans* **92**, 7049-7059.

Pichat S., Douchet C. and Albarède F. (2003) Zinc isotope variations in deep-sea carbonates from the eastern equatorial Pacific over the last 175 ka. *Earth and Planetary Science Letters* **210**, 167-178.

Planquette H. and Sherrell R. M. (2012) Sampling for particulate trace element determination using water sampling bottles: methodology and comparison to in situ pumps. *Limnology and Oceanography: Methods* **10**, 367-388.

Planquette H., Sherrell R. M., Stammerjohn S. and Field M. P. (2013) Particulate iron delivery to the water column of the Amundsen Sea, Antarctica. *Marine Chemistry* **153**, 15-30.

Plocke D. J., Levinthal C. and Vallee B. L. (1962) Alkaline Phosphatase of Escherichia coli: A Zinc Metalloenzyme*. *Biochemistry* **1**, 373-378.

Pollard R., Tréguer P. and Read J. (2006) Quantifying nutrient supply to the Southern Ocean. *Journal of Geophysical Research: Oceans* **111**.

Pollard R. T., Lucas M. I. and Read J. F. (2002) Physical controls on biogeochemical zonation in the Southern Ocean. *Deep Sea Research Part II: Topical Studies in Oceanography* **49**, 3289-3305.

Price N. M. and Morel F. M. M. (1990) Cadmium and cobalt substitution for zinc in a marine diatom. *Nature* **344**, 658-660.

Radic A., Lacan F. and Murray J. W. (2011) Iron isotopes in the seawater of the equatorial Pacific Ocean: New constraints for the oceanic iron cycle. *Earth and Planetary Science Letters* **306**, 1-10.

Raiswell R. (2011) Iceberg-hosted nanoparticulate Fe in the Southern Ocean: Mineralogy, origin, dissolution kinetics and source of bioavailable Fe. *Deep Sea Research Part II: Topical Studies in Oceanography* **58**, 1364-1375.

Raiswell R., Tranter M., Benning L. G., Siegert M., De'ath R., Huybrechts P. and Payne T. (2006) Contributions from glacially derived sediment to the global iron (oxyhydr)oxide cycle: Implications for iron delivery to the oceans. *Geochimica et Cosmochimica Acta* **70**, 2765-2780.

Raiswell R., Hawkings J. R., Benning L. G., Baker A. R., Death R., Albani S., Mahowald N., Krom M. D., Poulton S. W., Wadham J. and Tranter M. (2016) Potentially bioavailable iron delivery by iceberg-hosted sediments and atmospheric dust to the polar oceans. *Biogeosciences* **13**, 3887-3900.

Randall-Goodwin., Meredith. M. P., Jenkins. A., L.Yager. P., Sherrell. R. M., Abrahamsen. E. P., Guerrero. R., Yuan. X., Mortlock. R. A., Gavahan. K., Alderkamp. A.-C., Ducklow. H., R.Robertson. and Stammerjohn. S. E. (2015) Freshwater distributions and water mass structure in the Amundsen Sea Polynya region, Antarctica. *Elementa: Science of the Anthropocene* **3**, 000065.

Ratié G., Chrastný V., Guinoiseau D., Marsac R., Vaňková Z. and Komárek M. (2021) Cadmium Isotope Fractionation during Complexation with Humic Acid. *Environmental Science & Technology* **55**, 7430-7444.

Rauschenberg S. and Twining B. S. (2015) Evaluation of approaches to estimate biogenic particulate trace metals in the ocean. *Marine Chemistry* **171**, 67-77.

Raven J. A. and Falkowski P. G. (1999) Oceanic sinks for atmospheric CO2. *Plant, Cell & Environment* **22**, 741-755.

Redfield A. C. (1934) On the proportions of organic derivatives in sea water and their relation to the composition of plankton. *James Johnstone memorial volume*, 176-192.

Reeve K. A., Boebel O., Kanzow T., Strass V., Rohardt G. and Fahrbach E. (2016) A gridded data set of upper-ocean hydrographic properties in the Weddell Gyre obtained by objective mapping of Argo float measurements. *Earth Syst. Sci. Data* **8**, 15-40.

Rehkämper M., Schönbächler M. and Andreasen R. (2012) Application of Multiple-Collector Inductively Coupled Plasma Mass Spectrometry

to Isotopic Analysis in Cosmochemistry. In *Isotopic Analysis*. pp. 275-315.

Rignot E., Mouginot J., Scheuchl B., van den Broeke M., van Wessem M. J. and Morlighem M. (2019) Four decades of Antarctic Ice Sheet mass balance from 1979–2017. *Proceedings of the National Academy of Sciences* **116**, 1095-1103.

Rignot E., Bamber J. L., van den Broeke M. R., Davis C., Li Y., van de Berg W. J. and van Meijgaard E. (2008) Recent Antarctic ice mass loss from radar interferometry and regional climate modelling. *Nature Geoscience* **1**, 106-110.

Rijkenberg M. J. A., de Baar H. J. W., Bakker K., Gerringa L. J. A., Keijzer E., Laan M., Laan P., Middag R., Ober S., van Ooijen J., Ossebaar S., van Weerlee E. M. and Smit M. G. (2015) "PRISTINE", a new high volume sampler for ultraclean sampling of trace metals and isotopes. *Marine Chemistry* **177**, 501-509.

Ripperger S., Rehkämper M., Porcelli D. and Halliday A. N. (2007) Cadmium isotope fractionation in seawater — A signature of biological activity. *Earth and Planetary Science Letters* **261**, 670-684.

Rosca C., Schoenberg R., Tomlinson E. L. and Kamber B. S. (2019) Combined zinc-lead isotope and trace-metal assessment of recent atmospheric pollution sources recorded in Irish peatlands. *Science of The Total Environment* **658**, 234-249.

Rouxel O., Dobbek N., Ludden J. and Fouquet Y. (2003) Iron isotope fractionation during oceanic crust alteration. *Chemical Geology* **202**, 155-182.

Rouxel O., Toner B. M., Manganini S. J. and German C. R. (2016) Geochemistry and iron isotope systematics of hydrothermal plume fall-out at East Pacific Rise 9°50′ N. *Chemical Geology* **441**, 212-234.

Rouxel O. J. and Auro M. (2010) Iron Isotope Variations in Coastal Seawater Determined by Multicollector ICP-MS. *Geostandards and Geoanalytical Research* **34**, 135-144.

Rudnick R. L. and Gao S. (2003) Composition of the continental crust. In *The crust* (eds. H. D. Holland., R. L. Rudnick. and K. K. Turekian.). Elsevier-Pergamon, Oxford, UK.

Sabine C. L., Feely R. A., Gruber N., Key R. M., Lee K., Bullister J. L., Wanninkhof R., Wong C. S., Wallace D. W. R., Tilbrook B., Millero F. J., Peng T.-H., Kozyr A., Ono T. and Rios A. F. (2004) The Oceanic Sink for Anthropogenic CO2. *Science* **305**, 367-371.

Saito M. A., Goepfert T. J. and Ritt J. T. (2008) Some thoughts on the concept of colimitation: Three definitions and the importance of bioavailability. *Limnology and Oceanography* **53**, 276-290.

Sallée J.-B., Matear R. J., Rintoul S. R. and Lenton A. (2012) Localized subduction of anthropogenic carbon dioxide in the Southern Hemisphere oceans. *Nature Geoscience* **5**, 579-584.

Samanta M., Ellwood M. J. and Strzepek R. F. (2018) Zinc isotope fractionation by Emiliania huxleyi cultured across a range of free zinc ion concentrations. *Limnology and Oceanography* **63**, 660-671.

Sanchez N., Reiss C. S., Holm-Hansen O., Hewes C. D., Bizsel K. C. and Ardelan M. V. (2019) Weddell-Scotia Confluence Effect on the Iron Distribution in Waters Surrounding the South Shetland (Antarctic Peninsula) and South Orkney (Scotia Sea) Islands During the Austral Summer in 2007 and 2008. *Frontiers in Marine Science* **6**.

Sañudo-Wilhelmy S. A., Olsen K. A., Scelfo J. M., Foster T. D. and Flegal A. R. (2002) Trace metal distributions off the Antarctic Peninsula in the Weddell Sea. *Marine Chemistry* **77**, 157-170.

Sarmiento J. L., Gruber N., Brzezinski M. A. and Dunne J. P. (2004) High-latitude controls of thermocline nutrients and low latitude biological productivity. *Nature* **427**, 56-60.

Sarthou G., Baker A. R., Kramer J., Laan P., Laës A., Ussher S., Achterberg E. P., de Baar H. J. W., Timmermans K. R. and Blain S. (2007) Influence of atmospheric inputs on the iron distribution in the subtropical North-East Atlantic Ocean. *Marine Chemistry* **104**, 186-202.

Schaffer J., Kanzow T., von Appen W.-J., von Albedyll L., Arndt J. E. and Roberts D. H. (2020) Bathymetry constrains ocean heat supply to Greenland's largest glacier tongue. *Nature Geoscience* **13**, 227-231.

Schlitzer R. (2020) Ocean Data View.

Schlitzer R.Anderson R. F.Dodas E. M.Lohan M.Geibert W.Tagliabue A.Bowie A.Jeandel C.Maldonado M. T.Landing W. M.Cockwell D.Abadie C.Abouchami W.Achterberg E. P.Agather A.Aguliar-Islas A.van Aken H. M.Andersen M.Archer C.Auro M.de Baar H. J.Baars O.Baker A. R.Bakker K.Basak C.Baskaran M.Bates N. R.Bauch D.van Beek P.Behrens M. K.Black E.Bluhm K.Bopp L.Bouman H.Bowman K.Bown J.Boyd P.Boye M.Boyle E. A.Branellec P.Bridgestock L.Brissebrat G.Browning T.Bruland K. W.Brumsack H.-J.Brzezinski M.Buck C. S.Buck K. N.Buesseler K.Bull A.Butler E.Cai P.Mor P. C.Cardinal D.Carlson C.Carrasco G.Casacuberta N.Casciotti K. L.Castrillejo M.Chamizo E.Chance R.Charette M. A.Chaves J. E.Cheng H.Chever

F.Christl M.Church T. M.Closset I.Colman A.Conway T. M.Cossa D.Croot P.Cullen J. T.Cutter G. A.Daniels C.Dehairs F.Deng F.Dieu H. T.Duggan B.Dulaquais G.Dumousseaud C.Echegoyen-Sanz Y.Edwards R. L.Ellwood M.Fahrbach E.Fitzsimmons J. N.Russell Flegal A.Fleisher M. Q.van de Flierdt T.Frank M.Friedrich J.Fripiat F.Fröllje H.Galer S. J. G.Gamo T.Ganeshram R. S.Garcia-Orellana J.Garcia-Solsona E.Gault-Ringold M.George E.Gerringa L. J. A.Gilbert M.Godoy J. M.Goldstein S. L.Gonzalez S. R.Grissom K.Hammerschmidt C.Hartman A.Hassler C. S.Hathorne E. C.Hatta M.Hawco N.Hayes C. T.Heimbürger L.-E.Helgoe J.Heller M.Henderson G. M.Henderson P. B.van Heuven S.Ho P.Horner T. J.Hsieh Y.-T.Huang K.-F.Humphreys M. P.Isshiki K.Jacquot J. E.Janssen D. J.Jenkins W. J.John S.Jones E. M.Jones J. L.Kadko D. C.Kayser R.Kenna T. C.Khondoker R.Kim T.Kipp L.Klar J. K.Klunder M.Kretschmer S.Kumamoto Y.Laan P.Labatut M.Lacan F.Lam P. J.Lambelet M.Lamborg C. H.Le Moigne F. A. C.Le Roy E.Lechtenfeld O. J.Lee J.-M.Lherminier P.Little S.López-Lora M.Lu Y.Masque P.Mawji E.McClain C. R.Measures C.Mehic S.Barraqueta J.-L. M.van der Merwe P.Middag R.Mieruch S.Milne A.Minami T.Moffett J. W.Moncoiffe G.Moore W. S.Morris P. J.Morton P. L.Nakaguchi Y.Nakayama N.Niedermiller J.Nishioka J.Nishiuchi A.Noble A.Obata H.Ober S.Ohnemus D. C.van Ooijen J.O'Sullivan J.Owens S.Pahnke K.Paul M.Pavia F.Pena L. D.Peters B.Planchon F.Planquette H.Pradoux C.Puigcorbé V.Quay P.Queroue F.Radic A.Rauschenberg S.Rehkämper M.Rember R.Remenyi T.Resing J. A.Rickli J.Rigaud S.Rijkenberg M. J. A.Rintoul S.Robinson L. F.Roca-Martí M.Rodellas V.Roeske T.Rolison J. M.Rosenberg M.Roshan S.Rutgers van der Loeff M. M.Ryabenko E.Saito M. A.Salt L. A.Sanial V.Sarthou G.Schallenberg C.Schauer U.Scher H.Schlosser C.Schnetger B.Scott P.Sedwick P. N.Semiletov I.Shelley R.Sherrell R. M.Shiller A. M.Sigman D. M.Singh S. K.Slagter H. A.Slater E.Smethie W. M.Snaith H.Sohrin Y.Sohst B.Sonke J. E.Speich S.Steinfeldt R.Stewart G.Stichel T.Stirling C. H.Stutsman J.Swarr G. J.Swift J. H.Thomas A.Thorne K.Till C. P.Till R.Townsend A. T.Townsend E.Tuerena R.Twining B. S.Vance D.Velazquez S.Venchiarutti C.Villa-Alfageme M.Vivancos S. M.Voelker A. H. L.Wake B.Warner M. J.Watson R.van Weerlee E.Alexandra Weigand M.Weinstein Y.Weiss D.Wisotzki A.Woodward E. M. S.Wu J.Wu Y.Wuttig K.Wyatt N.Xiang Y.Xie R. C.Xue Z.Yoshikawa H.Zhang J.Zhang P.Zhao Y.Zheng L.Zheng X.-Y.Zieringer

M.Zimmer L. A.Ziveri P.Zunino P. and Zurbrick C. (2018) The GEOTRACES Intermediate Data Product 2017. *Chemical Geology* **493**, 210-223.

Schmitt A.-D., Galer S. J. G. and Abouchami W. (2009) Mass-dependent cadmium isotopic variations in nature with emphasis on the marine environment. *Earth and Planetary Science Letters* **277**, 262-272.

Schroth A. W., Crusius J., Chever F., Bostick B. C. and Rouxel O. J. (2011) Glacial influence on the geochemistry of riverine iron fluxes to the Gulf of Alaska and effects of deglaciation. *Geophysical Research Letters* **38**, L16605.

Sedwick P. N. and DiTullio G. R. (1997) Regulation of algal blooms in Antarctic Shelf Waters by the release of iron from melting sea ice. *Geophysical Research Letters* **24**, 2515-2518.

Sedwick P. N., Bowie A. R. and Trull T. W. (2008) Dissolved iron in the Australian sector of the Southern Ocean (CLIVAR SR3 section): Meridional and seasonal trends. *Deep Sea Research Part I: Oceanographic Research Papers* **55**, 911-925.

Sedwick P. N., Garcia N. S., Riseman S. F., Marsay C. M. and DiTullio G. R. (2007) Evidence for high iron requirements of colonial Phaeocystis antarctica at low irradiance. In *Phaeocystis, major link in the biogeochemical cycling of climate-relevant elements* (eds. M. A. van Leeuwe, J. Stefels, S. Belviso, C. Lancelot, P. G. Verity and W. W. C. Gieskes). Springer Netherlands, Dordrecht. pp. 83-97.

Selz V., Lowry K. E., Lewis K. M., Joy-Warren H. L., Poll W., Nirmel S., Tong A. and Arrigo K. R. (2018) Distribution of Phaeocystis antarctica-dominated sea ice algal communities and their potential to seed phytoplankton across the western Antarctic Peninsula in spring. *Marine Ecology Progress Series* **586**, 91-112.

Severmann S., Johnson C. M., Beard B. L. and McManus J. (2006) The effect of early diagenesis on the Fe isotope compositions of porewaters and authigenic minerals in continental margin sediments. *Geochimica et Cosmochimica Acta* **70**, 2006-2022.

Severmann S., McManus J., Berelson W. M. and Hammond D. E. (2010) The continental shelf benthic iron flux and its isotope composition. *Geochimica et Cosmochimica Acta* **74**, 3984-4004.

Severmann S., Johnson C. M., Beard B. L., German C. R., Edmonds H. N., Chiba H. and Green D. R. H. (2004) The effect of plume processes on the Fe isotope composition of hydrothermally derived Fe in the deep

ocean as inferred from the Rainbow vent site, Mid-Atlantic Ridge, 36 °14´ N. *Earth and Planetary Science Letters* **225**, 63-76.

Shaked Y., Xu Y., Leblanc K. and Morel F. M. M. (2006) Zinc availability and alkaline phosphatase activity in Emiliania huxleyi: Implications for Zn-P co-limitation in the ocean. *Limnology and Oceanography* **51**, 299-309.

Shaw T. J., Raiswell R., Hexel C. R., Vu H. P., Moore W. S., Dudgeon R. and Smith K. L. (2011) Input, composition, and potential impact of terrigenous material from free-drifting icebergs in the Weddell Sea. *Deep Sea Research Part II: Topical Studies in Oceanography* **58**, 1376-1383.

Shepherd A., Wingham D. and Rignot E. (2004) Warm ocean is eroding West Antarctic Ice Sheet. *Geophysical Research Letters* **31**.

Shepherd A., Ivins E. R., A G., Barletta V. R., Bentley M. J., Bettadpur S., Briggs K. H., Bromwich D. H., Forsberg R., Galin N., Horwath M., Jacobs S., Joughin I., King M. A., Lenaerts J. T. M., Li J., Ligtenberg S. R. M., Luckman A., Luthcke S. B., McMillan M., Meister R., Milne G., Mouginot J., Muir A., Nicolas J. P., Paden J., Payne A. J., Pritchard H., Rignot E., Rott H., Sørensen L. S., Scambos T. A., Scheuchl B., Schrama E. J. O., Smith B., Sundal A. V., van Angelen J. H., van de Berg W. J., van den Broeke M. R., Vaughan D. G., Velicogna I., Wahr J., Whitehouse P. L., Wingham D. J., Yi D., Young D. and Zwally H. J. (2012) A Reconciled Estimate of Ice-Sheet Mass Balance. *Science* **338**, 1183.

Sherrell R. M., Lagerström M. E., Forsch K. O., Stammerjohn S. E. and Yager P. L. (2015) Dynamics of dissolved iron and other bioactive trace metals (Mn, Ni, Cu, Zn) in the Amundsen Sea Polynya, Antarctica. *Elementa: Science of the Anthropocene* **3**, 000071.

Shiel A. E., Weis D. and Orians K. J. (2010) Evaluation of zinc, cadmium and lead isotope fractionation during smelting and refining. *Science of The Total Environment* **408**, 2357-2368.

Sieber M., Conway T. M., de Souza G. F., Hassler C. S., Ellwood M. J. and Vance D. (2019a) High-resolution Cd isotope systematics in multiple zones of the Southern Ocean from the Antarctic Circumnavigation Expedition. *Earth and Planetary Science Letters* **527**, 115799.

Sieber M., Conway T. M., de Souza G. F., Hassler C. S., Ellwood M. J. and Vance D. (2020) Cycling of zinc and its isotopes across multiple zones of the Southern Ocean: Insights from the Antarctic Circumnavigation Expedition. *Geochimica et Cosmochimica Acta* **268**, 310-324.

Sieber M., Conway T. M., de Souza G. F., Hassler C. S., Ellwood M. J. and Vance D. (2021) Isotopic fingerprinting of biogeochemical processes and iron sources in the iron-limited surface Southern Ocean. *Earth and Planetary Science Letters* **567**, 116967.

Sieber M., Conway T. M., de Souza G. F., Obata H., Takano S., Sohrin Y. and Vance D. (2019b) Physical and biogeochemical controls on the distribution of dissolved cadmium and its isotopes in the Southwest Pacific Ocean. *Chemical Geology* **511**, 494-509.

Sieber M., Lanning N. T., Bian X., Yang S. C., Takano S., Sohrin Y., Weber T. S., Fitzsimmons J. N., John S. G. and Conway T. M. (2023a) The Importance of Reversible Scavenging for the Marine Zn Cycle Evidenced by the Distribution of Zinc and Its Isotopes in the Pacific Ocean. *Journal of Geophysical Research: Oceans* **128**, e2022JC019419.

Sieber M., Lanning N. T., Bunnell Z. B., Bian X., Yang S.-C., Marsay C. M., Landing W. M., Buck C. S., Fitzsimmons J. N., John S. G. and Conway T. M. (2023b) Biological, Physical, and Atmospheric Controls on the Distribution of Cadmium and Its Isotopes in the Pacific Ocean. *Global Biogeochemical Cycles* **37**, e2022GB007441.

Siebert C., Nägler T. F. and Kramers J. D. (2001) Determination of molybdenum isotope fractionation by double-spike multicollector inductively coupled plasma mass spectrometry. *Geochemistry, Geophysics, Geosystems* **2**, 1032.

Smith Jr W. O. and Gordon L. I. (1997) Hyperproductivity of the Ross Sea (Antarctica) polynya during austral spring. *Geophysical Research Letters* **24**, 233-236.

Smith Jr W. O. and Comiso J. C. (2008) Influence of sea ice on primary production in the Southern Ocean: A satellite perspective. *Journal of Geophysical Research: Oceans* **113**.

Sohrin Y., Iwamoto S., Matsui M., Obata H., Nakayama E., Suzuki K., Handa N. and Ishii M. (2000) The distribution of Fe in the Australian sector of the Southern Ocean. *Deep Sea Research Part I: Oceanographic Research Papers* **47**, 55-84.

St-Laurent P., Yager P. L., Sherrell R. M., Stammerjohn S. E. and Dinniman M. S. (2017) Pathways and supply of dissolved iron in the Amundsen Sea (Antarctica). *Journal of Geophysical Research: Oceans* **122**, 7135-7162.

St-Laurent P., Yager P. L., Sherrell R. M., Oliver H., Dinniman M. S. and Stammerjohn S. E. (2019) Modeling the Seasonal Cycle of Iron and

Carbon Fluxes in the Amundsen Sea Polynya, Antarctica. *Journal of Geophysical Research: Oceans* **124**, 1544-1565.

Stevenson E. I., Fantle M. S., Das S. B., Williams H. M. and Aciego S. M. (2017) The iron isotopic composition of subglacial streams draining the Greenland ice sheet. *Geochimica et Cosmochimica Acta* **213**, 237-254.

Strzepek R. F., Hunter K. A., Frew R. D., Harrison P. J. and Boyd P. W. (2012) Iron-light interactions differ in Southern Ocean phytoplankton. *Limnology and Oceanography* **57**, 1182-1200.

Sun M., Archer C. and Vance D. (2021) New Methods for the Chemical Isolation and Stable Isotope Measurement of Multiple Transition Metals, with Application to the Earth Sciences. *Geostandards and Geoanalytical Research* **45**, 643-658.

Sunda W. G. and Huntsman S. A. (1995) Cobalt and zinc interreplacement in marine phytoplankton: Biological and geochemical implications. *Limnology and Oceanography* **40**, 1404-1417.

Sunda W. G. and Huntsman S. A. (1998a) Control of Cd Concentrations in a Coastal Diatom by Interactions among Free Ionic Cd, Zn, and Mn in Seawater. *Environmental Science & Technology* **32**, 2961-2968.

Sunda W. G. and Huntsman S. A. (1998b) Interactions among Cu2+, Zn2+, and Mn2+ in controlling cellular Mn, Zn, and growth rate in the coastal alga Chlamydomonas. *Limnology and Oceanography* **43**, 1055-1064.

Sunda W. G. and Huntsman S. A. (2000) Effect of Zn, Mn, and Fe on Cd accumulation in phytoplankton: Implications for oceanic Cd cycling. *Limnology and Oceanography* **45**, 1501-1516.

Sunda W. G. and Huntsman S. A. (2005) Effect of CO2 supply and demand on zinc uptake and growth limitation in a coastal diatom. *Limnology and Oceanography* **50**, 1181-1192.

Tagliabue A., Bopp L. and Aumont O. (2009) Evaluating the importance of atmospheric and sedimentary iron sources to Southern Ocean biogeochemistry. *Geophysical Research Letters* **36**.

Tagliabue A., Aumont O. and Bopp L. (2014a) The impact of different external sources of iron on the global carbon cycle. *Geophysical Research Letters* **41**, 920-926.

Tagliabue A., Sallée J.-B., Bowie A. R., Lévy M., Swart S. and Boyd P. W. (2014b) Surface-water iron supplies in the Southern Ocean sustained by deep winter mixing. *Nature Geoscience* **7**, 314-320.

Tagliabue A., Bowie A. R., Boyd P. W., Buck K. N., Johnson K. S. and Saito M. A. (2017) The integral role of iron in ocean biogeochemistry. *Nature* **543**, 51-59.

Tagliabue A., Mtshali T., Aumont O., Bowie A. R., Klunder M. B., Roychoudhury A. N. and Swart S. (2012) A global compilation of dissolved iron measurements: focus on distributions and processes in the Southern Ocean. *Biogeosciences* **9**, 2333-2349.

Tagliabue A., Barrier N., Du Pontavice H., Kwiatkowski L., Aumont O., Bopp L., Cheung W. W. L., Gascuel D. and Maury O. (2020) An iron cycle cascade governs the response of equatorial Pacific ecosystems to climate change. *Global Change Biology* **26**, 6168-6179.

Tagliabue A., Bopp L., Dutay J.-C., Bowie A. R., Chever F., Jean-Baptiste P., Bucciarelli E., Lannuzel D., Remenyi T., Sarthou G., Aumont O., Gehlen M. and Jeandel C. (2010) Hydrothermal contribution to the oceanic dissolved iron inventory. *Nature Geoscience* **3**, 252-256.

Takano S., Tanimizu M., Hirata T., Shin K.-C., Fukami Y., Suzuki K. and Sohrin Y. (2017) A simple and rapid method for isotopic analysis of nickel, copper, and zinc in seawater using chelating extraction and anion exchange. *Analytica Chimica Acta* **967**, 1-11.

Tang D. and Morel F. M. M. (2006) Distinguishing between cellular and Fe-oxide-associated trace elements in phytoplankton. *Marine Chemistry* **98**, 18-30.

Thoma M., Jenkins A., Holland D. and Jacobs S. (2008) Modelling Circumpolar Deep Water intrusions on the Amundsen Sea continental shelf, Antarctica. *Geophysical Research Letters* **35**.

Thuróczy C.-E., Alderkamp A.-C., Laan P., Gerringa L. J. A., Mills M. M., Van Dijken G. L., De Baar H. J. W. and Arrigo K. R. (2012) Key role of organic complexation of iron in sustaining phytoplankton blooms in the Pine Island and Amundsen Polynyas (Southern Ocean). *Deep Sea Research Part II: Topical Studies in Oceanography* **71-76**, 49-60.

Tian H.-A., van Manen M., Bunnell Z. B., Jung J., Lee S. H., Kim T.-W., Reichart G.-J., Conway T. M. and Middag R. (2023a) Biogeochemistry of iron in coastal Antarctica: isotopic insights for external sources and biological uptake in the Amundsen Sea polynyas. *Geochimica et Cosmochimica Acta* **363**, 51-67.

Tian H.-A., van Manen M., Wille F., Jung J., Lee S., Kim T.-W., Aoki S., Eich C., Brussaard C. P. D., Reichart G.-J., Conway T. M. and Middag R. (2023b) The biogeochemistry of zinc and cadmium in the Amundsen Sea, coastal Antarctica. *Marine Chemistry* **249**, 104223.

Tortell P. D., Maldonado M. T. and Price N. M. (1996) The role of heterotrophic bacteria in iron-limited ocean ecosystems. *Nature* **383**, 330-332.

Tovar-Sanchez A., Sañudo-Wilhelmy S. A., Garcia-Vargas M., Weaver R. S., Popels L. C. and Hutchins D. A. (2003) A trace metal clean reagent to remove surface-bound iron from marine phytoplankton. *Marine Chemistry* **82**, 91-99.

Tovar-Sánchez A., Duarte C. M., Alonso J. C., Lacorte S., Tauler R. and Galbán-Malagón C. (2010) Impacts of metals and nutrients released from melting multiyear Arctic sea ice. *Journal of Geophysical Research: Oceans* **115**.

Turner J., Guarino M. V., Arnatt J., Jena B., Marshall G. J., Phillips T., Bajish C. C., Clem K., Wang Z., Andersson T., Murphy E. J. and Cavanagh R. (2020) Recent Decrease of Summer Sea Ice in the Weddell Sea, Antarctica. *Geophysical Research Letters* **47**, e2020GL087127.

Twining B. S. and Baines S. B. (2013) The Trace Metal Composition of Marine Phytoplankton. *Annual Review of Marine Science* **5**, 191-215.

Twining B. S., Baines S. B. and Fisher N. S. (2004) Element stoichiometries of individual plankton cells collected during the Southern Ocean Iron Experiment (SOFeX). *Limnology and Oceanography* **49**, 2115-2128.

Twining B. S., Baines S. B., Fisher N. S., Maser J., Vogt S., Jacobsen C., Tovar-Sanchez A. and Sañudo-Wilhelmy S. A. (2003) Quantifying Trace Elements in Individual Aquatic Protist Cells with a Synchrotron X-ray Fluorescence Microprobe. *Analytical Chemistry* **75**, 3806-3816.

Vallee B. L. and Auld D. S. (1990) Zinc coordination, function, and structure of zinc enzymes and other proteins. *Biochemistry* **29**, 5647-5659.

Van Heukelem L. and Thomas C. S. (2001) Computer-assisted high-performance liquid chromatography method development with applications to the isolation and analysis of phytoplankton pigments. *Journal of Chromatography A* **910**, 31-49.

van Leeuwe M. A., Villerius L. A., Roggeveld J., Visser R. J. W. and Stefels J. (2006) An optimized method for automated analysis of algal pigments by HPLC. *Marine Chemistry* **102**, 267-275.

van Manen M., Aoki S., Brussaard C. P. D., Conway T. M., Eich C., Gerringa L. J. A., Jung J., Kim T.-W., Lee S., Lee Y., Reichart G.-J., Tian H.-A., Wille F. and Middag R. (2022) The role of the Dotson Ice Shelf and Circumpolar Deep Water as driver and source of dissolved and particulate iron and manganese in the Amundsen Sea polynya, Southern Ocean. *Marine Chemistry* **246**, 104161.

Vance D., de Souza G. F., Zhao Y., Cullen J. T. and Lohan M. C. (2019) The relationship between zinc, its isotopes, and the major nutrients in the North-East Pacific. *Earth and Planetary Science Letters* **525**, 115748.

Vance D., Little Susan H., de Souza Gregory F., Khatiwala S., Lohan Maeve C. and Middag R. (2017) Silicon and zinc biogeochemical cycles coupled through the Southern Ocean. *Nature Geoscience* **10**, 202-206.

Vaughan D. G. (2008) West Antarctic Ice Sheet collapse – the fall and rise of a paradigm. *Climatic Change* **91**, 65-79.

Vernet M., Geibert W., Hoppema M., Brown P. J., Haas C., Hellmer H. H., Jokat W., Jullion L., Mazloff M., Bakker D. C. E., Brearley J. A., Croot P., Hattermann T., Hauck J., Hillenbrand C. D., Hoppe C. J. M., Huhn O., Koch B. P., Lechtenfeld O. J., Meredith M. P., Naveira Garabato A. C., Nöthig E. M., Peeken I., Rutgers van der Loeff M. M., Schmidtko S., Schröder M., Strass V. H., Torres-Valdés S. and Verdy A. (2019) The Weddell Gyre, Southern Ocean: Present Knowledge and Future Challenges. *Reviews of Geophysics* **57**, 623-708.

Wåhlin A. K., Yuan X., Björk G. and Nohr C. (2010) Inflow of Warm Circumpolar Deep Water in the Central Amundsen Shelf. *Journal of Physical Oceanography* **40**, 1427-1434.

Wåhlin A. K., Kalén O., Arneborg L., Björk G., Carvajal G. K., Ha H. K., Kim T. W., Lee S. H., Lee J. H. and Stranne C. (2013) Variability of Warm Deep Water Inflow in a Submarine Trough on the Amundsen Sea Shelf. *Journal of Physical Oceanography* **43**, 2054-2070.

Walker D. P., Brandon M. A., Jenkins A., Allen J. T., Dowdeswell J. A. and Evans J. (2007) Oceanic heat transport onto the Amundsen Sea shelf through a submarine glacial trough. *Geophysical Research Letters* **34**, L02602.

Wang R. M., Archer C., Bowie A. R. and Vance D. (2019) Zinc and nickel isotopes in seawater from the Indian Sector of the Southern Ocean: The impact of natural iron fertilization versus Southern Ocean hydrography and biogeochemistry. *Chemical Geology* **511**, 452-464.

Wang W., Lough A., Lohan M. C., Connelly D. P., Cooper M., Milton J. A., Chavagnac V., Castillo A. and James R. H. (2021) Behavior of iron isotopes in hydrothermal systems: Beebe and Von Damm vent fields on the Mid-Cayman ultraslow-spreading ridge. *Earth and Planetary Science Letters* **575**, 117200.

Watson A. J., Meredith M. P. and Marshall J. (2014) The Southern Ocean, carbon and climate. *Philosophical Transactions of the Royal Society A: Mathematical, Physical and Engineering Sciences* **372**, 20130057.

Weber T., John S., Tagliabue A. and DeVries T. (2018) Biological uptake and reversible scavenging of zinc in the global ocean. *Science* **361**, 72.

Westerlund S. and öhman P. (1991) Cadmium, copper, cobalt, nickel, lead, and zinc in the water column of the Weddell Sea, Antarctica. *Geochimica et Cosmochimica Acta* **55**, 2127-2146.

Wilchinsky A. V. and Feltham D. L. (2009) Numerical simulation of the Filchner overflow. *Journal of Geophysical Research: Oceans* **114**.

Wombacher F., Rehkämper M., Mezger K. and Münker C. (2003) Stable isotope compositions of cadmium in geological materials and meteorites determined by multiple-collector ICPMS. *Geochimica et Cosmochimica Acta* **67**, 4639-4654.

Wyatt N. J., Milne A., Woodward E. M. S., Rees A. P., Browning T. J., Bouman H. A., Worsfold P. J. and Lohan M. C. (2014) Biogeochemical cycling of dissolved zinc along the GEOTRACES South Atlantic transect GA10 at 40°S. *Global Biogeochemical Cycles* **28**, 44-56.

Xie R. C., Galer S. J. G., Abouchami W., Rijkenberg M. J. A., De Jong J., de Baar H. J. W. and Andreae M. O. (2015) The cadmium–phosphate relationship in the western South Atlantic — The importance of mode and intermediate waters on the global systematics. *Marine Chemistry* **177**, 110-123.

Xie R. C., Galer S. J. G., Abouchami W., Rijkenberg M. J. A., de Baar H. J. W., De Jong J. and Andreae M. O. (2017) Non-Rayleigh control of upper-ocean Cd isotope fractionation in the western South Atlantic. *Earth and Planetary Science Letters* **471**, 94-103.

Xu Y. and Morel F. M. M. (2013) Cadmium in Marine Phytoplankton. In *Cadmium: From Toxicity to Essentiality.* (eds. Astrid Sigel, Helmut Sigel and R. K. Sigel). Springer, Dordrecht. pp. 509-528.

Xue Z., Rehkämper M., Schönbächler M., Statham P. J. and Coles B. J. (2012) A new methodology for precise cadmium isotope analyses of seawater. *Analytical and Bioanalytical Chemistry* **402**, 883-893.

Xue Z., Rehkämper M., Horner T. J., Abouchami W., Middag R., van de Flierd T. and de Baar H. J. W. (2013) Cadmium isotope variations in the Southern Ocean. *Earth and Planetary Science Letters* **382**, 161-172.

Yager P., Sherrell R., Stammerjohn S., Ducklow H., Schofield O., Ingall E., Wilson S., Lowry K., Williams C., Riemann L., Bertilsson S., Alderkamp A.-C., Dinasquet J., Logares R., Richert I., Sipler R., Melara A., Mu L.,

Newstead R., Post A., Swalethorp R. and van Dijken G. L. (2016) A carbon budget for the Amundsen Sea Polynya, Antarctica: Estimating net community production and export in a highly productive polar ecosystem. *Elementa: Science of the Anthropocene* **4**, 000140.

Yager P. L., Sherrell R. M., Stammerjohn S. E., Alderkamp A.-C., Schofield O., Abrahamsen E. P., Arrigo K. R., Bertilsson S., Garay D. L., Guerrero R., Lowry K. E., Moksnes P.-O., Ndungu K., Post A. F., Randall-Goodwin E., Riemann L., Severmann S., Thatje S., Van Dijken G. L. and Wilson S. (2012) ASPIRE: The Amundsen Sea Polynya International Research Expedition. *Oceanography* **25**, 40-53.

Yang H., Krebs-Kanzow U., Kleiner T., Sidorenko D., Rodehacke C. B., Shi X., Gierz P., Niu L., Gowan E. J., Hinck S., Liu X., Stap L. B. and Lohmann G. (2022) Impact of paleoclimate on present and future evolution of the Greenland Ice Sheet. *PLOS ONE* **17**, e0259816.

Yang S.-C., Lee D.-C. and Ho T.-Y. (2015) Cd isotopic composition in the suspended and sinking particles of the surface water of the South China Sea: The effects of biotic activities. *Earth and Planetary Science Letters* **428**, 63-72.

Yee D. and Morel F. M. M. (1996) In vivo substitution of zinc by cobalt in carbonic anhydrase of a marine diatom. *Limnology and Oceanography* **41**, 573-577.

Zhang F., Zhu X., Yan B., Kendall B., Peng X., Li J., Algeo T. J. and Romaniello S. (2015) Oxygenation of a Cryogenian ocean (Nanhua Basin, South China) revealed by pyrite Fe isotope compositions. *Earth and Planetary Science Letters* **429**, 11-19.

Zhang R., Jensen L., Fitzsimmons J., Sherrell R. M., Lam P., Xiang Y. and John S. (2021) Iron Isotope Biogeochemical Cycling in the Western Arctic Ocean. *Global Biogeochemical Cycles* **35**, e2021GB006977.

Zhao Y., Vance D., Abouchami W. and de Baar H. J. W. (2014) Biogeochemical cycling of zinc and its isotopes in the Southern Ocean. *Geochimica et Cosmochimica Acta* **125**, 653-672.

BIBLIOGRAPHY

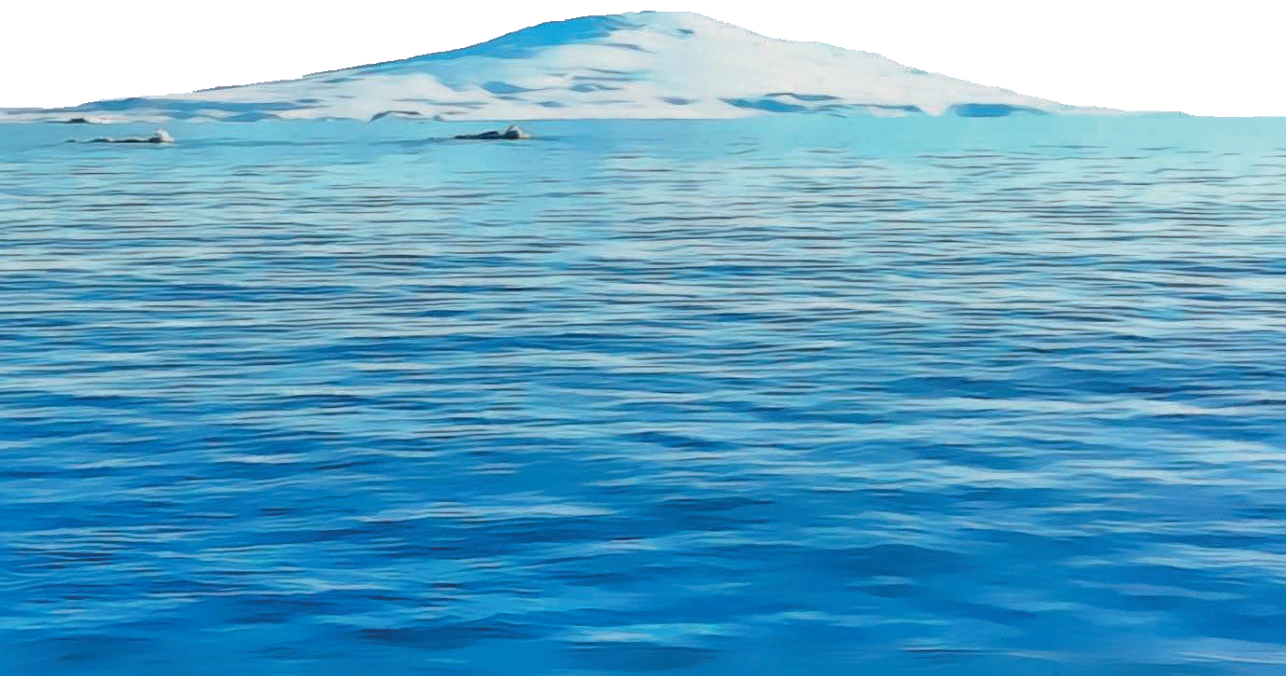

Tian H.-A., van Manen M., Reichart G.-J., Conway T. M. and Middag R. (**In preparation**) Dissolved zinc and cadmium isotope systematics in the Amundsen and Weddell coastal Antarctic marginal seas.

Tian H.-A., van Manen M., Bunnell Z. B., Reichart G.-J., Conway T. M. and Middag R. (**In preparation**) Isotopic composition of dissolved Fe in the Weddell Sea: fate of sedimentary Fe and evidence for its transport.

Tian H.-A., van Manen M., Bunnell Z. B., Jung J., Lee S. H., Kim T.-W., Reichart G.-J., Conway T. M. and Middag R. (**2023**) Biogeochemistry of iron in coastal Antarctica: isotopic insights for external sources and biological uptake in the Amundsen Sea polynyas. Geochimica et Cosmochimica Acta 363, 51-67.

Tian H.-A., van Manen M., Wille F., Jung J., Lee S., Kim T.-W., Aoki S., Eich C., Brussaard C. P. D., Reichart G.-J., Conway T. M. and Middag R. (**2023**) The biogeochemistry of zinc and cadmium in the Amundsen Sea, coastal Antarctica. Marine Chemistry 249, 104223.

van Manen M., Aoki S., Brussaard C. P. D., Conway T. M., Eich C., Gerringa L. J. A., Jung J., Kim T.-W., Lee S., Lee Y., Reichart G.-J., **Tian H.-A.**, Wille F. and Middag R. (**2022**) The role of the Dotson Ice Shelf and Circumpolar Deep Water as driver and source of dissolved and particulate iron and manganese in the Amundsen Sea polynya, Southern Ocean. Marine Chemistry 246, 104161.

Eich C., Biggs T. E. G., van de Poll W. H., van Manen M., **Tian H.-A.**, Jung J., Lee Y., Middag R. and Brussaard C. P. D. (**2022**) Ecological Importance of Viral Lysis as a Loss Factor of Phytoplankton in the Amundsen Sea, Microorganisms 10.

Liao W.-H., Takano S., **Tian H.-A.**, Chen H.-Y., Sohrin Y. and Ho T.-Y. (**2021**) Zn elemental and isotopic features in sinking particles of the South China Sea: Implications for its sources and sinks. Geochimica et Cosmochimica Acta 314, 68-84.

Takano S., Liao W.-H., **Tian H.-A.**, Huang K.-F., Ho T.-Y. and Sohrin Y. (**2020**) Sources of particulate Ni and Cu in the water column of the northern South China Sea: Evidence from elemental and isotope ratios in aerosols and sinking particles. Marine Chemistry 219, 103751.

ACKNOWLEDGEMENTS

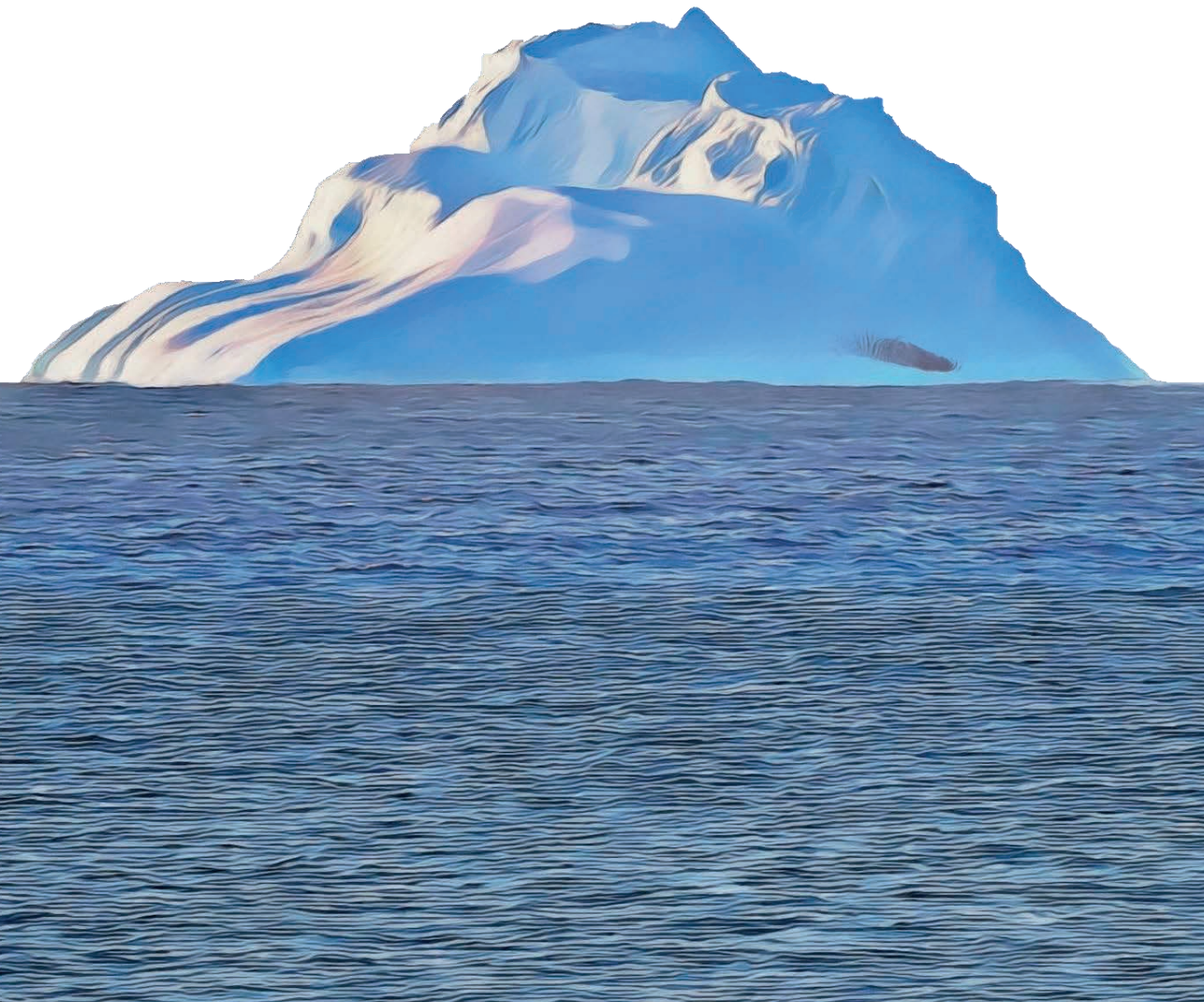

This thesis would not have seen the light of day without the amazing teamwork and the incredible support I received from the people I met along this journey. It is a product of team effort. Therefore, I would like to dedicate this section to present my sincere appreciation to them.

I would like to start with my primary supervisor **Rob**. You not only gave me this opportunity to explore the beauty of marine trace metal biogeochemistry but also walked with me through ups and downs during my adventure in the Netherlands. Working with you has been nothing but fruitful, I have learned so much knowledge about trace metals as well as how to be an independent sea-going scientist. I enjoy swinging by your office to either discuss scientific ideas or share my personal issues – no matter how busy you were, you always managed to take time to sit and chat with me. Your positive energy and patience has set a model of an excellent supervisor for me, which inspires me to be a supervisor like you if I continue as a marine scientist in the future. Writing papers with you is another particularly joyful thing, you replied quickly and gave me right amount of guidance (meaning a lot of space and flexibility for me to learn and grow while writing), which made writing fairly exciting and fun. I would like to thank you for the guidance and trust in me, I cannot be happier that you are the one with me at the end my Ph.D. journey.

My sincere thanks go to my thesis promotor **Gert-Jan**. Your insightful ideas and depth of knowledge have been invaluable throughout our many meetings. Thank you for making sure I had enough resources to conduct my study and for your consistent support at every stage. I also would like to thank you for always cheering me up while I was depressed and lack of confidence; studying abroad is not easy, but your support made it significantly more manageable.

I am very lucky to have an oversea supervisor like **Tim**. None of the discussions about isotopes in this thesis can be done without you. You are my beacon in the sea of trace metal isotopes. Working with you

has been so much fun and educational, the comments and criticisms you gave to my papers/chapters were very constructive and to-the-point; but at the same time, you always made sure to motivate me by leaving shot comments like “this is neat!” or “I really like this one!”. I remember I was extremely excited to hear that you will be my co-supervisor in my Ph.D. project as I did not get the chance to work with you when I applied for Ph.D. program at USF a year before I came to NIOZ. Guess what, you cannot get rid of me that easily. Thank you for offering me your guest room when I visited you to learn all the isotope magic you are doing in your lab. I enjoyed our chats by your swimming pool and BBQ at David’s house on 4th of July. I also appreciate that you shared many epic pictures you took for wild birds and allegators at Florida and named the allegators after me and Rob. Together with Rob, you are not only my scientific gurus, but also close friends in my personal life.

I would like to extend my heartfelt gratitude to the **members of the dissertation committee** for their invaluable dedication in reading, evaluating, and participating in the defence of this thesis, whether in person or virtually.

My experiences during the expeditions to the Southern Ocean and coastal Antarctica were truly remarkable, but they also relied heavily on the collaborative efforts of those on board. I would like to express my appreciation to **Indah**, **Sharyn**, **Charlotte**, **Sven (Pont)**, **Scott**, **Erin**, **Bram**, and **Sven (Ober)** for their help with ultra-clean CDT sampling, shipboard nutrient analysis, and bio-assay experiments, as well as the unwavering support provided by **Corina** from shore. I would also like to thank other **external scientists and crew members** who were on Korean ice braker **RV Araon** (expedition number: ANA08B) and German ice breaker **RV Polarstern** (expedition number: PS117). Your contributions played a pivotal role in ensuring the smooth sampling work. Special thank also goes to the director of DMT Marine

Equipment **Piet ter Schure**, thank you for making our ultra-clean CDT sampling on RV Aaron possible.

A big thank you to the OCS family, this family took me in six year ago and have been supportive to me ever since. In particular, I want to thank **Loes** for often inviting me for dinner at her place, looking out for my well-being. You and **Hans** have shared so much of your life experience with me, from which I learned a ton and enjoyed very much. Thank you also to **Rick**, **Peter**, **Furu,** and **Jan-Berend** for providing me tips to do a Ph.D. with plenty of fun and laughter. Additionally, I cannot appreciate enough for the help of **Patrick** and **Bas** – thank you for keeping the clean room running smoothly and being super patient whenever I had questions or samples to analyse. **Wen-Hsuan**, even though you joined NIOZ at the end of my contract, your knowledge of trace metal isotopes was priceless, and I'm seriously grateful for that. Furthermore, to my OCS fellow (previous and present) students: **Evaline**, **Linda**, **Alice**, **Hans**, and **Esmee**, thank you for helping me to settle in at my early stage here; **Sabine**, **Siham**, **Kristen**, you have made my PhD journey a blast; **Yasmina** and **Miriam**, thank you for always looking after Mochi when I was away; **Szabina**, although I was already over half way of my Ph.D. when you came on board, you understood me very well and we shared a lot of inside jokes and happiness; **Laura**, you are not just a great office mate but also an awesome friend. Our time together in and out of the office has been amazing. For other OCS members I came across in the past six years (not in particular order): **Geert-Jan**, **Sabine**, **Matthew**, **Femke**, **Henko**, **Karel**, **Wim**, **Piet**, **Bob**, **Jan**, **Margaux**, **Lara**, **Lotta**, **Rebecca**, **Matina**, **Ben**, **Louise**, **Peter**, **Nora**, **Isabel**, **Florine**, **Niek**, **Mei**, **Virginia**, **Daan**, **Guangnan**, **Daniel**, **Elodie, Iza**, **Floor**, **Laurien, Anouk**, **Marian**, **Ruth**, **Ragna**, your company has been just as important, and I'm genuinely grateful for all the good times we have shared.

My gratitude also goes to other NIOZ colleagues and friends from de Potvis and Den Helder (also not in particular order): **Eva, Marisa,**

Suzanne, **Josh**, **Su**, **Annlisa**, **Anandi**, **Emna**, **Inga**, **Tom**, **Wencong**, **Swan**, **Carlos**, **Milou**, **Hisham**, **Amin**, **Saara**, **Ionna**, **Konstantina**, **Anne (Mol)**, **Zeynep**, **Misha**, **Hebo**, **Bingjie**, **Jon, Jeras, Tim, Ginny, Cornelie, Livi, Bram, Anne (Kruijt)**. We have had some seriously epic times together, like sipping on coffee and tea in the NIOZ canteen, strolling along the Texel beach during sunsets, shooting hoops at that super rare basketball court in Den Helder, and dancing our hearts out at de Potvis bar till the sun came up. And let's not forget the precious moments with Mochi being all adorable in front of de Potvis – I would need a whole book to list all the memories we have made together!

My life outside NIOZ has been a colourful adventure, all thanks to the incredible people I have had the pleasure of meeting. In the GEOTRACE community, my appreciation goes to **Jannelle**, **Nathan**, **Gemma**, **Saša**, **Berenice** – not only did we geek out over trace metal science, but we also knew how to have fun doing what we do. I am grateful for that science brought us together. I also want to specifically thank **Matthias** for helping me with trace metal isotope analysis and double spike technique; your experience is very valuable to me. Moreover, **Zach**, thanks a million for carrying out the second-stage column chemistry for me at USF and providing your opinions on our Fe isotope paper. In the non-academic world, I would like to thank my lovely friends **Christine**, **Cherie**, **Lina**, **Femke**, **Alinde**, **Penny**, **Yandeh**, **Annemarie**, you guys were my lifeline whenever I needed a break from the endless writing and lab work. It has been an amazing ride with all of you. To my pals back in Taiwan: **阿淳**, **柏諺**, **格唯**, **豬油**, thanks for keeping me in the loop with all the news from home and having my back. I would also like to thank **姿妤** for being my rock and giving me the confidence boost I needed on this journey. Your support means the world to me.

A really big thank you goes to my family in the Netherlands and Germany. **Mathijs**, we have been through so much together, from sharing a cabin in Antarctica, hosting countless CTD sampling parties,

to travelling place to place and being cranky to each other when we spent too much time together. The company and laughter you brought into my life meant the world. I honestly cannot finish this thesis if I did not have you as my teammate. **Uli** and **David**, you guys were the first friends I made in the Netherlands, and if it were not for you, I would probably still be lost somewhere around de Potvis hunting for my house keys. Our travels around the world are etched in my heart as a vital part of my Ph.D. adventures. And celebrating Christmas with you (plus **Vivi** and **Bo**) has set the bar for a perfect holiday season. **Anna**, my partner in crime, your boundless enthusiasm for, well, everything, taught me to keep an open mind and dive into new experiences. Those sweet and bitter moments we shared will stay with me forever. **Coral**, or should I say, freshly-made Dr. Coral, I cannot thank you enough for having my back since day one. We both made it to the finish line, just like we promised each other. **Gonçalo**, you are not just a brilliant scientist but also a thoughtful friend with some seriously impressive cooking skills. You have this uncanny ability to read my mind with just a glance – I am beyond lucky to have you around. **Sofia,** you will always be my top office mate. Thanks for keeping me in check when I accidentally blurted out something inappropriate. Our friendship has been a rollercoaster of hilarity and honesty. **Fons**, my man, I met you first time at the gym and since then we have become not only gym buddy but also close friends without secrets. I wish I can use a GIF in this thesis to show how stoked I am to have you as a friend. **Tara** and **Scott** (and little **Bodhi**), you guys always had me in your thoughts, and your sweetness, genuineness, and hospitality has warmed my heart. **Lia** and **Byron** (and sassy **Bokkie**), even though we exchange inappropriate gestures on the daily, I am thankful our floofs get along, making me love you guys a bit more. **Sam**, hanging out with you has been an absolute pleasure. Your sense of humour has me in stitches, and I am so glad we crossed paths. **Ruth**, your honest and unfiltered opinions have taught me so much. Our conversations, whether meaningful or

completely random, have been a blast. **Yiting (意婷)**, our paths crossed back in Taiwan, and our journey continues in Europe. I will always remember our virtual writing sessions where we pushed each other not to give up. We both made it!

最後，我想要感謝我的爸爸，雖然海洋研究對你來說很陌生，但你仍然很努力地學習就為了要能和我溝通，感謝你這些年來的支持和鼓勵，我終於做到了！我也要感謝我的哥哥，謝謝你不斷地提供我學習的資源、激勵我成長，並且在我不在台灣的時候一肩扛下照顧家人和經濟支援的責任。還有我在台灣的所有家人，感謝你們在我迷失的時候成為我的避風港，讓我知道我不是孤單一人。

Last but definitely not least, a huge shout-out to my little floof **Mochi** for waltzing into my life. If there is one soul who has seen all my highs and lows and never once left my side, it is you. You have taught me the art of patience and love, and the happiness you have brought me far outweighs any little trouble you have stirred up. I know you probably do not understand a word of what I am typing here, but I just want to say thanks for all the love you have showered on me and for being my best co-author. I will get you some fancy canned food after my defence.

ABOUT THE AUTHOR

Hung-An Tian (Stanley) was born on 18th of October 1990, in Taitung, Taiwan. He pursued a Bachelor of Science in Oceanography at National Sun Yat-Sen University. During the final two years of his undergraduate studies, he started learning the art of trace metal science through a research project. Securing University Student Research Project Funding from the Ministry of Science and Technology, Taiwan, he conducted research on the effects of pH change in preconcentration process on the analysis of trace metal iron in natural water. Additionally, he joined a research expedition to collect natural water samples at every major estuaries in Taiwan where he carried out his very first trace-metal-clean sampling that absolutely opened his eyes to the trace metal realm. Following the completion of his bachelor's degree in 2013, Hung-An pursued a Master of Science at National Taiwan University, further exploring his

passion for trace metals. His research centered on the interaction between ^{238}U-series radionuclides (^{234}Th, ^{210}Pb, ^{210}Po) and marine particulates in the lagoon water of Dongsha Atoll, Taiwan. Engaging in fieldwork on Dongsha Island, he independently operated a motorboat to collect size-fractionated marine plankton using a multilayer apparatus system, an experience that ignited his aspiration to become a sea-going scientist. In 2015, immediately after obtaining his master's degree, Hung-An joined the Marine Biogeochemistry Laboratory at Academia Sinica, Taiwan, as a research assistant. Here, he not only became involved in the international GEOTRACES program but also conducted the chemical analysis of particulate trace metals collected from the Southeast Asian time series station.

In September 2017, Hung-An entered a Ph.D. program at Royal Netherlands Institute for Sea Research (NIOZ), expending his research focus from tropical oceans to the Southern Ocean. His doctoral research investigated the sources and biogeochemistry of bio-active trace metals and their isotopes in the Southern Ocean and coastal Antarctica. Throughout his Ph.D., he spent a cumulative four months on two research expeditions in the Southern Ocean, collecting vast quantities of seawater for trace metal isotope analysis and eventually put his feet on both floating sea ice and Antarctica. Additionally, he developed a protocol for trace metal isotope analysis with double spike technique at NIOZ. His research not only enhances our understanding of sources of trace metals and their biogeochemical processes but also provides valuable perspectives on using isotopic compositions as tools to investigate marine trace metal cycling. In September 2023, six years after joining NIOZ, Hung-An transitioned to a postdoctoral trace metal researcher at NIOZ. This time, he shifted his focus from the South Pole to the North Pole, studying the role of particulate micronutrients in marine ecosystems and their cycling in Arctic-Atlantic transition zones. He now is always making fun of himself that he has become a "bi-Polar" scientist, in a good way.

Utrecht University
Faculty of Geosciences
Department of Earth Sciences

ISSN 2211-4335